

International Journal of Thermodynamics

Editor-in-Chief

L. Kuddusi

Honorary Editors

A. Bejan

M. J. Moran

J. Szargut

G. Tsatsaronis

A. Valero

M. R. von Spakovsky

Abstracting and Indexing:

Chemical Abstracts Services, Copernicus, DOAJ, EBSCO, Emerging Sources Citation Index, Engineering Index, Google Scholar, Scopus, and ULAKBIM



***International Centre for
Applied Thermodynamics***

International Journal of Thermodynamics

<https://dergipark.org.tr/tr/pub/ijot>

Editor-in-Chief

Prof. Dr. Lütfullah KUDDUSİ

Associate Editor-in-Chief

Assoc. Prof. Dr. Patrice ESTELLÉ

Prof. Dr. Enrico SCIUBBA

Associate Editor

Prof. Dr. Ali KOSAR

Prof. Dr. Rahul TEVATIA

Prof. Dr. Derya Burcu ÖZKAN

Prof. Dr. Mustafa ÖZDEMİR

Prof. Dr. Ahmet DURMAYAZ

Assoc. Prof. Dr. Onur TAYLAN

Prof. Dr. Mehmet ARİK

Prof. Dr. Ayşegül ABUŞOĞLU

Assoc. Prof. Dr. Ersin SAYAR

Prof. Dr. Hakan Fehmi ÖZTOP

Assoc. Prof. Dr. Silvio De Oliveira JUNIOR

Editorial Board

Prof. Dr. Yasar DEMİREL

Prof. Dr. Lütfullah KUDDUSİ

Prof. Dr. Ahmet DURMAYAZ

Prof. Dr. Derya Burcu ÖZKAN

Prof. Dr. Mustafa ÖZDEMİR

Prof. Dr. Ali KOSAR

Assoc. Prof. Dr. Ersin SAYAR

Prof. Dr. Mehmet ARİK

Assoc. Prof. Dr. Abdussamet SUBASI

Daniel FAVRAT

Francois MARECHAL

Prof. Silvia Azucena NEBRA

Luis SERRA

Assoc. Prof. Dr. Onur TAYLAN

Rahul TEVATIA

Prof. Dr. Ayşegül ABUŞOĞLU

Vittorio VERDA

Assoc. Prof. Dr. Silvio DE OLIVEIRA

Gian Paolo BERETTA

Abel HERNANDEZ-GUERRERO

Nilufer EGRİCAN

Dr. Sean WRIGHT

Prof. Dr. Hakan Fehmi ÖZTOP

Assoc. Prof. Dr. Silvio De Oliveria JUNIOR

Prof. Dr. Enrico SCIUBBA

International Journal of Thermodynamics

<https://dergipark.org.tr/tr/pub/ijot>

Publishing Editor

Assoc. Prof. Dr. Abdussamet SUBASI

Assist Prof. Dr. Mustafa Yasin GÖKASLAN

Res. Assist. Ali Murat BİNARK

Language Editor

Assoc. Prof. Dr. Abdussamet SUBASI

Journal Contacts

Editor-in-Chief

Prof. Dr. Lütfullah Kuddusi

ISTANBUL TECHNICAL UNIVERSITY

kuddusi@itu.edu.tr

+902122931300/2452

*Department of Mechanical Engineering
Istanbul Technical University
Gumussuyu, 34437 Istanbul Turkey*

Volume: 26

Issue: 2

Web: <https://dergipark.org.tr/tr/pub/ijot>

International Journal of Thermodynamics (IJoT)

ISSN:1301-9724 / e-ISSN:2146-1511

CONTENTS	
<u>Research Article</u>	
1. Semi-Analytical Solution for Modelling Moving Heat Sources in a Semi-Infinite Medium with Radiative and Convective Boundary Conditions	1-11
Antonio Metallo	
<u>Research Article</u>	
2. Modelling and Simulation of Existing Geothermal Power Plant: A Case Study of Darajat Geothermal Power Plant	13-20
Kurnia Fajar Adhi Sukra, Diki Ismail Permana, Willy Adriansyah	
<u>Research Article</u>	
3. Modeling of the Vapor-Liquid Equilibria Properties of Binary Mixtures for Refrigeration Machinery	22-33
Youcef Maalem, Youcef Tamene, Hakim Madani	
<u>Research Article</u>	
4. Thermoelastic Analysis For A Thick Plate Under The Radiation Boundary Conditions	35-44
Geeta Dhameja, Lalsingh Khalsa, Vinod Varghese	
<u>Research Article</u>	
5. Thermally-Induced Stresses in a Pre-Buckling State of a Circular Plate within the Fractional-Order Framework	46-55
Geeta Dhameja, Lalsingh Khalsa, Vinod Varghese	
<u>Research Article</u>	
6. Investigation of Kalina Cycle for Power Generation from Heat Dissipation of Tarasht Power Plant	57-63
Somayyeh Sadri, S.Y.S. Mohseni	
<u>Research Article</u>	
7. Design of a Coal Drying System with Solar-Assisted Heat Pump and Waste Heat Utilisation	65-71
Mert Ökten	
<u>Research Article</u>	
8. The Effect of the Conversion Coefficients of Platinum-Based Resistance Thermometers on the Uncertainty Estimation	73-76
Fatma Melda Patan Alper	
<u>Research Article</u>	
9. Optimization of a Dry Peeling System for Tomatoes Using Approximate Solutions	78-87
Antonio Metallo	

Research Article

Semi-Analytical Solution for Modelling Moving Heat Sources in a Semi-Infinite Medium with Radiative and Convective Boundary Conditions

*A. Metallo 

Industrial Engineering Department, University of Salerno, Italy
E-mail: antonio.metallo@libero.it

Received 3 April 2022, Revised 22 February 2023, Accepted 22 February 2023

Abstract

The weld quality is highly related to the thermal history of the weld and there have been many trials to monitor the quality using an infrared (IR) sensor. To obtain the real temperature of a surface based on the brightness temperature values measured by an IR camera, the emissivity value must be derived. For an accurate assessment of the emissivity, one must be aware of the melting point isotherm. The temperature profiles only depend on three factors during laser processing, specified as constants the characteristics of the material: laser beam speed (v), laser beam diameter (d), and power (P). Predicting the width of the melted zone reached during the welding process as the parameters vary is a tool for helping a quality laser processing and for determination of true temperature in laser welding using IR camera. This study describes the semi-analytical (SA) solution of the heat conduction equation for a localized moving Gaussian heat source with constant parameters on a semi-infinite medium. The solution, simple and quick to obtain, provides information on the width of the melted zone with an average error $< 5\%$. The outcome is assessed numerically and contrasted with FEM solutions for a Gaussian source, the latter having undergone experimental validation. With two distinct defocus values, def_0 and def_6 , and by varying the speed and power settings, two separate types of experiments were run. Thus, the SA solution was obtained and compared after the FEM solution had been obtained with a good approximation (max err 4.3 %, average err 2.7 %). Only in regard to the 1AL test is an error more than 5 % detected; in the other case, the average error is 3.75 %. Two more tests at the defocus values of def_4 and def_8 were conducted to confirm the model's validity as the parameters varied. Overall, the average error between the semi-analytical and the FEM solution is 4.1%. The SA solution may be used to effectively estimate the isotherms related to the melting point of aluminum (770 K). This allows to obtain a tool which helps restoring the real temperature based on the brightness values measured by the IR camera during laser welding. At the same time, this effective tool allows to investigate the importance of different processing parameters in laser manufacturing.

Keywords: *Semi-analytical solution; laser welding; integral method; semi-infinite medium.*

1. Introduction

The temperature of the object, including laser welding is one of the key parameters of thermal processes [1,2]. The temperature and temperature gradient determine the speed of phase transitions, chemical reactions, microstructure and properties of the material [3]. During laser processing, defined as constants the properties of the material, the temperature profiles depend exclusively on three parameters: laser beam speed (v), laser beam diameter (d) and power (P).

Predicting temperatures reached during the welding process as the parameters vary is a tool for helping a quality laser processing and for determination of true temperature in laser welding using IR camera [4-5]. To restore the real temperature, based on the brightness temperature values measured by the IR camera, the emissivity must be evaluated. For this purpose, firstly, the isotherms corresponding to the melting point were calculated to compare it with the temperature distribution measured in the laser irradiation zone. The calculated and measured data were compared with the width of the melted zone. Using the melting point isotherm, the value of emissivity could be calculated, and the true temperature could be restored [6,24].

The phenomenon of laser welding has been the subject of extensive experimental and analytical study. Rosenthal [25] and Rykalin et al. [26] have studied classical solutions of the heat conduction equations. A complete reference book with analytical solutions to the heat conduction equation has been created by Carslaw and Jaeger [27]. The heat sources used in this study are point sources, line sources and plane sources since these types of geometry offer the most straightforward analytical solutions. These sources are well adapted to forecast the thermal history far from the source. They are useless, however, if they are close to the heat source as the temperature would become infinite. Eagar and Tsai [28] introduced 2D heat sources to address this issue. The first to introduce a 3D heat source, was Goldak et al. [29]. He employed finite element modeling to determine the temperature field using a pair of moving ellipsoids as heat sources. A closed form analytical solution for these types of 3D heat sources in a thick plate or a semi-infinite body was recently developed by Nguyen et al. [30,31]. The solution is particularly difficult since the mirror image approach must be employed when applying it on the finished slabs. The detailed derivation of the analytical approximation solution

for a double ellipsoidal density heat source in a finite thick plate is described by M. Van Elsen et al. in detail [32]. In this instance, the solution for the transient temperature field was determined using a complicated and time-consuming numerical approach. Thomas F. Flint et al. [33] and R.T. Forslund et al. [34] both proposed analytical solutions that take into account a moving Gaussian heat flow and a double ellipsoidal volumetric heat source, respectively. The solutions in this case, in addition to being time-consuming, only explain the transient temperature field in the components without evaluated the width of the melted zone.

The proposed SA solution simplifies the calculation of the width of the melted zone and eliminates the need for laborious numerical procedures. Using the SA solution it is possible to evaluate the isotherms corresponding to the melting point as the parameters vary. The solutions obtained approximating with a very small error (err < 5 %) the width of the melted zone. The use of a FEM model, modeled and validated by comparison with the laser tests, is certainly an alternative, but in any case presents much longer calculation times if referred to the semi-analytical solution. The solution is presented based on some assumptions and linearization.

2. Mathematical Model

A mathematical model of heat conduction overlap welding by a laser beam was developed. Assumptions and simplifications were made to reduce computational cost. As we are purely interested in the evaluation of the melting point isotherm and not other aspects, for example such as, the depth of penetration (key hole) or the study of phenomena concerning the phase change or evaporation, this assumptions can be considered valid. The main simplifications of the model are presented and discussed below;

- The phase transformations and in turn the latent heats of melting and solidification are ignored. This causes somewhat overestimated temperatures around the melting isotherm (which should consume latent heat) and vice versa underestimated temperatures around the solidification isotherm. Usually, the temperature in the central melt pool domain becomes somewhat too high. This simplification is justified by the reason that we are interested in the evaluation of the width of the melted zone.

- Thermophysical material properties are assumed to be temperature independent (though suitable mean values can be chosen in place of the values for ambient temperature).

- The heat source moves with constant speed v along x axis and its center coincide with the origin of the moving Cartesian x - y coordinate system at surface $z=0$ (Figure 1).

The beam power density profile $\dot{q}(x, y)$ is modelled by spatially superimposing several Gaussian beams in a suitable manner: $\dot{q}_g(x, y) = \frac{2 \cdot P}{\pi \cdot r_0^2} \text{Exp}\left(-\frac{2 \cdot r^2}{r_0^2}\right)$ wit $r = \sqrt{x^2 + y^2}$.

The work piece has six faces where boundary conditions have to be specified. At the bottom surface $z = \varepsilon$ and on the four lateral faces the condition of thermal insulation has been assumed, and at the top surface $z = 0$, a combined Gaussian source (\dot{q}_g) and convection-radiation boundary condition is assumed (Figure 1). The medium is assumed initially in equilibrium with the ambient at temperature $T_0 = T_\infty$.

Given the above information, the problem can now be formulated as follows. The three-dimensional, transient heat conduction equation is:

$$\frac{\partial^2 T}{\partial x^2} + \frac{\partial^2 T}{\partial y^2} + \frac{\partial^2 T}{\partial z^2} = \frac{1}{\alpha} \frac{\partial T}{\partial t} \quad (1)$$

where α is the thermal diffusivity which is described by $\alpha = k/(\rho \text{ cp})$, k is the thermal conductivity, ρ is the mass density and cp the specific heat. The initial and boundary conditions are written as:

$$T(x, y, z, 0) = T_\infty \quad (2)$$

$$\left. \frac{\partial T}{\partial x} \right|_{x=-\frac{L}{2}} = 0 \quad (3)$$

$$\left. \frac{\partial T}{\partial x} \right|_{x=\frac{L}{2}} = 0 \quad (4)$$

$$\left. \frac{\partial T}{\partial y} \right|_{y=-\frac{L}{2}} = 0 \quad (5)$$

$$\left. \frac{\partial T}{\partial y} \right|_{y=\frac{L}{2}} = 0 \quad (6)$$

$$k \left. \frac{\partial T}{\partial z} \right|_{z=0} = -\dot{q}_{gauss} + h \cdot T(x, y, 0, t) - T_\infty + \varepsilon \cdot \sigma \cdot T^4(x, y, 0, t) - T_\infty^4 \quad (7)$$

$$\left. \frac{\partial T}{\partial z} \right|_{z=\varepsilon} = 0 \quad (8)$$

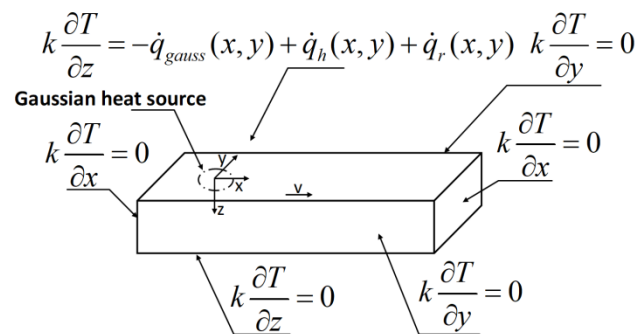


Figure 1. Model for analysis of the moving source of a bar.

If a coordinate system fixed to the heat source is chosen, according to the moving heat source theory [7], a mathematical statement of the three dimensional thermal conductive problem is:

$$\frac{\partial^2 T}{\partial x^2} + \frac{\partial^2 T}{\partial y^2} + \frac{\partial^2 T}{\partial z^2} = \frac{1}{\alpha} \left(\frac{\partial T}{\partial t} - v \frac{\partial T}{\partial x} \right) \quad (9)$$

The dimensionless energy balance equation and the related boundary conditions lead to a non-homogeneous linear problem:

$$\frac{\partial^2 \theta}{\partial \xi^2} + \frac{\partial^2 \theta}{\partial \psi^2} + \frac{\partial^2 \theta}{\partial \zeta^2} = \frac{\partial \theta}{\partial \tau} - \frac{\partial \theta}{\partial \xi} \quad (10)$$

$$\left. \frac{\partial \theta}{\partial \xi} \right|_{\xi=-\infty} = 0 \quad (11)$$

$$\left. \frac{\partial \theta}{\partial \xi} \right|_{\xi=\infty} = 0 \quad (12)$$

$$\left. \frac{\partial \theta}{\partial \psi} \right|_{\psi=-\infty} = 0 \quad (13)$$

$$\left. \frac{\partial \theta}{\partial \psi} \right|_{\psi=\infty} = 0 \quad (14)$$

$$\left. \frac{\partial \theta}{\partial \zeta} \right|_{\zeta=0} = -\frac{1}{v} \text{Exp} \left(-2 \frac{\sigma^2}{\sigma_0^2} \right) + B_i \cdot \theta(\xi, \psi, 0) + A_1 \cdot \theta^4(\xi, \psi, 0) \quad (15)$$

$$\left. \frac{\partial \theta}{\partial \zeta} \right|_{\zeta=\infty} = 0 \quad (16)$$

$$\theta \cdot \xi, \psi, \zeta, 0 = 0 \quad (17)$$

where the following dimensionless parameters have been introduced: $\theta = (T - T_\infty) / \Delta T_{\text{ref}}$ is the temperature; the group $\Delta T_{\text{ref}} = C_{\text{abs}} \cdot P / (\pi \cdot k \cdot r_0)$ is a reference temperature difference with C_{abs} representing the absorption coefficient, a reference length $x_{\text{ref}} = a/v$ and a reference radius $r_{\text{ref}} = P_1 \cdot x_{\text{ref}}$ where P_1 represents the proportionality coefficient. In this way it was possible to obtain a solution that best approximates both the maximum temperature profile and the fusion isotherm; the reference time is $t_{\text{ref}} = x_{\text{ref}}^2 / \alpha$ and reference velocity $v_{\text{ref}} = 2 \cdot a / r_0$. The dimensionless space variable was defined such as $\xi = \frac{x}{x_{\text{ref}}}$; $\psi = \frac{y}{x_{\text{ref}}}$; $\zeta = \frac{z}{x_{\text{ref}}}$; $\sigma = r / r_{\text{ref}}$, and the dimensionless time resulted $\tau = t_{\text{ref}} / t_{\text{ref}}$. Finally, dimensionless velocity resulted $v = v / v_{\text{ref}}$, $B_i = h \cdot x_{\text{ref}} / k$ is the Biot number and $A_1 = \varepsilon \cdot \sigma \cdot x_{\text{ref}} \cdot \Delta T_{\text{ref}}^3 / k$ is a dimensionless coefficient. The semi-infinite slab model is justified because x_{ref} is small compared to the sample size. Thus, it is possible to simplify the problem and evaluate a stationary solution.

3. Materials and Method

It was considered a base metal corresponding to the standard EN 45100 aluminum (Table 1). For the purposes of this work, a Yb: YAG disk laser source supplied in fiber, operating in continuous wave emission, was considered (Table 2). The movement of the laser head was performed by a 6-axis industrial robot with a dedicated controller, and an integrated 3-way power nozzle was attached to the laser head (Figure 2).

Argon was injected as a carrier gas at a flow rate of 30 L / min. The helium was coaxially blown to the laser beam at a flow rate of 10 L / min as a shielding gas on the melting bath.

A tilt angle of 4° was set for the laser head, in accordance with common practice for processing highly reflective

metals [8] to prevent rear reflections from entering the optical train. We have therefore been defined the main governance parameters and the crucial response variables to consider [9,23].

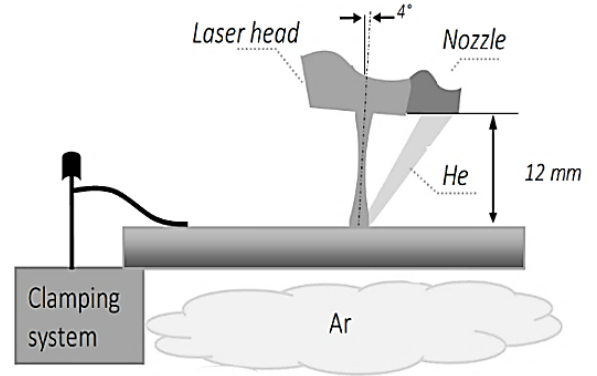


Figure 2. Schematic of the laser head with three-way feed nozzle; components not to scale.

Table 1. Nominal Chemical Composition (wt %) of Base Metals.

chemical components	%
Si	4.5÷6
Fe	0.5
Cu	2.6÷3.6
Mn	0.55
Mg	0.20÷0.45
Cr	/
Ni	0.1
Zn	0.1
Sn	0.05
Ti	0.2

This choice is usually based on both the literature and past experience. Many variables are involved in laser welding, primarily, power and welding speed since they determine the heat input to the work-piece [10].

Table 2. Welding System Technical Data.

Maximum output power [kW]	4.0
Laser light wavelength λ [nm]	1030
Beam Parameter Product [nm x mrad]	8.0
Focal beam waist d [mm]	0.3
Rayleigh range [mm]	2.81
Focal length f [mm]	200
Maximum power density [kW/mm ²]	56.6
Laser beam diameter at defocus 0 [mm]	0.3
Laser beam diameter at defocus -2 [mm]	0.44
Laser beam diameter at defocus -4 [mm]	0.71
Laser beam diameter at defocus -6 [mm]	1.11
Laser beam diameter at defocus -8 [mm]	1.32

In addition, successful laser welding requires the optimization of other parameters such as the size and the location of the focal spot. Thus, finally, defocusing d (the distance of the focal point with respect to the top surface) has been included in the experimental plan.

The range for power in the experimental plan has been decided so that the specific threshold irradiance for conduction to key-hole transition would be overcome. Sensible values for welding speed have been found via

preliminary trials in the form of bead-on-plate tests aiming at producing full penetration with no significant drop-through on the lower surface, thus matching the requirements as defined in the referred standard [11].

3.1. Numerical Modeling: Finite Element Method.

The FEM model was built using COMSOL Multiphysics software. For the correct construction of the model have been defined:

Model parameters: needed to build the numerical model such as the type of materials, sample size, wavelength, and work parameters: power, scan speed and laser beam diameter (Table. 2).

Materials' Properties: as we are interested at the temperature profile corresponding to the melting isotherm, which then develops inside the melting zone, we have chosen to use the properties at the melting temperature value for both the specific heat and the thermal conductivity coefficient [12-13], both as regards density [14-15] (Table. 1b). The absorption values were chosen for aluminum 0.23 [16,17].

Geometry and mesh modeling: One of the most important steps in FEM modeling is the definition of the mesh geometry. The geometry of the model consists of two thin sheets. A 3-D solid blocks of (40 x 30 x 6) mm³ were created. Several different grid distributions have been tested to ensure that the calculated results are grid independent. Maximum temperature differences of the fields are less than 0.1 percent by doubling the mesh nodes. The two parts are meshed using tetrahedral geometry meshes. The minimum and maximum size of the element for the mesh is 0.1 and 0.15 mm for the block where one boundary condition has been applied and 0.15 and 0.5 mm for the other (Figure 3). The complete mesh consists of 2659767 volume elements, 258806 surface elements, and 1184 elements for upper block and of 4242245 volume elements, 281738 surface elements, and 2212 elements lower block.

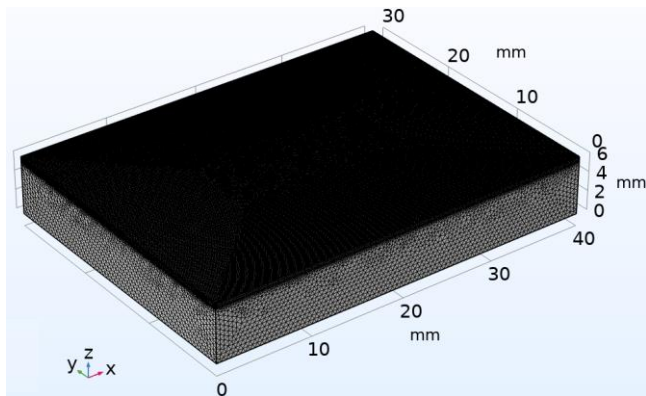


Figure 3. The minimum and maximum size of the element for the mesh.

Boundary conditions and initial condition: The laser beam incident on the surface $z = 0$ was characterized by a second type boundary condition where the imposed flux is the heat source. In addition, the third type boundary condition on face $z = 0$ was considered. In the hypothesis of natural convection, the model was given a constant thermal convection coefficient $h = 10 \text{ W m}^{-2} \text{ K}^{-1}$ [18-21]. It was also considering radiative cooling: a constant value was set $\epsilon = 0.1$ [17] for aluminum. Furthermore, the condition of thermal insulation has been assumed on the remaining surfaces. The ambient temperature and the initial temperature conditions of the plate are equal to 293 K.

Ultimately, the generation of plasma, and hence the attenuation of the beam, can be neglected since in this application, vaporization is prevented [22].

Laser beam modeling: Let us consider a thin layer, infinite in the x and y dimensions, with a thickness in the z dimension. We establish the coordinate system in such a way that the top surface of the layer is at $z = 0$ and the bottom surface is at $z = L_z$ (Figure 4).

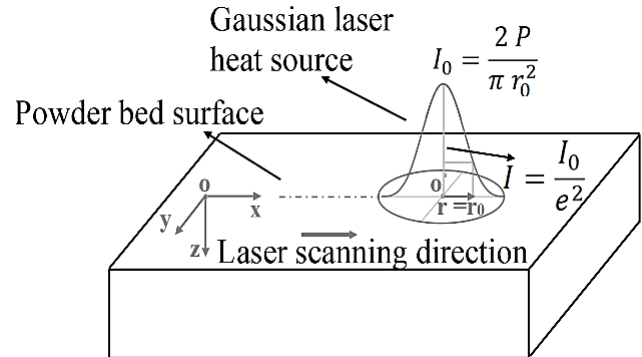


Figure 4. Sketch of the workpiece and coordinate system.

We assume that in the z -direction the heat source is concentrated at a level immediately below the upper surface ($z = 0$). The irradiation of the beam gradually decreases at the edges.

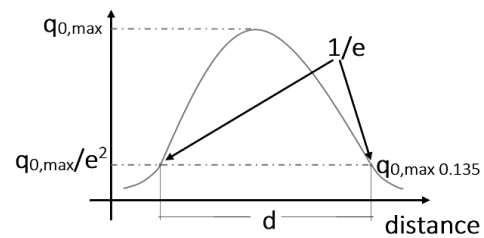


Figure 5. Gauss laser beam modelling.

Table 3. Gauss Laser Beam Modeling.

	Power in Range[%]
$\frac{2 \cdot P}{\pi \cdot r_0^2} \text{Exp} \left(-\frac{2 \cdot ((x-x_0)^2 + (y-y_0)^2)}{r_0^2} \right)$	89

To define beam width for Gaussian beams was used a 1/e2 method. The width of the beam is calculated by measuring the distance between the two points where the intensity is 1/e2 of the peak value (Figure 5, Table 3). So only about 86.5 % of the laser power is contained within the 1/e2 width (Eq. (18)).

$$\int_{x=-\sigma}^{\sigma} \int_{y=-\sigma}^{\sigma} \dot{q}_{gauss}(x, y) \cdot dx dy = 86.5 \% P \quad (18)$$

4. Result and Discussion

4.1 Experimental Tests

Two types of tests were carried out at different defocus values as shown in Table 4. A rectangular section plate of sizes (Lx=100 x Ly=50 x Lz=6 mm) was used.

Each test was analyzed under an electron microscope which made it possible to obtain an image of the trace in TIF format (Figure 6). The traces were divided 17 parts at 4 mm

intervals. For each section the size of the trace , mean values and standard deviations were evaluated (Table 5).

Table 4. Welding system technical data.

	Power P [W]	welding speed v [mm s ⁻¹]	Defocus def [mm]	Beam Diameter d [mm]
1AL	2500	50	0	0.30
2AL	3000	50	0	0.30
3AL	3000	35	0	0.30
5AL	3500	50	-6	1.01
8AL	3750	40	-6	1.01
9AL	4000	40	-6	1.1

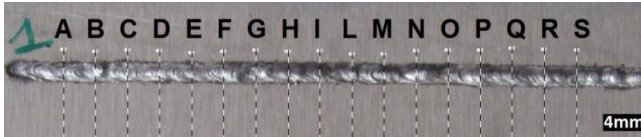


Figure 6. Test IAL Width of the Melted Zone Sections.

Table 5. Mean Value of a Width of the Melted Zone IAL.

Sez.	s[mm]	Sez.	s[mm]
a	2.26	m	2.57
b	2.34	n	2.49
c	2.34	o	2.44
d	2.16	p	2.57
e	2.34	q	2.39
f	2.55	r	2.39
g	2.34	s	2.39
h	2.49	Mean	2.40
i	2.34	Dev.St	0.11
l	2.31		

These results (Table 6) will be used to validate the numerical model. For this purpose the isotherms corresponding to the melting point (ρ_y) were calculated used through the finite element method.

Table 6. Mean Value of a Width of the Melted Zone

Test	Width of the melted zone w_z [mm]	Dev. st
1AL	2.40	0.11
2AL	2.58	0.15
3AL	2.88	0.15
5AL	2.87	0.10
8AL	3.18	0.13
9AL	3.40	0.08

The calculated ρ_y data were compared with the width of the melted zone (w_z).

4.2 FEM Result

The simulation process allowed us to extrapolate the maximum temperature and the values corresponding to the fusion isotherm (770 K) on the plane at $z = 0$ (Figure 7).

The data were fitted using an ellipsoidal model (Tables 7-8) where the coefficients have been defined in (Table 9).

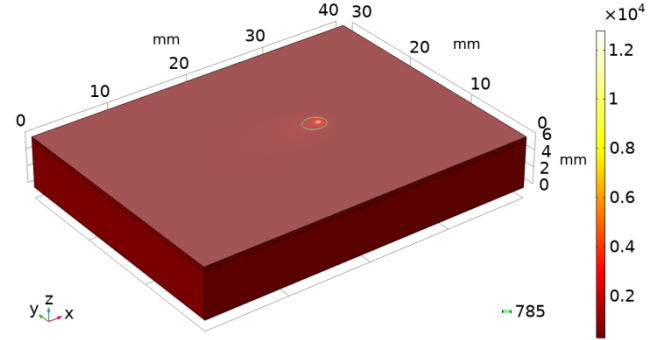


Figure 7. FEM result: Test IAL weld track.

Table 7. Coordinate of the Best Fit Ellipse.

$$x(r) = X_0 + a \cdot \cos \theta_r$$

$$y(r) = Y_0 + b \cdot \sin \theta_r$$

$$0 \leq \theta_r \leq 2 \cdot \pi$$

Table 8. Structure that Defines the Best Fit Ellipse.

a	sub axis (radius) of the X axis of the non-tilt ellipse
b	sub axis (radius) of the Y axis of the non-tilt ellipse
ϕ	orientation in radians of the ellipse (tilt)
X_0	center at the X axis of the non-tilt ellipse
Y_0	center at the Y axis of the non-tilt ellipse
ρ_x	size of the long axis of the ellipse
ρ_y	size of the short axis of the ellipse

In this way it was possible to quickly obtain the value of the diameter of the isotherms corresponding to the melting ρ_y .

Table 9. Fit Parameter FEM.

	1AL	2AL	3AL	5AL	8AL	9AL
a	1.372	1.573	1.519	1.733	1.803	1.881
b	1.159	1.324	1.378	1.481	1.600	1.664
X_0	9.525	9.401	8.057	9.326	8.380	8.339
Y_0	9.999	9.999	10.000	9.999	10.000	9.999
ρ_x	2.744	3.147	3.038	3.467	3.607	3.763
ρ_y	2.318	2.649	2.756	2.961	3.201	3.329
Err %	0.110	0.257	0.419	0.075	0.093	0.184
Tmax [K]	5977	6418	6823	14294	1694	17096
Dev.St [K]	45	57	50	320	290	300

As shown in the figure for the type of test with defocus 0, being characterized by a smaller spot diameter, they have a higher power concentration, which translates into higher temperature profiles as regards the maximum temperature (Figures 8-9, Table 9).

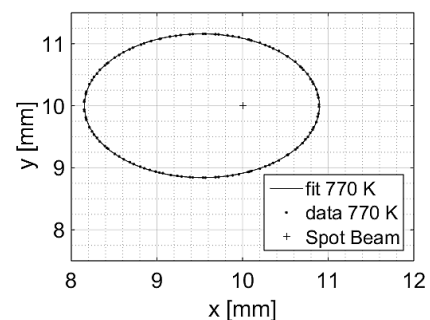


Figure 8. Test IAL, isotherms corresponding to the melting point, FEM data fit at time = 0.1 s.

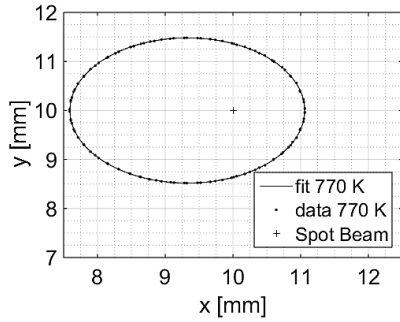


Figure 9. Test 5AL, isotherms corresponding to the melting point, FEM data fit at time = 0.1 s; T_{max} on $z=0$ plane.

In addition, to the same spot beam, the extension of the melted zone and therefore the diameter of the fusion isotherm increases as the maximum temperature reached increases. As shown in Figure 10,

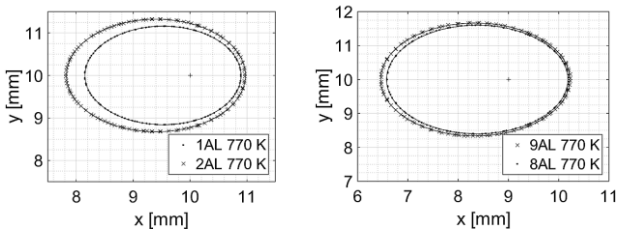


Figure 10. Comparison between isotherms corresponding to the melting point FEM test 1AL vs 2AL; 8AL vs 9AL.

fixed beam diameter and scan speed, as the power delivered by the laser increases, the T_{max} and the extension of the diameter corresponding to the melting temperature increase. Once the beam diameter and laser power are fixed, the maximum temperature reached during laser welding increases as the scan speed decreases. Consequently, the diameter ρ_y also increases with decreasing speed (Figure 11).

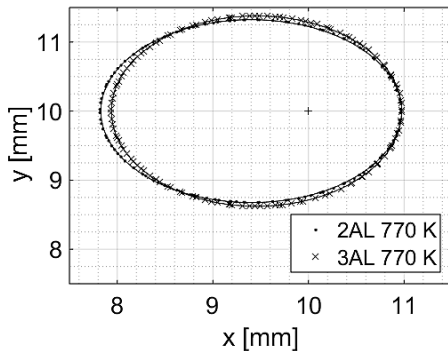


Figure 11. Comparison between isotherms corresponding to the melting point, FEM test 2AL vs 3AL.

The timing of the transient extinction is very little, about 0.01 s for defocus def_0 and 0.04 s for defocus def_6 , just as we expected. Therefore, for each test, the percentage error between the isotherms corresponding to the melting point (ρ_y numerically evaluated) and the extension of the melted zone (w_z , obtained through experimental tests) was evaluated.

As shown in the Table 10, the error for all types of tests presents an error below 5%. Thus, we can say that the constructed FEM model can provide a useful approximation to reality with a low average error.

Table 10. Isotherm Corresponding to the Melting Point Compared with the Width of the Melted Zone.

	Tmax[K]	Dev.st	ρ_y	wz	Err %
1AL	14294	320	2.3183	2.40	3.46
2AL	16945	290	2.6490	2.58	2.64
3AL	17096	300	2.7568	2.88	4.37
5AL	5977.8	45	2.9619	2.87	3.15
8AL	6418.9	57	3.2010	3.18	0.65
9AL	6823.8	50	3.3293	3.40	2.10

4.3 Semi-Analytical Solution

In order to linearize the radiative boundary condition, an average temperature was chosen to ensure that the relationship between the radiative and the convective contribution remains approximately the same.

$$\begin{aligned} \dot{Q}_r &= 4 \cdot \varepsilon \cdot \sigma \cdot A T^4(x, y, z, t) - T_p^4 \\ &\approx 10^{-1} \cdot 10^{-8} \cdot 10^{-5} \cdot 10^{16} = 10^2 \end{aligned} \quad (19)$$

$$\dot{Q}_c \approx 10 \cdot 10^{-5} \cdot 10^4 = 1 \quad (20)$$

As it is possible to observe the ratio between $\frac{\dot{Q}_r}{\dot{Q}_c} = 100$.

Consequently

$$\frac{\dot{Q}_r}{\dot{Q}_c} = \frac{h_r A T^4(x, y, z, t) - T_p^4}{h_c A T^4(x, y, z, t) - T_p^4} = \frac{h_r}{h_c} = 100 \quad (21)$$

The temperature that would allow to obtain a radiative heat exchange coefficient about 100 times the convective one was therefore chosen as the reference temperature for the linearization. Since a convective heat exchange coefficient of $10 \frac{W}{m^2 \cdot K}$ was chosen:

$$\dot{Q}_{r,l} = h_r A T^4(x, y, z, t) - T_p^4 \quad (22)$$

$$T_r = 4000 \text{ K} \Rightarrow h_r = 4 \cdot \varepsilon \cdot \sigma \cdot T_r^3 \approx 10^3 \left[\frac{W}{m^2 \cdot K} \right] \quad (23)$$

In this way the ratio between radiatively and convectively exchanged thermal power is kept unchanged, with the advantage of being able to linearize the radiative boundary condition as follows:

$$\begin{aligned} \left. \frac{\partial \theta}{\partial \zeta} \right|_{\zeta=0} &= -\frac{1}{v} \text{Exp} \left(-2 \frac{\sigma^2}{\sigma_0^2} \right) \\ &+ Bi \cdot \theta(\xi, \psi, 0) + Bi_r \cdot \theta(\xi, \psi, 0) \end{aligned} \quad (24)$$

Since the problem is linear, in stationary case, the solution can be sought as the sum of two partial solutions $\theta_1(\zeta)$ and $\theta_2(\xi, \psi)$, with the first affected by a non-homogeneity arising from the Gaussian heating source. Then, the two partial solutions have to satisfy two distinct problems derived from the basic one:

$$\left\{ \begin{array}{l} \frac{\partial^2 \theta_1}{\partial \zeta^2} = 0 \\ \frac{\partial \theta_1}{\partial \zeta} \Big|_{\zeta=0} = -\frac{1}{v} \text{Exp} \left(-2 \frac{\sigma_r^2}{\sigma_0^2} \right) \\ \quad + Bi \cdot \theta_1(0) + Bi_r \cdot \theta_1(0) \\ \frac{\partial \theta_1}{\partial \zeta} \Big|_{\zeta=3} = 0 \end{array} \right. \quad (25)$$

$$\left\{ \begin{array}{l} \frac{\partial^2 \theta_2}{\partial \xi^2} + \frac{\partial^2 \theta_2}{\partial \psi^2} + \frac{\partial \theta_2}{\partial \xi} = 0 \\ \frac{\partial \theta_2}{\partial \xi} \Big|_{\xi=-3} = 0 \\ \frac{\partial \theta_2}{\partial \xi} \Big|_{\xi=3} = 0 \\ \frac{\partial \theta_2}{\partial \psi} \Big|_{\psi=-3} = 0 \\ \frac{\partial \theta_2}{\partial \psi} \Big|_{\psi=3} = 0 \end{array} \right. \quad (26)$$

Numerically, the value 3 has been chosen as the extreme of integration to infinity, as it has been verified that at the value of 3 x_{ref} the temperature remains almost fixed at the initial value. The analytical solution of the problem 1.1a was obtained:

$$\theta_1 \zeta = -\frac{e^{-2 \frac{\sigma_r^2}{\sigma_0^2}} - 3 + \zeta}{v \cdot 1 + 3Bi + 3Bi_r} \quad (27)$$

The second problem was solved by applying the integral method. It was possible to obtain the solution of problem 2 by choosing an approximate solution that makes explicit the dependence of the spatial variable:

$$\theta_2^+ \xi, \psi = a \psi \cdot \text{Exp} \left(-v \frac{\xi + \psi}{P_2} \right) \quad (28)$$

Equation 2 has been integrated into the spatial coordinate and ξ :

$$\int_{\xi=0}^{\xi=3} \left(\frac{\partial^2 \theta_2}{\partial \xi^2} + \frac{\partial^2 \theta_2}{\partial \psi^2} + \frac{\partial \theta_2}{\partial \xi} \right) \cdot d\xi = 0 \quad (29)$$

By imposing that the approximate analytic equation satisfies the integral and applying a boundary conditions, we obtain:

$$\frac{\left(\text{exp} \left(-\frac{v \cdot \psi}{P_2} \right) - \text{exp} \left(-\frac{v \cdot 3 - \psi}{P_2} \right) \right)}{P_2 \cdot v} \cdot v \cdot -P_2 + 2 \cdot v \cdot a \psi + P_2 \cdot -2 \cdot v \cdot a' \psi + P_2 \cdot a'' \psi \quad (30)$$

$$\begin{aligned} \text{b.c.1} \quad \frac{\partial \theta_1 \zeta + \theta_2^+ \xi, \psi}{\partial \psi} \Big|_{\psi=0} &= 0 \\ \Rightarrow -\frac{\text{exp} \left(-\frac{v \cdot \xi}{P_2} \right) \cdot v \cdot a}{P_2} + \text{exp} \left(-\frac{v \cdot \xi}{P_2} \right) \cdot a' &= 0 \end{aligned} \quad (31)$$

$$\begin{aligned} \text{b.c.2} \quad \theta_1 \zeta + \theta_2^+ \xi, 3 &= 0 \\ \Rightarrow -\frac{\text{exp} \left(-\frac{2 \cdot \sigma_r^2}{\sigma_0^2} \right) \cdot -3 + \zeta}{v \cdot 1 + 3Bi + 3Bi_r} \\ + \text{exp} \left(-\frac{v \cdot 3 + \xi}{P_2} \right) \cdot a \cdot 3 &= 0 \end{aligned} \quad (32)$$

The solution $a(\psi)$ were obtained:

$$\begin{aligned} a \psi &= \frac{\text{Exp} \left(-3 \frac{v}{P_2} + \frac{3 \cdot \sqrt{P_2^2 \cdot P_2 - v \cdot v}}{P_2^2} + \frac{v \cdot 3 + \xi}{P_2} - \frac{2 \cdot \sigma_r^2}{\sigma_0^2} \right)}{\left(1 + \text{Exp} \left(\frac{6 \cdot \sqrt{P_2^2 \cdot P_2 - v \cdot v}}{P_2^2} \right) \right) \cdot v \cdot 1 + 3Bi + 3Bi_r} \\ &+ \text{Exp} \left(\frac{P_2 \cdot v - \sqrt{P_2^2 \cdot P_2 - v \cdot v} \cdot \psi}{P_2^2} \right) \\ &+ \text{Exp} \left(\frac{P_2 \cdot v + \sqrt{P_2^2 \cdot P_2 - v \cdot v} \cdot \psi}{P_2^2} \right) \cdot (3 + \zeta) \end{aligned} \quad (33)$$

and therefore the complete solution:

$$\begin{aligned} \theta_{sa} \xi, \psi \zeta &= \theta_1 \zeta + \theta_2^+ \xi, \psi = \\ &-\frac{\text{Exp} \left(-2 \frac{\sigma_r^2}{\sigma_0^2} - 3 + \zeta \right)}{v \cdot 1 + 3Bi + 3Bi_r} + a \psi \cdot \text{Exp} \left(-v \frac{\xi + \psi}{P_2} \right) \end{aligned} \quad (34)$$

4.4 Semi-Analytical Solution Results

The solution was obtained using, for the two types of tests (def₀-def₆), different parameter values as shown in the Table. 11. The coefficients P₁ and P₂ have been introduced in order to obtain a valid solution for all defocus values and therefore for each radius beam value (r). Remembering to have defined $x_{ref} = \frac{\alpha}{v}$, therefore independent of r_{ref} , we noticed how, by choosing the radius of the spot as reference, the solution was strongly dependent on this value, allowing to obtain a solution valid only for a fixed value of r.

Table 11. Proportionality Coefficients.

def	P1	P2
0	0.142857	11.5
-6	0.337838	10.9

We have therefore done so to link r_{ref} to x_{ref} and to the defocus value through the coefficients P1 and P2. After obtaining the temperature profile corresponding to the $z = 0$ plane (Figure 12) using a semi-analytical solution, the isothermal surface corresponding to 770 ° K was obtained (Figure 13).

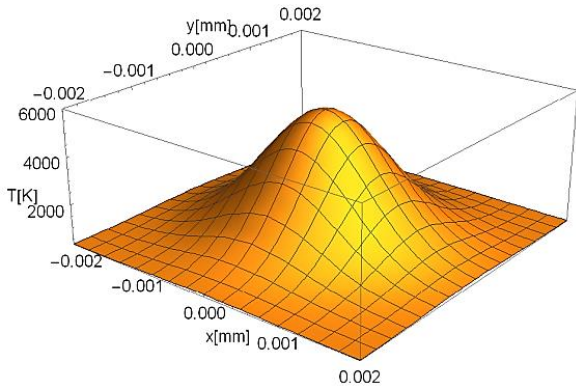


Figure 12. SA 5AL Temperature profile corresponding to the $z = 0$ plane.

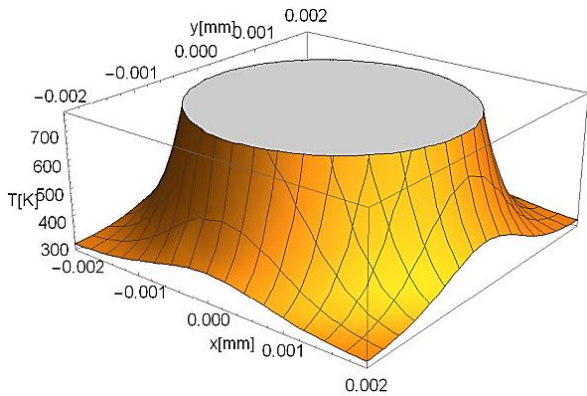


Figure 13. SA 5AL Temperature profile corresponding to the $z = 0$ plane; isothermal surface corresponding to 770 K.

Also, in this case the data have been fitted using an ellipse (Table 12).

Table 12. Fit Parameter –SA.

	1AL.	2AL	3AL	5AL	8AL	9AL
a	1.302	1.337	1.336	1.642	1.669	1.691
b	1.264	1.298	1.318	1.538	1.602	1.622
X_0	9.550	9.700	8.190	9.400	8.500	8.500
Y_0	10.00	10.00	10.00	10.00	10.00	10.00
ρ_x	2.603	2.674	2.673	3.285	3.339	3.382
ρ_y	2.528	2.596	2.636	3.077	3.204	3.245
w_z	2.40	2.58	2.88	2.87	3.18	3.40
Fit Err %	0.38	0.47	0.39	0.38	0.39	0.42
Tmax [K]	13932	16670	16690	5589	6095	6434

and subsequently the profiles of the isotherms were compared (Figures 14-16).

From the comparison it is evident that the error on ρ_y is very small (Table 13). As well as for the maximum temperature. Significantly greater is the error on ρ_x , but not relevant in this study and for our purposes.

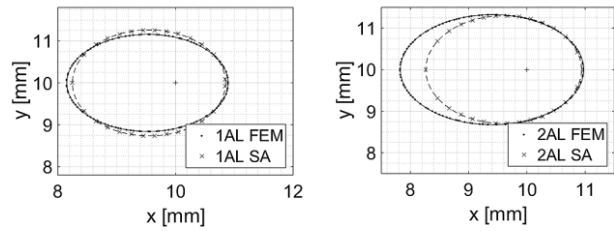


Figure 14. Isotherms corresponding to the melting point FEM vs SA; 1AL, 2AL.

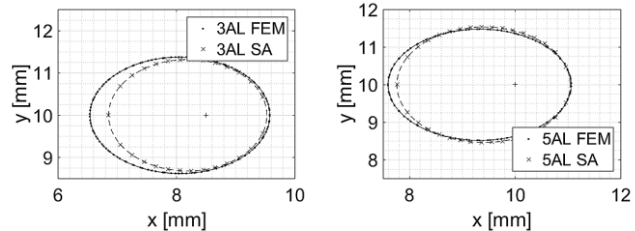


Figure 15. Isotherms corresponding to the melting point FEM vs SA; 3AL, 5AL.

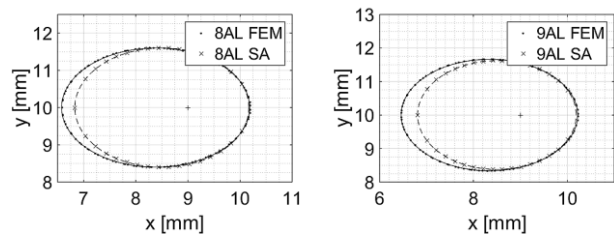


Figure 16. Isotherms corresponding to the melting point FEM vs SA; 8AL, 9AL.

Table 13. Comparison of Numerical and Semi-Analytical Solutions.

	FEM		SA		Err %	
	Tmax [K]	ρ_y [mm]	Tmax [K]	ρ_y [mm]	Tmax [K]	ρ_y [mm]
1AL	14294	2.318	13932	2.528	2.5	8.5
2AL	16945	2.649	16670	2.596	1.6	3.2
3AL	17096	2.756	16690	2.636	2.4	4.4
5AL	5977.8	2.961	5589	3.076	6.7	3.8
8AL	6418.9	3.201	6095	3.204	5.1	0.1
9AL	6823.8	3.329	6433	3.245	5.8	2.5

An error greater than 5% is found only in relation to the 1AL test, while the average error is equal to 3.75 %. In order to obtain a solution that is also valid for different defocus values, the coefficients P1 and P2 have been linearly interpolated to the respective defocus values def_0 and def_6 , and the relations $P_1(def)$ and $P_2(def)$ have been obtained :

$$\begin{cases} P_1(def)=0.0314 \cdot def+0.1493 \\ P_2(def)=-0.1 \cdot def+11.5 \end{cases} \quad (35)$$

Two further tests were then carried out at the defocus values def_4 , def_8 using the respective coefficients as shown in Table.14.

Table 14. Test Coefficients and Parameters.

	P1	P2	P[W]	v [mm·s ⁻¹]	def[mm]	d[mm]
4AL	0.2749	11.1	3000	50	-4	0.71
6AL	0.4005	10.7	3500	50	-8	1.32

First, the semi-analytical solution was evaluated, extrapolating the temperature profiles corresponding to the fusion isotherm (Table 15, Figures 17-18).

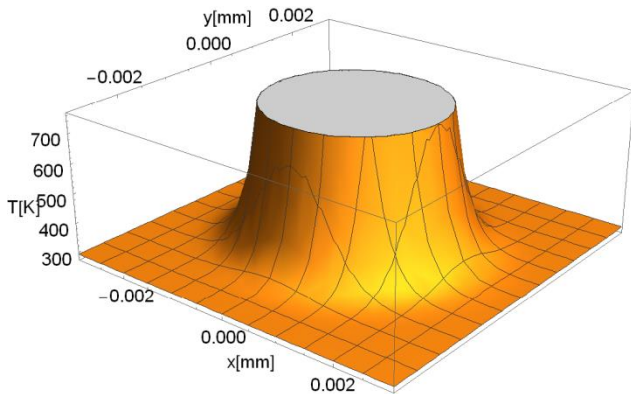


Figure 17. SA, test 4AL, Temperature profile corresponding to the $z = 0$ plane. ; isothermal surface corresponding to 770 K.

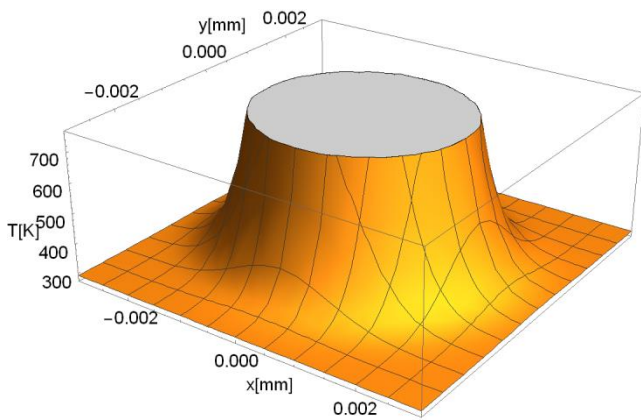


Figure 18. SA, test 6AL, Temperature profile corresponding to the $z = 0$ plane; isothermal surface corresponding to 770 K.

Table 15. Fit Parameter –de focus -4,-8. FEM Tests.

	4AL.		6AL	
	FEM	SA	FEM	SA
a	1.534	1.493	1.764	1.725
b	1.329	1.421	1.497	1.593
X_0	9.422	9.400	9.351	9.400
Y_0	9.999	10.000	10.000	10.000
ρ_x	3.067	2.986	3.529	3.067
ρ_y	2.659	2.821	2.993	3.126
Fit Err %	0.29	0.51	0.34	0.54
w_z [mm]	2.60	2.60	2.87	2.87
Err %	2.2	5.1	4.1	8.1
T_{max} [K]	7393	7159	4547	4479
Dev.St [K]	55.7	/	29.5	/

Subsequently after having carried out the tests through FEM simulation and extrapolated the profiles corresponding to the fusion isotherm (Table 15),

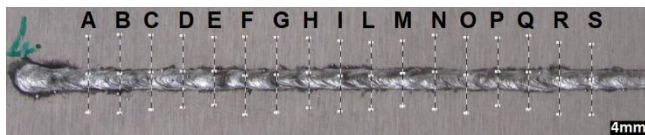


Figure 19. Test 4AL welding trace.

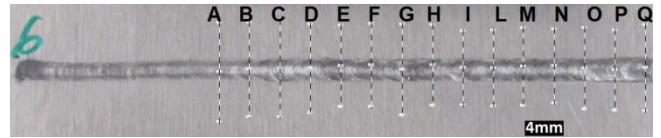


Figure 20. Test 6AL welding trace.

and it is compared to the width of the melt zone derived from experimental tests (Figures 19-20). Also in this case the error is less than 5%. Overall, the FEM tests were assessed with a maximum inaccuracy of 4.3% and an average err of 2.7%.

The isotherms corresponding to the melting point, obtained through FEM simulation and semi-analytical solution, are then compared (Table 16, Figures 21-22).

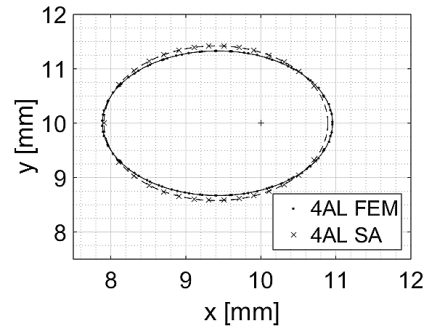


Figure 21. Isotherms corresponding to the melting point, FEM vs SA at time = 0.3 s Test 4AL..

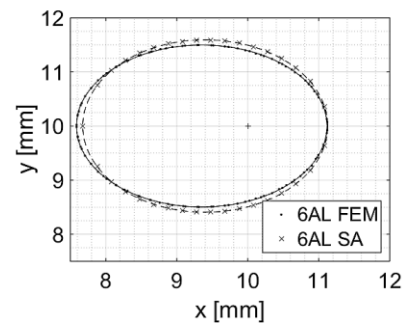


Figure 22. Isotherms corresponding to the melting point, FEM vs SA at time = 0.3 s Test Test 6AL.

Table 16. Tests at de focus -4,-8. FEM vs SA.

		ρ_y [mm]	ρ_y err %	T_{max} [K]	T_{max} err %
4AL	SA	2.821	6	7159	3.2
	FEM	2.993		4547	
6AL	FEM	2.659	4.3	7393	1.5
	SA	3.126		4479	

In this case the error is slightly higher (Table 16), but by appropriately modifying the proportionality coefficients it is possible to obtain a more accurate solution. Nonetheless, the total average error remains at an acceptable 4.1%.

5. Conclusions

We have seen how the semi-analytical solution recovers, with a small error, the value of the width of the melted zone. The semi-analytical solution has a strong dependence on the parameters involved, in particular on the value of the diameter of the laser beam. This means that having chosen the trial function for a given defocus value, the solution is valid only for the combined values of P and v at that fixed def value. In order to make the solution valid also for other defocus values, the proportionality coefficients have been

introduced. In particular, the coefficient P_1 refers to the reference quantity $r_{ref} = P_1 \cdot x_{ref}$, and serves to correct the value of ρ_y , while the coefficient P_2 , referred to the trial function, has an effect on the maximum temperature.

So, after defining the proportionality coefficients to the defocus def_0 and def_6 values, the coefficients P_1 and P_2 have been linearly interpolated to the respective defocus values, and the relations P_1 (def) and P_2 (def) have been obtained. In this way it was possible to use a single trial function capable of providing a well approximated solution (err 5%), in terms of maximum temperature and ρ_y , as the working parameters (P , v , d) vary. This allowed it to value the emissivity [35] after setting parameters and measuring the width of the melted zone ($w_{mz} = \rho_y$) by SA solution.

Nomenclature

d	Beam diameter	mm
r_0	Beam radius	mm
def	Focal beam waist	mm
v	Welding speed	mm s ⁻¹
w_z	Width of the melted zone	mm
ρ_y	Isotherm corresponding to the melting point	mm
P	Laser power	W
L_x	Slab length	mm
L_y	Slab width	mm
L_z	Slab depth	mm
C_{abs}	Absorption coefficient	/
k	Thermal conductivity	W m ⁻¹ K ⁻¹
h	Thermal convection coefficient	W m ⁻² K ⁻¹
ε	Emissivity	/
ρ	Mass density	Kg m ⁻³
α	Thermal diffusivity coefficient	m ² s ⁻¹
c_p	Specific heat.	J kg ⁻¹ K ⁻¹
a	Radius of the X axis of the non-tilt ellipse	mm
b	Radius of the Y axis of the non-tilt ellipse	mm
φ	Orientation of the ellipse (tilt)	rad
X_0	Center at the X axis of the non-tilt ellipse	mm
Y_0	Center at the Y axis of the non-tilt ellipse	mm
ρ_x	Size of the long axis of the ellipse	
P_1	Proportionality coefficients	/
P_2	Proportionality coefficients	/
θ	Dimensionless temperature	/
ΔT_{ref}	Reference temperature	K
x_{ref}	Reference length	mm
r_{ref}	Reference radius	mm
t_{ref}	Reference time	s
v_{ref}	Reference velocity	m s ⁻¹
ξ	Dimensionless space variable	/
ψ	Dimensionless space variable	/
ζ	Dimensionless space variable	/
FEM	Finite element method	/
B_i	Biot number	
\dot{q}_g	Gaussian source	W m ⁻³




References:

- [1] P. Kumar, A. N. Sinha, "Studies of temperature distribution for laser welding of dissimilar thin sheets through finite element method", *J Braz. Soc. Mech. Sci., Eng.* 40, 455, 2018.
- [2] M Miccio, R. Pierri, G. Cuccurullo, A. Metallo, P. Brachi, "Process intensification of tomato residues drying by microwave heating: experiments and simulation", *Chem. Eng. Process. Process Intensif.*, 156, 2020.
- [3] I. Smurov, M. Doubenskaia, *Laser-Assisted Fabrication of Materials*, Springer Series in Materials Science 161, 373-422, 2013.
- [4] T. Staudt, E. Eschner, M. Schmidt, "Temperature determination in laser welding based upon a hyperspectral imaging technique", *Manufacturing Technology*, CIRP Annals, 68 (1), 225-228, 2019.
- [5] M. Doubenskaia, M. Pavlov, S. Grigoriev, I. Smurov, "Definition of brightness temperature and restoration of true temperature in laser cladding using infrared camera", *Surface and Coatings Technology* 220, 244-247, 2013.
- [6] D. Rosenthal, *The Theory of Moving Sources of Heat and its Application to Metal Treatments*, Metals Handbook, 1981, 9th Ed., TranSASME, 68, pp. 3515-3528. 17 ASM, Metal Park, OH 1946.
- [7] V. Alfieri, F. Caiazzo, V. Sergi, "Autogenous laser welding of AA2024 aluminum alloy: Process Issues and Bead Features", *Procedia CIRP*, 33, 2015.
- [8] A. M. Leitner, T. Leitner, A. Schmon, K. Aziz, G. Pottlacher, "Thermophysical Properties of Liquid Aluminum", *Metall Mater Trans A* 48, 3036-3045, 2017.
- [9] Q. G. Meng, H. Y. Fang, J. G. Yang, S. D. Ji, "Analysis of temperature and stress field in Al alloy's twin wire welding", *Theoretical and Applied Fracture Mechanics*, 44 (2), 178-186, 2005.
- [10] E. Kaschnitz, W. Funk, T. Pabel, "Electrical resistivity measured by millisecond pulse-heating in comparison to thermal conductivity of the aluminum alloy Al-7Si-0.3Mg at elevated temperature", *High Temperatures-High Pressures*, 43 (2), 175-191, 2014.
- [11] K. Narender, A. S. M. Rao, K. G. K. Rao, N. G. Krishna, "Temperature Dependence of Density and Thermal Expansion of Wrought Aluminum Alloys 7041, 7075 and 7095 by Gamma Ray Attenuation Method", *Journal of Modern Physics*, 4 (3), 2013.
- [12] M. Bjelić, K. Kovanda, L. Kolařík, M. N Vukićević, "Numerical modeling of two-dimensional heat-transfer and temperature-based calibration using simulated annealing optimization method: Application to gas metal arc welding", *Thermal Science*, 20, 255-265, 2016.
- [13] C. Ratti, A. S. Mujumdar, *Infrared Drying*, Handbook of Industrial Drying by Taylor & Francis Group, LLC, 2006.
- [14] J. Heigel, P. Michaleris, E. Reutzel, "Thermo-mechanical model development and validation of directed energy deposition additive manufacturing of Ti-6Al-4V", *Addit. Manuf.*, 5, 9-19, 2015.

- [15] Z. Fan, L. Frank, "Numerical modeling of the additive manufacturing (AM) process of titanium alloy", *Titanium Alloys—Towards Achieving Enhanced Properties for Diversified Applications*, A.K.M. Ed., 3–28, 2012.
- [16] R. Paschotta, *Encyclopedia of Laser Physics and Technology*, Wiley-VCH: Berlin, Germany, 2008.
- [17] K. Suresh Kumar, T. Sparks, F. Liou, "Parameter determination and experimental validation of a wire feed Additive Manufacturing model", *International Solid Freeform Fabrication Symposium*, Austin, TX, USA, 2015.
- [18] C. Wen, I. Mudawar, "Experimental investigation of emissivity of aluminum alloys and temperature determination using multispectral radiation thermometry (MRT) algorithms", *J. Mater. Eng. Perform.*, 11, 551–562, 2002.
- [19] W. Steen, J. Mazumder, *Laser Material Processing*, Springer: Berlin, Germany, 2010.
- [20] AWS, *Specification for Fusion Welding for Aerospace Applications*, American Welding Society, Miami, Fla, USA, 2001.
- [21] W. W. Duley, *Laser welding*, John Wiley and Sons Inc., New York, 1999.
- [22] M. Doubenskaia, I. Zhirnov, V. I. Teleshevskiy, Ph. Bertrand, I. Smurov, "Determination of True Temperature in Selective Laser Melting of Metal Powder Using Infrared Camera", *Materials Science Forum*, 834, 93-102, 2015.
- [23] A. Mosavia, F. Salehib, L. Nadaie, Z. Karoly, N. Gorjid, "Modeling the temperature distribution during laser hardening process", *Results in Physics*, 16, 2020.
- [24] J. Sundqvist, A.F.H. Kaplana, L. Shachaf, C. Kongc, "Analytical heat conduction modelling for shaped laser beams", *Journal of Materials Processing Tech.*, 247, 48–54, 2017.
- [25] D. Rosenthal, "Mathematical theory of heat distribution during welding and cutting", *Weld. J.*, 20 (5), 220–234, 1941.
- [26] N. Rykalin, A. Uglov, A. Kokora, O. Glebov, *Laser Machining and Welding*, Mir Publishers, Moscow, 1978.
- [27] H. Carslaw, J. Jaeger, *Conduction of Heat in Solids*, Oxford Science Publications, 1990.
- [28] T.W. Eagar, N.S. Tsai, "Temperature fields produced by traveling distributed heat sources", *Weld. J.* 62 (12), 346–355, 1983.
- [29] J. Goldak, A. Chakravarti, M. Bibby, *A double ellipsoid finite element model for welding heat sources*, IIW Doc. No. 212-603-85, "A new finite element model for welding heat sources", *Metall Mater Trans B* 15, 299–305, 1984.
- [30] N.T. Nguyen, A. Otha, K. Matsuoka, N. Suzuki, Y. Maeda, "Analytic solutions for transient temperature of semi-infinite body subjected to 3-D moving heat sources", *Weld. Res. Suppl.*, 265–274, 1999.
- [31] N.T. Nguyen, Y.-W. Mai, S. Simpson, A. Otha, "Analytical approximate solution for double ellipsoidal heat source in finite thick plate", *Weld. Res.*, 82–93, 2004.
- [32] M. Van Elsen, M. Baelmans, P. Mercelis, J.P. Kruth, "Solutions for modelling moving heat sources in a semi-infinite medium and applications to laser material processing", *International Journal of Heat and Mass Transfer*, 50 (23), 4872–4882, 2007.
- [33] T. F. Flint, J. A. Francis, J. R. Yates, "Analytical solutions of the transient thermal field induced in finite bodies with insulating and convective boundary conditions subjected to a welding heat source", *Transactions, SMiRT-22*, San Francisco, California, USA, 2013.
- [34] R. Forslunda, A. Snisa, S. Larsson, "Analytical solution for heat conduction due to a moving Gaussian heat flux with piecewise constant parameters", *Appl. Math. Model.*, 66, 227-240, 2019.
- [35] A. Metallo, "Emissivity Prediction for an IR Camera During Laser Welding of Aluminum", *International Journal of Thermodynamics*, 25(4), 24-34, 2022.

Research Article

Modelling and Simulation of Existing Geothermal Power Plant: A Case Study of Darajat Geothermal Power Plant

K. F. A. Sukra¹, D. I. Permana^{2*}, W. Adriansyah³

¹Research Center for Transportation Technology, National Research and Innovation Agency, South Tangerang, 15314, Indonesia

²Doctoral School of Mechanical Engineering, Hungarian University of Agriculture and Life Science, 2100 Godollo, Hungary

²Department of Mechanical Engineering, Institut Teknologi Nasional Bandung, 40124 Bandung, Indonesia

³Thermodynamic Laboratories, 3rd floor PAU Building, Institut Teknologi Bandung, 40116 Bandung, Indonesia
E-mails: ¹kurnia.fajar.adhi.sukra@brin.go.id , ^{2*}dicky91permana@itenas.ac.id , ³willy.adriansyah@gmail.com

Received 19 May 2022, Revised 27 January 2023, Accepted 26 February 2023

Abstract

The electrical energy needs grow every year, increasing awareness and use of renewable energy even higher. Geothermal power plants (GPP) are even ogled as a renewable energy source that has a lot of potential worldwide. Technology for GPP continues to evolve. However, tools for analyzing a system of GPP are still inadequate. In this study, a simple analysis tool was designed. The usefulness of this analysis tool is to be able to know the state of the GPP works. This tool will help simulate the conditions that may occur in the plant system. The simulation results will also be known operating conditions that may occur, so the operator can determine what should be done if things happen. Modeling started using Microsoft Excel, which has been equipped with thermodynamic properties. Modeling includes turbine, condenser, cooling tower, and extraction systems non-condensable gas. After validated, the model run simulation in variations that may occur such as decline in the condition of the condenser and cooling tower and environmental conditions, represented by relative humidity. The simulation with variation of condition will decrease the power generated from turbine 3 – 5%.

Keywords: Geothermal energy; design; simulation; power loss; environmental relative humidity.

1. Introduction

The world's energy needs are increasing daily along with the increase in the world's population, including in every sector in Indonesia as shown in the Figure 1. PT PLN, as the actor in the energy supply policy in Indonesia, issued a policy to electrify areas spread across Indonesia. Renewable energy sources will be used, such as solar, wind, water, biomass, geothermal, and non-renewable energy sources, such as coal, oil, and natural gas [1,2].

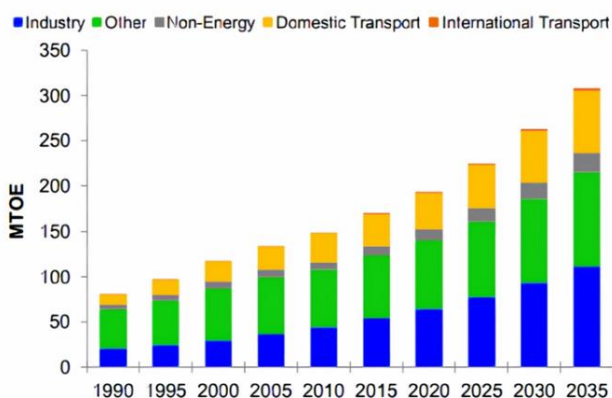


Figure 1. Indonesia's energy sector need [3] (Figure is in color in the on-line version of the paper).

However, the energy sources available in Indonesia are very diverse and quite abundant. Technology to process energy sources that will run out is already quite advanced and Table, but renewable energy now needs to be further developed so that there is no dependence on non-renewable energy sources. In line with this, the government through the directorate of Energy and Mineral Resources in the field of Renewable Energy (EBTKE) has also made a policy targeting the development of 23% renewable energy by 2025 [2].

Geothermal technology has long been developed worldwide and is considered one of the most reliable and provide a clean source of energy [4], especially in Indonesia, with about 29,164 MWe potential and only around 1341 MW is installed [5]. Geothermal energy uses heat energy stored in the earth, which is now expected to be clean renewable energy and can be used for various purposes such as heating district [6,7], agriculture [8,9], and energy generation [10–14]. However, the geothermal power plant (GPP) is quite sensitive to changes in air conditions because the working fluid is cooled using ambient air. When there is a change in environmental conditions, there will be a change in the power generated by the turbine. Michaelides [15] has conducted a study of the effect of ambient temperature fluctuation on the performance of GPP and the result is temperature of the GPP changes result in more than 20% of

power fluctuations. Kahraman et al [16] conduct a thermodynamic and thermo-economic analysis of air-cooled GPP and determined the effect of ambient temperature variation to GPP performance. While Sohel [17] changes the outlet temperature of the condenser with the ambient temperature, vaporized equilibrium pressure and temperature will be change. Lastly Rudyanto et al [18] conducted a study case in Kamojang GPP in Indonesia, where he varies of ambient temperature from 17 to 20 °C.

Moreover, the literature study about ambient temperature in geothermal research is mostly related to secondary application such as binary cycle [19,20], Kalina cycle [21,22], organic Rankine cycle (ORC) and hybrid cycle [23,24].

From the available literature review[15,25–27], few authors study modeling from existing geothermal plants and simulating variables from ambient temperature with the resulting GPP performance. The lack of tools for quick, simple, and comprehensive analysis and simulation of a geothermal power generation system makes it difficult to carry out a basic analysis. The tool is needed to carry out initial analysis and possible steps to be taken if there is a change or deviation in operating conditions. The tool will make it easier for operators and users to predict changes in the generating system to some changes in environmental conditions. In this study, the authors conduct research in the form of making a tool to analyze the performance of a geothermal generating system so that it will be easier to make decisions if there is a change in circumstances from what has been determined and how to deal with it.

2. Darajat Geothermal Power Plant

The Darajat GPP is about 22 kilometers west of Garut, West Java. This geothermal region is roughly 10 kilometers southwest of the Kamojang geothermal field. Darajat is comparable to Kamojang in that it has a vapor-dominated reservoir. In this regard, these two reservoirs differ from Indonesia's more frequent geothermal water-dominated reservoir. The Darajat geothermal power plant has three units that generate a total of 270 MW. Darajat Unit I, which began operations in 2000, produces 55 MW; Darajat Unit II, which began construction in 2004 and began operations in 2007, produces 95 MW; and Darajat Unit III produces 121 MW.

Chevron owns Darajat and Gunung Salak before to the acquisition of Star Energy and Indonesia Power. Chevron is the world's largest geothermal producer, with 1273 MW capacity, and it created almost 27% of global geothermal power [32] Darajat generates energy using a dry-steam power plant due to its vapor-dominated reservoir. Steam from the reservoir rises to the surface and passes through a pressure regulator valve, which maintains a constant pressure. The steam travels into the scrubber through this valve, which enhances its quality by removing moisture. Dry steam pours into a turbine, spinning the turbine blade. The spinning of the turbine is what allows the generator to generate power. To keep the system running, steam from the exhaust turbine goes into the condenser.

We choose Darajat GPP as case study due to simplicity of the system. We would like to model simple analysis tool to help the operator know the condition of their GPP. The Darajat GPP still active as base load supply for Java, Madura, and Bali power transmission and one of the biggest renewable power plants in Java Island.

3. Methods

The implementation of this tool begins with obtaining operating data of the GPP system which can be used for modelling and validating the model that has been made. Furthermore, modelling is carried out for each equipment and merging the equipment into a single generating system. The modelled equipment includes turbines, condensers, cooling towers, and non-condensable gas extraction systems.

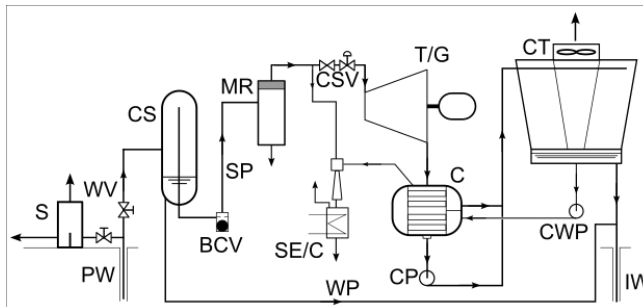


Figure 2. GPP schematic diagram [28].

Figure 22 and Figure 33 shows the scheme of the GPP system to be used as well as the Ts diagram of the geothermal power plant process. PW is a production well where water vapor is obtained and will be used as a working fluid. WV is valve while S is silencer. CS is a cyclone separator that separate the vapor phase and liquid phase so that only pure steam enters the flow from the separator to the MR, mist remover, to get the steam as clean as possible to flow into the turbine. SE/C is a steam ejector/condenser that removes non-condensable gas in the condenser, C, which works using part of the steam for the turbine, T. CP and CWP are pumps for circulation between the condenser and cooling tower, CT. Finally, the water will be put back into the bowels of the earth through IW, injection well.

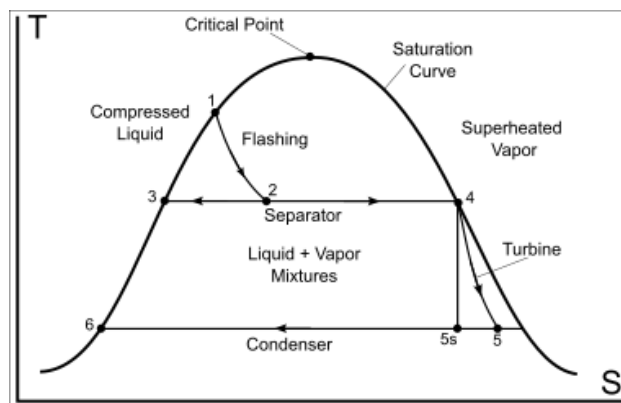


Figure 3. GPP T-s diagram [28].

3.1 Steam Turbine Model

This turbine modelling includes turbine efficiency factor ($\eta_{Turbine}$). The efficiency is obtained from the calculation of the operating conditions that are already running. From the operating data, the enthalpy value of the steam leaving the turbine can be determined. From this enthalpy value, turbine efficiency can be calculated under these conditions [29]. Turbine efficiency is used as a parameter in the next turbine modelling. Equation (1) is used for turbine modelling.

$$\eta_{Turbine} = \frac{h_4 - h_5}{h_4 - h_{5s}} \quad (1)$$

$$\dot{W}_{Turbine} = \dot{m}_4(h_4 - h_5) = x_2 \dot{m}_1(h_4 - h_5) \quad (2)$$

3.2 Condenser Model

The steam from the turbine expansion will go directly to the condenser. The steam is cooled and then injected into the bowels of the earth. The condenser used in this model is a direct contact type, where the steam coming out of the turbine is directly in contact with the cooling fluid in the form of water which is sprayed on the top of the condenser. The cooling tower cools the water leaving the condenser. Figure 4 shows the condenser modelling system used.

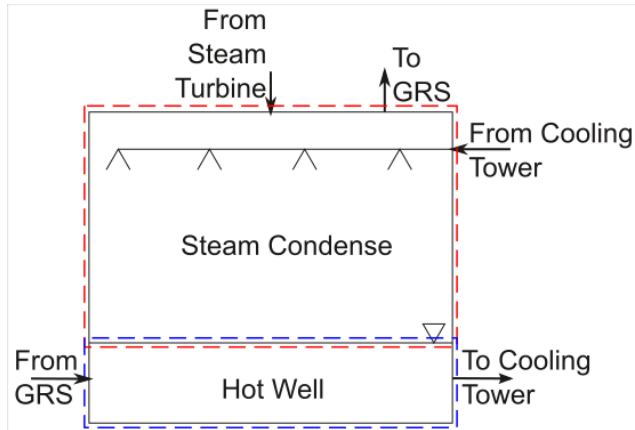


Figure 4. Condenser model.

The condenser system used is direct contact type. The condenser is modelled in the direct contact heat transfer process section and the hot well section. Figure 44 shows the division of the condenser modelling process; the condensation section is modelled by the direct contact process between steam from the turbine and water from the cooling tower in a saturated condition so that the final condition is water in a saturated liquid condition. Meanwhile, in the hot well section, the bottom part is modelled by mixing conditions between water from the gas removal system (GRS) and saturated liquid conditions because of cooling steam and water to cool so that an equilibrium condition of water temperature will be obtained which will flow into the cooling tower. The cooling water requirement can be calculated using the equation below.

$$\dot{m}_{cw} = x_2 \dot{m}_1 \left| \frac{h_5 - h_6}{c_p(T_6 - T_{cw})} \right|, \quad (3)$$

The pressure in the condenser is usually made as vacuum as possible so that the power generated by the turbine can be as large as possible. In steam from geothermal heat, there is usually gas that cannot be condensed and will collect in the condenser, which will impact the pressure in the condenser [29,30]. To prevent this, a GRS system is needed to remove the gas.

3.3 Cooling Tower Model

The next modelled component is the cooling tower. The cooling tower serves to prepare cooling water for the condenser by cooling the water from the condenser using ambient air. The ability of the cooling tower is very dependent on environmental conditions; changes in environmental conditions will cause the cooling water to be inappropriate and may reduce the power produced by the turbine. Figure 55 is a modelling form for a cooling tower system.

The cooling tower system is modelled into two parts. The fogging section and the hot well section. At the top is the cooling water from the condenser, which is atomized and mixed with the ambient air. The cooled water is partly carried away by the environmental air and partly down to the hot well. The ambient air that cools the water from the condenser will increase in humidity, so that the air leaving the cooling tower will become saturated with water. Increasing the moisture level in the air will reduce the cooling effectiveness of the cooling tower.

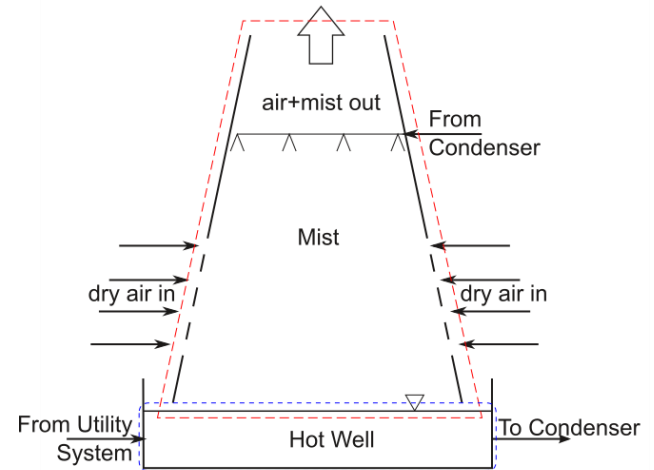


Figure 5. Cooling tower model.

Figure 6 shows a schematic diagram of a cooling tower. Using the principle of energy conservation, we get the equation (4); the heat removed will be equal the heat absorbed by the working fluid. The water coming from the steam condensate will be cooled by the outside air, but some of the water will be carried away until the air condition comes out to reach its saturation point. Water not carried will fall into the blow-down or reservoir and flow to the condenser.

$$\dot{m}_7 h_7 - \dot{m}_8 h_8 = \dot{m}_d h_d - \dot{m}_a h_a + \dot{m}_b h_b, \quad (4)$$

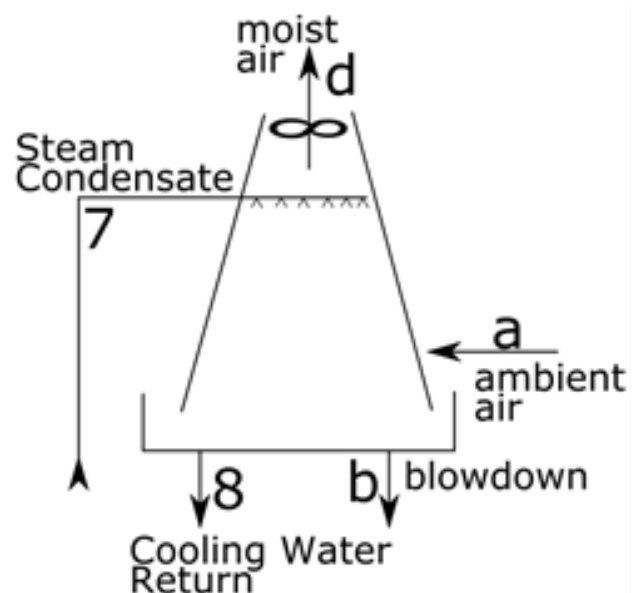


Figure 6. Simple schematic of cooling tower [29].

3.4 Gas Removal System

The GRS configuration consists of an ejector, inter condenser, liquid ring vacuum pump (LRVP), and after

condenser. The components that will be modelled in this study are only the ejector and inter condenser. Figure 7 shows a schematic diagram of the GRS.

The ejector modelling process uses a system done in previous studies [31]. It begins by considering the need for motive steam or the main steam which is part of the steam going to the turbine. To obtain the steam requirement, a compression ratio with a specific value is used for a particular ejector, because, in the ejector the parameters are determined from the dimensions and operating area which are quite narrow. In addition, it is necessary to determine the entrainment ratio for the two fluids. The entrainment ratio formula [32] can be calculated using equation (5). After obtaining the entrainment ratio of each fluid, then the total air equivalent (TAE) is calculated by adding up the product of the mass flow rate and the entrainment ratio for the two fluids or can be seen in equation (6). NCG is a non-condensable gas, MS is the main vapor stream.

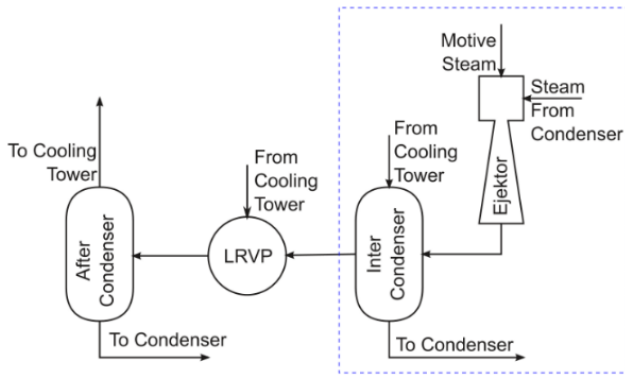


Figure 7. Gas removal system schematic diagram.

$$ER_f = \left[(5,73 \times 10^{-4} + 18,36) + \frac{2,01 \times M_f^{0,86}}{18,36 + M_f^{0,86}} \right] \quad (5)$$

$$TAE = \dot{m}_{NCG} \cdot E_{NCG} + \dot{m}_{MS} \cdot E_{MS}, \quad (6)$$

Furthermore, the calculation of the compression ratio and degree of expansion is carried out. The compression ratio (E) is the pressure ratio between the ejector outlet pressure and the non-condensable gas pressure or the pressure in the condenser. While the degree of expansion (K) is the ratio of the main vapor pressure to the pressure of the non-condensable gas or can be seen in equation (7).

$$E = \frac{P_{ejector}}{P_{NCG}} \quad (7)$$

$$K = \frac{P_{MS}}{P_{NCG}} \quad (8)$$

The value of the compression ratio and the degree of expansion then matched on the graph (Figure 88) to get the ratio of air to steam so that the steam needed for the ejector will be obtained.

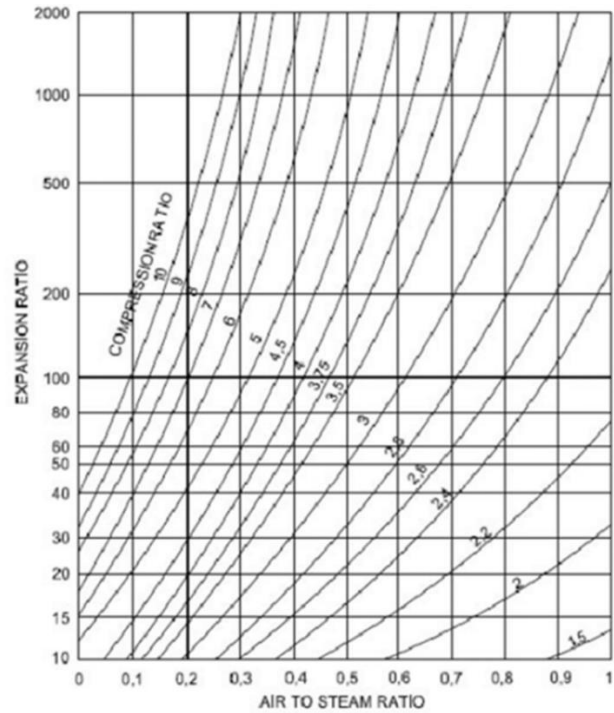


Figure 8. Air to steam ratio[32,33].

3.5 Geothermal Power Plant System

After all components can be modelled into interconnected system. The system modelling scheme is carried out in the following steps.

1. Enter the operating condition data of the entire system.
2. The P_{cond} is obtained from the model. The $T_{cond,out}$ value from the modelling results is used for input to the cooling tower components, as well as for the GRS system.
3. After the $T_{cooling}$ enters the cooling tower, the calculation of the cooling tower model is known to obtain input data for the condenser. This value is used as a convergence criterion for the iteration process so that the difference between the new and previous counts has a difference of 0.1%.

Table 1. Model Validation to Actual Condition.

Parameter	Unit	Model Result	Actual Condition	Differences
P_{cond}	bar	0.1055	0.1050	+0.0005 (0.48%)
$T_{cond,out}$	°C	43.81	43.80	+0.01 (0.02%)
$T_{cooling}$	°C	25.53	25.5	+0.03 (0.11%)
$P_{ejector,suct}$	bar	0.099	0.098	+0,001 (0.11%)
$P_{ejector,out}$	bar	0.196	0.22	-0,024 (10.82%)
$\dot{m}_{ejector}$	kg/h	4980	4980	0
$T_{intercond, out}$	°C	43.33	45.50	-2.17 (4.76%)
$W_{turbine}$	MW	56.42	55	+1.42 (2.58%)

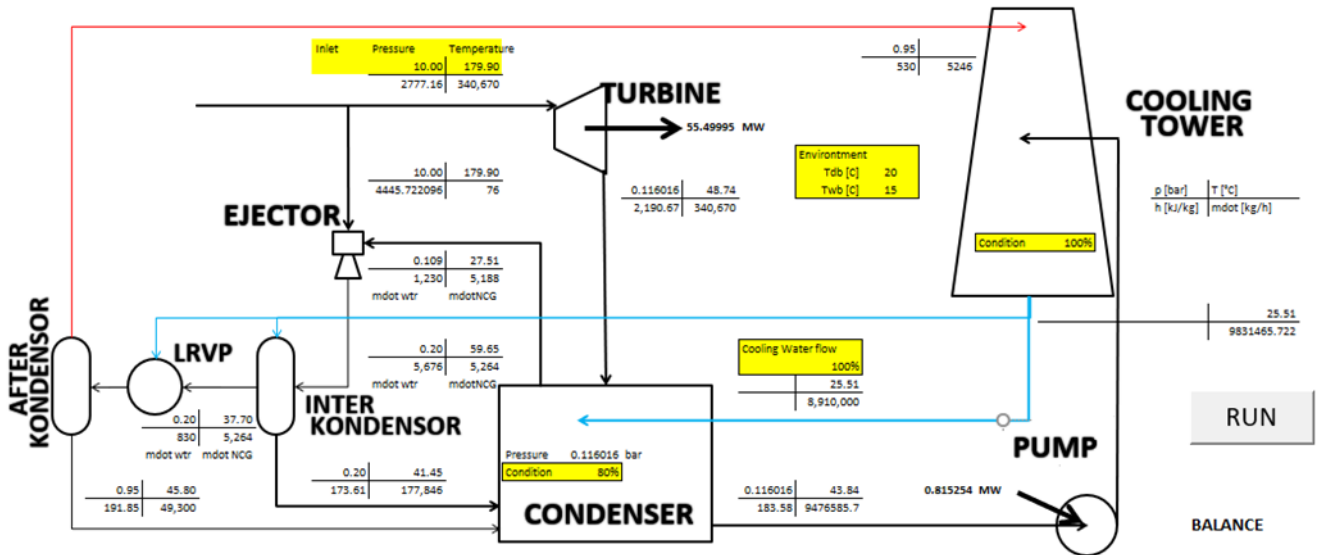


Figure 9. GPP model diagram.

4. Results and Discussion

Figure 9 show the GPP p model that used in this simulation. The simulations were carried out on existing modeling in Microsoft Excel coupled with Coolprop using three parameters; variations in condenser conditions represented by UA_{Cond} , variations in cooling tower capabilities represented by UA_{CT} , and variations in environmental conditions, especially variations in humidity represented by relative humidity (RH).

4.1 Model Validation

After each component has been successfully modelled and can be combined into a unified system that can iterate, the final schematic diagram of the analysis tool is obtained. The condition of the cooling tower and condenser is whether the condition of the two equipment can work properly or not. Wet and dry bulb represent the environmental condition. After the GPP system model can operate properly, validate the data from the modelling results and the actual operating conditions of the system as shown in Table 1.

In the modelling conditions, there is a significant difference in the ejector outlet pressure. This may be due to the difference between the modelling conditions that do not reflect the actual condition of the ejector itself. To get more precise conditions and according to actual conditions, it is necessary to conduct further research related to ejector modelling.

4.2 Results of Air Relative Humidity Variation

As we can see in Figure 10, shows the results of variations in relative humidity to turbine power and condenser pressure using a validated model. The increase in the relative humidity of the ambient air will increase the condenser pressure which decrease the turbine power produced. This shows that environmental conditions impact turbine performance, so environmental conditions need to be observed to know the changes that occur in the GPP system. GPP is very dependent on environmental conditions used to cool water by air from the surrounding environment. The cooled water is used to cool the water vapor in the condenser. Environmental conditions that are not by the initial design conditions will have an impact on turbine performance. This model shows by varying the relative humidity of the environmental air. The relative humidity parameter is used

because in the cooling tower, the relative humidity has an important factor in lowering the water temperature.

Figure 10 shows the impact of changes in environmental conditions on changes in condenser pressure that occur in the modelling in this study. The condenser pressure is related to the temperature of the cooling water entering the condenser to cool the water vapor. When the ability of the ambient air to cool the cooling water in the cooling tower decreases, indicated by an increase in relative humidity, the temperature of the cooling water entering the condenser will increase. This condition causes an increase the pressure in the condenser. This condenser pressure increment will decrease the turbine power generated. This is because the pressure influence the expansion process of water vapor in the turbine. If the condenser pressure increases, the steam expansion process will not be optimal and reduce the turbine power. Increasing the relative humidity of the ambient air by up to 90% will reduce turbine power by up to 2.26%. Jian li et al shows that the increase of air relative humidity will decrease the power generated in geothermal power plant. The power generated in geothermal power plant sensitive to the ambient condition in the view of relative variation [34].

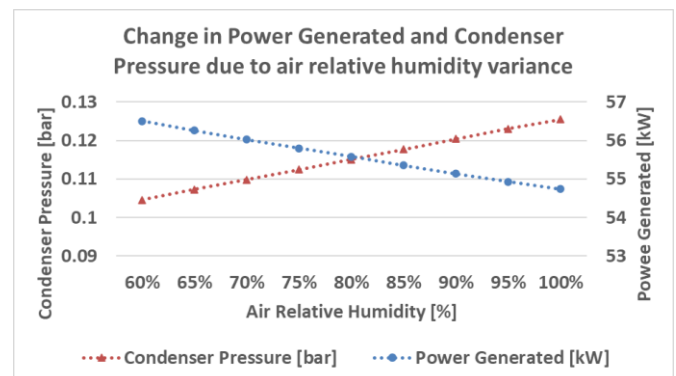


Figure 10. Change in power generated and condenser pressure due to air relative humidity variance (Figure is in color in the on-line version of the paper).

4.3 Result of Condition Cooling Tower Variation

The next simulation is to change condition on the cooling tower. The value of UA_{CT} physically can be likened to the condition of the cooling tower. How well the cooling tower can cool the water that will later be used in the condenser. This simulation does not consider changes that occur in the

environment. Changes condition can be caused by a decrease in the number of working nozzles, and the presence of dirt in the packing section.

The parameter to be reviewed first is the change that occurs in the condenser pressure. Figure 11 illustrates the effect of changing the cooling tower condition on the condenser pressure. As with the worse condition of cooling tower will increase the pressure in the condenser. Even if the condition of the cooling tower decreases to 60%, the condenser pressure is close to the operating limit. If the cooling tower condition continues to be lowered until the condenser working pressure limit is reached, which is 0.015 bar, then the cooling tower condition limit is 56%. In this condition, the condenser will turn off.

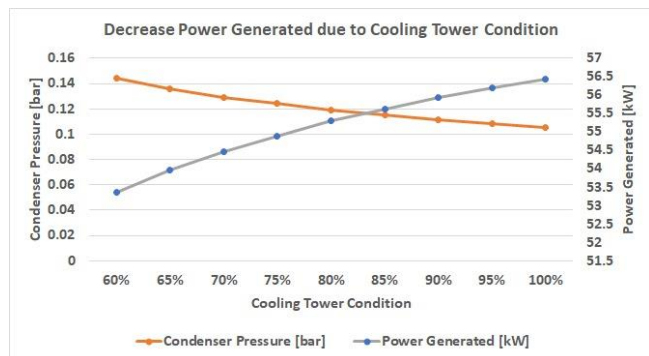


Figure 11. The effect of cooling tower condition to the change of condenser pressure and power generation (Figure is in color in the on-line version of the paper).

Meanwhile the blue line show in Figure 11 shows the relationship between changes in the cooling tower condition to the turbine power generated by this generator system model. The turbine power produced will decrease as the condition of cooling tower worsened.

4.4 Result of Condition Condenser Variation

The amount of UA_{COND} on the condenser represents the condition of the condenser. Physically, UA_{COND} can be interpreted from how good the condition of the condenser is. In this modeling, UA_{COND} is used during the process of condensing the steam into water, so several things that will affect the value of UA_{COND} include the condition of the nozzles on the condenser used to mist the cooling water, then the amount of non-condensable gas that changes. Both can reduce the ability of the condenser to condense steam from the turbine. The first parameter to be reviewed is the impact of changes in condenser pressure by changes in the condenser condition as shown in Figure 12. In the Figure 12, as we can see as the condition of the condenser decreases from 100% to 60%, the condenser pressure will continue to increase. This means that the vacuum level in the condenser decreases.

Meanwhile in the same of Figure 12, the parameter that is reviewed after the water condition in the condenser is the turbine power that is generated when there is a decrease in the condenser condition is the power generated. Turbine power is the most visible parameter compared to other parameters because it is the output that will be used directly. The increase in condenser pressure will result around the interior of the cycle being reduced so that the total power generated will also decrease. In this study, decreasing the quality of the condenser up to 60% will reduce the turbine power by 4.63%.

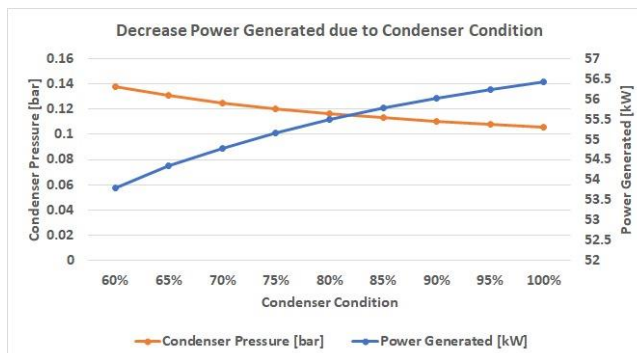


Figure 12. The effect of condenser condition to the change of condenser pressure and power generation (Figure is in color in the on-line version of the paper).

5. Conclusion

The results obtained in this study include:

- The modeling of the geothermal power plant system can be modeled using Microsoft Excel software and has been validated using the operating conditions of the geothermal power plant system owned by PT. Indonesia Power in Mount Darajat. This model can be used as quick help tools to know the condition and effect in any GPP that using vapor as working fluid.
- Changes in the condition of condenser and cooling tower and environmental condition have direct impact to the turbine performance. With varying the condition of cooling tower, condenser, and environmental decrease the turbine power generated 5.41%, 4.63%, and 2.26% respectively. The decrease turbine power generated by changes in environmental condition fit with Jian li research results.
- It needs further research and modelling to get better model and understanding in NCG extraction system.

Nomenclature

C_p	Specific heat	(kJ/kg.K)
E	compression ratio	(-)
ER	Entrainment ratio	(-)
h	Enthalpy specific	(kJ/kg)
K	degree of expansion	(-)
Mr	fluids mass molar relative	(g/mol)
\dot{m}	mass flow rate	(kg/h)
\dot{m}_a	mass flow rate of ambient	(kg/h)
\dot{m}_b	mass flow rate of blowdown	(kg/h)
\dot{m}_d	mass flow rate of air	(kg/h)
P	Pressure	(bar)
T	Temperature	(°C)
UA	Total coefficient of heat transfer	(W/m ² .K)
\dot{W}	Work	(kW)
x	fraction	(-)
η	Efficiency	(%)

Subscripts

a	ambient
b	blowdown
$cond$	condenser
$cond,out$	Condenser out
$Cooling$	Cooling
CT	Cooling tower
$ejector,suct$	Suction of ejector
$intercond,out$	Outlet of inter-condenser
cw	Cooling water
d	air

<i>f</i>	fluids
<i>ms</i>	Motive steam
<i>turbine</i>	turbine

Abbreviations

<i>BCV</i>	Ball check valve
<i>CP</i>	Cooling pump
<i>CWP</i>	Cooling water pump
<i>CS</i>	Cyclone separator
<i>EBTKE</i>	Energy and Mineral Resources directorate in the field of Renewable Energy Conservation
<i>GPP</i>	Geothermal power plant
<i>GRS</i>	Gas remover system
<i>LMTD</i>	Log mean temperature difference
<i>LRVP</i>	Liquid ring vacuum pump
<i>MR</i>	Mist remover
<i>MTOE</i>	Mega tonnes of oil equivalent
<i>MV</i>	Main vapour steam
<i>NCG</i>	Non-condensable gas
<i>ORC</i>	Organic Rankine cycle
<i>PC</i>	Pump circulation
<i>PLN</i>	Perusahaan listrik negara
<i>RH</i>	Relative humidity
<i>SE/C</i>	Ejector system
<i>TAE</i>	Total air equivalent
<i>WV</i>	Water valve

Author contribution statement

KFAS as main contributor write the manuscript, developing the model program in excel, collecting the data. DIP write the introduction section, final review and correspondences. WA is as supervisor for this research and conceive the research idea.

References:

- [1] Perusahaan Listrik Negara, *Rencana Usaha Penyediaan Tenaga Listrik (RUPTL) 2021 - 2030 PT PLN (Persero)* [online]. Available: <https://web.pln.co.id/statics/uploads/2021/10/ruptl-2021-2030.pdf> (accessed Des, 8, 2021).
- [2] ESDM, *Terus Dorong Percepatan Pengembangan EBT, Pemerintah Siapkan PLN Khusus EBT* [online]. 2016. available: <https://ebtke.esdm.go.id/post/2016/01/07/1075/terus.dorong.percepatan.pengembangan.ebt.pemerintah.siapkan.pln.khusus.ebt> (accessed Des, 8, 2021).
- [3] Badan Pengkajian dan Penerapan Teknologi, *Outlook Energi Indonesia 2014; Pengembangan Energi untuk Mendukung Program Substitusi BBM*. Jakarta: Pusat Teknologi Pengembangan Sumberdaya Energi, 2014.
- [4] M. I. Kömürçü and A. Akpınar, "Importance of geothermal energy and its environmental effects in Turkey," *Renew. Energy*, vol. 34, no. 6, pp. 1611–1615, 2009.
- [5] Dirjen EBTKE, *Statistik EBTKE 2016*. Jakarta: EBTKE, 2016.
- [6] A. Hepbasli, "A review on energetic, exergetic and exergoeconomic aspects of geothermal district heating systems (GDHSs)," *Energy Convers. Manag.*, vol. 51, no. 10, pp. 2041–2061, 2010.
- [7] A. Hepbasli and C. Canakci, "Geothermal district heating

- applications in Turkey: A case study of Izmir-Balcova," *Energy Convers. Manag.*, vol. 44, no. 8, pp. 1285–1301, 2003.
- [8] K. Popovski and S. P. Vasilevska, "Prospects and problems for geothermal use in agriculture in Europe," *Geothermics*, vol. 32, no. 4, pp. 545–555, 2003.
- [9] B. Tomaszewska *et al.*, "Utilization of renewable energy sources in desalination of geothermal water for agriculture," *Desalination*, vol. 513, 2021.
- [10] P. Jiang, X. Li, R. Xu, and F. Zhang, "Heat extraction of novel underground well pattern systems for geothermal energy exploitation," *Renew. Energy*, vol. 90, no. 2016, pp. 83–94, 2016.
- [11] Y. Yuan, T. Xu, Z. Jiang, and B. Feng, "Prospects of power generation from the deep fractured geothermal reservoir using a novel vertical well system in the Yangbajing geothermal field, China," *Energy Reports*, vol. 7, pp. 4733–4746, Nov. 2021.
- [12] L. Zhang, S. Chen, and C. Zhang, "Geothermal power generation in China: Status and prospects," *Energy Sci. Eng.*, vol. 7, no. 5, pp. 1428–1450, 2019.
- [13] Massachusetts Institute of Technology, "The Future of Geothermal Energy," 2006.
- [14] M. A. Ehyaei, A. Ahmadi, M. A. Rosen, and A. Davarpanah, "Thermodynamic optimization of a geothermal power plant with a genetic algorithm in two stages," *Processes*, vol. 8, no. 10, pp. 1–16, 2020.
- [15] E. E. Michaelides and D. N. Michaelides, "The effect of ambient temperature fluctuation on the performance of geothermal power plants," *Int. J. Exergy*, vol. 8, no. 1, pp. 86–98, 2011.
- [16] M. Kahraman, A. B. Olcay, and E. Sorgüven, "Thermodynamic and thermoeconomic analysis of a 21 MW binary type air-cooled geothermal power plant and determination of the effect of ambient temperature variation on the plant performance," *Energy Convers. Manag.*, vol. 192, no. April, pp. 308–320, 2019.
- [17] M. I. Sohel, M. Sellier, L. J. Brackney, and S. Krumdieck, "An iterative method for modelling the air-cooled organic Rankine cycle geothermal power plant," *Int. J. Energy Res.*, vol. 35, no. 5, pp. 436–448, Apr. 2011.
- [18] B. Rudyanto *et al.*, "Preliminary analysis of dry-steam geothermal power plant by employing exergy assessment: Case study in Kamojang geothermal power plant, Indonesia," *Case Stud. Therm. Eng.*, vol. 10, pp. 292–301, 2017.
- [19] M. Aneke, B. Agnew, and C. Underwood, "Performance analysis of the Chena binary geothermal power plant," *Appl. Therm. Eng.*, vol. 31, no. 10, pp. 1825–1832, 2011.
- [20] H. Ghasemi, M. Paci, A. Tizzanini, and A. Mitsos, "Modeling and optimization of a binary geothermal power plant," *Energy*, vol. 50, no. 1, pp. 412–428, 2013.
- [21] X. Zhang, M. He, and Y. Zhang, "A review of research on the Kalina cycle," *Renew. Sustain. Energy Rev.*, vol. 16, no. 7, pp. 5309–5318, 2012.

- [22] H. Li, D. Hu, M. Wang, and Y. Dai, "Off-design performance analysis of Kalina cycle for low temperature geothermal source," *Appl. Therm. Eng.*, vol. 107, pp. 728–737, 2016.
- [23] D. I. Permana, D. Rusirawan, and I. Farkas, "Waste heat recovery of tura geothermal excess steam using organic rankine cycle," *Int. J. Thermodyn.*, vol. 24, no. 4, pp. 32–40, 2021.
- [24] K. Li, C. Liu, S. Jiang, and Y. Chen, "Review on hybrid geothermal and solar power systems," *J. Clean. Prod.*, vol. 250, 2020.
- [25] A. Dagdas, M. T. Akkoyunlu, and T. Basaran, "Performance Analysis of Supercritical Binary Geothermal Power Plants," *Adv. Mech. Eng.*, vol. 7, no. 1, 2015.
- [26] H. Moon and S. J. Zarrouk, "Efficiency of Geothermal Power Plants: a Worldwide Review," *Geothermics*, vol. 51, no. November 2012, pp. 142–153, 2014.
- [27] B. Ciapała, J. Jurasz, M. Janowski, and B. Kępińska, "Climate factors influencing effective use of geothermal resources in SE Poland: the Lublin trough," *Geotherm. Energy*, vol. 9, no. 1, pp. 1–16, 2021.
- [28] R. DiPippo, *Geothermal Power Plants; Principles, Applications, Case Studies and Environmental Impact*, 2nd ed. New York: McGraw-Hill, Inc., 2007.
- [29] P. K. Nag, *Power Plant Engineering*, 3rd ed., vol. 1. New Delhi: McGraw-Hill, Inc., 2008.
- [30] M. H. Dickson and M. Fanelli, "What is geothermal energy? International Geothermal Association (IGA): [htt:iga.igg.cnr.it/geo/geoenergy.php](http://iga.igg.cnr.it/geo/geoenergy.php)," pp. 1–33, 2004.
- [31] M. Hasan, "Analisi Kinerja Ejektor Terhadap Kenaikan Persentase Gas Tak Terkondensasi Unit 1 dan 2 PLTP Gunung Salak," Insitut Teknologi Bandung, 2007.
- [32] N. Y. Özcan and N. Y. Ozcan, "Modeling, Simulation and Optimization of Flashed-Steam Geothermal Power Plants from the Point of View of Noncondensable Gas Removal Systems," Izmir Institute of Technology, 2010.
- [33] Geothermal Institute, "Gas Extraction System," in *Course note of Geothermal Institute*, Auckland University, 1996, p. 75.
- [34] J. Li, Z. Yang, Z. Yu, J. Shen, and Y. Duan, "Influences of climatic environment on the geothermal power generation potential," *Energy Convers. Manag.*, vol. 268, no. April, p. 115980, 2022.

Research Article

Modeling of the Vapor-Liquid Equilibria Properties of Binary Mixtures for Refrigeration Machinery

¹Y.Maalem , ^{2*}Y.Tamene , ³H.Madani 

^{1,2,3} Laboratory of Studies of Industrial Energy Systems (LESEI), Department of Mechanical Engineering, Faculty of Technology, University of Batna 2, 05000 Batna, Algeria
E-mails: ¹y.maalem@univ-batna2.dz, ^{2*}y.tamene@univ-batna2.dz, ³h.madani@univ-batna2.dz

Received 4 July 2022, Revised 24 December 2022, Accepted 13 April 2023

Abstract

The presence of both critical and azeotropic states in the vapor-liquid equilibria (VLE) is a very important issue in the chemical and refrigeration engineering. The knowledge of the phase behavior (subcritical phase/supercritical phase) of refrigerant allows designing and optimizing the refrigeration industrial processes. However, it is rare to find data for this information, which poses a great challenge for researchers to develop predictive and correlative thermodynamic models. The present study proposes the computation of the compositions and pressures of critical and azeotropic points of the isothermal VLE as well as the correlation of experimental VLE data. Firstly, experimental data (PTxy) was used to predict the vapor-liquid phase of both critical and azeotropic behaviors and to determine their properties using the relative volatility model. Secondly, the thermodynamic model (PR-MC-WS-NRTL) was applied to correlate the data of the binary refrigerant systems and describe their isothermal (VLE) behavior. The results proved that there is good agreement between predicted values obtained by the developed model and the experimental reference data. The relative error of both critical and azeotropic properties does not exceed 4.3 % for the molar fraction and 7.5 % for the pressure using relative volatility model. On other hand the relative deviation is respectively less than 2.60 % and 2.58 % for the liquid and vapor mole fractions using (PR-MC-WS-NRTL) model. This shows the ability of these models to give a reliable solution to predict and modulate the phase behavior of the binary refrigerant systems.

Keywords: Binary mixtures; critical point; azeotropic point; relative volatility; mixing rules.

1. Introduction

Search for eco-friendly and sustainable fluids to replace the conventional working fluids such as CFCs (chlorofluorocarbons), HCFCs (hydrochlorofluorocarbons), and HFCs (hydrofluorocarbons) is the major challenge for the industrial field and especially the refrigeration engineering due to the release of both CFCs and HCFCs, which have high ozone depletion potentials (ODPs). The CFCs and HCFCs are therefore being phased out as a result of the international Montreal Protocol on substances that deplete the ozone layer enacted in 1987. This led to the urgent need in the refrigeration industry to find an alternative for these substances. One possible class of refrigerants is HFCs on account of their zero ODPs. However, these types of fluids are also regulated by the international Kyoto Protocol (1997) due to their global warming potentials (GWPs) [1].

The current search for environmentally friendly refrigerants is driven by the recent approval of increasingly restrictive regulations that limit the use of substances with high GWP, and the need to maintain high process efficiencies (Figure 1). In this context, refrigerant blends like the binary or ternary and or even quaternary systems containing fluids with low GWP are of special importance, since their excellent environmental characteristics, thermodynamic properties, and high cycle performance [2].

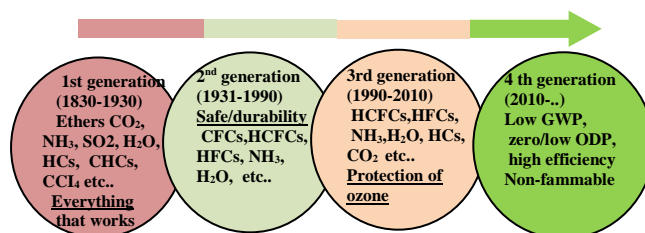


Figure 1. Different generations of refrigerants [3].

The detailed knowledge of the thermodynamic properties of these refrigerant mixtures, and particularly the fluid-phase behavior in both subcritical and supercritical regions in a wide range of temperatures and pressures is necessary to design and optimize the thermodynamic systems involving these mixtures, in the production and separation units such as organic cycles, heat pumps, refrigeration systems, etc.

For instance, to design evaporator or condenser devices with and without phase changing in the mechanical vapor compression cycle for refrigeration machines, it is important to know the state of the blend and to evaluate the level of the temperature glide when they change phase in both the condenser and evaporator. In this case, it is

important to know if the blend system behaves like a single-fluid (azeotropic behavior) or not.

This information can be acquired primarily through some experimental measurements. However, experimental data on the thermodynamic properties (critical and azeotropic points) of refrigerant blends are scarce. To overcome the problem of lack of the data on various kinds of refrigerant systems (binary mixture, ternary mixture, quaternary mixture, etc.) on an industrial scale, the researchers propose the use of numerical methods with thermodynamic developed models which are very reliable in solving many problems of the engineering under temperature and pressure conditions [4-8], these models are mainly divided into predictive or correlative thermodynamic models including equations of state, mixing rules and activity coefficient models [9].

The use of these thermodynamic models has motivated many numbers of several researchers to develop computational models to determine VLE properties of the refrigerant blends and especially the azeotropic and critical points. Teja and Rowlinson [10] computed homogeneous azeotropes of binary mixtures using an equation of state (EoS) as a tool for the VLE prediction.

Artemenko and Mazur [11] developed a model computation for the prediction of azeotrope formation in a mixture that does not require VLE computation. The model computation employs neural networks and global phase diagram methodologies to correlate azeotropic behavior for the binary working fluids based only on critical pressure, critical temperature and acentric factors of the individual refrigerants in mixtures. Fidkowski et al [12] presented an interesting homotopy continuation model for finding homogeneous azeotropes. Tolsma and Barton [13] developed Fidkowski's work to calculate heterogeneous azeotropes and presented the necessary proofs regarding the computation of all homogeneous and heterogeneous azeotropes for multi-component blends. Kolar and Kojima [14] predicted critical points for fifteen binary systems using the PSRK group contribution equation of state.

In other work, Dong et al [15] presented a simple model based on the Newton method to determine the homogeneous azeotropes for the binary blends, they have used the Wilson activity coefficients model and Antoine equation in their approaches, then they verified their model, with six binary blends. Heidemann and Khalil [16] developed a new computational procedure for the calculation of critical points with cubic equations of state for multi-component blends. Dan Nichita [17] has

developed a computational modification of the Heidemann-Khalil method for calculating critical points.

Maier et al [18-19] presented an arithmetic model based on interval analysis and Newton algorithm to verify the existence of homogeneous azeotropes and to locate all homogeneous azeotropes. He et al [19] presented a new correlation, based on the computational method and newly obtained experimental data, to predict the critical temperature and the critical pressure of multi-component mixtures. Hu et al [20] predicted the VLE properties of many (HFCs) binary refrigerant systems with a corresponding equation. The mathematical model only needed the vapor pressures, critical constants and dipole moments of pure refrigerants, without any adjustable parameters or interaction coefficients. In the study of Dong et al [21], the authors proposed four approaches based on the UNIFAC model to predict the azeotropes without any experimental data for binary refrigerant mixtures. The thermodynamic criterion of the four methods is the first derivative of the pressure with respect to the composition, which equals zero at the azeotropic point for binary systems; they concluded that by using those methods, the cost and time of experiments could be saved.

From the literature review survey about the study of both critical and azeotropic properties cited above, it was noticed that the most approaches made by authors are difficult to implement, due to the mathematical computation complexity, since convergence is often difficult to obtain the vapor-liquid equilibria properties.

Our main objective in this paper is to use two thermodynamic models simple, rapid and accurate described by our team [22], to predict and determine the fluid-phase behavior of six binary refrigerant systems and especially the azeotropic and critical properties for those blends

- Firstly from the experimental data PTxy (Relative volatility);
- Secondly with the prediction model (PR-MC-WS-NRTL).

The six binary mixtures studied are: [R744 (Cas: 124-38-9)+R134a (Cas: 811-97-2)], [R1234ze (Cas: 29118-24-9)+R744(Cas: 124-38-9)], [R1234yf (Cas: 754-12-1)+R290 (Cas: 74-98-6)], [R1234yf (Cas: 754-12-1)+R600a(Cas: 75-28-5)], [R32 (CAS: 75-10-5)+R1234yf (Cas: 754-12-1)], [R32 (Cas: 75-10-5)+R152a(Cas: 75-37-6)],

The properties of the pure substances composing those binary mixtures are presented in Table1; they were obtained from the following references [24-30].

Table 1. Properties summary of various fluid candidates.


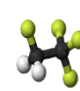
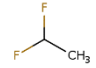
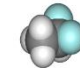
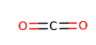

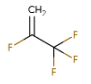
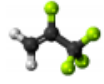
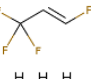
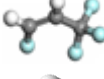
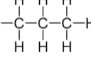
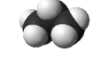
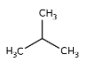

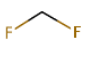

Substance	Type	Cas N°	Tc [K]	Pc [MPa]	GWP	ODP	Chemical structure	Molecular structure
R134a	HFC	811-97-2	374.21	4.0593	1430	0		
R152a	HFC	75-37-6	386.41	4.5168	124	0		
R744	Natural	124-38-9	304.13	7.3770	1	0		

Table 1. Properties summary of various fluid candidates “(continue)”.

R1234yf	HFO	754-12-1	367.85	3.3823	4	0		
R1234ze	HFO	29118-24-9	382.51	3.6349	6	0		
R290	Natural	74-98-6	369.89	4.2512	3	0		
R600a	Natural	75-28-5	407.85	3.6400	3	0		
R32	HFC	75-10-5	351.26	5.7820	650	0		

2. Computational Models

The detailed knowledge of the VLE properties for the binary working fluids (Figure 2) is very important in engineering applications. Nowadays, several theoretical and empirical models have been proposed for a better representation of the VLE, taking into account the behavior of the various systems commonly encountered in energetic applications.

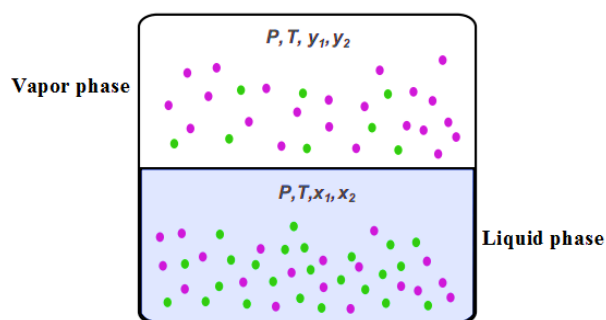


Figure 2. VLE of binary refrigerant system.

The temperature change during heating or cooling process in the condenser and the evaporator requires knowledge of the VLE data for the different phenomena of vapor-liquid equilibria of working fluids (Figure 3).

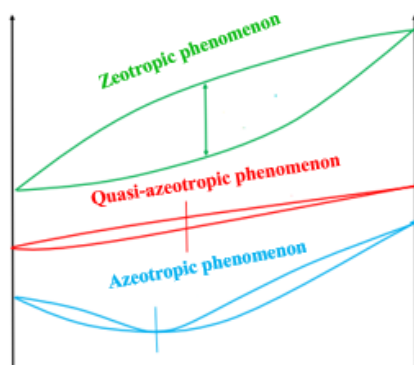


Figure 3. Different phenomena of vapor-liquid equilibria of binary refrigerant system.

In this study two modeling approaches (Figure 4) was proposed to predict and determine the isothermal (VLE) properties. Especially the azeotropic and the critical

properties (x_{az} , P_{az} , x_c , and P_c) in the isothermal (VLE) of the binary refrigerant systems for refrigeration machinery.

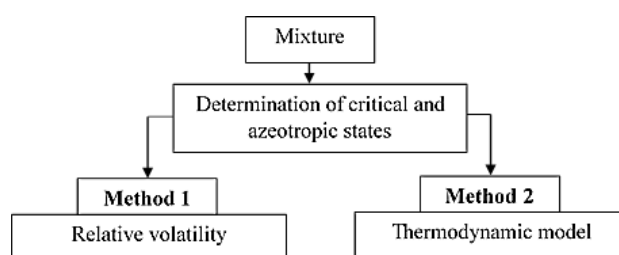


Figure 4. Methods proposed.

In the first section, the relative volatility model was used to predict and estimate the both critical and azeotropic properties in the binary refrigerants based on (PTxy) experimental data.

In the second section, the thermodynamic model: «PR-MC-WS-NRTL» was chosen in order to predict and describe the behavior of both azeotropic and critical states in the binary refrigerant systems.

2.1 Relative Volatility Model

The relative volatility (α_{ij}) represents the ratio of the equilibria constants of the (i) and (j) components. The model of the (α_{ij}) for binary working fluids is expressed as follows [2]:

$$\alpha_{12} = \frac{K_1}{K_2} = \frac{(y_1/x_1)}{(y_2/x_2)} \quad (1)$$

With:

$$x_1 + x_2 = y_1 + y_2 = 1 \quad (2)$$

In the remainder of this work, this model will be used for all the computations of the relative volatility.

The algorithm for calculating critical and azeotropic properties from the relative volatility is given as:

- For each isotherm, trace either the relative volatility (α_{12}) according to the molar fraction of the most volatile pure substance x_1 , or according to the pressure;
- Using Excel software, the plotted points are either fitted using a second order polynomial curve or a linear trend line;

- The equation of the curve of tendency is equalized to unity;
- By solving the obtained equation, the values of both critical and azeotropic properties are obtained.

2.2 Thermodynamic Correlation for the VLE Properties

The need of predicting the (isothermal/isobaric) VLE behavior of working fluids (binary mixture, ternary mixture, etc.) is primordial to design and optimize the different processes in the cooling systems. The VLE properties of the working fluids for a wider range of temperatures, pressures, and compositions can be obtained by theoretical models. It is well known that the phase diagrams (isothermal/isobaric) can provide important and effective information for the thermodynamic analysis of the energetic systems such as heat pumps, refrigeration systems and air-conditioning.

Therefore, to correlate the isothermal VLE behavior of the binary refrigerant systems and predict the both azeotropic and critical properties, the thermodynamic model: “PR–MC–WS–NRTL” was proposed and employed in the present work (Figure 5).

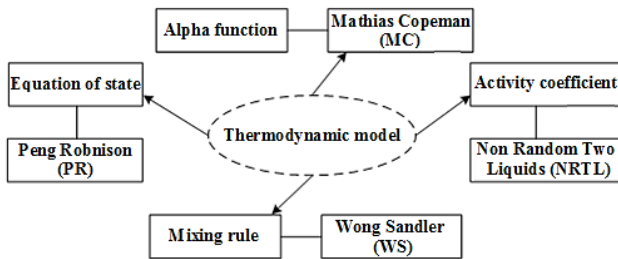


Figure 5. Thermodynamic model proposed.

The Peng–Robinson (Peng and Robinson, 1976) equation of state (PR–EoS) is one of the most popular equation of state (EoS) used to describe the thermo-physical properties and especially the (VLE) of fluids in the academic and industrial fields. It has an advantage of both simple form and its calculation accuracy can meet the general engineering requirements.

The second model proposed in this study to correlate the experimental data combines the popular cubic equation of state of (PR–EoS) with the Mathias–Copeman (MC) alpha function, and the NRTL excess free energy model, using the Wong–Sandler (WS) mixing rules.

The cubic equation of state of (PR–EoS) [24] can be written as:

$$P = \frac{RT}{v-b} - \frac{a\alpha(T)}{(v^2 + 2vb - b^2)} \quad (3)$$

Where P is the pressure in MPa, R is the universal gas constant in $\text{J mol}^{-1} \text{K}^{-1}$, v is the molar volume in $\text{m}^3 \text{mol}^{-1}$, T is the temperature in K and a , b are the energy and co-volume parameters of (PR–EoS).

For a pure component i , the parameters of (PR–EoS) can be given as:

$$a = 0.457240 \frac{R^2 T_c^2}{P_c} \quad (4)$$

$$b = 0.07780 \frac{RT_c}{P_c} \quad (5)$$

The values of critical temperature (T_c) and critical pressure (P_c) for each pure refrigerants are provided in Table 1.

The (MC) alpha function [25] is:

$$\alpha(T) = \left(1 + c_1 \left(1 - \sqrt{\frac{T}{T_c}} \right) + c_2 \left(1 - \sqrt{\frac{T}{T_c}} \right)^2 + c_3 \left(1 - \sqrt{\frac{T}{T_c}} \right)^3 \right)^2 \quad (6)$$

If $T > T_c$:

$$\alpha(T) = \left(1 + c_1 \left(1 - \sqrt{\frac{T}{T_c}} \right) \right)^2 \quad (7)$$

Where c_1 , c_2 and c_3 are three adjustable parameters of Mathias Copeman (MC), which has been listed in Table 2.

Table 2. Mathias–Copeman (MC) coefficients [26].

Compound	c_1	c_2	c_3
R134a	0.8497	0.0065	-0.0535
R744	0.7046	-0.3148	1.8908
R1234yf	0.8293	-0.8477	3.4559
R1234ze	0.8767	-0.7751	3.0689
R290	0.6000	-0.0006	0.1738
R600a	0.6524	-0.1493	0.5992
R32	0.8218	-0.3977	0.7622
R152a	0.7743	0.0576	-0.2902

To describe the isothermal vapor-liquid equilibria (VLE) behavior of the binary refrigerant systems, the Wong–Sandler (WS) mixing rules are used in this work to obtain (EoS) parameters for a binary refrigerant blends from those of the pure components. The Wong–Sandler mixing rules are chosen here from the excellent representation of the isothermal VLE properties of the binary working fluids.

These mixing rules for a (EoS) can be written as [27]:

$$b_m = \frac{\sum_i \sum_j x_i x_j \left(b - \frac{a}{RT} \right)}{1 - \left(\frac{\sum_i x_i \frac{a_i}{b_i}}{RT} + \frac{g_\gamma^E(T, P = \infty, x)}{CRT} \right)} \quad (8)$$

$$b - \frac{a}{RT} = \sum_i \sum_j x_i x_j \left(b - \frac{a}{RT} \right)_{ij} \quad (9)$$

With:

$$\left(b - \frac{a}{RT} \right)_{ij} = \frac{1}{2} \left[\left(b - \frac{a}{RT} \right)_i + \left(b - \frac{a}{RT} \right)_j \right] (1 - k_{ij}) \quad (10)$$

Where k_{ij} is an adjustable binary interaction parameter and C a numerical constant depends on the (PR–EoS).

The component activity parameters of binary blend systems are calculated with NRTL model [28].

$$\ln \gamma_i = \frac{\sum_{j=1}^n \tau_{ji} G_{ji} x_j}{\sum_{k=1}^n G_{ki} x_k} + \sum_{j=1}^n \frac{x_j G_{ij}}{\sum_{k=1}^n G_{ki} x_k} \left(\tau_{ij} - \frac{\sum_{k=1}^n x_k \tau_{kj} G_{kj}}{\sum_{k=1}^n G_{ki} x_k} \right) \quad (11)$$

The excess Gibbs energy model [28] chosen is the NRTL local composition model is:

$$g^E = \sum_i x_i \sum_j \frac{x_j \exp\left(-\alpha_{ji} \frac{\tau_{ji}}{RT}\right)}{\sum_k x_k \exp\left(-\alpha_{ki} \frac{\tau_{ki}}{RT}\right)} \tau_{ji} \quad (12)$$

Where $\tau_{ii}=0$, $\alpha_{ii}=0$, α_{ji} , τ_{ji} and τ_{ij} are adjustable parameters. It is recommended to use $\alpha_{ji} = 0.3$ for systems like this one.

3. Results and Discussion

From the above procedures, the location of the critical and azeotropes points has been calculated in the following subsection. The studied binary blends are environment-friendly which containing natural and synthetic refrigerants.

3.1 Prediction of Azeotropic and Critical Properties

The experimental data (PTxy) are necessary for predicting the phase behavior of the binary refrigerant systems. Therefore, for each isotherm in a binary mixture, the values of relative volatility (α_{12}) have been calculated and plotted according to the molar fraction of the most volatile pure substance x_1 . In fact, it is well known that the relative volatility is supposed vary as a decreasing function (exponential or polynomial) of the liquid molar fraction, this can be verified from the following results.

Figures 6-11 illustrate the variation of relative volatility versus different molar fractions of the binary refrigerant systems: (R1234yf+R600a), (R1234yf+R290), (R744+R134a), (R744+R1234ze), (R32+R1234yf) and (R32+R152a), respectively at different isotherms, where the symbol curves represent the results values obtained with the relative volatility model and the dashed red line represents where the relative volatility is equal to unity ($\alpha_{12}=1$).

It can be seen that the relative volatility for studied mixtures decreases when the temperature and the molar fraction of the most volatile pure substance increase (Figure 6-11), this is predictable because the model of relative volatility is a function of compositions and pressure. Additionally, since an increase in the pressure requires an increase in the temperature, this also affects the relative volatility.

Moreover, it can be seen from the results of the relative volatility displayed in figures 6-11, that the two blends (R1234yf+R600a) and (R1234yf+R290) indicate an azeotropic behavior (mixtures behaves like a pure fluid and then its components cannot be separated by simple distillation) for the all investigated temperature range studied: T= (283.15; 293.15; 303.15; 313.15 and 313.15) K and T= (253.15; 263.15; 273.15; 283.15 and 293.15) K, respectively, where it is observed that the calculated α_{12}

values of both mixtures cross the line of constant relative volatility ($\alpha_{12}=1$) for all studied temperatures which can be expected due to the stronger molecular interactions and close values of the vapor pressures of the pure compounds of the studied refrigerant blends.

The azeotropic phenomena is located at high molar fractions of the most volatile pure substance for (R1234yf+R600a) and at low molar fractions of the most volatile pure substance for (R1234yf+R290), respectively.

The model of relative volatility accurately predicts the azeotropic behavior at ($\alpha_{12}=1$) in each isotherm (Figures 6-7). At the azeotropes, the compositions in the liquid phase and the vapor phase are identical, leading to a relative volatility ($\alpha_{12}=1$). In addition, it was also found from the results of the relative volatility of (R1234yf+R600a and R1234yf+R290) blends that systems composed of R1234yf mixed with hydrocarbons (HCs) like isobutane (R600a) and propane (R290), leading to the formation of azeotropes in the binary mixtures. These facts should be taken into account when designing new low GWP refrigerants since azeotropic mixtures are preferred among different types of refrigerant mixtures.

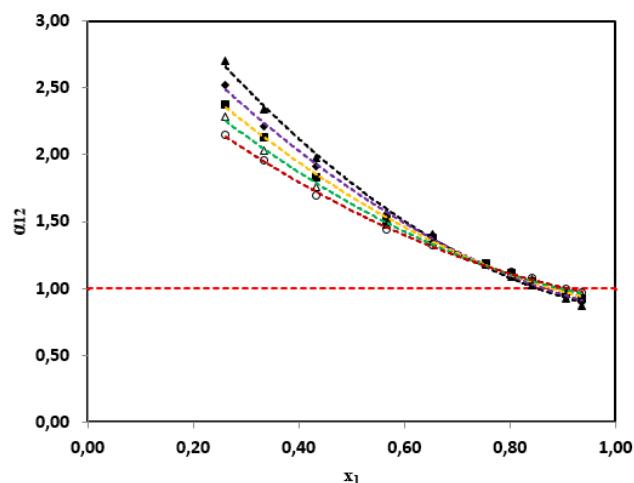


Figure 6. Plot of relative volatility (α_{12}) daigram for R1234yf+R600a system. ((\blacktriangle) 283.15K ;(\blacklozenge) 293.15K; (\blacksquare) 303.15 K; (\blacktriangle) 313.15 K; (\circ) 313.15 K; (...)) line of constant relative volatility ($\alpha_{12} = 1$)).

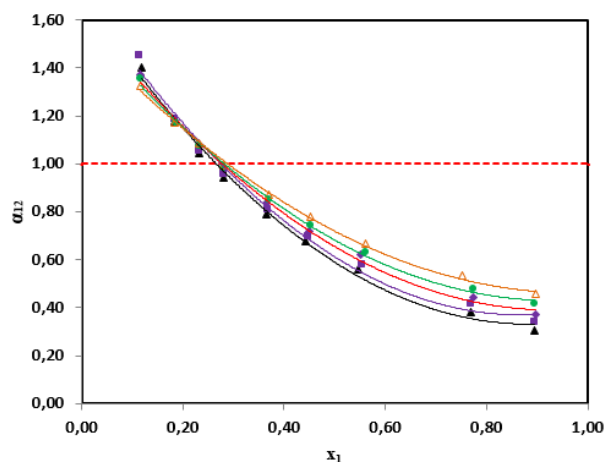


Figure 7. Plot of relative volatility (α_{12}) daigram for R1234yf+R290 system. ((\blacktriangle) 253.15 K; (\blacksquare) 263.15 K; (\blacklozenge) 273.15 K; (\bullet) 283.15 K; (\blacktriangle) 293.15 K; (...)) line of constant relative volatility ($\alpha_{12} = 1$)).

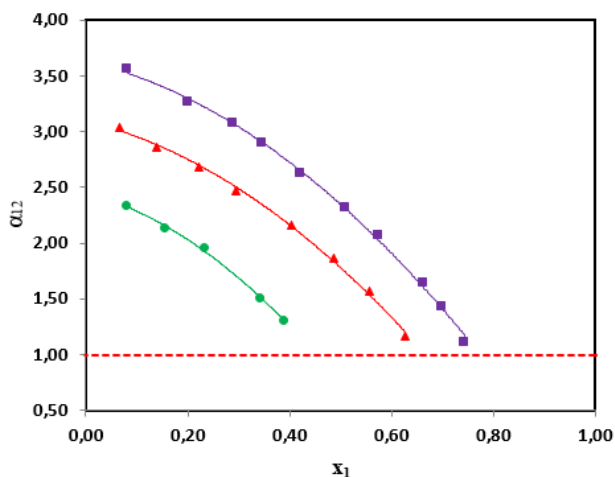


Figure 8. Plot of relative volatility (α_{12}) diagram for R744+R134a system. ((■) 329.60 K; (▲) 339.1 K; (●) 354 K; (---) line of constant relative volatility ($\alpha_{12} = 1$)).

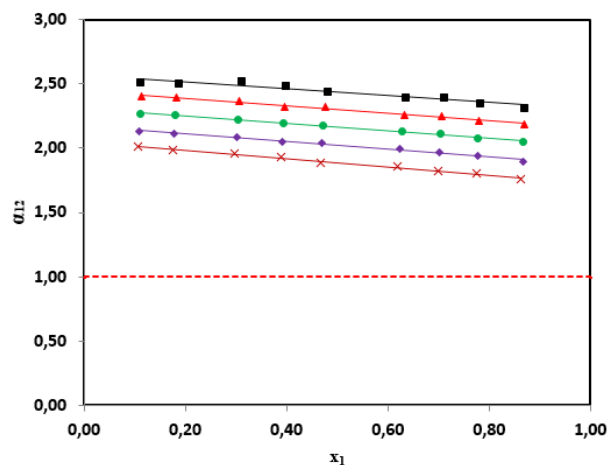


Figure 11. Plot of relative volatility (α_{12}) diagram for R32+R152a system. ((■) 283.15 K; (▲) 293.15 K; (●) 303.15 K; (◆) 313.15 K; (×) 323.15 K; (---) line of constant relative volatility ($\alpha_{12} = 1$)).

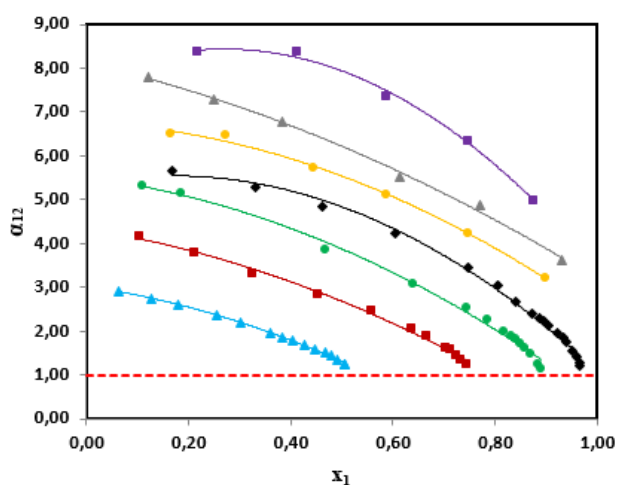


Figure 9. Plot of relative volatility (α_{12}) diagram for R744+R1234ze system. ((■) 283.32 K; (▲) 293.15 K; (●) 298.15 K; (◆) 308.15 K; (●) 318.11 K; (■) 333.01 K; (▲) 353.02 K; (---) line of constant relative volatility ($\alpha_{12} = 1$)).

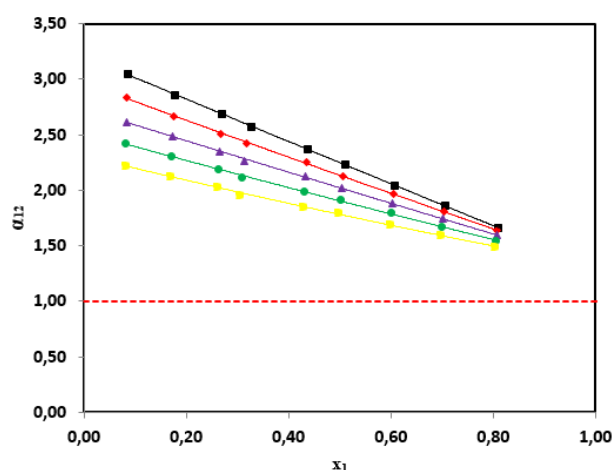


Figure 10. Plot of relative volatility (α_{12}) diagram for R32+R1234yf system. ((■) 283.15 K; (◆) 293.15 K; (▲) 303.15 K; (●) 313.15 K; (■) 323.15 K; (---) line of constant relative volatility ($\alpha_{12} = 1$)).

In the case of the two binary systems (R744+R1234ze) and (R744+R134a), it was found that both systems exhibit a critical behavior (Figures 8-9) at temperatures higher than the critical temperature of pure carbon dioxide (T_c (R744) = 304.13 K), where it was observed that the calculated α_{12} values of both mixtures accurately predict the critical behavior and therefore, the limit of the instability phase domain (critical point corresponds to the limit of stability).

The critical behavior was observed between the temperature interval, which corresponds to four isotherms $T = (308.15; 318.11; 333.01$ and $353.02)$ K for R744+R1234ze system and three isotherms for $T = (329.60; 339.1$ and $354)$ K for the R744+R134a system. This last feature is the consequence of the stronger intermolecular interactions occurring in the systems (R744+R1234ze and R744+R134a). Thus, for temperatures higher than the critical temperature of the most volatile pure substance (carbon dioxide (R744)), the binary systems conventionally has a critical point.

On other hand, a zeotropic behavior (behavior differs from pure fluids (mixtures having gliding temperature and the intermolecular interactions could be neglected) it can be found for all isotherms investigated $T = (283.15; 293.15; 303.15; 313.15$ and $323.15)$ K in binary refrigerant systems (R32+R1234yf) and (R32+R152a) (Figures 10-11), where is clearly observed that the calculated α_{12} values do not cross the line of constant relative volatility ($\alpha_{12} = 1$) for all studied temperatures. Additionally, the values of relative volatility are all greater than 1, which indicates that the components of mixtures can be separated by ordinary distillation.

It fully indicates that the relative volatility model can satisfactorily predict the isothermal (VLE) properties of binary refrigerant mixtures. Overall, results show that the relative volatility model can be used as a computational tool to know the behavior VLE properties and the thermodynamic behavior (subcritical and critical phase behavior) of these mixtures.

3.2 Determination of Azeotropic and Critical Properties

The values of the molar fraction and the pressure calculated of the data experimental ones and those obtained from the model are illustrated in Tables 3-4.

Table 3. Comparison between experimental data and theoretical calculations of azeotropic properties.

T [K]	$x_{az,exp}$	$x_{az,cal}$	$p_{az,exp}$	$p_{az,cal}$
R1234yf+R290				
253.15	0.2800	0.2759	0.2672	0.2655
263.15	0.2810	0.2750	0.3776	0.3741
273.15	0.2800	0.2781	0.5184	0.5134
283.15	0.2810	0.2818	0.6949	0.6881
293.15	0.2810	0.2885	0.9121	0.9018
R1234yf+R600a				
283.15	0.8413	0.8521	0.4465	0.4454
293.15	0.8463	0.8620	0.6011	0.6013
303.15	0.8484	0.8747	0.7925	0.7930
313.15	0.9038	0.8937	1.0230	1.0260
323.15	0.9059	0.8979	1.3108	1.3115

Table 4. Comparison between experimental data and theoretical calculations of critical properties.

T [K]	$x_{c,exp}$	$x_{c,cal}$	$p_{c,exp}$	$p_{c,cal}$
R744+R134a				
329.60	0.7640	0.7746	7.3690	7.4470
339.10	0.6612	0.6678	7.0980	7.1299
354	0.4560	0.4509	6.0430	6.1617
R744+R1234ze				
308.13	0.9790	1.0000	7.6480	7.7676
318.11	0.8970	0.9344	7.6030	8.0978
333.01	0.7650	0.7985	7.3990	7.9549
353.02	0.5400	0.5580	6.4520	6.8139

Indeed, the calculated values of the x (molar fraction) and P (pressure in MPa) for each blend are compared to the experimental ones as follows:

$$\Delta x(\%) = \frac{(x^{Exp} - x^{Cal})}{x^{Exp}} * 100 \quad (13)$$

$$\Delta P(\%) = \frac{(P^{Exp} - P^{Cal})}{P^{Exp}} * 100 \quad (14)$$

The comparison of the calculated results with the relative volatility model and the experimental data demonstrates a high consistency between the two.

The relative error values plotted in Figures 12-15 indicate that this method gives good computational of both critical and azeotrope locations. It can be seen that the relative error does not exceed 4.3 % for the molar fraction (x) and 7.5 % for the pressure (P).

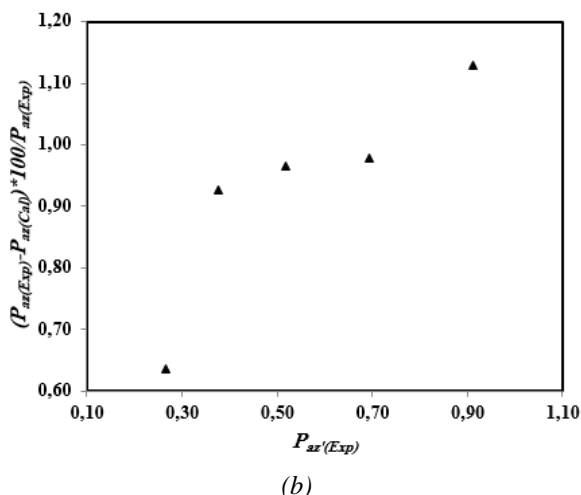
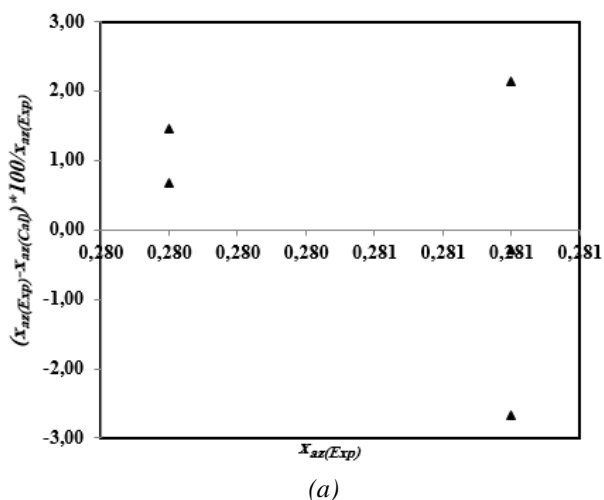


Figure 12. Relative error of mole fractions (a) and pressures (b) of R1234yf+R290 system.

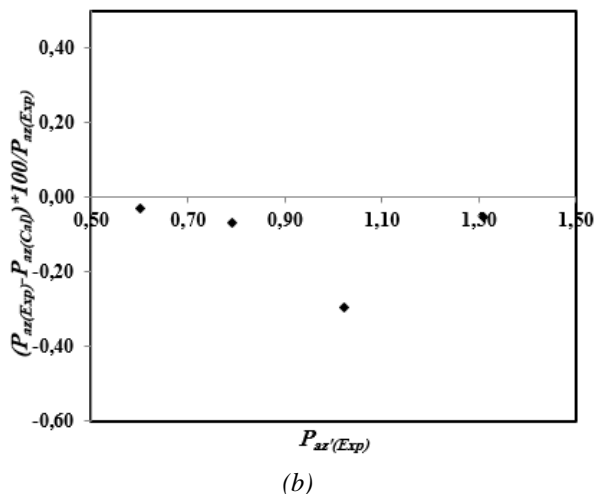
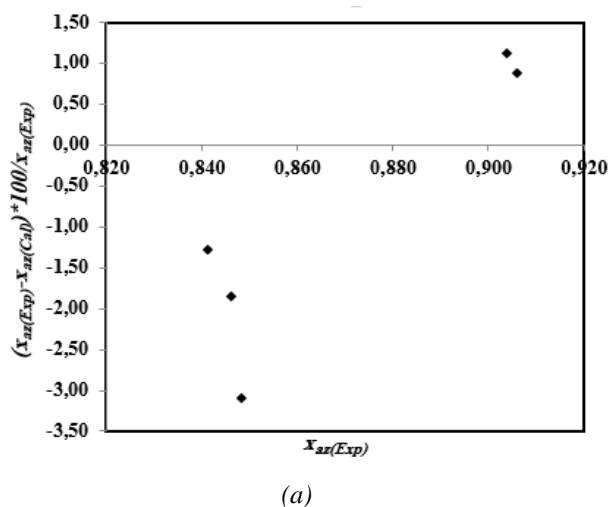
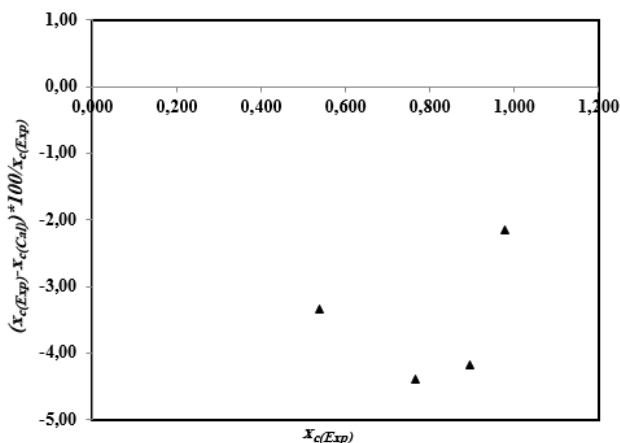


Figure 13. Relative error of mole fractions (a) and pressures (b) of R1234yf+R600a system.

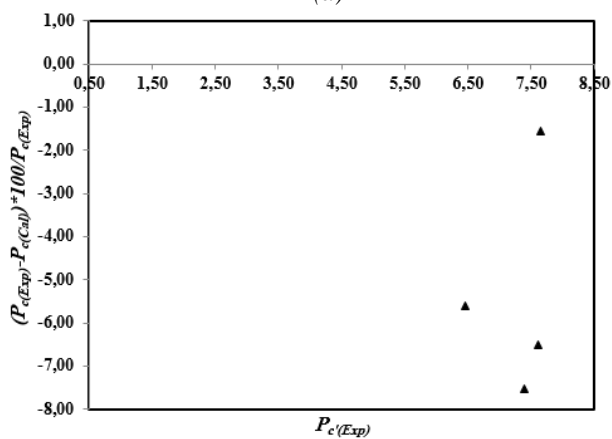
3.3 Phase Behavior of Binary Refrigerant Systems

Figures 16-21 present the (P - x - y) relationship between the isothermal dew and bubble curves of the binary refrigerant systems: R744+R134a, R744+R1234ze, R1234yf+R290, R1234yf+R600a, R32+R1234yf and R32+R152a at different temperatures. The symbol curves denote the isothermal experimental (VLE) data taken from the literature and the dashed line curves are the results of predictions and modeled data using the cubic equation of state of (PR-EoS) associated with the (MC) alpha function

and coupled with the (WS) mixing rule and the NRTL G^E model. From the variation of the bubble and dew point pressure curves in the phase diagram (P-x-y), different thermodynamic behaviors can be observed, when the molar fraction of the mixture changes.



(a)



(b)

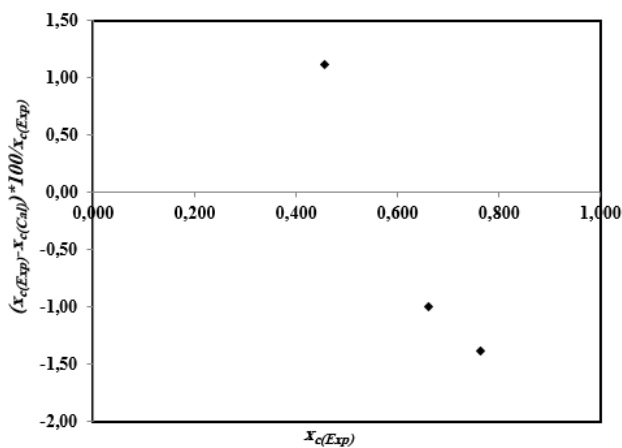
Figure 14. Relative error of mole fractions (a) and pressures (b) of R744+R1234ze system.

As can be seen from the figures 16-21, the model: “PR–MC–WS–NRTL” is able to perfectly accurately predicts the phase behavior and the location of the both critical and azeotropes points of the blends, where the results show that there is excellent agreement between the computation values obtained with our prediction model and the published isothermal VLE data, where it found that the relative deviation is less than 2.60 % and 2.58 % for the liquid and vapor mole fractions, respectively (see Table 5)).

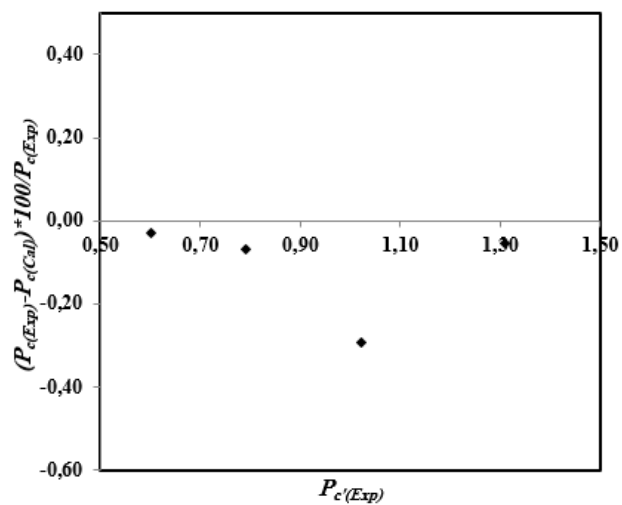
The binary mixture (R744+R1234ze) was studied at seven different isotherms ranging from 283.32 to 353.02 K, whereas the binary mixture (R744+R134a) was studied at three different isotherms ranging from 329.60 to 354 K.

It can be found that both mixtures exhibits a critical behavior, due to the intermolecular interactions occurring in these systems. The critical behavior was observed for the three isotherms (329.60; 339.1 and 354 K) above the critical temperature (T_c) of the carbon dioxide (T_c (R744) = 304.13 K) for the blend R744+R134a (Figure 16). Whereas, for the blend R744+R1234ze, the critical behavior was observed for the four isotherms (308.15; 318.11; 333.01 and 353.02 K) above the critical temperature (T_c) of the carbon dioxide (T_c (R744) = 304.13 K) (Figure 17). This last feature is the consequence for temperatures higher than the critical temperature of the most volatile pure substance

(carbon dioxide), the binary systems conventionally has a critical point.



(a)



(b)

Figure 15. Relative error of mole fractions (a) and pressures (b) of R744+R134a system.

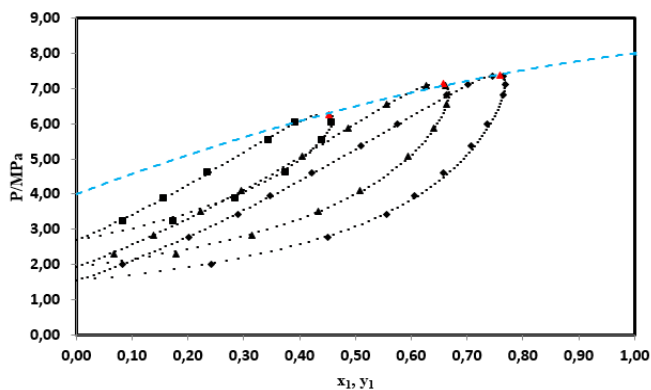


Figure 16. P-x-y diagram for the isothermal vapor-liquid equilibria of R744+R134a system. (Experimental data at various isotherms [23]: (♦) 329.60 K; (▲) 339.10 K; (■) 354 K; (▲) locus of critical points; (---) critical line; (...): Calculated (VLE) properties using the proposed model).

On the other hand, it can be directly observed that the two binary systems (R1234yf+R290) and (R1234yf+R600a) show an azeotropic behavior (mixtures have the same behavior as a pure substance during the change of state (condensation or evaporation) in the all

temperatures range studied, where the bubble and dew curve are tangent to each other and these two curves do not intersect (Figures 18-19). This azeotrope is a homogeneous azeotrope at maximum pressure, where the composition of the phases of the liquid and the vapor are identical ($x_i=y_i$) and the relationship between P and x_i at azeotropic point satisfying this condition ($dP/dx_i=0$). The azeotropes phenomenon was observed between the mole fractions (0.2 and 0.4) and (0.8 and 0.9) for both binary mixtures (R1234yf+R290) and (R1234yf+R600a) in the isothermal range between 253.15 to 293.15 K and 283.15 to 323.15 K, respectively.

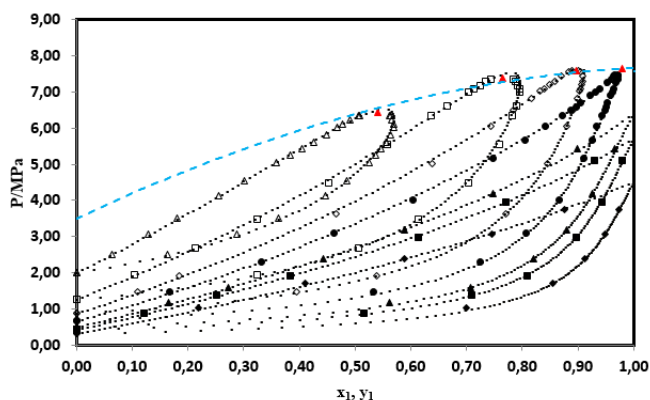


Figure 17. P - x - y diagram for the isothermal vapor-liquid equilibria of R744+R1234ze system. (Experimental data at various isotherms [29]: (◆) 283.32 K; (■) 293.15 K; (▲) 298.15 K; (●) 308.13 K; (◇) 318.11 K; (□) 333.01 K; (△) 353.02 K; (▲) locus of critical points; (---) critical line; (...): Calculated (VLE) properties using the proposed model).

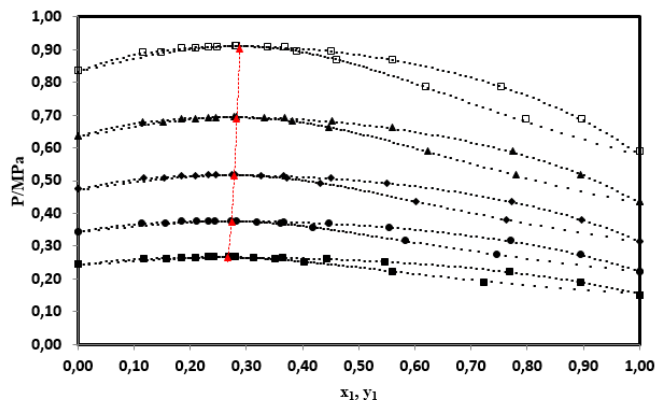


Figure 18. P - x - y diagram for the isothermal vapor-liquid equilibria of R1234yf+R290 system. (Experimental data at various isotherms [30]: (■) 253.15 K; (●) 263.15 K; (◆) 273.15 K; (▲) 283.15 K; (□) 293.15 K; (▲) locus of azeotropic points; (---) azeotropic line; (...): Calculated (VLE) properties using the proposed model).

The azeotropes occur in the blends with compounds having similar molecular properties, which are reflected on their thermodynamic properties by having close values of the vapor pressures and the critical temperatures. These blends could be useful for refrigeration applications, where with the same evaporation pressure; the binary systems will have a constant evaporation temperature in the evaporator of the cooling unit.

In the case of the two blends (R32+R1234yf and R32+R152a), it can be found obviously from the graphical

VLE representations that the refrigerant blends shows a zeotropic behavior (Figures 20-21) (the bubble and dew curve are not tangent to each other) over the whole ranges of temperature (283.15 to 323.15 K), where these systems have an almost ideal behavior and the intermolecular interactions could be neglected.

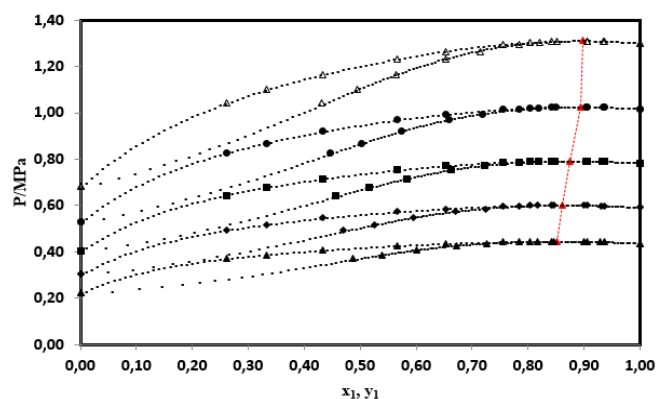


Figure 19. P - x - y diagram for the isothermal vapor-liquid equilibria of R1234yf+R600a system. (Experimental data at various isotherms [31]: (▲) 283.15 K; (◆) 293.15 K; (■) 303.15 K; (●) 313.15 K; (△) 323.15 K; (▲) locus of azeotropic points; (---) azeotropic line; (...): Calculated (VLE) properties using the proposed model).

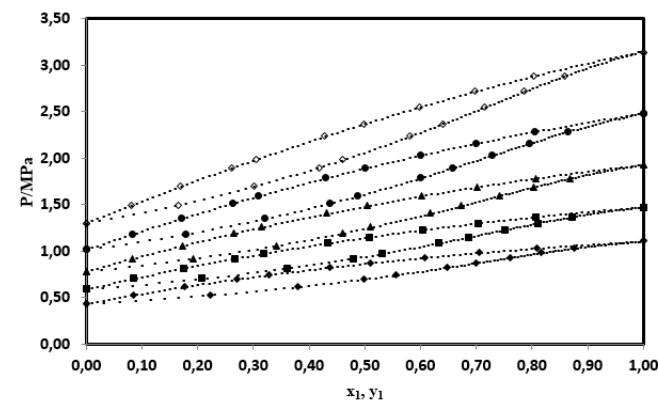


Figure 20. P - x - y diagram for the isothermal vapor-liquid equilibria of R32+R1234yf system. (Experimental data at various isotherms [32]: (◆) 283.15 K; (■) 293.15 K; (▲) 303.15 K; (●) 313.15 K; (◇) 323.15 K; (...): Calculated (VLE) properties using the proposed model).

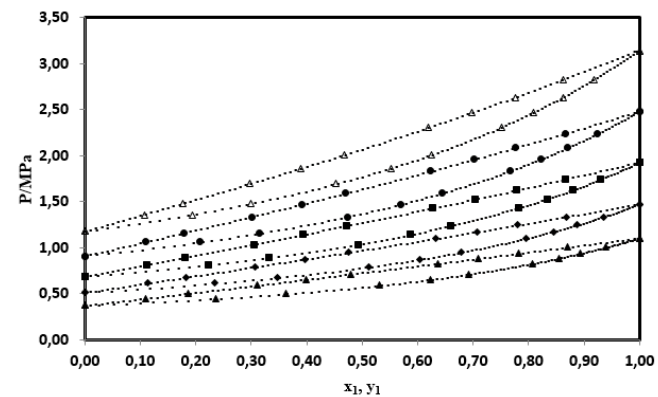


Figure 21. P - x - y diagram for the isothermal vapor-liquid equilibria of R32+R152a system. (Experimental data at various isotherms [33]: (▲) 283.15 K; (◆) 293.15 K; (■) 303.15 K; (●) 313.15 K; (△) 323.15 K; (...): Calculated (VLE) properties using the proposed model).

To check the accuracy of our thermodynamic model «PR–MC–WS–NRTL» used in this study to correlate the isothermal (VLE) data of the binary refrigerant blends, the deviations, MRDU, and the BIASU [34] between the experimental data available in literature and the results of the mathematical modeling of binary refrigerant systems are applied for both vapor and liquid phases mole fractions, respectively by Eqs. (15) and (16):

$$\text{BIASU} = \left(\frac{100}{N} \right) \sum \left(\frac{U_{\text{Cal}} - U_{\text{Exp}}}{U_{\text{Exp}}} \right) \quad (15)$$

$$\text{MRDU} = \left(\frac{100}{N} \right) \sum \left| \frac{U_{\text{Cal}} - U_{\text{Exp}}}{U_{\text{Exp}}} \right| \quad (16)$$

Where N is the number of data points, $U=x_j$ or y_j and the subscripts Exp, and Cal denote the measured and calculated quantities.

These indicators give information about the agreement between model and experimental results. The deviations between the published experimental values and the results of computation of the liquid and vapor compositions are reported in Table 5.

Table 5. The MRDU and BIASU obtained in fitting experimental isothermal (VLE) data with the proposed model for the binary refrigerant systems.

T [K]	Bias x %	MRD x %	Bias y %	MRD y %
R744+R134a				
329.60	2.60	2.61	0.78	0.88
339.10	2.52	2.54	1.18	1.24
354	1.42	1.48	2.58	2.70
329.60	2.60	2.61	0.78	0.88
R744+R1234ze				
283.32	-1.13	1.77	-0.52	0.72
293.15	-0.89	1.45	-0.05	0.37
298.15	-0.80	1.25	-0.64	0.84
308.13	0.01	0.57	-0.27	0.31
318.11	-0.64	1.03	-0.37	0.39
333.01	0.03	0.80	0.01	0.25
353.02	-0.53	0.53	-0.48	0.59
R1234yf+R290				
253.15	1.17	0.78	0.24	0.66
263.15	1.12	1.75	0.66	0.78
273.15	0.37	0.98	-0.17	0.76
283.15	0.34	0.83	-0.08	0.57
293.15	-0.84	1.24	-0.99	1.08
R1234yf+R600a				
283.15	-0.21	0.64	-0.06	0.41
293.15	-0.32	0.57	0.03	0.59
303.15	-0.14	0.27	-0.10	0.40
313.15	-0.12	0.29	0.00	0.26
323.15	-0.03	0.14	-0.02	0.33
R32+R1234yf				
283.15	-0.04	0.07	0.03	0.09
293.15	-0.05	0.05	0.07	0.15
303.15	0.01	0.08	0.14	0.20
313.15	-0.02	0.12	0.18	0.27
323.15	-0.12	0.24	0.22	0.44
R32+R152a				
283.15	0.11	0.24	-0.80	0.80
293.15	0.12	0.22	-0.50	0.54
303.15	0.16	0.18	-0.33	0.34
313.15	0.19	0.26	-0.24	0.24
323.15	0.18	0.28	-0.09	0.09

4. Conclusions

In the present study, six binary refrigerant systems have been studied with the aim to predict their phase behavior and determine the thermodynamic properties (critical and

azeotropic points) in isothermal (VLE) using two models: “Relative volatility model” and the thermodynamic model “PR–MC–WS–NRTL”.

In the first part of this work, the possibility of presence of azeotropic or critical states in the binary working fluids has been verified and computing their properties (compositions and pressures) in each isotherm was made. It can be seen that the relative error does not exceed 4.3 % for the molar fraction and 7.5 % for the pressure.

In the second part, the thermodynamic model, which combines the cubic equation of state of Peng–Robinson (PR–EoS) with the (MC) alpha function, and the NRTL G^E model, using the WS mixing rules has been employing to correlate the data of isothermal (VLE) properties of this blends and describe their phase behavior.

The results of mathematical modeling showed that the isothermal VLE of the studied binary working fluids is well correlated using the proposed model. The obtained results for the binary refrigerant systems proved that the model described accurately their behavior in both subcritical and supercritical regions, where the relative deviation is less than 2.60 % and 2.58 %, respectively for the liquid and vapor mole fractions.

From the discussion of the obtained results in this work, the main conclusions are:

- The computation model “Relative volatility” gives good predictions of azeotropic and critical behavior of binary refrigerant systems;
- the relative volatility model has the ability to determine the thermodynamic properties;
- The (PR–MC–WS–NRTL) model has high accuracy in the prediction of isothermal (VLE) properties;
- The binary blends (R744+R134a and R744+R1234ze) exhibits critical behavior;
- The refrigerant blends: (R1234yf+R290 and R1234yf+R600a) have exhibited azeotropic behavior;
- The blends R32+R1234yf and R32+R152a have showed zeotropic behavior.

Nomenclature

Symbols

a	Energy parameter ($\text{J m}^3 \text{mol}^{-2}$)
b	Molar co volume parameter ($\text{m}^3 \text{mol}^{-1}$)
c_1, c_2, c_3	Mathias-Copeman coefficient
C	Numerical constant equal to -0.62323
N	Number of experimental points
g	Gibbs energy (J)
G	Molar Gibbs energy (J mol^{-1})
K_{ij}	Binary interaction parameter
K_1	Partition coefficient
P	Pressure (MPa)
R	Universal gas constant ($\text{J mol}^{-1} \text{K}^{-1}$)
T	Temperature (K)
v	Molar volume ($\text{m}^3 \text{mol}^{-1}$)
x	Liquid mole fraction
y	Vapor mole fraction

Greek symbols

$\alpha(T)$	Alpha function
α_{ij}	Relative volatility between component i and j
γ_i	Activity coefficient of component i
∞	Infinite pressure reference state

τ Binary interaction coefficients in NRTL activity model

Subscripts

az Azeotrope property
c Critical property
i,j Molecular species
1 Most volatile pure substance
2 Less volatile pure substance
Cal Calculated property
Exp Experimental property

Superscript

E Excess property

Abbreviations

GWP Global warming potential
ODP Ozone depleting potential
VLE Vapor liquid equilibria
EoS Equation of state
PR Peng–Robinson
MC Mathias–Copeman
WS Wong–Sandler
NRTL Non Random Two Liquids

Refrigerants

R744 Carbon dioxide
R134a 1,1,1,2-tetrafluoroethane
R1234yf 2,3,3,3-tetrafluoroprop-1-ene
R1234ze Trans-1,3,3,3-tetrafluoropropene
R290 Propane
R600a Isobutane
R32 Difluoromethane
R152a 1,1-Difluoroethane

References:

- [1] C. Coquelet, A. Chareton, and D. Richon, "Vapour-liquid equilibrium measurements and correlation of the difluoromethane (R32) + propane (R290) + 1,1,1,2,3,3,3-heptafluoropropane (R227ea) ternary mixture at temperatures from 269.85 to 328.35K," *Fluid Phase Equilib.*, 218, 209–214, 2004, doi:10.1016/j.fluid.2003.12.009.
- [2] Y. Maalem, A. Zarfa, Y. Tamene, S. Fedali, and H. Madani, "Prediction of thermodynamic properties of the ternary azeotropic mixtures," *Fluid Phase Equilib.*, 517, 112613, 2020, doi:10.1016/j.fluid.2020.112613.
- [3] JM. Calm, "The next generation of refrigerants – Historical review, considerations, and outlook," *Int. J. Refrig.*, 31, 1123–1133, 2008, doi:10.1016/j.ijrefrig.2008.01.013.
- [4] S. Kato and D. Bluck, "Practical Applications of a Pure Prediction Method for Binary VLE to the Establishment of a High-Precision UNIFAC," *J. Chem. Eng. Data.*, 61, 4236–4244, 2016, doi:10.1021/acs.jced.6b00593.
- [5] A. Jakob, H. Gensemann, J. Lohmann, and J. Gmehling, "Further Development of Modified UNIFAC (Dortmund): Revision and Extension 5," *Ind. Eng. Chem. Res.*, 45, 7924–7933, 2006, doi:10.1021/ie060355c.
- [6] K. Zheng, H. Wu, C. Geng, G. Wang, Y. Yang, and Y. Li, "A Comparative Study of the Perturbed-Chain Statistical Associating Fluid Theory Equation of State and Activity Coefficient Models in Phase Equilibria Calculations for Mixtures Containing Associating and Polar Components," *Ind. Eng. Chem. Res.*, 57, 3014–3030, 2018, doi:10.1021/acs.iecr.7b04758.
- [7] P. Anila, K. Rayapa Reddy, G. Srinivasa Rao, PVS. Sai Ram, D. Ramachandran, and C. Rambabu, "Activity coefficients and excess Gibbs energy functions of acetophenone with 1,2-dichloroethane and 1,1,2,2-tetrachloroethane binary mixtures by using NRTL, UNIQUAC, UNIFAC and VAN LAAR models at a local atmospheric pressure of 95.3 kPa," *Karbala Int. J. Mod. Sci.*, 2, 211–218, 2016, doi:10.1016/j.kijoms.2016.07.001.
- [8] H. Mokarizadeh, S. Moayedfard, and M. Mozaffarian, "Comparison of MOSCED (NRTL) model results with regular correlative and predictive models based on vapor-liquid equilibrium calculations for azeotropic systems," *Fluid Phase Equilib.*, 516, 112592, 2020, doi:10.1016/j.fluid.2020.112592.
- [9] G. Yu, C. Dai, and Z. Lei, "Modified UNIFAC-Lei Model for Ionic Liquid-CH₄ Systems," *Ind. Eng. Chem. Res.*, 57, 7064–7076, 2018, doi:10.1021/acs.iecr.8b00986.
- [10] AS. Teja and JS. Rowlinson, "The prediction of the thermodynamic properties of fluids and fluid mixtures — IV. Critical and azeotropic states," *Chem. Eng. Sci.*, 28, 529–538, 1973, doi:10.1016/0009-2509(73)80050-8.
- [11] S. Artemenko and V. Mazur, "Azeotropy in the natural and synthetic refrigerant mixtures," *Int. J. Refrig.*, 30, 831839, 2007, doi:10.1016/j.ijrefrig.2006.11.010.
- [12] ZT. Fidkowski, MF. Malone, and MF. Doherty, "Computing azeotropes in multicomponent mixtures," *Comput. Chem. Eng.*, 17, 1141–1155, 1993, doi:10.1016/0098-1354(93)80095-5.
- [13] JE. Tolsma and PI. Barton, "Computation of heteroazeotropes. Part I: Theory," *Chem. Eng. Sci.*, 55, 3817–3834, 2000, doi:10.1016/S0009-2509(00)00032-4.
- [14] P. Kolář and K. Kojima, "Prediction of critical points in multicomponent systems using the PSRK group contribution equation of state," *Fluid Phase Equilib.*, 118, 175–200, 1996, doi:10.1016/0378-3812(95)02850-1.
- [15] XQ. Dong, MQ. Gong, Y. Zhang, and JF. Wu, "Prediction of homogeneous azeotropes by Wilson equation for binary HFCs and HCs refrigerant mixtures," *Fluid Phase Equilib.*, 269, 6–11, 2008, doi:10.1016/j.fluid.2008.04.012.
- [16] RA. Heidemann and AM. Khalil, "The calculation of critical points," *AIChE J.*, 26, 769–779, 1980, doi:10.1002/aic.690260510.
- [17] DV. Nichita, "Calculation of critical points using a reduction method," *Fluid Phase Equilib.*, 228–229, 223–231, 2005, doi:10.1016/j.fluid.2004.09.036.
- [18] RW. Maier, JF. Brennecke, and MA. Stadtherr, "Reliable computation of homogeneous azeotropes," *AIChE J.*, 44, 1745–1755, 1998, doi:10.1002/aic.690440806.

- [19] M. He, Y. Liu, and X. Liu, "Prediction of critical temperature and critical pressure of multi-component mixtures," *Fluid Phase Equilib.*, 441, 2–8, 2017, doi:10.1016/j.fluid.2016.11.017.
- [20] P. Hu, Z-S. Chen, and W-L. Cheng, "Prediction of vapor–liquid equilibria properties of several HFC binary refrigerant mixtures," *Fluid Phase Equilib.*, 204, 75–84, 2003, doi: 10.1016/S0378-3812(02)00216-9.
- [21] X. Dong, M. Gong, Y. Zhang, J. Liu, and J. Wu, "Prediction of Homogeneous Azeotropes by the UNIFAC Method for Binary Refrigerant Mixtures," *J. Chem. & Eng. Data.*, 55, 52–57, 2010, doi:10.1021/jc900693q.
- [22] S. Fedali, H. Madani, and C. Bougriou, "Prediction method of both azeotropic and critical points of the binary refrigerant mixtures," *J. Appl. Eng. Sci. & Technol.*, Vol 3 No 1, 2017.
- [23] G. Silva-Oliver and LA. Galicia-Luna, "Vapor–liquid equilibria for carbon dioxide + 1,1,1,2-tetrafluoroethane (R-134a) systems at temperatures from 329 to 354 K and pressures upto 7.37 MPa," *Fluid Phase Equilib.*, 199, 213–222, 2002, doi:10.1016/S0378-3812(01)00816-0.
- [24] D-Y. Peng and DB. Robinson, "A New Two-Constant Equation of State," *Ind. Eng. Chem. Fundam.*, 15, 59–64, 1976, doi:10.1021/i160057a011.
- [25] PM. Mathias and TW. Copeman, "Extension of the Peng-Robinson equation of state to complex mixtures: Evaluation of the various forms of the local composition concept," *Fluid Phase Equilib.*, 13, 91–108, 1983, doi:10.1016/0378-3812(83)80084-3.
- [26] Dortmund Data Bank (DDB), Version 97, "DDBST Software and Separation Technology GmbH," Oldenburg, Germany, 1997.
- [27] DSH. Wong and SI. Sandler, "A theoretically correct mixing rule for cubic equations of state," *AIChE J.*, 38, 671–680, 1992, doi:10.1002/aic.690380505.
- [28] H. Renon and JM. Prausnitz, "Local compositions 1 in thermodynamic excess functions for liquid mixtures," *AIChE J.*, 14, 135–144, 1968, doi:10.1002/aic.690140124.
- [29] S. Wang, R. Fauve, C. Coquelet, A. Valtz, C. Houriez, P-A. Artola, E. El Ahmar, B. Rousseau, and H. Haitao, "Vapor–liquid equilibrium and molecular simulation data for carbon dioxide (CO₂) + trans-1,3,3,3-tetrafluoroprop-1-ene (R-1234ze(E)) mixture at temperatures from 283.32 to 353.02 K and pressures up to 7.6 MPa," *Int. J. Refrig.*, 98, 362–371, 2019, doi:10.1016/j.ijrefrig.2018.10.032.
- [30] Q. Zhong, X. Dong, Y. Zhao, H. Li, H. Zhang, H. Guo, and M. Gong, "Measurements of isothermal vapour–liquid equilibrium for the 2,3,3,3-tetrafluoroprop-1-ene + propane system at temperatures from 253.150 to 293.150 K," *Int. J. Refrig.*, 81, 26–32, 2017, doi:10.1016/J.IJREFRIG.2017.05.016.
- [31] P. Hu, L-X. Chen, and Z-S. Chen, "Vapor–liquid equilibria for binary system of 2,3,3,3-tetrafluoroprop-1-ene (HFO-1234yf) + isobutane (HC-600a)," *Fluid Phase Equilib.*, 365, 1–4, 2014, doi:10.1016/j.fluid.2013.12.015.
- [32] X. Hu, T. Yang, X. Meng, S. Bi, and J. Wu, "Vapor liquid equilibrium measurements for difluoromethane (R32) + 2,3,3,3-tetrafluoroprop-1-ene (R1234yf) and fluoroethane (R161) + 2,3,3,3-tetrafluoroprop-1-ene (R1234yf)," *Fluid Phase Equilib.*, 438, 10–17, 2017, doi:10.1016/j.fluid.2017.01.024.
- [33] T. Yang, X. Hu, X. Meng, and J. Wu, "Vapor–Liquid Equilibria for the Binary and Ternary Systems of Difluoromethane (R32), 1,1-Difluoroethane (R152a), and 2,3,3,3-Tetrafluoroprop-1-ene (R1234yf)," *J. Chem. Eng. Data.*, 63, 771–780, 2018, doi:10.1021/acs.jced.7b00950.
- [34] H. Madani, A. Valtz, F. Zhang, J. El Abbadi, C. Houriez, P. Paricaud, and C. Coquelet, "Isothermal vapor-liquid equilibrium data for the trifluoromethane (R23) + 2,3,3,3-tetrafluoroprop-1-ene (R1234yf) system at temperatures from 254 to 348 K," *Fluid Phase Equilib.*, 415, 158–165, 2016, doi:10.1016/j.fluid.2016.02.005.

Research Article

Thermoelastic Analysis For A Thick Plate Under The Radiation Boundary Conditions

¹G. Dhameja , ²L. Khalsa , ^{3*}V. Varghese 

^{1,2,3} Department of Mathematics, M.G. College, Armori, Gadchiroli, India
E-mails: ¹dhameja.geeta0311@gmail.com, ²lalsinghkhalsa@yahoo.com, ^{3*}vino7997@gmail.com

Received 2 September 2022, Revised 15 January 2023, Accepted 25 January 2023

Abstract

A fractional Cattaneo model for studying the thermoelastic response for a finite thick circular plate with source function is considered. The thick plate is subjected to radiation-type boundary conditions on the upper and lower surfaces, and its curved surface is kept at zero temperature. The theory of integral transformations is used to solve the generalized fractional Cattaneo-type, classical Cattaneo-Vernotte and Fourier heat conduction model. The analytical expressions of displacement components using thermoelastic displacement potentials; and thermal-stress distribution are computed and depicted graphically. The effects of the fractional-order parameter and the relaxation time on the temperature fields and their thermal stresses are investigated. The findings show that the higher the fractional-order parameter, the higher the thermal response. The greater the relaxation period, the longer the heat flux propagates on thick structures.

Keywords: Fractional Cattaneo-type equation; fractional calculus; non-Fourier heat conduction; thick plate; thermal stress; integral transform.

1. Introduction

It is required to preserve the structural elements from wear, corrosion, and delamination in high-temperature environments such as the cosmos, thermal power stations, and internal combustion engines. These kinds of environments have incredibly high temperatures. The development of functionally graded materials has been done to alleviate the effects of thermal and residual stresses. Functionally graded materials can avoid destruction because of the gradual change in the material properties. Recently, Haskul [1,2] obtained analytical solutions for the stresses and displacements of a functionally graded cylindrically curved beam subjected to a heat load in the radial direction using von Mises' yield criterion. Haskul et al. [3,4] investigated the elastic stress response of a thick-walled cylindrically curved panel subjected to a radial temperature gradient under the assumption of generalized plane strain according to both yield criteria, Tresca and von Mises.

As everyone knows, the heat current is based on particles or quasi-particle motion from the macroscopic experience. The same reflects in Fourier's law within the framework of the classical parabolic heat conduction equation in which the velocity of heat transport is not limited. A modified Fourier's law fulfilled these conditions explicitly by considering the finite propagation velocity of heat in the conduction equation by the so-called hyperbolic heat conduction equation. Furthermore, technological development with advancements in Science helps to revolutionize by introducing the heat relaxation time to the non-equilibrium heat conduction mechanism [5-8]. Cattaneo [9] and Vernotte [10] multiplied the thermal relaxation time to a partial time derivative of the

heat flux. This so-called Cattaneo-Vernotte hyperbolic heat conduction equation can predict the non-equilibrium heat conduction progression combined with the energy equation. Meanwhile, Compte and Metzler [11] proposed four possible generalizations of the Cattaneo telegraph equation. Though the theoretical modeling of Cattaneo-Vernotte equations overcomes the infinite heat propagation speed for the non-equilibrium process, few nonconformities in the experimental results were noticed by Jiang et al. [12].

Povstenko [13] proposed a quasi-static uncoupled theory of thermoelasticity based on a fractional heat conduction equation. Povstenko [14] published highly cited literature reviews on fractional thermoelasticity. The above literature emphasizes that coupling between deformation and heat conduction in the heat equation into account does not complicate the Neumann boundary value problem in the quasi-static theory framework. In the framework of fractional thermoelasticity, Povstenko [15] also proposed the time-fractional Cattaneo heat conduction equation from the time-non-local generalization of the Fourier law using different kernels, i.e., Mittag-Leffler type, within the framework of corresponding thermal stress theory. Mishra and Rai [16] obtained the fractional single-phase-lagging heat conduction model by applying the fractional Taylor series formula to the single-phase-lagging heat conduction model. Few researchers [17-22] recently got the mathematical solutions of the fractional Cattaneo-Vernotte heat conduction problem with Neumann boundary conditions on a finite or semi-infinite medium. However, based on the Cattaneo-Vernotte fractional model, the heat conduction of the finite thickness along with the radiation

boundary condition has been less studied. Therefore, the analytical solution for the time-fractional heat conduction of Cattaneo in a finite thick plate under radiation conditions is studied in this paper. The heat conduction mechanism that differs from the fractional-order parameters is analyzed. The time-fractional thermoelastic analysis of the Cattaneo-type for a thick plate under radiation boundary conditions has not been investigated to the best of the author's knowledge.

The outline of the remaining paper is as follows. Section 2 presents the mathematical modeling of the generalized heat conduction equation in the framework of fractional Cattaneo-type, with its associated thermal stresses. Section 3 obtains the solution of time-fractional Cattaneo analysis under radiation conditions. Section 4 gives deduction and validation of the results. Section 5 gives outcomes that are graphically shown. Finally, conclusive comments are summarized in Section 6.

2. Mathematical Model

2.1 Fractional Cattaneo-Type Heat Conduction

The classical Cattaneo model [23] as

$$q + \tau \frac{\partial q}{\partial t} = -k \nabla T \quad (1)$$

By combining Eq. (1) with the continuity equation

$$\rho C_v \frac{\partial T}{\partial t} = -\nabla \cdot q \quad (2)$$

leads to the hyperbolic heat conduction equation

$$\frac{\partial T}{\partial t} + \tau \frac{\partial^2 T}{\partial t^2} = \kappa \Delta T \quad (3)$$

in which q is the heat flux vector, τ is the relaxation time, k is the heat conductivity of a solid, κ is the thermal diffusivity coefficient, ρ is the density, C_v is the calorific value, ∇ is the gradient operator, T is the temperature and t is the time, respectively.

The fractional generalization [24] of the classical Cattaneo model by introducing the fractional Taylor formula [21] as

$$q + \tau^p \frac{\partial^p q}{\partial t^p} = -k \nabla T, \quad 0 < p \leq 1, \quad (4)$$

where without losing the generality $\Gamma(1+p)$ appearing in the Taylor series is merged in τ^p terms, Γ is the gamma function, p is introduced to keep the dimension in order and $\partial^p / \partial t^p$ is the fractional time derivative based on Caputo fractional definition [25]. For the limiting case of $\tau = 0$ (or $p=0$), Eq. (4) reduces to classical Fourier heat conduction and the standard Cattaneo heat conduction equation for $p=1$. The estimated ranges of relaxation time (in seconds) usually involve $(10^{-11} \square 10^{-14})$ for metals, $(10^{-8} \square 10^{-10})$ for gases, and $(10 \square 10^2)$ for porous materials [26].

Combining Eq. (4) with the law of conservation of energy shown in Eq. (2), leads to the fractional generalized Cattaneo equation as

$$\frac{\partial T}{\partial t} + \tau^p \frac{\partial^{p+1} T}{\partial t^{p+1}} = \kappa \Delta T, \quad 0 < p \leq 1 \quad (5)$$

Taking the Laplace transform [27-29] of Eq. (4), one obtains

$$q^*(s) = -\frac{\kappa \nabla T^*(s)}{(1 + \tau^p s^p)}, \quad 0 < p \leq 1 \quad (6)$$

in which the asterisk denotes the transform and s is a transform parameter. Using the inversion theorem of the Laplace transform, one gets the solution of Eq. (6) as

$$q(t) = -\frac{k}{\tau^p} \int_0^t (t-\gamma)^{p-1} E_{p,p} \left[-\frac{(t-\gamma)^p}{\tau^p} \right] \nabla T(\gamma) d\gamma \quad (7)$$

where $E()$ is the generalized Mittag-Leffler functions. Here Eq. (7) with $\tau^p = \zeta$ was obtained by Povstenko [13-15].

2.2 The Plate Under Radiation Boundary Conditions

Figure 1 shows a schematic sketch of the studied thermoelasticity problem and the cylindrical coordinate axes r, θ, z .

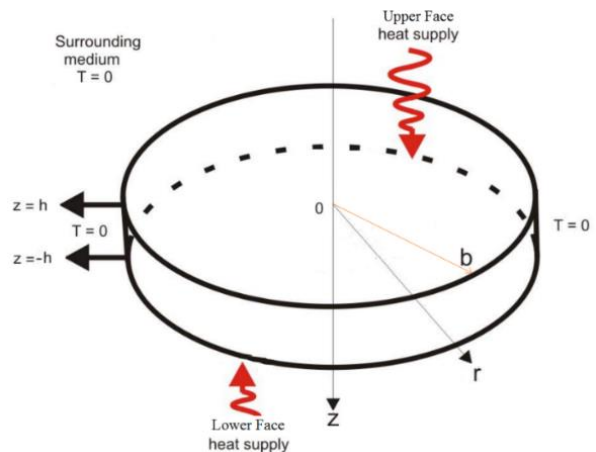


Figure 1 Plate configuration and heating conditions.

It is used to describe a time-fractional thermoelastic analysis of the thick plate under radiation boundary conditions. The two-dimensional finite thick circular plate occupies the domain $D = \{(r, z) \in [0, b] \times [-h, h]\}$ in the unstressed reference configuration. Equations governing the time-fractional Cattaneo-type heat conduction equation as

$$\frac{\partial T}{\partial t} + \tau^p \frac{\partial^{p+1} T}{\partial t^{p+1}} = \kappa \left[\frac{1}{r} \frac{\partial}{\partial r} \left(r \frac{\partial T}{\partial r} \right) + \frac{\partial^2 T}{\partial z^2} \right] + \chi(r, z, t), \quad (8)$$

$$0 \leq p \leq 1, 0 \leq r \leq b, -h \leq z \leq h, t > 0,$$

with zero initial condition

$$t = 0: T = 0, \frac{\partial T}{\partial t} = 0, 0 \leq r \leq b, -h \leq z \leq h \quad (9)$$

under the Dirichlet-type boundary condition on the curved surface

$$r = b: T = 0, -h \leq z \leq h, t > 0, \quad (10)$$

where $T=T(r,z,t)$ is the temperature in cylindrical coordinates, $\kappa=k/(\rho C_v)$ is the thermal diffusivity of the material, k is the conductivity of the medium, ρ is its density, C_v is the calorific capacity, assumed to be constant, and $\chi(r,z,t)$ is the source function having physical dimension $[\chi]=^\circ\text{C}/\text{m}^2$, respectively.

Povstenko [30-32] has recently investigated the time-fractional heat conduction equation with Caputo derivative under mathematical and physical Robin-type boundary conditions. Another equivalent name in use is radiation-type boundary condition [33-37], a specification of a linear combination of the values of a temperature function and its normal derivative on the domain's boundary and can be given as $[\beta_i f + \alpha_i (\partial f / \partial z)]_{z=\pm h} = A_i(r,t)$ [36]. Here α_i and β_i ($i=1,2$) are the constant thermal parameters related to the conduction and convection coefficients whose value can be positive, negative, or zero acting on surfaces $z = \pm h$ and A_i ($i=1,2$) is temperature distributions of the surrounding media. As a particular case, these conditions of radiation-type contour acting on surfaces $z = -h$ and $z = h$ can be taken as

$$\begin{aligned} z = h : T + k_1 \frac{\partial T}{\partial z} &= \xi \frac{\delta(r-r_0)}{r_0} \left(1 + \tau^p \frac{\partial^p}{\partial t^p} \right) f(t), \\ z = -h : T - k_2 \frac{\partial T}{\partial z} &= \xi \frac{\delta(r-r_0)}{r_0} \left(1 + \tau^p \frac{\partial^p}{\partial t^p} \right) f(t), \end{aligned} \quad (11)$$

where the radiation constant coefficients on the upper and lower surfaces are taken as $\beta_1 = \beta_2 = 1$, $\alpha_1 = k_1$, $\alpha_2 = k_2$ for a specified temperature on the boundary, ξ is the heat transfer coefficient having the physical dimension $[\xi]=^\circ\text{C m}$, $\delta(\)$ is the Dirac delta function, $f(t) = H(t) - H(t-t_0)$ is the difference of two Heaviside functions, r_0 and t_0 is a fixed value, $H(\)$ is the Heaviside function, and for the sake of brevity, we consider internal heat generation as

$$\chi(r,z,t) = Q_0 \frac{\delta(r-r_0)\delta(z)}{r_0} f(t), \quad 0 \leq r_0 \leq b, \quad (12)$$

in which the coefficient Q_0 characterizes the stream of heat and has the physical dimension $[Q_0]=^\circ\text{C m}^2$.

2.3 Thermoelastic Formulation

The Navier's equations [38] without the body forces can be expressed as

$$\begin{aligned} \nabla^2 u_r - \frac{u_r}{r^2} + \frac{1}{1-2\nu} \frac{\partial e}{\partial r} - \frac{2(1+\nu)}{1-2\nu} \alpha_i \frac{\partial T}{\partial r} &= 0, \\ \nabla^2 u_z - \frac{1}{1-2\nu} \frac{\partial e}{\partial z} - \frac{2(1+\nu)}{1-2\nu} \alpha_i \frac{\partial T}{\partial z} &= 0, \end{aligned} \quad (13)$$

where the displacement components in radial and axial directions are

$$\begin{aligned} u_r &= \frac{\partial \varphi}{\partial r} - \frac{\partial^2 L}{\partial r \partial z}, \\ u_z &= \frac{\partial \varphi}{\partial z} + 2(1-\nu) \nabla^2 L - \frac{\partial^2 L}{\partial z^2}, \end{aligned} \quad (14)$$

and the dilatation is

$$e = \frac{\partial u_r}{\partial r} + \frac{u_r}{r} + \frac{\partial u_z}{\partial z}, \quad (15)$$

with α_i as the thermal expansion coefficient, ν represents Poisson's ratio, $L(r,z,t)$ is Love's function [37], and $\varphi(r,z,t)$ is Goodier's displacement potential that must satisfy the equation [38]

$$\nabla^2 \varphi = K_0 T, \quad (16)$$

and Love's function must satisfy the equation

$$\nabla^2 \nabla^2 L = 0, \quad (17)$$

where

$$K_0 = [(1+\nu)/(1-\nu)]\alpha_i. \quad (18)$$

The stress component [38] is

$$\begin{aligned} \sigma_{rr} &= 2G \left\{ \left(\frac{\partial^2 \varphi}{\partial r^2} - \nabla^2 \varphi \right) + \frac{\partial}{\partial z} \left[\nu \nabla^2 L - \frac{\partial^2 L}{\partial r^2} \right] \right\}, \\ \sigma_{\theta\theta} &= 2G \left\{ \left(\frac{1}{r} \frac{\partial \varphi}{\partial r} - \nabla^2 \varphi \right) + \frac{\partial}{\partial z} \left[\nu \nabla^2 L - \frac{1}{r} \frac{\partial L}{\partial r} \right] \right\}, \\ \sigma_{zz} &= 2G \left\{ \left(\frac{\partial^2 \varphi}{\partial z^2} - \nabla^2 \varphi \right) + \frac{\partial}{\partial z} \left[(2-\nu) \nabla^2 L - \frac{\partial^2 L}{\partial z^2} \right] \right\}, \\ \sigma_{rz} &= 2G \left\{ \frac{\partial^2 \varphi}{\partial r \partial z} + \frac{\partial}{\partial r} \left[(1-\nu) \nabla^2 L - \frac{\partial^2 L}{\partial z^2} \right] \right\}, \end{aligned} \quad (19)$$

in which G is the shear modulus, ν is Poisson's ratio, and the Laplacian operator as

$$\nabla^2 = \frac{\partial^2}{\partial r^2} + \frac{1}{r} \frac{\partial}{\partial r} + \frac{\partial^2}{\partial z^2}. \quad (20)$$

The traction-free boundary conditions can be represented as follows:

$$r = b : \sigma_{rr} = \sigma_{rz} = 0, \quad (21)$$

and the other boundary conditions on the lower and upper surfaces are set free. Eqs. (8) to (21) constitute the mathematical formulation of the problem.

3. Solutions For The Plate Under Radiation Conditions

3.1 Solution Of Time-Fractional Cattaneo Analysis

Firstly, introducing the Hankel integral transform [39] and its inversion theorem as

$$T_n\{f(r)\} = f_{(r)}^{(\cdot)} = \int_0^b r J_0(\beta_n r) f(r) dr, \quad (22)$$

$$f(r) = \sum_n f_{(n)}^{(\cdot)} k_0(\beta_n r),$$

where n be the transform parameter and the kernel for the finite transform defined by

$$k_0(\beta_n r) = \frac{2}{b^2} \left[\frac{J_0(\beta_n r)}{\beta_n J_1^2(\beta_n b)} \right], \quad (23)$$

with β_n are the positive roots of the characteristic equation $J_0(\beta b) = 0$. We recall another integral transform proposed by Marchi and Fasulo [36] that responds to the radiation boundary conditions given in Eq. (11) as

$$T_p [g(z)] = g_{(z)}^{(\cdot)} = \int_{-h}^h g(z) P_m(z) dz, \quad (24)$$

$$g(z) = \sum_m \frac{g_{(m)}^{(\cdot)}}{\lambda_m} P_m(z),$$

where the orthogonal function gives the nucleus as

$$P_m(z) = Q_m \cos(a_m z) - W_m \sin(a_m z),$$

$$Q_m = a_m (k_2 + k_1) \cos(a_m h),$$

$$W_m = 2 \cos(a_m h) + (k_2 - k_1) a_m \sin(a_m h), \quad (25)$$

$$\lambda_m = \int_{-h}^h P_m^2(z) dz = h [Q_m^2 + W_m^2] + \frac{\sin(2a_m h)}{2a_m} [Q_m^2 - W_m^2].$$

and the eigenvalues a_m are the positive roots of the characteristic equation

$$[k_1 a \cos(ah) + \sin(ah)] [\cos(ah) + k_2 a \sin(ah)] = [k_2 a \cos(ah) - \sin(ah)] [\cos(ah) - k_1 a \sin(ah)]. \quad (26)$$

Following the rules defined in Eq. (22) and (24) to equation (8), one obtains

$$\left(\frac{d}{dt} + \tau^p \frac{d^{p+1}}{dt^{p+1}} \right) T_{(n,m,t)}^{(2)} + \kappa \Lambda T_{(n,m,t)}^{(2)} = H_{n,m} f(t), \quad (27)$$

subjected to the transformed initial condition (9) as

$$t = 0: T_{(n,m,t)}^{(2)} = 0, \quad \frac{\partial}{\partial t} T_{(n,m,t)}^{(2)} = 0, \quad (28)$$

where

$$\Lambda = a_m^2 + \beta_n^2, \quad (29)$$

$$H_{n,m} = \left\{ \left[\frac{P_m(h)}{k_1} - \frac{P_m(-h)}{k_2} \right] \xi + Q_0 P_m(z) \right\} k(\beta_n r_0). \quad (30)$$

Then, the transformed temperature of Eq. (27) in the Laplace domain is

$$T_{(n,m,s)}^{(3)} = H_{n,m} T_{(s)}^{(3)}, \quad (31)$$

where

$$T_{(n,m,s)}^{(3)} = \int_0^\infty T_{(n,m,t)}^{(2)} e^{-st} dt, \quad F(s) = \int_0^\infty f(t) e^{-st} dt, \quad (32)$$

and

$$T_{(s)}^{(3)} = \frac{F(s)}{\kappa(s + \tau^p s^{1+p}) + \Lambda}. \quad (33)$$

Eq. (33) is expanded into the following form [21]

$$T_{(s)}^{(3)} = \sum_{l=0}^{\infty} (-1)^l \frac{\Lambda^{2l} \tau^{-(l+1)p} s^{-(l+1)}}{\kappa(s^p + \tau^{-p})^{l+1}}. \quad (34)$$

Applying the convolution theorem, the inversion of Laplace transforms for Eq. (34)

$$T_{(n,m,t)}^{(2)} = H_{n,m} k(\beta_n r_0) \int_0^t T_{(\eta)}^{(2)} f(t-\eta) d\eta. \quad (35)$$

By adopting the discretization method [40], one obtains

$$T_{(t)}^{(2)} = L^{-1}\{T_{(s)}^{(3)}\} = L^{-1} \left\{ \sum_{l=0}^{\infty} (-1)^l \frac{\Lambda^{2l} \tau^{-(l+1)p} s^{-(l+1)}}{\kappa(s^p + \tau^{-p})^{l+1}} \right\}$$

$$= \sum_{l=0}^{\infty} (-1)^l \frac{\Lambda^{2l} \tau^{-(l+1)p} t^{l(p+1)+p}}{\kappa l!} E_{p,1+p+l}^{(l)} \left(-\frac{t^p}{\tau^p} \right), \quad (36)$$

where $E_{\alpha,\beta}^{(l)}$ is the generalized Mittag-Leffler functions [26]

$$E_{\alpha,\beta}^{(l)}(z) = \frac{d^n}{dz^n} E_{\alpha,\beta}(z) = \sum_{j=0}^{\infty} \frac{(j+n)! z^j}{j! \Gamma(\alpha j + \alpha n + \beta)}. \quad (37)$$

Applying the inversion theorems of transformation rules defined in Eqs. (22) and (24) on equation (35), one obtains

$$T(r, z, t) = \sum_{n=1}^{\infty} \sum_{m=1}^{\infty} \wp_{n,m} \left\{ \int_0^t T_{(\eta)}^{(2)} f(t-\eta) d\eta \right\} P_m(z) k(\beta_n r), \quad (38)$$

where

$$\wp_{n,m} = H_{n,m} k(\beta_n r_0) / (\lambda_m \Lambda). \quad (39)$$

Thus, Eq. (38) represents the temperature at every instant of the time-fractional Cattaneo heat conduction model and at all points of a thick circular plate when there are radiation-type conditions. Substituting the expression (31) into Eq. (16), one obtains Goodier's potential as

$$\varphi(r, z, t) = -K_0 \sum_{n=1}^{\infty} \sum_{m=1}^{\infty} \frac{\wp_{n,m}}{\Lambda} \left\{ \int_0^t T_{(\eta)}^{(2)} f(t-\eta) d\eta \right\} P_m(z) k_0(\beta_n r). \quad (40)$$

Similarly, Eq. (31) satisfying Eq. (17), one gets Love's function as

$$L(r, z, t) = -K_0 \sum_{n=1}^{\infty} \sum_{m=1}^{\infty} \frac{\wp_{n,m}}{\Lambda} \left\{ \int_0^t T_{(n)}^{(2)} f(t-\eta) d\eta \right\} \cosh(\beta_n z) \times [A_n J_0(\beta_n r) + C_n(\beta_n r) J_1(\beta_n r)], \quad (41)$$

in which unknown arbitrary functions A_n and C_n are to be determined later. Using Eqs. (21) and (22) into Eq. (14), one obtains

$$u_r = K_0 \sum_{n=1}^{\infty} \sum_{m=1}^{\infty} \frac{\wp_{n,m}}{\Lambda} \left\{ \int_0^t T_{(n)}^{(2)} f(t-\eta) d\eta \right\} \left\{ \beta_n \sinh(\beta_n z) \times [A_n(-\beta_n) J_1(\beta_n r) + C_n \beta_n(\beta_n r) J_0(\beta_n r)] + (2/b^2) \times [J_1(\beta_n r) / J_1(\beta_n b)] p_m(z) \right\}, \quad (42)$$

$$u_z = K_0 \sum_{n=1}^{\infty} \sum_{m=1}^{\infty} \frac{\wp_{n,m}}{\Lambda} \left\{ \int_0^t T_{(n)}^{(2)} f(t-\eta) d\eta \right\} \left\{ a_m [Q_m \sin(a_m z) + W_m \cos(a_m z)] k_0(\beta_n r) + A_n \beta_n^2 J_0(\beta_n r) (4\nu - 3) \times \cosh(\beta_n z) + C_n \beta_n^2 [4(1-\nu) J_0(\beta_n r) + (\beta_n r) J_1(\beta_n r) \times (4\nu - 3)] \cosh(\beta_n z) \right\}, \quad (43)$$

The stress components were evaluated using Eqs. (19)-(21) in (19)

$$\sigma_{rr} = -2G K_0 \sum_{n=1}^{\infty} \sum_{m=1}^{\infty} \frac{\wp_{n,m}}{\Lambda} \left\{ \int_0^t T_{(n)}^{(2)} f(t-\eta) d\eta \right\} \times \left\{ \left[a_m^2 J_0(\beta_n r) - \beta_n \left(\frac{J_1(\beta_n r)}{r} \right) \right] \left[\frac{2}{b^2 \beta_n J_1(\beta_n b)} \right] \times P_m(z) + \beta_n^3 C_n [(2\nu - 1) J_0(\beta_n r) + (\beta_n r) J_1(\beta_n r)] \times \sinh(\beta_n z) + \beta_n^2 A_n \left[\beta_n J_0(\beta_n r) - \frac{J_1(\beta_n r)}{r} \right] \sinh(\beta_n z) \right\}, \quad (44)$$

$$\sigma_{\theta\theta} = -2G K_0 \sum_{n=1}^{\infty} \sum_{m=1}^{\infty} \frac{\wp_{n,m}}{\Lambda} \left\{ \int_0^t T_{(n)}^{(2)} f(t-\eta) d\eta \right\} \times \left\{ \left[\beta_n \left(\frac{J_1(\beta_n r)}{r} \right) - \Lambda J_0(\beta_n r) \right] \left[\frac{2}{b^2 \beta_n J_1(\beta_n b)} \right] \times P_m(z) + \beta_n^2 A_n \sinh(\beta_n z) \left(\frac{J_1(\beta_n r)}{r} \right) \sinh(\beta_n z) + \beta_n^3 C_n (2\nu - 1) J_0(\beta_n r) \sinh(\beta_n z) \right\}, \quad (45)$$

$$\sigma_{zz} = -2G K_0 \sum_{n=1}^{\infty} \sum_{m=1}^{\infty} \frac{\wp_{n,m}}{\Lambda} \left\{ \int_0^t T_{(n)}^{(2)} f(t-\eta) d\eta \right\} \times \left\{ \frac{2}{b^2} \frac{\beta_n J_0(\beta_n r)}{J_1(\beta_n b)} P_m(z) - \beta_n^3 A_n J_0(\beta_n r) \sinh(\beta_n z) + \beta_n^3 C_n \times [2(2-\nu) J_0(\beta_n r) - (\beta_n r) J_1(\beta_n r)] \sinh(\beta_n z) \right\}, \quad (46)$$

$$\sigma_{rz} = -2G K_0 \sum_{n=1}^{\infty} \sum_{m=1}^{\infty} \frac{\wp_{n,m}}{\Lambda} \left\{ \int_0^t T_{(n)}^{(2)} f(t-\eta) d\eta \right\} \left\{ -a_m [W_m \cos(a_m z) + Q_m \sin(a_m z)] \frac{2}{b^2} \frac{J_1(\beta_n r)}{J_1(\beta_n b)} + \beta_n^3 A_n J_1(\beta_n r) \cosh(\beta_n z) - \beta_n^3 C_n [2(1-\nu) J_1(\beta_n r) + (\beta_n r) J_0(\beta_n r)] \cosh(\beta_n z) \right\}. \quad (47)$$

Using Eqs. (21), (44) and (47), one obtains

$$A_n = \frac{2\{[2(1-\nu)\beta_n] \operatorname{csch}(\beta_n z) P_m(z) + (\beta_n b) \operatorname{sech}(\beta_n z) P_m'(z)\}}{(\beta_n^2 b)^2 J_1(\beta_n b) \{1 - \beta_n^2 + \beta_n [b - 2(1-\nu)/b]\}}, \quad (48)$$

$$C_n = \frac{2[-\beta_n \operatorname{csch}(\beta_n z) P_m(z) + \operatorname{sech}(\beta_n z) P_m'(z)]}{(\beta_n^2 b)^2 J_1(\beta_n b) [\beta_n^2 b - 2(1-\nu)]}.$$

where prime denotes the differentiation of the function.

3.2 Solution Of The Classical Cattaneo-Vernotte Model

Taking $p = 1$, Eq. (8) can be reduced to Cattaneo-Vernotte heat conduction model as

$$\kappa \left(\frac{\partial T}{\partial t} + \tau \frac{\partial^2 T}{\partial t^2} \right) = \frac{1}{r} \frac{\partial}{\partial r} \left(r \frac{\partial T}{\partial r} \right) + \frac{\partial^2 T}{\partial z^2} + \chi(r, z, t), \quad (49)$$

$$0 \leq r \leq b, -h \leq z \leq h, t > 0.$$

Following the procedure in subsection 3.1, the solution of Eq. (49) can be obtained as

$$T(r, z, t) = \sum_{n=1}^{\infty} \sum_{m=1}^{\infty} \wp_{n,m} \left\{ \frac{1}{2\Lambda \sqrt{1-4\tau\Lambda}} \exp \left[-\frac{(t-t_0)(1+\sqrt{1-4\tau\Lambda})}{2\tau} \right] \times \left\{ -1 + \exp \left[\frac{(t-t_0)(1+\sqrt{1-4\tau\Lambda})}{2\tau} \right] (1-2\sqrt{1-4\tau\Lambda}) \right. \right. \quad (50)$$

$$\left. \left. + \exp \left[\frac{(t-t_0)(1+\sqrt{1-4\tau\Lambda})}{\tau} \right] (1+\sqrt{1-4\tau\Lambda}) \right\} H(t-t_0) \right\} \times P_m(z) k_0(\beta_n, r).$$

3.3 Solution Of The Fourier Heat Conduction Model

Taking $\tau = 0$, Eq. (8) can be reduced to the classical Fourier conduction model as

$$\kappa \frac{\partial T}{\partial t} = \frac{1}{r} \frac{\partial}{\partial r} \left(r \frac{\partial T}{\partial r} \right) + \frac{\partial^2 T}{\partial z^2} + \chi(r, z, t), \quad (51)$$

$$0 \leq r \leq b, -h \leq z \leq h, t > 0.$$

Following the procedure in subsection 3.1, the solution of Eq. (51) can be obtained as

$$T(r, z, t) = \sum_{n=1}^{\infty} \sum_{m=1}^{\infty} \wp_{n,m} \left\{ (\exp[-\Lambda(t-t_0)] - 1) H(t-t_0) \right\} \times P_m(z) k_0(\beta_n, r). \quad (52)$$

4. Numerical Results, Discussion And Remarks

To interpret the numerical computations, we consider the material properties of Aluminum metal, which can be commonly used in both wrought and cast forms. In the following calculation, the physical parameters taken are $b = 1$, $h = 0.8$, $k_1 = k_2 = 0.86$ and $T_0 = 150^\circ\text{C}$. The time, coordinate, displacement and stresses are normalized as follows

$$\bar{r} = r/b, \bar{z} = [z - (-h/2)]/b, \bar{t} = \kappa t/b^2, \bar{\tau} = \kappa \tau/b^2, \quad (53)$$

$$\bar{T} = T/T_0, \bar{u}_i = u_i/K_0 T_0 b, \bar{\sigma}_{ij} = \sigma_{ij}/E\alpha T_0 \quad (i, j = r, z),$$

and (k_i, ξ, Q_0) is also taken into account when introducing nondimensional quantities for numerical calculation. The numerical results with various values of the fractional parameter p and the relaxation time $\bar{\tau}$ are taken between 0 to 10. The thermomechanical properties [34] of isotropic material at room temperature are considered in Table 1.

Table 1. Thermo-mechanical properties: Aluminum.

Dimension	Value
Modulus of Elasticity, E	68 GPa
Poisson's ratio	0.35
Thermal Expansion Coeff., α_t	$25.5 \times 10^{-6} / ^\circ\text{C}$
Thermal diffusivity, κ	$84.18 \times 10^{-6} \text{ m}^2\text{s}^{-1}$
Thermal conductivity, λ	$204.2 \text{ Wm}^{-1}\text{K}^{-1}$
Shear modulus, G	27 GPa
Density, ρ	$2,710 \text{ Kg/m}^3$
Specific heat capacity, C_v	921.096 J/kg-K

Figures 2 and 3 represent the temperature distributions along radial and thickness directions for the thick plate with $\bar{r}_0 = 0.5$, $\bar{z}_0 = 0.5$, $\bar{t}_0 = 0.5$ and $\bar{t} = (0.1, 0.3, 0.5, 0.9, 1.2)$. Figure 2 shows that the temperature decreases when the dimensionless radial position is less than 0.5 in spite of an increase in the time value, which might be due to internal energy availability. The temperature increases up to 0.8 and again attains zero at the right boundary. The small temperature bump represents the absorption of heat from the external source. However, the area integral of the temperature distribution along the thickness direction shows a grown temperature bump and follows the standard bell-shaped curve irrespective of time variation. Figure 3 shows the dimensionless temperature profile for different values of the fractional-order p when $\bar{t} = 0.6$ is fixed. It shows that the tensile force is high at the left boundary, which reduces as it approaches the right edge. The maximum tensile strength is central in the thickness direction, with both ends having high compressive force, as shown in Figure 5. It can be seen in Figures 6 and 7 that the temperature distribution on the heated surface increases as time proceeds. The increment in temperature trend with a rise in fractional-order parameter and relaxation time is seen in Figures 6 and 7. In Figures 8 and 9 show the results for the thermal radial stress $\bar{\sigma}_{rr}$ for the different parameter values of p . Figure 8 shows that the maximum value of compressive stresses occurs up to $\bar{r} = 0.46$ along the radial direction, and the tensile stress acts towards the end. Figure 9 shows that the tensile stresses are maximum at the central part of thickness which is later overlaid by the compressive stress at both ends along the thickness direction. Figures 10 through 13 show the effects of fractional order p on tangential stress and axial direction. Initially, high tensile stress is noticed on the left boundary along the radial direction, as shown in Figures 10 and 12, which further show damping sine wave-like characteristics by attaining the minimum value. Figures 11 and 13 show a bimodal distribution along the thickness direction. Figures 14 and 15 display the dimensionless shear stress profile at different fractional-order parameters along the radial and thickness directions. Figure 14 shows that the maximum values of shear stresses occur on the plate's left boundary along the radial direction, which pretends as a damped sinusoidal function whose magnitude approaches zero as the radius position increases. In Figure 15, it is noted that the fluctuation occurs along the thickness direction.

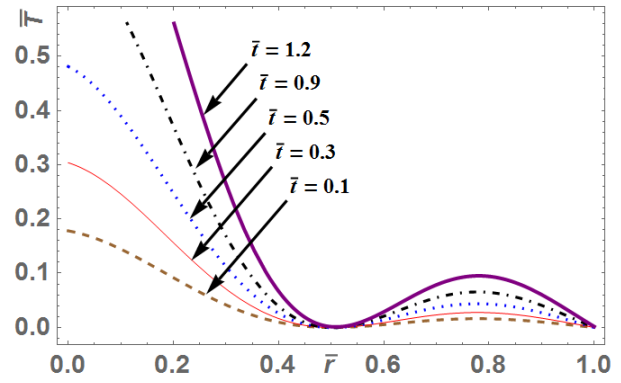


Figure 2. Temperature profile at a different time when $p = 0.8$ along the \bar{r} - direction.

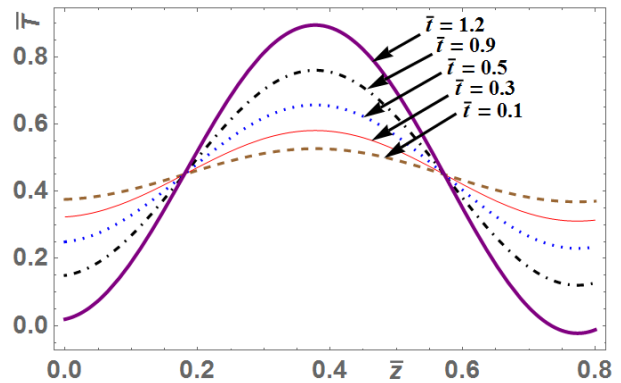


Figure 3. Temperature profile at a different time when $p = 0.8$ along the \bar{z} - direction.

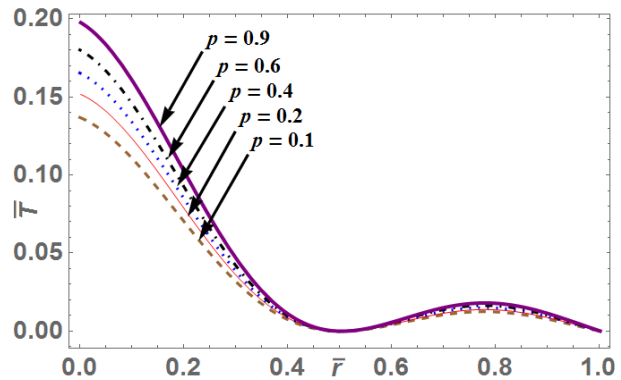


Figure 4. Temperature variation at various p when $\bar{t} = 0.6$ along the \bar{r} - direction.

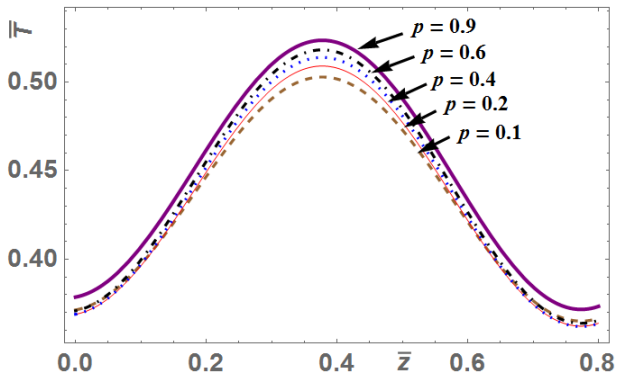


Figure 5. Temperature variation at various p when $\bar{t} = 0.6$ along the \bar{z} - direction.

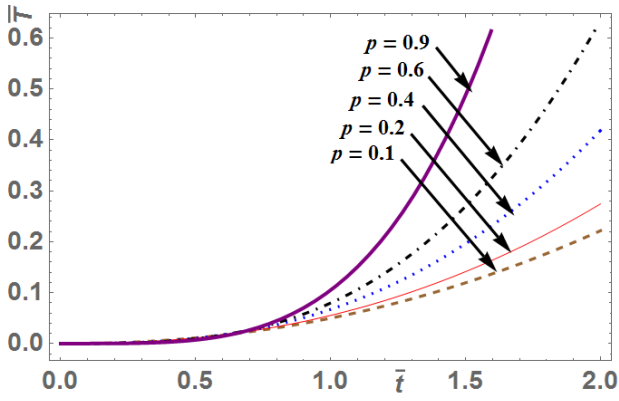


Figure 6. Temperature distribution along dimensionless time at various p when $\tau = 0.6$.

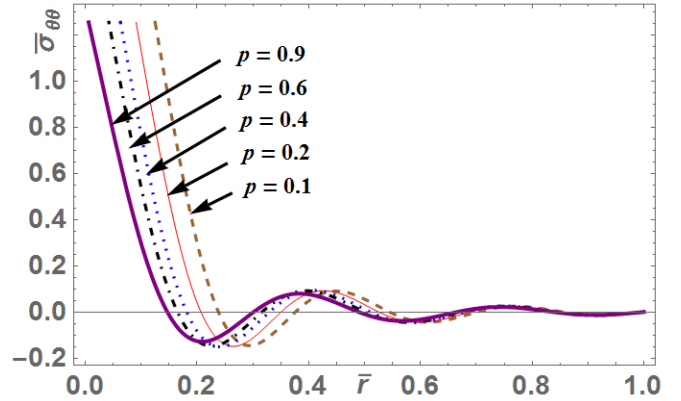


Figure 10. Effects of fractional order p on tangential stress along the \bar{r} - direction.

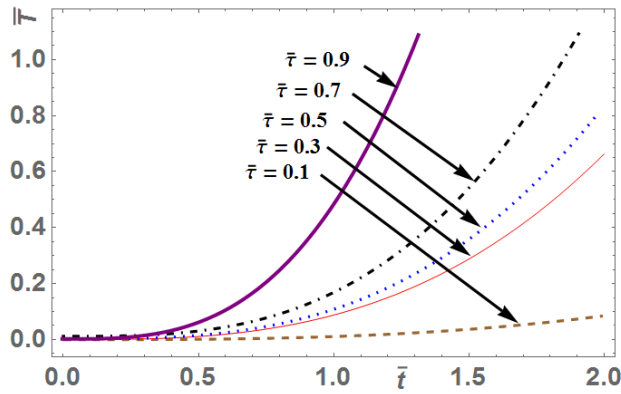


Figure 7. Temperature distribution along the time at various τ when $p = 0.6$ is fixed.

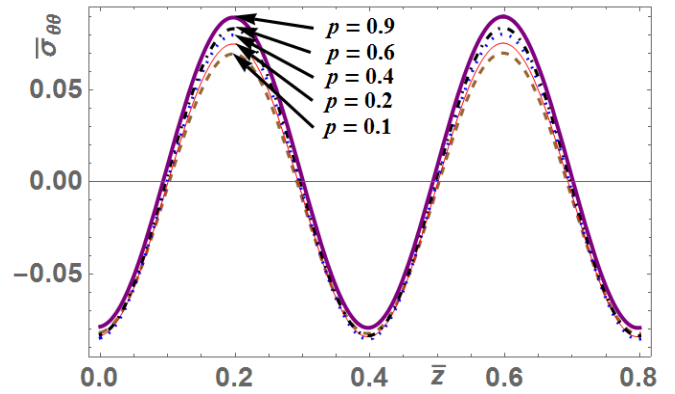


Figure 11. Effects of fractional order p on tangential stress along the \bar{z} - direction.

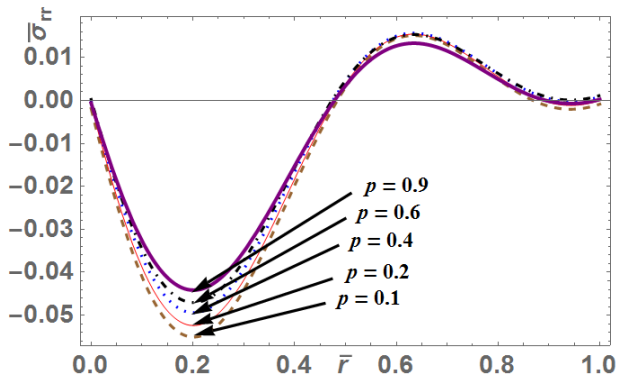


Figure 8. Radial stress profile at a different fractional order p along the \bar{r} - direction.

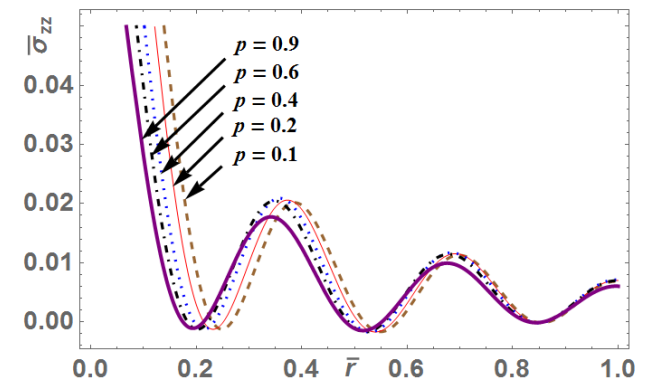


Figure 12. Dimensionless axial stress variation at a different p along the \bar{r} - direction.

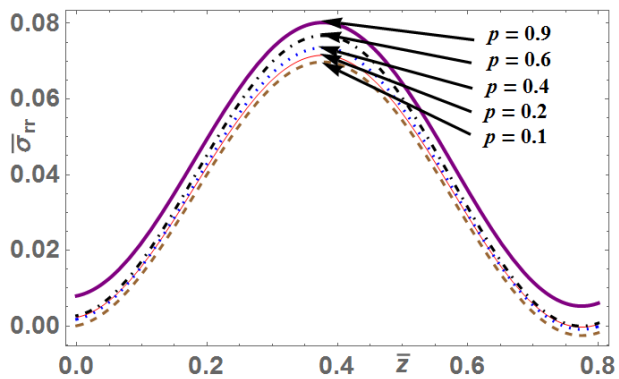


Figure 9. Radial stress profile at a different fractional order p along the \bar{z} - direction.

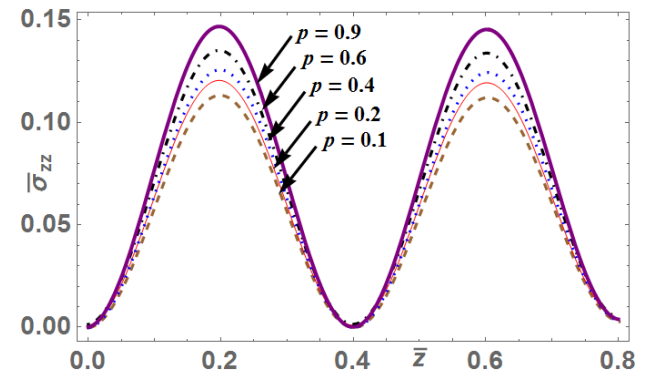


Figure 13. Dimensionless axial stress variation at a different p along the \bar{z} - direction.

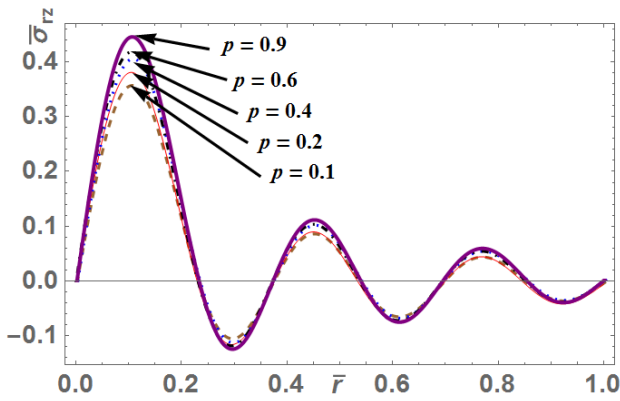


Figure 14. Shear stress distribution at different p along the \bar{r} - direction.

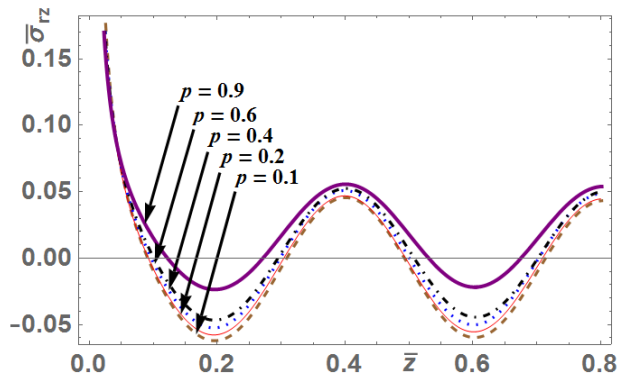


Figure 15. Shear stress distribution at different p along the \bar{z} - direction.

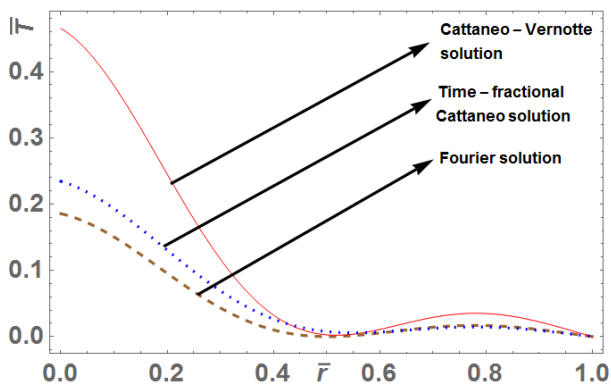


Figure 16. Comparing classical Cattaneo-Vernotte, fractional-order Cattaneo and Fourier models along the \bar{r} - direction.

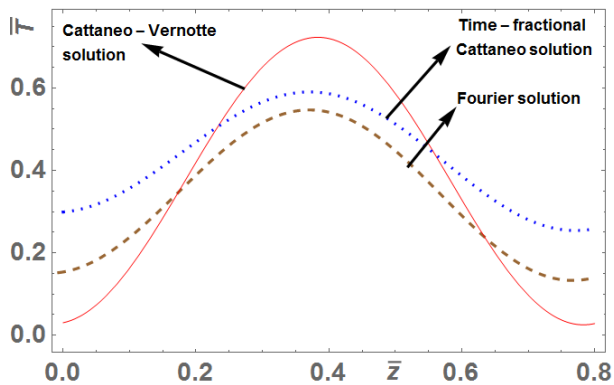


Figure 17. Comparing classical Cattaneo-Vernotte, fractional-order Cattaneo and Fourier models along the \bar{z} - direction.

Figures 16 and 17 show the dimensionless temperature distribution profile compared to the classical Cattaneo-Vernotte, fractional-order Cattaneo and Fourier model fractional-order parameters along the radial and thickness direction. Figure 16 shows that the temperature field's maximum values occur on the plate's left boundary, whose magnitude approaches zero along the radial direction. Figure 17 shows that the temperature distribution along the thickness direction depicts a normal bell-shaped curve bump for all three model solutions.

4. Deduction And Validation Of The Results

This section refers to the deduction of the conclusions derived in the previous section regarding the classical uncoupled thermoelasticity model and the classical Cattaneo-Vernotte thermoelasticity theory for a homogeneous thick plate

- (i) Taking $p=1$ in Eq. (5), the equation results in the classical Cattaneo-Vernotte heat conduction model [24] as given in Eq. (49) with a solution in Eq. (50).
- (ii) Taking $\tau = 0$ in Eq. (5), the equation reduces to the classical Fourier heat conduction model [41] as given in Eq. (51) with a solution in Eq. (52).

The key that was derived by Deshmukh et al. [41] for an isotropic, homogeneous, elastic hollow is compatible with the present thermoelastic solutions that were determined. In this piece of research, a fractional-order constitutive model and the classic continuity equation are brought together. Recent research [47,48] shows that it is possible for a non-Fourier constitutive model and a non-trivial continuity equation based on the Boltzmann transport theory to coexist. The findings demonstrate that the constitutive model and the continuity equation are not independent of one another, which is something that this work does not take into consideration.

5. Conclusion

In this problem, the fractional Cattaneo model is derived for studying the thermoelastic response for a finite thick circular plate impacted by an assigned temperature. At the same time, heat supply appears as a source in the energy equation. The integral transformation theory is used to obtain the analytical solution for the fractional Cattaneo and classical Fourier models. The temperature distribution dependence and its thermoelastic response on the fractional-order parameter and relaxation time are studied for different times and positions. It is observed that the fractional Cattaneo model gives continuous temperature and thermal stress variation irrespective of the fractional-order parameter. It is also detected that the heat flux flows from higher temperatures to lower for the fractional Cattaneo and classical Fourier models. Based on the findings of this study, we have come to the following conclusions:

1. The fractional parameter does have a substantial impact on the various components. Somewhere along the line, the fractional parameter will cause the variations to move in the opposite direction. In contrast, in other places, it will cause the amplitude of the variation to shift.
2. When looking at the stress component, the conductive temperature, the temperature change, and the cubic dilatation components, it is observed that the pattern of changes consists of rapid descents and jumps.

3. As the variations are studied, the thermal stress function, the stress components, and the smooth face either grow or decrease.
4. In the future, it will be possible to build such a mathematical model for a transversely isotropic media, and then it will be possible to investigate the changes.
5. Those who are engaged in studying thermodynamics and thermoelasticity will find this model to be of great assistance to them.
6. The solution to the problem can be applied to a two-dimensional problem with a dynamic response caused by a variety of thermal sources; this solution has a number of geophysical and industrial applications.

Nomenclature:

α_t linear coefficient of thermal expansion ($^{\circ}C$)
 κ thermal diffusivity (m^2s^{-1})
 k thermal conductivity ($W/m.K$)

Greek symbols

μ Lamé's constants (GPa)
 ν Poisson's ratio
 ρ density (kg/m^3)
 σ_{ij} components of stress tensor




References:

- [1] M. Haskul, "Elastic state of functionally graded curved beam on the plane stress state subject to thermal load," *Mech. Based Des. Struct. Mach.*, 48 (6), 739-754, 2020. DOI: 10.1080/15397734.2019.1660890.
- [2] E. Arslan, M. Haskul, "Generalized plane strain solution of a thick-walled cylindrical panel subjected to radial heating," *Acta Mech*, 226, 1213–1225, 2015. <https://doi.org/10.1007/s00707-014-1248-4>
- [3] M. Haskul, E. Arslan and W. Mack, "Radial heating of a thick-walled cylindrically curved FGM-panel," *Z. Angew. Math. Mech.*, 97, 309-321, 2017. <https://doi.org/10.1002/zamm.201500310>
- [4] M. Haskul, "Yielding of functionally graded curved beam subjected to temperature," *Pamukkale University Journal of Engineering Sciences*, 26 (4), 587-593, 2020. DOI: 10.5505/pajes.2019.92331
- [5] E. Hoashi, T. Yokomine, A. Shimizu, and T. Kunugi, "Numerical analysis of wave-type heat transfer propagating in a thin foil irradiated by short-pulsed laser," *Int. J. Heat Mass Transf.*, 46 (19), 4083–4095, 2003. DOI: 10.1016/S0017-9310(03)00225-4.
- [6] X. Ai and B. Q. Li, "Numerical simulation of thermal wave propagation during laser processing of thin films," *J. Electron. Mater.*, 34 (5), 583–591, 2005. DOI: 10.1007/s11664-005-0069-6.
- [7] T. T. Lam and E. Fong, "Application of solution structure theorem to non-Fourier heat conduction problems: Analytical approach," *Int. J. Heat Mass Transf.*, 54, 4796–4806, 2011. DOI: 10.1016/j.ijheatmasstransfer.2011.06.028.
- [8] T. T. Lam, "A unified solution of several heat conduction models," *Int. J. Heat Mass Transf.*, 56 (1–2), 653–666, 2013. DOI: 10.1016/j.ijheatmasstransfer.2012.08.055.
- [9] C. Cattaneo, "Sur une forme de l'équation de la chaleur éliminant le paradoxe d'une propagation instantanée," *C. R. Acad. Sci.*, 247, 431–433, 1958.
- [10] P. Vernotte, "Les paradoxes de la théorie continue de l'équation de la chaleur," *C. R. Acad. Sci.*, 246, 3154–3155, 1958.
- [11] A. Compte and R. Metzler, "The generalized Cattaneo equation for the description of anomalous transport processes," *J. Phys. A: Math. Gen.*, 30, 7277–7289, 1997.
- [12] F. M. Jiang, D. Y. Liu, and J. H. Zhou, "Non-Fourier heat conduction phenomena in porous material heated by microsecond laser pulse," *Microscale Thermophys. Eng.*, 6 (4), 331–346, 2003. DOI: 10.1080/10893950290098386.
- [13] Y. Povstenko, *Fractional thermoelasticity*, Springer, New York, 2015.
- [14] Y. Povstenko, "Fractional heat conduction equation and associated thermal stress," *J. Therm. Stresses*, 28 (1), 83–102, 2005.
- [15] Y. Povstenko, "Fractional Cattaneo-type equations and generalized thermoelasticity," *J. Therm. Stresses*, 34 (2), 97–114, 2011. DOI: 10.1080/01495739.2010.511931.
- [16] T. N. Mishra and K. N. Rai, "Numerical solution of FSPL heat conduction equation for analysis of thermal propagation," *Appl. Math. Comput.*, 273, 1006–1017, 2016. DOI: 10.1016/j.amc.2015.10.082.
- [17] H. Qi, H. Xu, and X. Guo, "The Cattaneo-type time fractional heat conduction equation for laser heating," *Comput. Math. Appl.*, 66 (5), 824–831, 2013. DOI: 10.1016/j.camwa.2012.11.021.
- [18] H. Qi, and X. Guo, "Transient fractional heat conduction with generalized Cattaneo model," *Int. J. Heat Mass Transf.*, 76, 535–539, 2014.
- [19] H. Xu, H. Qi, and X. Jiang, "Fractional Cattaneo heat equation on a semi-infinite medium," *Chin. Phys. B*, 22 (1), 014401, 2013. DOI: 10.1088/1674-1056/22/1/014401.
- [20] G. Xu, J. Wang, and Z. Han, "Study on the transient temperature field based on the fractional heat conduction equation for laser heating," *Appl. Math. Mech.*, 36, 844–849, 2015.
- [21] G. Xu and J. Wang, "Analytical solution of time fractional Cattaneo heat equation for finite slab under pulse heat flux," *Appl. Math. Mech.*, 39 (10), 1465–1476, 2018. DOI: 10.1007/s10483-018-2375-8.
- [22] G. Xu, J. Wang, and Z. Han, "Notes on 'The Cattaneo-type time fractional heat conduction equation for laser heating' [*Comput. Math. Appl.* 66 (2013) 824–831]," *Comput. Math. Appl.*, 71 (10), 2132–2137, 2016. DOI: 10.1016/j.camwa.2016.03.011.
- [23] C. Cattaneo, "Sulla conduzione del calore," *Atti Sem. Mat. Fis. Univ. Modena*, 3, 83–101, 1948.
- [24] H. R. Ghazizadeh, M. Maerefat, and A. Azimi, "Explicit and implicit finite difference schemes for

- fractional Cattaneo equation," *J. Comput. Phys.*, 229 (16), 7042–7057, 2010. DOI: 10.1016/j.jcp.2010.05.039.
- [25] Z. M. Odibat, N. T. Shawagfeh, "Generalized Taylor's formula," *Appl. Math. Comput.*, 186, 286–293, 2007.
- [26] I. Podlubny, *Fractional Differential Equations*, Academic Press, New York, 1999.
- [27] Z. Zhang and D.Y. Liu, "Advanced in the study of non-Fourier heat conduction," *Advance Mechanics*, 30, 446-456, 2000.
- [28] R. Gorenflo and F. Mainardi, *Fractional Calculus: Integral and Differential Equations of Fractional Order*, A. Carpinteri and F. Mainardi (Editors): *Fractals and Fractional Calculus in Continuum Mechanics*, 223-276, Springer Verlag, Wien and New York, 1997.
- [29] A. A. Kilbas, H. M. Srivastava, and J. J. Trujillo, *Theory and applications of fractional differential equations*, 204, Elsevier Science, Amsterdam, 2006.
- [30] Y. Povstenko, "Axisymmetric Solutions to Time-fractional heat conduction equation in a half-space under Robin boundary conditions," *Int. J. Differ. Equ.*, 1–13, 2012. DOI: 10.1155/2012/154085.
- [31] Y. Povstenko, "Axisymmetric solutions to fractional diffusion-wave equation in a cylinder under Robin boundary condition," *Eur. Phys. J. Spec. Top.*, 222, 1767–1777, 2013. DOI: 10.1140/epjst/e2013-01962-4.
- [32] Y. Povstenko, "Fundamental solutions to the fractional heat conduction equation in a ball under Robin boundary condition," *Centr. Eur. J. Math.*, 12 (4), 611–622, 2014. DOI: 10.2478/s11533-013-0368-8.
- [33] H. S. Carslaw and J.C. Jaeger, *Conduction of Heat in Solids*, 2nd ed., Oxford University Press, Oxford, 1959.
- [34] G. M. L. Gladwell, J. R. Barber, and Z. Olesiak, "Thermal problems with radiation boundary conditions," *Q. J. Mech. Appl. Math.*, 36 (3), 387–401, 1983. DOI: 10.1093/qjmam/36.3.387.
- [35] E. Marchi and G. Zgrablich, "Heat conduction in hollow cylinders with radiation," *Proc. Edimburgh Math. Soc.*, 14(11), 159-164, 1964.
- [36] E. Marchi and A. Fasulo, "Heat conduction in sector of hollow cylinder with radiation," *Atti, della Acc. Sci. di Torino*, 101, 373-382, 1967.
- [37] R. Kumar, N. K. Lamba, and V. Varghese, "Analysis of thermoelastic disc with radiation conditions on the curved surfaces," *Mater. Phys. Mech.*, 16 (2), 175-186, 2013.
- [38] N. Noda, R. B. Hetnarski, Y. Tanigawa, *Thermal stresses*, 2nd ed., Taylor and Francis, New York, 2003.
- [39] A. E. H. Love, *A Treatise on the mathematical theory of elasticity*, 4th ed., Dover publications, New York, 1944.
- [40] W. Nowacki, *Thermoelasticity*, 2nd ed., PWN-Polish Scientific Publishers, Warsaw and Pergamon Press, Oxford, 1986.
- [41] J. J. Tripathi, K. C. Deshmukh and J. Verma, Fractional Order Generalized Thermoelastic Problem in a Thick Circular Plate with Periodically Varying Heat Source, *Int. J. Thermodyn.*, 20 (3), 132-138, 2017. DOI: 10.5541/ijot.5000190819.
- [42] K. C. Deshmukh, S. D. Warbhe, and V. S. Kulkarni, "Brief Note on Heat Flow With Arbitrary Heating Rates in a Hollow Cylinder," *Therm. Sci.*, 15 (1), 275–280, 2011. DOI: 10.2298/TSCI100817063D.
- [43] S. N. Li, B. Y. Cao, "Fractional Boltzmann transport equation for anomalous heat transport and divergent thermal conductivity," *Int. J. Heat Mass Transf.*, 137, 84-89, 2019. DOI: 10.1016/j.ijheatmasstransfer.2019.03.120.
- [44] S. N. Li, B. Y. Cao, "Fractional-order heat conduction models from generalized Boltzmann transport equation," *Philos. Trans. R. Soc. A*, 378, 20190280, 2020. DOI: 10.1098/rsta.2019.0280.

Research Article

Thermally-Induced Stresses in a Pre-Buckling State of a Circular Plate within the Fractional-Order Framework

¹G. Dhameja , ²L. Khalsa , ^{3*}V. Varghese 

^{1,2,3} Department of Mathematics, M.G. College, Armori, Gadchiroli, India
E-mails: ¹dhameja.geeta0311@gmail.com, ²lalsinghkhalsa@yahoo.com, ^{3*}vino7997@gmail.com

Received 2 September 2022, Revised 17 January 2023, Accepted 30 January 2023

Abstract

This paper considers a transient thermoelastic problem in an isotropic homogeneous elastic thin circular plate with clamped edges subjected to thermal load within the fractional-order theory framework. The prescribed ramp-type surface temperature is on the plate's top face, while the bottom face is kept at zero. The three-dimensional heat conduction equation is solved using a Laplace transformation and the classical solution method. The Gaver–Stehfest approach was used to invert Laplace domain outcomes. The thermal moment is derived based on temperature change, and its bending stresses are obtained using the resultant moment and resultant forces per unit length. The results are illustrated by numerical calculations considering the material to be an Aluminum-like medium, and corresponding graphs are plotted.

Keywords: *Fractional-order derivatives; fractional calculus; non-Fourier heat conduction; circular plate; thermal deflection; thermal deflection thermal stress; integral transform.*

1. Introduction

Fractional calculus has been applied in many disciplines in recent times, such as electromagnetism, control engineering, signal processing, chemistry, astrophysics, quantum mechanics, nuclear physics, quantum field theory, etc. A few highly cited books explaining the principle of fractional calculus and several alternate definitions of fractional derivatives have been Oldham and Spanier [1], Miller and Ross [2], Samko et al. [3], Podlubny [4], Hilfer [5] and Harmann [6]. Many analytical studies concerning thermoelasticity within the fractional-order theory framework have also been reported, summarized in the trailing portion. Povstenko [7-11] focused on heat conduction with time and space fractional derivatives and obtained the theory of thermal stresses using the Laplace transform and a direct approach. Youssef [12-18] studied the fractional-order generalized thermoelasticity using the Laplace transform and different techniques. Ezzat and El-Karamany [19-22] constructed a few mathematical models of time-fractional order in the context of the generalized theory of thermoelasticity, thermo-piezoelectricity, and thermo-viscoelasticity. Sherief and Abd El-Latif [23-25] developed thermoelasticity methods using fractional calculus and applied them to a one-dimensional thermal shock problem for a half-space.

Recently, Sur and Kanoria [26] developed a new theory of two-temperature generalized thermoelasticity in the context of heat conduction with fractional orders using the unified parameters in the form of a vector-matrix differential equation. Similarly, Bhattacharya and Kanoria [27] obtained the solution of the two-temperature thermoelastic-diffusion interaction inside a spherical shell in fractional order

generalized thermoelasticity using a direct approach. Zenkour and Abouelregal [28] determined the conductive and thermodynamic temperature for an infinite isotropic elastic body with a spherical cavity using Caputo's time-fractional derivative. Bachher [29] discussed the deformation due to periodic heat sources in a temperature-dependent porous material with a time-fractional heat conduction law. Santra et al. [30] employed eigenvalue approaches for obtaining a half-space solution within fractional order generalized thermoelasticity (Green–Lindsay) theory. Gupta and Das [31] used the eigenvalue approach to get a general solution scheme for the deformation of an unbounded transversely isotropic medium within fractional order generalized thermoelasticity with an instantaneous heat source. Bachher and Sarkar [32] investigated the theory of generalized thermoelasticity based on the heat conduction equation with the Caputo time-fractional derivative to study the magneto-thermoelastic response of a homogeneous isotropic two-dimensional rotating elastic half-space solid with an eigenvalue approach technique. Abbas [33] obtained the temperature, displacement, and stresses due to thermal shock loading on the inner surface cavity in an infinite medium with a cylindrical cavity in the fractional-order generalized thermoelasticity theory using an eigenvalue approach.

Similarly, Abbas [34] studied the effect of fractional order derivative on a two-dimensional problem due to thermal shock with weak, normal and strong conductivity in Green and Naghdi of type III model (GN III model) using fractional-order derivative with eigenvalues approach. Lata [35] investigated the thermomechanical interactions in the fractional theory for a thick circular using the Hankel

transform technique and a direct method without potential functions. Mittal and Kulkarni [36] proposed a fractional heat conduction model to investigate the thermal variations within the bounded spherical region in the context of the generalized two-temperature theory of fractional thermoelasticity. Bhoyar et al. [37] performed the thermoelastic analysis of an isotropic homogeneous multi-stacked elliptical in the context of the time-fractional derivative using a quasi-orthogonality relationship by modifying Vodicka's method and the Laplace transformation. Using von Mises' yield criterion, Haskul [38,39] has developed analytical solutions for the stresses and displacements of a functionally graded, cylindrically curved beam subjected to a radial heat load. Haskul et al. [40,41] studied the elastic stress response of a thick-walled, cylindrically curved panel subjected to a radial temperature gradient under the assumption of generalized plane strain according to both Tresca and von Mises yield criteria.

According to the review of the relevant literature, only a limited number of research initiatives have explored the thermal stress analysis in an isotropic homogeneous elastic thin circular plate with clamped edges that has been subjected to temperature or mechanical load. Therefore, the purpose of this study was to illustrate the thermoelastic induced stress analysis of a thin circular plate in a pre-buckling condition assumption utilizing the classical approach. The plate was also subjected to a ramp-type sectional heat supply inside the fractional-order framework. The novelty of this work lies in the fact that it employs a Laplace transformation and a classical solution method, both of which have not been carried out by any other researcher up to this point. This enables the authors to determine the influence of different fractional orders on a three-dimensional heat conduction equation.

This article is organized as follows: Section 2 presents the prerequisites of the time-fractional equation. Section 3 presents the problem's mathematical statement within the fractional-order theory. In Section 4, solutions of fractional-order equations are expressed in terms of the Bessels function in the Laplace domain. Section 5 is devoted to estimating solutions of numerical inversion of the Laplace transform, and its convergence is discussed. The numerical results, discussion, and remarks are put forward in Section 6. Finally, conclusions are drawn in Section 7.

2. Prerequisites Of Time Fractional Equation

The investigation of strains brought on by the temperature field that is derived from the parabolic heat conduction equation is the focus of the classical theory of thermoelasticity. The Fourier law serves as the foundation for the traditional idea of heat conduction.

$$q = -k \text{grad} T, \quad (1)$$

which establishing a connection between the temperature gradient T and the heat flux vector q . In non-classical theories, the Fourier law and the equation for heat conduction are supplanted by more generic equations. In the theory of heat conduction proposed by Gurtin and Pipkin [42], the Fourier law was generalized to time-non-local dependence between the heat flux vector and the temperature gradient, which resulted in an integrodifferential heat conduction equation. This was accomplished by applying the Fourier law to the relationship between the temperature gradient and the heat flux vector. Chen and Gurtin are the ones that came

up with the thermoelasticity theory and based it on this equation [43]. The constitutive equation for the heat flux that was proposed by Cattaneo [44,45] and Vernotte [46] can also be rewritten in a non-local form with the 'short-tail' exponential time-non-local kernel. This kernel allows for the equation to be rewritten in a non-local form. The concept of generalized thermoelasticity was first proposed by Kaliski [47] and Lord and Shulman [48], who based their work on the findings of Cattaneo and Vernotte. Within the framework of Green and Naghdi's [49], proposed theory of heat conduction, the relevant generalization of the Fourier law is discussed.

$$q = -k \int_0^t \text{grad} T(\tau) d\tau, \quad (2)$$

with k being the thermal conductivity. This can lead to getting the wave equation for temperature as well as thermoelasticity with memory

$$\frac{\partial T}{\partial t} = \kappa \int_0^t K(t-\tau) \Delta T(\tau) d\tau, \quad (3)$$

with κ being the thermal diffusivity and $K(t-\tau)$ is memory kernel. The time-non-local dependences between the heat flux vector and the temperature gradient, along with the "long-tail" power kernel, expressed in terms of fractional integrals and derivatives, and the time-fractional heat conduction equation [7-11] that results is given as

$$\frac{\partial^\alpha T}{\partial t^\alpha} = \kappa \Delta T, \quad 0 < \alpha \leq 2. \quad (4)$$

The uncoupled theory is the only one that has been taken into account by us. There is no consideration given to the impact that deformation has on the thermal state of a solid. The findings of Eq. (4) are presented for obtaining the thermally-induced stresses in a pre-buckling state of a thin circular plate in terms of heat conduction and thermoelasticity.

3. Formulation Of The Fractional Heat Conduction

Consider a circular plate of thickness h occupying the space $D: 0 < r \leq a, 0 \leq \theta \leq \theta_0 < 2\pi, -h/2 \leq z \leq h/2$, in the cylindrical coordinate system (r, θ, z) , as shown in Figure 1. The plate is kept at zero initial temperature. The annular region $D_1: r_0 < r < a$, of the upper face is subjected to temperature distribution as follows

$$\begin{aligned} T|_{z=h/2} &= \frac{T_0}{t_0} [H(r-r_0) - H(r-a)]t \text{ for } 0 \leq t \leq t_0, \\ &= T_0 [H(r-r_0) - H(r-a)] \text{ for } t \geq t_0. \end{aligned} \quad (5)$$

in which $f(r) = H(r-r_0) - H(r-a)$ is the difference in the Heaviside function, t is time, T_0 defines the reference temperature distribution, which does not produce stress or strain in the plate, and t_0 is a fixed ramp parameter value, respectively.

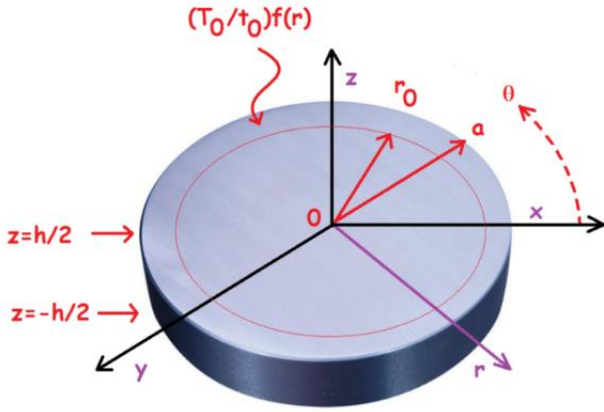


Figure 1. The geometry of a circular plate.

3.1 Transient Heat Conduction Formulation:

The heat conduction equation is

$$\frac{\partial^2 T}{\partial r^2} + \frac{1}{r} \frac{\partial T}{\partial r} + \frac{1}{r^2} \frac{\partial^2 T}{\partial \theta^2} + \frac{\partial^2 T}{\partial z^2} = \frac{1}{\kappa} \frac{\partial^\alpha T}{\partial t^\alpha}, \quad (6)$$

subjected to the boundary and initial conditions

$$T|_{r=0} \neq \infty, \frac{\partial T}{\partial r} \Big|_{r=a} = 0, \quad (7)$$

$$T|_{\theta=0} = T|_{\theta=\theta_0} = 0, \quad (8)$$

$$T|_{z=-h/2} = 0, T|_{z=h/2} = \begin{cases} (T_0/t_0)f(r)t & \text{for } 0 \leq t \leq t_0 \\ T_0 f(r) & \text{for } t \geq t_0, \end{cases} \quad (9)$$

$$T|_{t=0} = 0, \frac{\partial T}{\partial t} \Big|_{t=0} = 0, \quad (10)$$

in which

$$f(r) = \begin{cases} 1, & \text{for } r_0 < r < a \\ 0, & \text{for } 0 < r < r_0 \end{cases}, \quad (11)$$

with $T = T(r, \theta, z, t)$ is the temperature distribution at a point (r, θ, z) at a time t , $\kappa = k/c_v \rho$ is the coefficient of thermal diffusivity, c_v is the calorific capacity, ρ is the material density, k is the coefficient of thermal conductivity, and $\partial^\alpha T / \partial t^\alpha$ is the Caputo fractional derivative, respectively.

The temperature change from the initial temperature is given

$$\tau = T - T_i. \quad (12)$$

The Caputo fractional derivative [50,51] in Eq. (5) as

$$\frac{d^\alpha f(t)}{dt^\alpha} = \begin{cases} \frac{1}{\Gamma(n-\alpha)} \int_0^t (t-\tau)^{n-\alpha-1} \frac{d^n f(\tau)}{d\tau^n} d\tau, & n-1 < \alpha < n, \\ \frac{d^n f(\tau)}{d\tau^n}, & \alpha = n, \end{cases} \quad (13)$$

with the following Laplace transform rule

$$L\left\{\frac{d^\alpha f(t)}{dt^\alpha}\right\} = s^\alpha L\{f(t)\} - \sum_{k=0}^{n-1} f^{(k)}(0^+) s^{\alpha-1-k}, \quad (14)$$

in which s is the transform parameter, $n-1 < \alpha < n$, $n \in N = \{1, 2, \dots\}$.

3.2 Thermally-Induced Bending Stress Formulation

The stress components [52] along the neutral plane

$$\sigma_{rr} = \frac{E}{1-\nu^2} \left\{ \frac{\partial u_r}{\partial r} + \nu \left(\frac{u_r}{r} + \frac{1}{r} \frac{\partial u_\theta}{\partial \theta} \right) - z \left[\frac{\partial^2 w}{\partial r^2} + \nu \left(\frac{1}{r} \frac{\partial w}{\partial r} + \frac{1}{r^2} \frac{\partial^2 w}{\partial \theta^2} \right) \right] \right\} - \frac{E\alpha_i \tau}{1-\nu},$$

$$\sigma_{\theta\theta} = \frac{E}{1-\nu^2} \left\{ \nu \frac{\partial u_r}{\partial r} + \left(\frac{u_r}{r} + \frac{1}{r} \frac{\partial u_\theta}{\partial \theta} \right) - z \left[\nu \frac{\partial^2 w}{\partial r^2} + \left(\frac{1}{r} \frac{\partial w}{\partial r} + \frac{1}{r^2} \frac{\partial^2 w}{\partial \theta^2} \right) \right] \right\} - \frac{E\alpha_i \tau}{1-\nu}, \quad (15)$$

$$\sigma_{r\theta} = \frac{E}{2(1+\nu)} \left\{ \frac{1}{r} \frac{\partial u_r}{\partial \theta} + r \frac{\partial}{\partial r} \left(\frac{u_\theta}{r} \right) - 2z \frac{\partial}{\partial r} \left(\frac{1}{r} \frac{\partial w}{\partial \theta} \right) \right\},$$

in which u_r , u_θ and w are displacement functions along r , θ , and z directions at the neutral plane of the thin circular plate with its thickness, E is Young's modulus, α_i is the coefficient of thermal expansion in the thickness direction, and ν represent Poisson's ratio, respectively.

The resultant forces $(N_{ij}, i, j = r, \theta)$ and the resultant moments $(M_{ij}, i, j = r, \theta)$ per unit length of the plate is written as [52]

$$\begin{aligned} N_r &= \int_{-h/2}^{h/2} \sigma_{rr} dz, \quad N_\theta = \int_{-h/2}^{h/2} \sigma_{\theta\theta} dz, \\ N_{r\theta} &= \int_{-h/2}^{h/2} \sigma_{r\theta} dz, \quad M_r = \int_{-h/2}^{h/2} z \sigma_{rr} dz, \\ M_\theta &= \int_{-h/2}^{h/2} z \sigma_{\theta\theta} dz, \quad M_{r\theta} = - \int_{-h/2}^{h/2} z \sigma_{r\theta} dz. \end{aligned} \quad (16)$$

Substituting Eqs. (15) into (16), one obtains the resultant forces as

$$\begin{aligned} N_r &= \frac{Eh}{1-\nu^2} \left[\frac{\partial u_r}{\partial r} + \nu \left(\frac{u_r}{r} + \frac{1}{r} \frac{\partial u_\theta}{\partial \theta} \right) \right] - \frac{1}{1-\nu} N_T, \\ N_\theta &= \frac{Eh}{1-\nu^2} \left[\nu \frac{\partial u_r}{\partial r} + \left(\frac{u_r}{r} + \frac{1}{r} \frac{\partial u_\theta}{\partial \theta} \right) \right] - \frac{1}{1-\nu} N_T, \\ N_{r\theta} &= \frac{Eh}{2(1+\nu)} \left[\frac{1}{r} \frac{\partial u_r}{\partial \theta} + r \frac{\partial}{\partial r} \left(\frac{u_\theta}{r} \right) \right], \end{aligned} \quad (17)$$

and the resultant moments [52] as

$$M_r = -D \left[\frac{\partial^2 w}{\partial r^2} + \nu \left(\frac{1}{r} \frac{\partial w}{\partial r} + \frac{1}{r^2} \frac{\partial^2 w}{\partial \theta^2} \right) \right] - \frac{1}{1-\nu} M_T,$$

$$M_\theta = -D \left[\nu \frac{\partial^2 w}{\partial r^2} + \left(\frac{1}{r} \frac{\partial w}{\partial r} + \frac{1}{r^2} \frac{\partial^2 w}{\partial \theta^2} \right) \right] - \frac{1}{1-\nu} M_T, \quad (18)$$

$$M_{r\theta} = (1-\nu) D \frac{\partial}{\partial r} \left(\frac{1}{r} \frac{\partial w}{\partial \theta} \right).$$

in which the flexure rigidity is given as $D = E\ell^3 / 12(1-\nu^2)$, and the thermally induced resultant force N_T and the thermally induced resultant moment M_T are defined by [53]

$$N_T = \alpha_i E \int_{-h/2}^{h/2} \tau(r, \theta, z, t) dz,$$

$$M_T = \alpha_i E \int_{-h/2}^{h/2} z \tau(r, \theta, z, t) dz. \quad (19)$$

Now taking into account Eq. (18), the differential equation for deflection is given as [53]

$$\nabla^2 \nabla^2 w = - \frac{1}{(1-\nu)D} \nabla^2 M_T, \quad (20)$$

subjected to the boundary conditions for the thermally induced bending of the plate are [54]

$$w|_{r=a} = 0, \quad \left. \frac{\partial w}{\partial r} \right|_{r=a} = 0, \quad (21)$$

where

$$\nabla^2 = \frac{\partial^2}{\partial r^2} + \frac{1}{r} \frac{\partial}{\partial r} + \frac{1}{r^2} \frac{\partial^2}{\partial \theta^2}. \quad (22)$$

In order to evaluate N_{ij} ($i, j = r, \theta$), one can introduce [54] a stress function $F(r, \theta, t)$ as

$$N_r = \frac{1}{r} \frac{\partial F}{\partial r} + \frac{1}{r^2} \frac{\partial^2 F}{\partial \theta^2},$$

$$N_\theta = \frac{\partial^2 F}{\partial r^2}, \quad N_{r\theta} = - \frac{\partial}{\partial r} \left(\frac{1}{r} \frac{\partial F}{\partial \theta} \right). \quad (23)$$

Now taking into account Eq. (23) and the strain components, one obtains a relation [54]

$$\nabla^2 \nabla^2 F = - \nabla^2 N_T. \quad (24)$$

The thermal bending stress components [54] taken as

$$\sigma_{rr} = \frac{1}{h} N_r + \frac{12z}{h^3} M_r + \frac{1}{1-\nu} \left(\frac{1}{h} N_T + \frac{12z}{h^3} M_T - \alpha E \tau \right),$$

$$\sigma_{\theta\theta} = \frac{1}{h} N_\theta + \frac{12z}{h^3} M_\theta + \frac{1}{1-\nu} \left(\frac{1}{h} N_T + \frac{12z}{h^3} M_T - \alpha E \tau \right), \quad (25)$$

$$\sigma_{r\theta} = \frac{1}{h} N_{r\theta} - \frac{12z}{h^3} M_{r\theta}.$$

The Eqs. (5) to (25) constitute the mathematical formulation of the problem.

4. Solution For The Problem

4.1 Transient Heat Conduction Analysis

Applying the Laplace transform $\bar{f}(s) = \int_0^\infty \exp(-st) f(t) dt$ to the Eqs. (6)-(10), one obtains

$$\frac{\partial^2 \bar{T}}{\partial r^2} + \frac{1}{r} \frac{\partial \bar{T}}{\partial r} + \frac{1}{r^2} \frac{\partial^2 \bar{T}}{\partial \theta^2} + \frac{\partial^2 \bar{T}}{\partial z^2} = \frac{s^\alpha}{\kappa} \bar{T}, \quad (26)$$

$$\bar{T}|_{r=0} \neq \infty, \quad \left. \frac{\partial \bar{T}}{\partial r} \right|_{r=a} = 0, \quad (27)$$

$$\bar{T}|_{\theta=0} = \bar{T}|_{\theta=\theta_0} = 0, \quad (28)$$

$$\bar{T}|_{z=-h/2} = 0, \quad \bar{T}|_{z=h/2} = \frac{T_0}{t_0} \left(\frac{1 - e^{-st_0}}{s^2} \right) f(r) \sin m\theta, \quad (29)$$

in which f_i be a given function defined for all $t \geq 0$, $\bar{f}(s)$ is the transformed generating function of the determining function $f(t)$, \bar{T} is the transformed function of T , and s is the transformed Laplace parameter, respectively.

Now, we assume the temperature distribution is given by

$$\bar{T}(r, \theta, z, s) = \sum_{m=0}^{\infty} \sum_{n=1}^{\infty} A_n \sin m\theta J_0(\alpha_n r) \sinh \left\{ \gamma_n \left(z + \frac{h}{2} \right) \right\}. \quad (30)$$

The boundary conditions of Eq. (28), taking into account Eq. (27), are self-evidently satisfied in Eq. (26). The first equation of boundary condition (29) at $z = h/2$ is satisfied by Eq. (26). From the second equation of boundary condition (27) on $r = a$, we have α_n ($n = 0, 1, 2, \dots$) as the roots of the transcendental equation $J_1(\alpha_n a) = 0$.

To satisfy the second equation of boundary condition (29), assume the Fourier-Bessel series

$$f(r) = \sum_{n=1}^{\infty} B_n J_0(\alpha_n r). \quad (31)$$

Then from the theory of the Bessel function

$$B_n \int_0^a r [J_0(\alpha_n r)]^2 dr = \int_0^a f(r) r J_0(\alpha_n r) dr. \quad (32)$$

Using Eqs. (11) into (32), one obtains

$$B_n = \frac{-2r_0 J_1(\alpha_n r_0)}{\alpha_n a^2 [J_0(\alpha_n a)]^2}. \quad (33)$$

Substituting Eqs. (30) into (26), one obtains

$$\gamma_n^2 = (s^\alpha / \kappa) + \beta_{mn}^2, \quad \beta_{mn}^2 = (m / a^2) + \alpha_n^2. \quad (34)$$

Substituting Eq. (33) into the boundary condition (29) for $z = h/2$, one obtains

$$A_n = \frac{-2T_0 r_0 J_1(\alpha_n r_0)}{\alpha_n a^2 t_0 [J_0(\alpha_n a)]^2 \sinh\{\gamma_n h\}} \left(\frac{1 - e^{-s t_0}}{s^2} \right). \quad (35)$$

By replacing the values of Eqs. (35) into (30), one obtains

$$\begin{aligned} \bar{T}(r, \theta, z, s) = & \frac{2T_0}{a^2 t_0} \sum_{m=0}^{\infty} \sum_{n=1}^{\infty} \left(\frac{-r_0 J_1(\alpha_n r_0)}{\alpha_n [J_0(\alpha_n a)]^2 \sinh\{\gamma_n h\}} \right) \\ & \times J_0(\alpha_n r) \sin m\theta \\ & \times \left\langle \left(\frac{1 - e^{-s t_0}}{s^2} \right) \sinh \left[\left(\frac{s^\alpha}{\kappa} + \beta_{mn}^2 \right)^{1/2} \left(z + \frac{h}{2} \right) \right] \right\rangle. \end{aligned} \quad (36)$$

At $t = 0$, initial temperature condition $T_i = 0$, then Eq. (12) in the Laplace domain is shown as

$$\bar{t} = \bar{t}(r, \theta, z, s) = \bar{T}(r, \theta, z, s). \quad (37)$$

4.2 Thermoelastic Solution

Using Eq. (36) into transformed Eq. (19), the resultant force in the Laplace domain as

$$\begin{aligned} \bar{N}_r = & \frac{2\alpha_t E T_0}{a^2 t_0} \sum_{m=0}^{\infty} \sum_{n=1}^{\infty} \left(\frac{-r_0 J_1(\alpha_n r_0)}{\alpha_n [J_0(\alpha_n a)]^2 \sinh\{\gamma_n h\}} \right) \\ & \times J_0(\alpha_n r) \sin m\theta \phi_{mn}(s), \end{aligned} \quad (38)$$

in which

$$\begin{aligned} \phi_{mn}(s) = & \left(\frac{1 - e^{-s t_0}}{s^2} \right) \left(\frac{s^\alpha}{\kappa} + \beta_{mn}^2 \right)^{-1/2} \\ & \times \left\{ -1 + \cosh \left[\left(\frac{s^\alpha}{\kappa} + \beta_{mn}^2 \right)^{1/2} h \right] \right\}, \end{aligned} \quad (39)$$

and the resultant moment in the Laplace domain

$$\begin{aligned} \bar{M}_r = & \frac{\alpha_t E T_0}{a^2 t_0} \sum_{m=0}^{\infty} \sum_{n=1}^{\infty} \left(\frac{-r_0 J_1(\alpha_n r_0)}{\alpha_n [J_0(\alpha_n a)]^2 \sinh\{\gamma_n h\}} \right) \\ & \times J_0(\alpha_n r) \sin m\theta \varphi_{mn}(s), \end{aligned} \quad (40)$$

in which

$$\begin{aligned} \varphi_{mn}(s) = & \left(\frac{1 - e^{-s t_0}}{s^2} \right) \left(\frac{s^\alpha}{\kappa} + \beta_{mn}^2 \right)^{-1} \left\{ \left[\left(\frac{s^\alpha}{\kappa} + \beta_{mn}^2 \right)^{1/2} h \right] \right. \\ & \times \left\{ 1 + \cosh \left[\left(\frac{s^\alpha}{\kappa} + \beta_{mn}^2 \right)^{1/2} h \right] \right\} \\ & \left. - 2 \sinh \left[\left(\frac{s^\alpha}{\kappa} + \beta_{mn}^2 \right)^{1/2} h \right] \right\}. \end{aligned} \quad (41)$$

As a solution to transformed Eq. (20) satisfying Eq. (21), we assume $\bar{w}(r, \theta, s)$ as

$$\begin{aligned} \bar{w} = & \frac{\alpha_t E T_0}{a^2 t_0} \sum_{m=0}^{\infty} \sum_{n=1}^{\infty} C_n \left(\frac{-r_0 J_1(\alpha_n r_0)}{\alpha_n [J_0(\alpha_n a)]^2 \sinh\{\gamma_n h\}} \right) \varphi_{mn}(s) \\ & \times [J_0(\alpha_n r) - J_0(\alpha_n a)] \sin m\theta. \end{aligned} \quad (42)$$

From Eqs. (20), (35) and (42), and integrating with respect to r from limits 0 to a , one obtains $C_n = a / [(1 - \nu) D \alpha_n^2]$. Using Eqs. (19) and (21), the resultant moments as

$$\begin{aligned} \bar{M}_r = & \frac{\alpha_t E T_0}{a^2 t_0} \sum_{m=0}^{\infty} \sum_{n=1}^{\infty} \left(\frac{-r_0 J_1(\alpha_n r_0)}{\alpha_n [J_0(\alpha_n a)]^2 \sinh\{\gamma_n h\}} \right) \\ & \times \left\langle \frac{C_n D}{r^2} \left\{ -m^2 \nu J_0(\alpha_n a) + [(\alpha_n r)^2 + m^2 \nu] J_0(\alpha_n r) \right. \right. \\ & \left. \left. - (\alpha_n r)(2 + \nu) J_1(\alpha_n r) \right\} - \frac{J_0(\alpha_n r)}{1 - \nu} \right\rangle \sin m\theta \varphi_{mn}(s), \end{aligned} \quad (43)$$

$$\begin{aligned} \bar{M}_\theta = & \frac{\alpha_t E T_0}{a^2 t_0} \sum_{m=0}^{\infty} \sum_{n=1}^{\infty} \left(\frac{-r_0 J_1(\alpha_n r_0)}{\alpha_n [J_0(\alpha_n a)]^2 \sinh\{\gamma_n h\}} \right) \\ & \times \left\langle \frac{C_n D}{r^2} \left\{ m^2 J_0(\alpha_n a) - [(\alpha_n r)^2 \nu + m^2] J_0(\alpha_n r) \right. \right. \\ & \left. \left. + (\alpha_n r)(1 + 2\nu) J_1(\alpha_n r) \right\} - \frac{J_0(\alpha_n r)}{1 - \nu} \right\rangle \sin m\theta \varphi_{mn}(s), \end{aligned} \quad (44)$$

$$\begin{aligned} \bar{M}_{r\theta} = & (1 - \nu) \frac{\alpha_t E T_0}{a^2 t_0} \sum_{m=0}^{\infty} \sum_{n=1}^{\infty} \left(\frac{-r_0 J_1(\alpha_n r_0)}{\alpha_n [J_0(\alpha_n a)]^2 \sinh\{\gamma_n h\}} \right) \\ & \times \left\langle \frac{C_n D}{r^2} m [J_0(\alpha_n a) - J_0(\alpha_n r) + (\alpha_n r) J_1(\alpha_n r)] \right\rangle \\ & \times \cos m\theta \varphi_{mn}(s). \end{aligned} \quad (45)$$

Now we assume $\bar{F}(r, \theta, t)$ such that it satisfies Eq. (24), as

$$\begin{aligned} \bar{F}(r, \theta, t) = & \frac{2\alpha_t E T_0}{a^2 t_0} \sum_{m=0}^{\infty} \sum_{n=1}^{\infty} D_n \left(\frac{-r_0 J_1(\alpha_n r_0)}{\alpha_n [J_0(\alpha_n a)]^2 \sinh\{\gamma_n h\}} \right) \\ & \times J_0(\alpha_n r) \sin m\theta \phi_{mn}(s), \end{aligned} \quad (46)$$

in which the constant can be obtained using transformed Eq. (24) and integrating with respect to r from limits 0 to a , as

$$D_n = a^2 / \{3m^2 \alpha_n^2 [J_0(\alpha_n a) - (\pi/2) J_0(\alpha_n a) H_1(\alpha_n a)]\}, \quad (47)$$

where $H_1(\cdot)$ denotes the Struve function of the first kind. Substituting Eq. (46) into transformed Eq. (23), one gets the resultant forces as

$$\begin{aligned} \bar{N}_r = & \frac{2\alpha_t E T_0}{a^2 t_0} \sum_{m=0}^{\infty} \sum_{n=1}^{\infty} \frac{D_n}{r^2} \left(\frac{-r_0 J_1(\alpha_n r_0)}{\alpha_n [J_0(\alpha_n a)]^2 \sinh\{\gamma_n h\}} \right) \\ & \times \{-m^2 J_0(\alpha_n r) + (\alpha_n r) J_1(\alpha_n r)\} \sin m\theta \phi_{mn}(s), \end{aligned} \quad (48)$$

$$\begin{aligned} \bar{N}_\theta = & \frac{2\alpha_t E T_0}{a^2 t_0} \sum_{m=0}^{\infty} \sum_{n=1}^{\infty} D_n \left(\frac{-r_0 J_1(\alpha_n r_0)}{\alpha_n [J_0(\alpha_n a)]^2 \sinh\{\gamma_n h\}} \right) \\ & \times \{-m^2 J_0(\alpha_n r)\} \sin m\theta \phi_{mn}(s), \end{aligned} \quad (49)$$

$$\bar{N}_{r,\theta} = \frac{2\alpha_i E T_0}{a^2 t_0} \sum_{m=0}^{\infty} \sum_{n=1}^{\infty} \frac{m D_n}{r^2} \left(\frac{-r_0 J_1(\alpha_n r_0)}{\alpha_n [J_0(\alpha_n a)]^2 \sinh\{\gamma_n h\}} \right) \times \{(\alpha_n r) J_1(\alpha_n r) - J_0(\alpha_n r)\} \cos m\theta \phi_{mn}(s). \quad (50)$$

Now using Eqs. (36)-(40), (43)-(45) and (48)-(50) in (25), one obtains the expressions for thermal bending stresses $\bar{\sigma}_{rr}$, $\bar{\sigma}_{\theta\theta}$ and $\bar{\sigma}_{r\theta}$, and they are rather lengthy. Subsequently, the same has been omitted here for the sake of brevity but has been considered the stress equations during graphical discussion using MATHEMATICA software.

5. Inversion Of Laplace Transforms

Now to obtain the original solution of Eqs. (36)-(50), Laplace inversion theorem is to be used, which can be written as

$$f(t) = \frac{1}{2\pi i} \lim_{\beta \rightarrow \infty} \int_{\gamma-i\beta}^{\gamma+i\beta} \exp(st) \bar{f}(s) ds, \quad (51)$$

along any line $R(s) = \gamma \geq c$ converges to a function $f(t)$ which is independent of γ and whose Laplace transform is $\bar{f}(s)$, $R(s) < c$. The direct integration of Eq. (36) is usually complicated and not analytically feasible in certain situations. The inverse of the Laplace transform is thus obtained by using the Gaver–Stehfast algorithm [55-57], with the aim to approximate $f(t)$ by a sequence of functions as

$$f(t) \approx f_n(t) = \left[\frac{1}{t} \ln(2) \right] \sum_{n=1}^L a_n F \left[\frac{n}{t} \ln(2) \right], \quad n \geq 1, t > 0, \quad (52)$$

$$a_n = (-1)^{n+L/2} \sum_{k=\lfloor (n+1)/2 \rfloor}^{\min(n,L/2)} \frac{k^{L/2} (2k)!}{(L/2 - k)! k! (k-1)! (n-k)! (2k-n)!}, \quad n \geq 1, 1 \leq L \leq n \quad (53)$$

where $F[\cdot]$ is the Laplace transform of $f(t)$ and coefficients a_n depend only on the number of expansion terms n . It is also noted that the approximations $f_n(t)$ converge to $f(t)$ [58] if a function f is continuous at t and of bounded variation in a neighbourhood of t .

6. Numerical Results, Discussion, And Remarks

The numerical computations have been carried out for an Aluminum plate with thermo-mechanical properties, which is shown in Table 1.

Table 1. Thermo-mechanical properties: Aluminum.

Dimension	Value
Modulus of Elasticity, E	70 GPa
Poisson's ratio	0.35
Thermal Expansion Coefficient, α	$23 \times 10^{-6}/^\circ\text{C}$
Thermal diffusivity, κ	$84.18 \times 10^{-6} \text{ m}^2\text{s}^{-1}$
Thermal conductivity, k	$204.2 \text{ Wm}^{-1}\text{K}^{-1}$

The 3.831, 7.015, 10.173, 13.323, 16.470, 19.615, 22.760, 25.903, 29.046, 32.189, 35.332, 38.474, 41.617, 44.759, 47.901, are the positive and real roots of the

transcendental equation $J_1(\alpha_n a) = 0$. The physical parameter for the sector plate as $a = 1$, $h = 0.08$, $t_0 = 0.8$ and $T_0 = 150$. For the interest of simplicity, we introduce the following dimensionless values

$$\begin{aligned} \bar{r} &= r/a, \quad \bar{z} = [z - (-h/2)]/a, \quad \bar{\tau} = \kappa t/a^2, \quad \Theta = \tau/T_0, \\ \bar{w} &= w/\alpha_i T_0 a, \quad \bar{\sigma}_{ij} = \sigma_{ij}/E\alpha_i T_0 \quad (i, j = r, \theta), \\ \bar{F} &= F/E\alpha_i T_0 a^2, \quad \bar{N}_{ij} = N_{ij}/Ea^3, \quad \bar{M}_{ij} = M_{ij}/Ea^3 \end{aligned} \quad (54)$$

Figures (2)-(4) illustrate the numerical results for the circular plate's temperature distribution, using the thermal boundary conditions subjected to ramp-type sectional thermal load on the upper face while keeping the lower face at zero temperature.

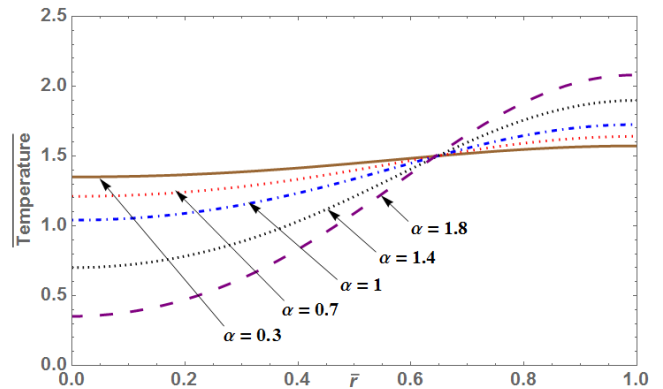


Figure 2. Temperatures distribution along the radial axis at different values of α .

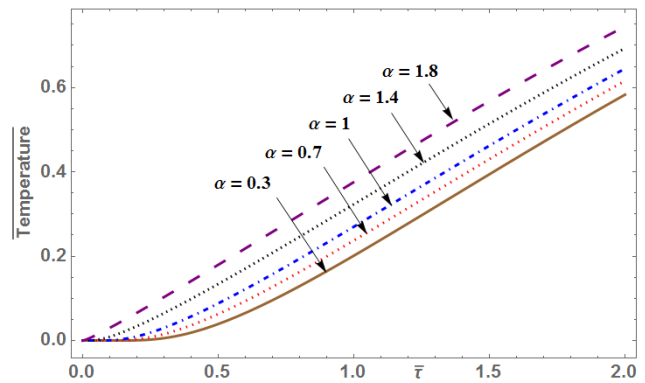


Figure 3. Temperatures distribution as time proceeds at various values of α .

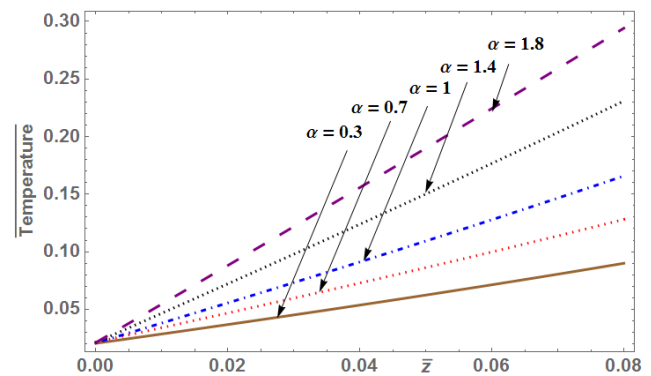


Figure 4. Temperatures distribution along thickness direction at various values of α .

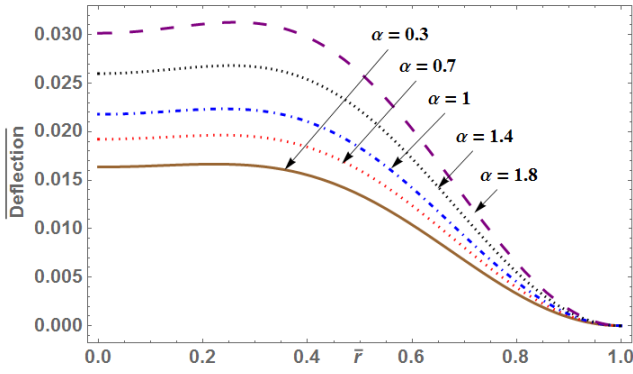


Figure 5. Thermal deflection along the radial axis at different values of α .

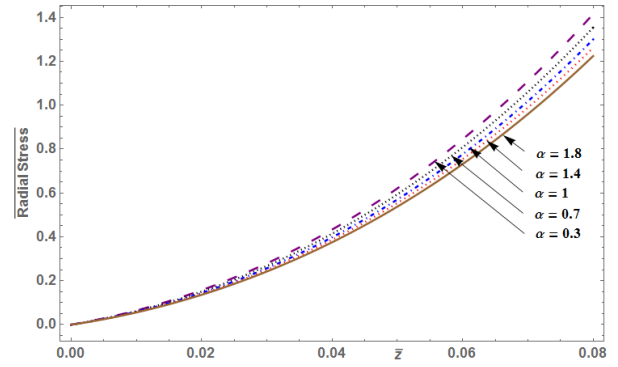


Figure 9. Variation in radial stress along thickness direction at different values of α .

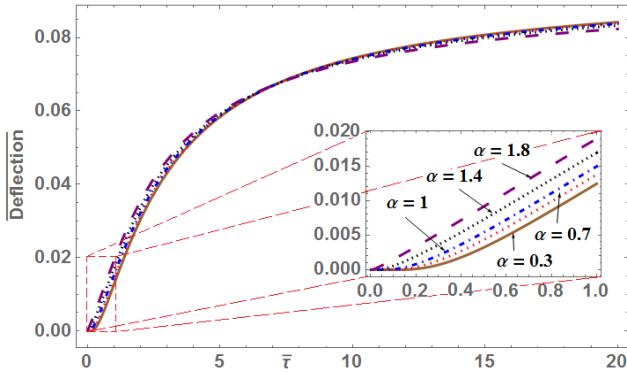


Figure 6. Deflection distribution along the time at various values of α .

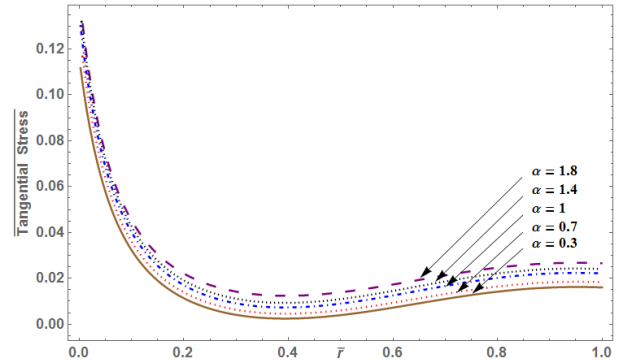


Figure 10. Thermal tangential stress along the radial axis at different values of α .

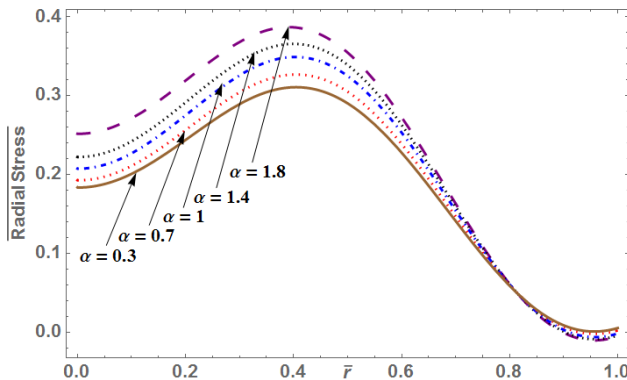


Figure 7. Thermal radial stress along the radial axis at different values of α .

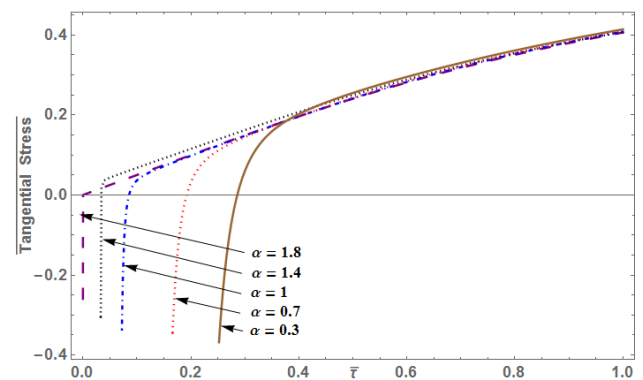


Figure 11. Variation in tangential stress along the time at different values of α .

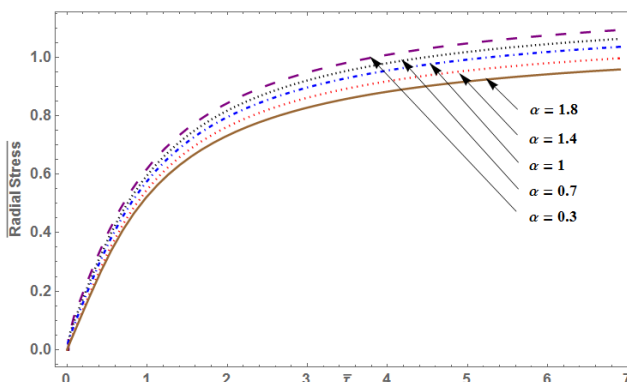


Figure 8. Variation in radial stress along the time at different values of α .

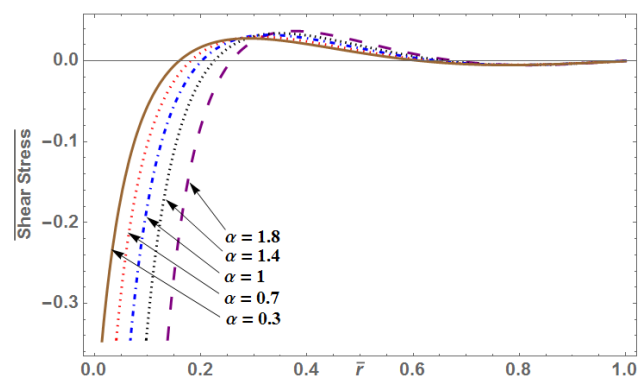


Figure 12. Dimensionless thermal shear stress along the radial axis at different values of α .

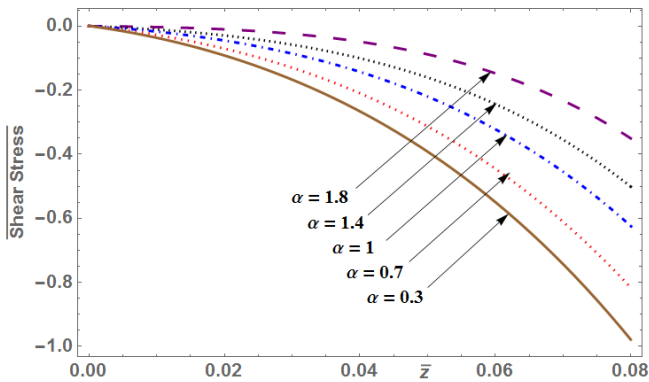


Figure 13. Variation in shear stress along with the thickness at different values of α .

Fig. 2 shows the variation in dimensionless temperature approaches to a maximum value at the extremum of the outer edge, which is impacted by the concentric ramp-type thermal load and drops at $\bar{r}_0 = 0.65$. It is depicted that considerable compressive stress occurs on the heated inner side, and tensile stress occurs on the outer edge along the radial direction. It is also noted that irrespective of the sectional heat source range, the temperature distribution characteristic is the same. As shown in Fig. 3, the temperature is initially zero at $\bar{r} = 0$, which approaches a maximum as time proceeds. It is observed that as $\bar{t} \rightarrow \infty$, the transient temperature distribution attains a constant value. Figure 4 shows the temperature distribution along the thickness direction for different values of α , which is maximum towards the outer edge due to energized heat supply. Figure 5 shows the variation in dimensionless thermal deflection is maximum at the mid of the plate, and the variation decreases remarkably approaching the plate's brink for different α , thus satisfying boundary conditions (21). The deflection is highest at the centre part due to the external energy supply. Figure 6 shows the variation in dimensionless thermal deflection as time proceeds to increase linearly and attain a pre-buckling state's constant value. Figures 7 to 13 show the variations of the circular plate's dimensionless thermal bending stresses subjected to thermal loading. Figure 7 shows that the maximum value of tensile stresses occurs in the middle surface along the radial direction, and then the compressive stress acts towards the end. For $\bar{\sigma}_{rr}$ in Figure 8, as time proceeds, the stress distribution gradually increases due to the accumulation of energy due to sectional heat supply and as $\bar{t} \rightarrow \infty$ the stress gets fixed towards a stable state. Figure 9 shows the variation in dimensionless radial stress distribution across thickness directions in which it is observed that high tensile stress occurs on the outer edge and attains the maximum stress value. Figure 10 shows the variation in the distribution of dimensionless tangential stress across the radial direction, indicating that tensile forces are high on the middle part and may be due to the available thermal energy. It is learned that the stresses move along the radial direction; the compressive forces are more dominant compared to tensile stresses. Figure 11 shows that the tangential stresses are more of a compressive type, and later on, they increase linearly as time proceeds till it attains maximum and stable tensile stress. Figure 12 depicts the variation in dimensionless shear stress distribution across thickness directions in which it is observed that high tensile stress occurs on the outer edge and attains the maximum stress value. Figure 13 shows the dimensionless thermal

shear stress along the thickness direction at different values of α . It is observed that the tensile stresses are maximum at the first part of thickness which is later overlaid by the compressive stress at the end along the thickness direction.

7. Conclusion

This article develops the classical techniques model to analyze the transient thermoelastic in a homogeneous elastic circular plate undergoing ramp-type heating on the concentric region within the fractional-order theory framework. The results obtained while carrying out research are described as follows:

- The value of dimensionless temperature approaches a maximum value at the end boundaries along the radial direction, which may be due to available energy in the form of a sectional heat supply. The overlapping of the curve occurs at the inner rim of the concentric ramp-type thermal load. Similarly, the temperature distribution along the thickness direction is more linear due to the plate's thinness.
- The value of dimensionless thermal deflection is maximum at the mid of the plate. The variation decreases remarkably approaching the plate's brink due to the accumulated energy supplied by the impacted thermal load.
- The value of radial stress has a maximum value at the mid of the plate along the radial direction due to the accumulation of energy and sectional heat supply.
- The value of tangential stress indicates that tensile forces are high in the middle part due to the available thermal energy.
- The value of shear stress shows that the tensile stresses are maximum at the first part of thickness which is later overlaid by the compressive stress at the end along the thickness direction.

Finally, as opposed to the instantaneous response predicted by the generalized theory of thermoelasticity, the fractional theory, currently under consideration, predicts a delayed response to physical stimuli, which can be observed in nature. This supports the motivation for this direction of research.

In this problem, we have used the thin circular plate with clamped edges by applying the time fractional order theory of thermoelasticity. We avoided using conventional potential functions in favour of taking a more direct approach to solving the problem. By doing this, the well-known difficulties that are involved with finding solutions via potential functions can be avoided. The material's conductivity is directly proportional to the measured fractional order parameter. By taking into account, the time-fractional derivative in the field equations, the equation system presented in this article can be beneficial when applied to the study of the thermal characteristics of a variety of entities in the context of real-world engineering challenges.

Acknowledgements:

The author(s) would like to extend utmost gratitude and indebtedness to the Reviewers and Editors for their suggestions.

Nomenclature

Definitions

- α linear coefficient of thermal expansion ($^{\circ}C$)
- κ thermal diffusivity ($m^2 s^{-1}$)

k thermal conductivity (W/m.K)

Greek symbols

μ Lamé's constants (GPa),

ν Poisson's ratio,

ρ density (kg/m³),

σ_{ij} components of the stress tensor.



References:

- [1] K. B. Oldham and J. Spanier, *The fractional calculus: Theory and applications of differentiation and integration to arbitrary order*, Academic Press, New York, 1974.
- [2] K. S. Miller and B. Ross, *An Introduction to the fractional integrals and derivatives: Theory and applications*, Wiley, New York, 1993.
- [3] S. G. Samko, A. A. Kilbas and O. I. Marichev, *Fractional integrals and derivatives: Theory and applications*, Gordon and Breach, New York, 1993.
- [4] I. Podlubny, *Fractional differential equations*, Academic Press, San Diego, 1999.
- [5] R. Hilfer, *Applications of fractional calculus in physics*, World Scientific Publishing, Singapore, 2000.
- [6] R. Herrmann, *Fractional calculus: An introduction for physicists*, World Scientific Publishing, Singapore, 2011.
- [7] Y. Povstenko, "Fractional heat conduction equation and associated thermal stress," *J. Therm. Stresses*, 28(1), 83-102, 2004. DOI: 10.1080/014957390523741.
- [8] Y. Povstenko, "Two-dimensional axisymmetric stresses exerted by instantaneous pulses and sources of diffusion in an infinite space in a case of time-fractional diffusion equation," *Int. J. Solids Struct.*, 44 (7–8), 2324-2348, 2007. DOI: 10.1016/j.ijsolstr.2006.07.008.
- [9] Y. Povstenko, "Fractional heat conduction equation and associated thermal stresses in an infinite solid with spherical cavity," *Q. J. Mech. Appl. Math.*, 61(4), 523-547, 2008. DOI: 10.1093/qjmam/hbn016.
- [10] Y. Povstenko, "Time-fractional radial heat conduction in a cylinder and associated thermal stresses," *Arch. Appl. Mech.*, 82, 345–362, 2012. DOI: 10.1007/s00419-011-0560-x.
- [11] Y. Povstenko, D. Avci, E. İskender and Ö. Necati, "Control of thermal stresses in axisymmetric problems of fractional thermoelasticity for an infinite cylindrical domain," *Therm. Sci.*, 21 (1A), 19-28, 2017. DOI: 10.2298/TSCI160421236P.
- [12] H.M. Youssef and E. A. Al-Lehaibi, "Variational principle of fractional order generalized thermoelasticity," *Appl. Math. Lett.*, 23(10), 1183-1187, 2010. DOI: 10.1016/j.aml.2010.05.008.
- [13] H.M. Youssef and E.A. Al-Lehaibi, "Fractional order generalized thermoelastic half-space subjected to ramp-type heating," *Mech. Res. Commun.*, 37(5), 448-452, 2010. DOI: 10.1016/j.mechrescom.2010.06.003.
- [14] H.M. Youssef and E.A. Al-Lehaibi, "Fractional order generalized thermoelastic infinite medium with cylindrical cavity subjected to harmonically varying heat," *Sci. Res. J.*, 3(1), 32-37, 2011. DOI: 10.4236/eng.2011.31004.
- [15] H.M. Youssef, "Two-dimensional thermal shock problem of fractional order generalized thermoelasticity," *Acta Mech.*, 223, 1219–1231, 2012. DOI: 10.1007/s00707-012-0627-y.
- [16] H. M. Youssef, "State-space approach to fractional order two-temperature generalized thermoelastic medium subjected to moving heat source," *Mech. Adv. Mater. Struct.*, 20, 47–60, 2013. DOI: 10.1080/15376494.2011.581414.
- [17] H. M. Youssef, K. A. Elsibai and A. A. El-Bary, *Fractional order thermoelastic waves of cylindrical gold nano-beam*, Proceedings of the ASME 2013 International Mechanical Engineering Congress and Exposition IMECE2013, November 15-21, San Diego, California, USA, 1-5, 2013. DOI: 10.1115/IMECE2013-62876.
- [18] H. M. Youssef, "Theory of generalized thermoelasticity with fractional order strain," *J. Vib. Control*, 22(18), 3840–3857, 2015. DOI: 10.1177/1077546314566837.
- [19] A. S. El-Karamany and M.A. Ezzat, "On fractional thermoelasticity," *Math. Mech. Solids*, 16 (3), 334-346, 2011. DOI: 10.1177/1081286510397228.
- [20] M. A. Ezzat and A. S. El-Karamany, "Two-temperature theory in generalized magneto-thermoelasticity with two relaxation times," *Meccanica*, 46, 785–794, 2011. DOI: 10.1007/s11012-010-9337-5.
- [21] M. A. Ezzat, A. S. El-Karamany, A.A. El-Bary and M.A. Fayik, "Fractional calculus in one-dimensional isotropic thermo-viscoelasticity," *Comptes Rendus Mécanique*, 341 (7), 553-566, 2013. DOI: 10.1016/j.crme.2013.04.001.
- [22] M. A. Ezzat, A. S. El-Karamany and A. A. El-Bary, "Application of fractional order theory of thermoelasticity to 3D time-dependent thermal shock problem for a half-space," *Mech. Adv. Mater. Struct.*, 24(1), 27-35, 2017. DOI: 10.1080/15376494.2015.1091532.
- [23] H. H. Sherief, A.M.A. El-Sayed and A.M. Abd El-Latif, "Fractional order theory of thermoelasticity," *Int. J. Solids Struct.*, 47(2), 269-275, 2010. DOI: 10.1007/978-94-007-2739-7_366.
- [24] H. H. Sherief and A. M. Abd El-Latif, "Application of fractional order theory of thermoelasticity to a 1D problem for a half-space," *J. Appl. Math. Mech.*, 94(6), 509-515, 2014. DOI: 10.1002/zamm.201200173.
- [25] H. H. Sherief and A. M. Abd El-Latif, "A one-dimensional fractional order thermoelastic problem for a spherical cavity," *Math Mech Solids*, 20(5), 512-521, 2015. DOI: 10.1177/1081286513505585.
- [26] A. Sur and M. Kanoria, "Fractional order two-temperature thermoelasticity with finite wave speed," *Acta Mech.*, 223(12), 2685-2701, 2012. DOI: 10.1007/s00707-012-0736-7.
- [27] D. Bhattacharya and M. Kanoria, "The influence of two-temperature fractional order generalized thermoelastic diffusion inside a spherical shell," *Int. j. appl. innov.*, 3(8), 96-108, 2014.

- [28] A. M. Zenkour and A. E. Abouelregal, "State-space approach for an infinite medium with a spherical cavity based upon two-temperature generalized thermoelasticity theory and fractional heat conduction," *Z. Angew. Math. Phys.*, 65, 149–164, 2014. DOI: 10.1007/s00033-013-0313-5.
- [29] M. Bachher, "Deformations due to periodically varying heat sources in a reference temperature dependent thermoelastic porous material with a time-fractional heat conduction law," *Int Res J Eng Techn.*, 2(4), 145-152, 2015.
- [30] S. Santra, N. C. Das, R. Kumar and A. Lahiri, "Three-dimensional fractional order generalized thermoelastic problem under the effect of rotation in a half space," *J. Therm. Stresses*, 38(3), 309-324, 2015. DOI: 10.1080/01495739.2014.985551.
- [31] N. D. Gupta and N. C. Das, "Eigenvalue approach to fractional order generalized thermoelasticity with line heat source in an infinite medium," *J. Therm. Stresses*, 39(8), 977-990, 2016. DOI: 10.1080/01495739.2016.1187987.
- [32] M. Bachher and N. Sarkar, Fractional order magneto-thermoelasticity in a rotating media with one relaxation time," *Mathematical Models in Engineering*, 2(1), 56-68, 2016.
- [33] I. A. Abbas, "Fractional order generalized thermoelasticity in an unbounded medium with cylindrical cavity," *J. Eng. Mech.*, 142(6), 04016033-1-5, 2016. DOI: 10.1061/(ASCE)EM.1943-7889.0001071.
- [34] I. A. Abbas, "A Study on fractional order theory in thermoelastic half-space under thermal loading," *Phys Mesomech*, 21, 150–156, 2018. DOI: 10.1134/S102995991802008X.
- [35] P. Lata, "Fractional order thermoelastic thick circular plate with two temperatures in frequency domain," *Appl. Appl. Math.*, 13(2), 1216 – 1229, 2018.
- [36] G. Mittal and V. S. Kulkarni, "Two temperature fractional order thermoelasticity theory in a spherical domain," *J. Therm. Stresses*, 42(9), 1136-1152, 2019. DOI: 10.1080/01495739.2019.1615854.
- [37] S. Bhojar, V. Varghese and L. Khalsa, "An exact analytical solution for fractional-order thermoelasticity in a multi-stacked elliptic plate," *J. Therm. Stresses*, 43(6), 762-783, 2020. DOI: 10.1080/01495739.2020.1748553.
- [38] M. Haskul, "Elastic state of functionally graded curved beam on the plane stress state subject to thermal load," *Mech. Based Des. Struct. Mach.*, 48(6), 739-754. 2020. DOI: 10.1080/15397734.2019.1660890.
- [39] E. Arslan, M. Haskul, "Generalized plane strain solution of a thick-walled cylindrical panel subjected to radial heating," *Acta Mech*, 226, 1213–1225, 2015. <https://doi.org/10.1007/s00707-014-1248-4>.
- [40] M. Haskul, E. Arslan and W. Mack, "Radial heating of a thick-walled cylindrically curved FGM-panel," *Z. Angew. Math. Mech.*, 97, 309-321, 2017. <https://doi.org/10.1002/zamm.201500310>.
- [41] M. Haskul, "Yielding of functionally graded curved beam subjected to temperature," *Pamukkale University Journal of Engineering Sciences*, 26(4), 587-593, 2020. DOI: 10.5505/pajes.2019.92331.
- [42] M. E. Gurtin and A. C. Pipkin, "A general theory of heat conduction with finite wave speed," *Arch. Rat. Mech. Anal.*, 31, 113–126, 1968.
- [43] P.J. Chen and M.E. Gurtin, "A second sound in materials with memory," *Z. Angew. Math. Phys.*, 21, 232–241, 1970.
- [44] C. Cattaneo, "On the conduction of heat," *Atti. Semin. Fis. Univ. Modena*, 3, 3–21, 1948.
- [45] C. Cattaneo, "Sur une forme de l'équation de la chaleur éliminant le paradoxe d'une propagation instantanée," *C. R. Acad. Sci.*, 247, 431–433, 1958.
- [46] P. Vernotte, "Les paradoxes de la théorie continue de l'équation de la chaleur," *ibid.*, 246, 3154–3155, 1958.
- [47] S. Kaliski, "Wave equation of thermoelasticity," *Bull. Acad. Polon. Sci. S'er. Sci. Techn.*, 13, 253–260, 1965.
- [48] H. W. Lord and Y. Shulman, "A generalized dynamical theory of thermoelasticity," *J. Mech. Phys. Solids*, 15, 299–309, 1967.
- [49] A. E. Green and P. M. Naghdi, "Thermoelasticity without energy dissipation," *J. Elast.*, 31, 189–208, 1993.
- [50] R. Gorenflo and F. Mainardi, *Fractional calculus: integral and differential equations of fractional order*, In: A. Carpinteri, F. Mainardi (eds.), *Fractals and fractional calculus in continuum mechanics*, 223-276, Springer, New York, 1997.
- [51] A. Kilbas, H.M. Srivastava and J.J. Trujillo, *Theory and applications of fractional differential equation*, Elsevier, Amsterdam, 2006.
- [52] N. Noda, R. B. Hetnarski, Y. Tanigawa, *Thermal Stresses* (2nd ed.), Taylor and Francis, New York, 2003.
- [53] M. R. Eslami, R. B. Hetnarski, J. Ignaczak, N. Noda, N. Sumi, and Y. Tanigawa, *Theory of elasticity and thermal stresses*, Springer New York, 2013. DOI: 10.1007/978-94-007-6356-2.
- [54] E. Ventsel, T. Krauthammer, *Thin plates and shells-Theory, Analysis, and Applications*, Marcel Dekker, New York, 2001.
- [55] D. P. Gaver, "Observing stochastic processes and approximate transform inversion," *Oper. Res.*, 14(3), 444–459, 1966. DOI: 10.1287/opre.14.3.444.
- [56] H. Stehfest, Algorithm 368, Numerical inversion of Laplace transforms," *Comm. Assn. Comp. Mach.*, 13(1), 47–49, 1970. DOI: 10.1145/361953.361969.
- [57] H. Stehfest, "Remark on algorithm 368: Numerical inversion of Laplace transforms," *Commun. Assn. Comput. Mach.*, 13(10), 624, 1970. DOI: 10.1145/355598.362787.
- [58] A. Kuznetsov, "On the convergence of the Gaver–Stehfest algorithm," *SIAM J. Num. Anal.*, 51(6), 2984–2998, 2013. DOI: 10.1137/13091974X.

Research Article

Investigation of Kalina Cycle for Power Generation from Heat Dissipation of Tarasht Power Plant

^{1*} S. Sadri , ² S.Y.S. Mohseni 

¹ Research Assistant, Thermal cycles and Heat Exchangers Department, Niroo Research Institute, Tehran, Iran,

² Graduate Student, Department of Mechanical Engineering, University of Science and Culture, Tehran, Iran

E-mail: ^{1*} ssadri@nri.ac.ir

Received 5 December 2022, Revised 5 March 2023, Accepted 29 March 2023

Abstract

Fuel consumption optimization in thermal power plants is one of the essential topics in the saving energy field in the world. Then; it is necessary to review and provide solutions to increase efficiency. The present manuscript has recovered the heat dissipation from power plant stacks. The Kalina cycle was studied to use exhaust gases to generate power in the Tarasht power plant. Net power output is calculated at about 2080 kW, which increases the total power production of the plant by about 5%. According to environmental analysis, this cycle will cause less damage to the environment due to lowering the temperature of the exhaust gases in the atmosphere and not using additional fossil fuels. Therefore; it is a good solution for using heat dissipation from power plants. The only thing to consider in this solution (based on economic analysis) is the high construction cost compared to other power plant units.

Keywords: Heat recovery; Kalina cycle; power generation; Tarasht power plant

1. Introduction

Optimizing fuel consumption in thermal power plants is one of the most critical topics in energy saving in the world. With the increase in oil prices and, consequently, the increase in the share of fuel in the cost price of electricity generated by power plants, the need to study and provide solutions to increase efficiency is well felt. In this regard, and considering the growth of energy consumption in power plants, the limitations and challenges in providing fossil fuels required by power plants, environmental considerations, and rising global prices for fossil fuels, how to meet these challenges for each power plant has been raised as a significant issue. In this regard, the present study deals with the recovery of waste heat from power plant stacks. For this purpose, the Kalina cycle (which is the same Rankine cycle with the difference in working fluid, i.e., water and ammonia with the characteristic feature of creating a variable boiling point at constant pressure), was investigated in the Tarasht power plant. A mixture of water and ammonia was first used in absorption cycles by Maloney and Robertson in 1950 [1]. Kalina proposed another cycle in 1983 with an efficiency of about 30%-60% higher than the steam power generation cycle [2]. L. Side and Terbius showed that when the Kalina and Rankine cycles are placed in the combined cycles, the efficiency of the Kalina cycle increases by about 10%-30% [3]. In 1989, Kalina and Libowitz proposed a cycle for the use of geothermal resources, with the Kalina cycle having a higher net power than the Rankine cycle with the isobutene working fluid [4]. In 1999, a co-production cycle of power and refrigeration was introduced by Goswami, in which the Rankine cycle and the absorption refrigeration cycle were combined [5-6]. In 2004, Ronald Deepipo studied the power

cycles of two-component water-ammonia mixtures to use heat energy [7]. Goswami et al. (2004) reported in a theoretical and laboratory study of a designed combined cycle that optimization of the second law of thermodynamics would be most effective if solar heat were used as the heat source [8]. In 2006, Zheng introduced a new water-ammonia cycle for simultaneous power generation and refrigeration [9]. In 2007, Methawa Hitarachchi used Kalina Cycle No. 11 (KCS11), or the Low-Temperature Kalina Cycle, to use low-temperature geothermal resources [10]. In 2007, Zhang and Lu designed a new hybrid cycle capable of simultaneously generating power and refrigeration using an external heat source, such as industrial waste heat or gas turbine exhaust. Another feature of the designed system was the replacement of the absorber with a condenser in the Rankine cycle [11]. Zhang and Lever presented several systems with water-ammonia base working fluid. Important and basic parameters for combining refrigeration and power systems to create optimal exergy efficiency by reducing exergy loss were investigated [12]. In 2007 Rouvas and Kerneus tested a Kalina cycle powered by steam and concluded that electricity generated from such a system was in a better position economically and environmentally than coal-fired and diesel-fired power generation systems [13]. In 2008, the Kalina cycle was studied by Ying Zang et al. According to the first law of thermodynamics and the adoption of the Peng Robinson equation as the general equation for the properties of ammonia mixtures in water; thermodynamic analysis was presented in a Kalina cycle distillation step [14]. In 2008, Jiang Feng et al. Proposed a hybrid power-refrigeration cogeneration cycle that combines the Rankine cycle with the absorption refrigeration cycle [15]. In 2009, Ogrisk

introduced the Kalina cycle process in a combined heat and power system to maximize heat generation with heat recovery without needing additional fuels [16]. In 2009, Lolos and R. Dakis used solar energy to provide the heat needed for the Kalina cycle. They concluded that using these heat sources would increase the cycle efficiency by about 5 to 10 percent [17]. In 2010, Philippi used the organic Rankine cycle with water-ammonia working fluid for heat recovery of boilers, examined the organic Rankine cycle with recovery (heat exchanger) and without recovery, and performed an exergy analysis on its cycle. It also determined the area required for the heat exchanger [18]. In 2012, a solar Kalina cycle was studied by Faming Sun and Yasuki Ekigami [19]. In 2013, Jiang Fengwag and Zhouyan Yang introduced a solar cycle. In this system, a storage system was used to store solar radiation energy as a heat source. Solar cycle simulations were also performed based on an extended mathematical model to evaluate system performance over a while [20]. In 2014, Anish Maddie and Frederic Haglund studied a Kalina cycle with a high-temperature source at 450 ° K and a pressure of 100 bar using a solar system. They compared the cycle in terms of efficiency and exergy with a simple Rankine cycle. [21]. In 2017, Anhua Wang and his colleagues studied the sliding density pressure method according to the previous study on the adjustment of ammonia mass to improve the efficiency of the Kalina cycle and considering that a local constant temperature was considered for the maximum operating point of the Kalina cycle [22]. In 2018, Shaubu Zhang et al. analyzed the modified Kalina cycle with parallel power generation and refrigeration (PPR-KC) [23]. In 2018, Hyung Hoon Kim et al. analyzed the Kalina Flash Cycle (KCF) and compared it to the Kalina cycle. This cycle is a new mode that has recently been proposed and operates using a low-temperature heat source [24]. In 2020, Gholamreza Salehi et al. evaluated the thermodynamic and economic analysis of heat recovery of Shahid Hasheminejad Gas Refinery steam network known as Khangiran by Kalina cycle and Rankine organic cycle with different fluids such as isobutane, cyclohexane, isopentane, hexane, isohexane and hexane [25].

In this study, the possibility of using the waste heat of the Tarasht power plant in the form of the Kalina cycle was evaluated. The analysis tool used is one of the modules of Thermoflow commercial software called Thermoflex [26], which calculates the outputs based on continuity equations and conservation of mass and energy. A unit of the Tarasht power plant was modeled, and the calculation results were compared with the available accurate information, and validation was performed. Exhaust gas specifications have been used as a hot source for the Kalina cycle.

2. Modeling

2.1 Introduction of Tarasht Power Plant

In 1955, Tehran Electricity Company signed a contract with the French company Alstom to purchase a 50,000 kW factory consisting of 4 units of steam power plants with a nominal power of 12.5 MW for \$ 3.6 million with a 10-year repayment and a 5% profit. In October 1959, this power plant was put into operation, providing more than 50% of the electricity required by Tehran. The height of this power plant is 1260 meters above sea level, and its practical power is 10 MW [27]. Table 1 provides general information about the Tarasht power plant.

Table 2. General Information of the Tarasht Power Plant.

Number of units	4
Nominal power per unit (MW)	12.5
Average Summer Operating Power (MW)	10
Average Winter Operating Power (MW)	10
Design efficiencies (%)	30
Current efficiency (%)	17.5
Generator voltage (kV)	11.5
Power plant output voltage (kV)	63
Manufacturer	Alstom
Boiler Manufacturer	Stein Industry
Turbine Manufacturer	Alstom
Generator Manufacturer	Alstom

2.2 Technical Specifications of the Power Plant

The steam turbines of Tarasht power plant are single cylinder and produce 12.5 MW of power in nominal conditions. The steam entering the turbine has a pressure of 40 bar and a temperature of 420 °C. There are three extracted steam flow in each turbine introduce steam into the heaters to heat the feed water. The cycle of the Tarasht power plant does not have a high-pressure feed water heater and only has two low-pressure heaters and a separator. The diffuser in these units does not have an air outlet and does not play the role of removing oxygen. Instead, a heat exchanger called a recuperator is located in the feed water path after the condenser, which is responsible for this task. Of course, between the recuperator and heater No. 1, there is another heat exchanger called an auxiliary heater. The auxiliary heater heats the feed water slightly with the help of recurrent saturated water from the shells of heaters No. 1 and 2, as well as part of the low-pressure flow of the turbine [27]. The boiler of the Tarasht power plant has natural circulation. Under normal conditions, the feed water enters the boiler at a temperature of 177 ° C, and the steam leaves at a temperature of 460 ° C and a pressure of 43 bar with a mass flow of 65 tons/hr. Tarasht power plant boiler is also capable of producing 91 tons/hr of steam. The boiler has no re-heater and has two superheaters. The boiler furnace of the Tarasht power plant is under vacuum in such a way that the two blowing and suction fans create these conditions. It should be noted that there is no air preheater in the units of this power plant. Four cooling towers are provided for each unit. The generator of the units is also cooled by water [28].

2.3 Power Plant Modeling

In this power plant, three extracted steam flow systems are installed for the turbine, through which some of the steam flow enters the heaters and causes the initial heating of the feed water, which has an effect on improving the efficiency of the steam power plants. The turbine output flow, after passing through the condenser, passes through the blower and is then pumped to the heaters. Figure 1 shows the placement of equipment and connections in the software. The inputs used in modeling are described in Table 2.

3. Results and Discussion

The results of power plant modeling are included in Table 3. They show that the net power of each unit is 10047 kW, which is being used with an efficiency of 21.15%. The characteristics of the exhaust gas are described in Table 4. The temperature of the exhaust gas is equal to 257 °C. The

modeling results of the Tarasht power plant are compared with the reference [29] in Table 5, and the relative power error calculated in the practical conditions of the power plant 3.48%.

Table 2. Input Data for Power Plant Modeling.

Equipment name attribute	Input characteristic	value
Main site	Site height (m)	1260
	Ambient temperature (°C)	37
	Relative humidity (%)	40
	Ambient wet bulb temperature (°C)	25.06
	Ambient pressure (bar)	0.8708
Boiler	Inlet fuel	Natural gas
	Inlet fuel pressure (bar)	1.724
	Outlet steam temperature (°C)	450
	Outlet steam flow (kg/s)	16.4
Turbine	Inlet steam pressure (bar)	40
	Number of shafts	1
	Shaft speed (rpm)	3000
	Mechanical efficiency (%)	99.8
Condenser	Design pressure (bar)	0.0689
	Increase in water cooling temperature (°C)	10
	Low condenser temperature (°C)	2
Condenser water source	Pressure (bar)	1.014
	Temperature (°C)	15
Blowdown	Temperature (°C)	15
Pump after Blowdown	Efficiency (%)	100
First heater	Pressure increment (bar)	5.859
Second heater	Outlet water temperature (°C)	74.25
	Design pressure (bar)	3.904
De-aerator	Output temperature (°C)	142.8
Pump after de-aerator	Efficiency (%)	100
Third heater	Pressure increment (bar)	41.21
	Outlet temperature (°C)	177
Stack	Outlet temperature (°C)	257

liquid-vapor separator because the working conditions of the Kalina cycle are at low temperatures. In the present modeling, to use the power plant exhaust heat with the characteristics of the exhaust gas, including temperature, pressure, and percentage of compounds, has been used as a low-temperature source. The heat exchange of this source with the evaporator plays an essential role in heating the water-ammonia mixture path. In the separator, the mixture with the separated steam phase goes to a special water-ammonia turbine to produce power. At the same time, the mixture with the liquid phase passes along the side path, during which it acts as a hot fluid in the high-temperature recuperator. It then combines with the expanded steam mixture from the turbine and passes from the low-temperature recuperator to the condenser.

Table 3. Results of Power Plant Modeling.

Gross Power (kW)	10653
Gross electric efficiency (%)	22.42
Gross heat rate (LHV)(kJ/kWh)	16057
Net Power (kW)	10047
Net electric efficiency (LHV) (%)	21.15
Net heat rate (LHV)(kJ/kWh)	17025
Net electric efficiency (HHV) (%)	19.1
Net heat rate (HHV)(kJ/kWh)	1848

Table 4. Specifications of Power Plant Exhaust Gas.

Temperature (°C)	257	
Mass flow (kg / s)	74.6	
Gas composition (Mole, %)	Oxygen	2.237
	Carbon dioxide	8.43
	Water vapor	18.72
	Nitrogen	69.78
	Argon	0.837

The Kalina model proposed by Ogrisk has a primary path and a secondary path. In the main path, the mixture is pumped after the condenser to the low-temperature recuperator, which is charged by the ammonia source. Next, the ammonia-water mixture is passed through a high-temperature recuperator and then an evaporator to reach the

Table 5. Verification.

Parameter	Quantity (unit)	Present modeling	Reference
Power	P (kW)	10047	10410
efficiency	η (%)	21.15	21.44

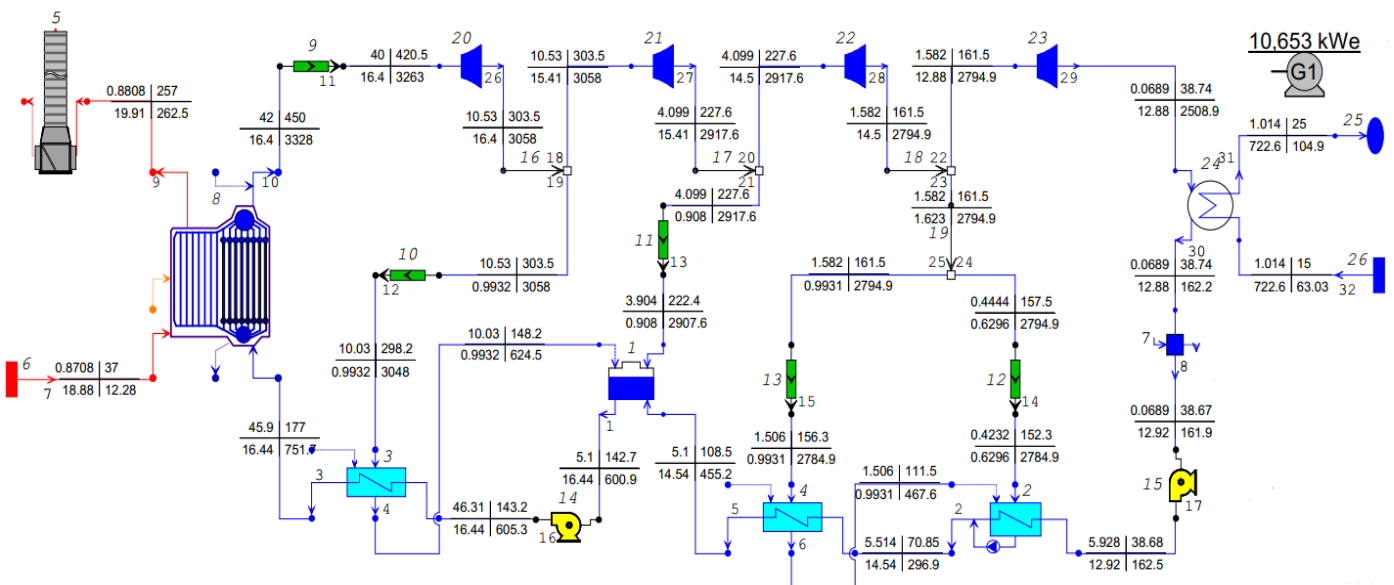


Figure 1. Schematic of Tarasht Power Plant Modeling.

Based on the modeling results (Figure 1) of a steam unit of the Tarasht power plant in the previous section, the available gas flow rate is obtained as 19.1 kg/s. According to the four available steam units in Tarasht power plant, the amount of gas flow rate available as a heat source in the Kalina cycle will equal 76.4 kg/s. Results are shown in Table 6, and the final schematic of the Kalina cycle with flow characteristics is in Figure 2. The net power output is calculated to be 2080.8 kW.

Table 6. Results of Kalina Modeling.

Gross Power (kW)	2205.6
Gross electric efficiency (%)	13.4
Gross heat rate (LHV)(kJ/kWh)	26864
Net Power (kW)	2080.8
Net electric efficiency (LHV) (%)	12.64
Net heat rate (LHV)(kJ/kWh)	28475

Table 7. The Energy Equations for Each Device.

Device	Equation
Separator	$\dot{m}_{10} = \dot{m}_1 + \dot{m}_2$
Turbine	$\dot{w}_T = \dot{m}_1(h_1 - h_3)$
Mixer after turbine	$\dot{m}_{12} = \dot{m}_3 + \dot{m}_9$
Condenser	$\dot{m}_7(h_7 - h_4) = \dot{m}_{14}(h_5 - h_{14})$
Pump	$\dot{w}_P = \dot{m}_4(h_{13} - h_4)$
LT recuperator	$\dot{m}_{17}h_{17} + \dot{m}_{12}h_{12} = \dot{m}_6h_6 + \dot{m}_7h_7$
HT recuperator	$\dot{m}_6h_6 + \dot{m}_2h_2 = \dot{m}_8h_8 + \dot{m}_9h_9$
Evaporator	$\dot{m}_8(h_{10} - h_8) = \dot{m}_{15}(h_{15} - h_{11})$

For the economic analysis of the Kalina cycle, the cost is estimated according to the power generation [30-31].

$$C_{inv} = C_{PC} + C_{land} + C_{cnt} \quad (1)$$

The following equation is used to estimate the cost of the power cycle:

$$C_{PC} = C_{PC.eqp} + C_{PC.misc} \quad (2)$$

The cost function of power cycle equipment is as follows:

$$C_{PC.eqp} = C_{tur} + C_{gen} + C_{pu} + \sum C_{re} + C_{sep} \quad (3)$$

The cost of purchasing turbines, pumps, and generators is calculated based on the following equations:

$$C_{tur} = 4405 \times \dot{W}_{tur}^{0.7} \quad (4)$$

$$C_{pu} = 1120 \times \dot{W}_{pu}^{0.7} \quad (5)$$

$$C_{gen} = 10 \times 10^6 \times \left(\frac{W_{gen}}{160 \times 10^3} \right)^{0.7} \quad (6)$$

The cost of heat exchangers is obtained based on the following equation:

$$C_{hx} = 32800 \times \left(\frac{A_{hx}}{80} \right)^{0.8} \times f_{pres} \times f_{temp} \quad (7)$$

In the heat exchanger cost equation, A_{hx} is the amount of heat transfer area, which is obtained by dividing the heat capacity of each exchanger by the heat transfer coefficient, which according to the reference [32] for the evaporator $1.1(kW/m^2K)$, for recuperator $0.7(kW/m^2K)$ and for condensers $0.5(kW/m^2K)$. f_{temp} and f_{pres} are temperature correction coefficient and pressure correction coefficient, respectively, obtained from the reference [33] according to the characteristics of the heat exchanger. In this analysis, due to the low temperature of the cycle, the temperature correction coefficient is equal to 1 and considering that the maximum pressure in the recuperator and evaporators is 30 bar, the pressure correction coefficient is equal to 1.3, and for the condenser is equal to 1. The separator cost function is calculated using the following equation:

$$C_{sep} = f_{pres} \times 10^{f_{s1} + f_{s2} \times \log H_{sep} + f_{s3} \times (\log H_{sep})^2} \quad (8)$$

In this function, H_{sep} is the height of the liquid inside the separator from the inlet nozzle in the first 3 minutes of the process, is considered 0.5 m. The coefficients f_{s1} , f_{s2} and f_{s3} are correction coefficients that depend on the geometric dimensions.

In the power miscellaneous cost function: $C_{PC.pip}$ is the cost of piping, $C_{PC.insc}$ the cost of control systems and instrumentation, $C_{PC.el}$ the cost of electrical equipment and materials, and $C_{PC.inst}$ the cost of installation. Their amount includes 66%, 10%, 10%, and 45% of the cost amount of cycle equipment.

The cost of land purchase is considered to be 1200 dollars per kilowatt of gross output power. In this analysis, the amount of contingent costs are 20% of the total amount of cycle costs and land purchase.

The value of the total investment cost function is written with the criteria of 2010. To convert it into daily units, an equation is needed to perform this conversion using the correction factor. Marshall and Swift's cost index [34] is one of the most reliable indices for converting costs in different years and this index has been used in this analysis.

$$C = C_{CF} \times f_{M\&S}^{2018} / f_{M\&S}^{CF,Y} \quad (9)$$

In the above function, C_{CF} is the sum of the cost functions, $f_{M\&S}^{CF,Y}$ is the Marshall and Swift coefficient in the year when the cost functions were written, which is 1.13 in 2010, and $f_{M\&S}^{2018}$ is the new coefficient Marshall and Swift, which is considered equal to 1.

The concept of irreversibility in the thermodynamic analysis is necessary. This approach is related to the exergy concept as the available work from certain input energy. The system deviation of the environment is called exergy. The exergy calculation can be expressed as it follows:

$$e_f = (h - h^*) - T_0(s - s^*) + \sum_{i=1}^n (\mu_i^* - \mu_i^0) \quad (10)$$

The first two terms present the physical exergy, and the third term presents the chemical exergy. The temperature, pressure, and concentration of the environment (T_0 , P_0 , w_0) can be called the global dead state that the related properties can be shown with 0 symbols. In the restricted dead state (*), in which only the temperature and pressure are changed to the environmental values [35]. The exergy destruction in each component can be evaluated based on fuel and product exergy [36]

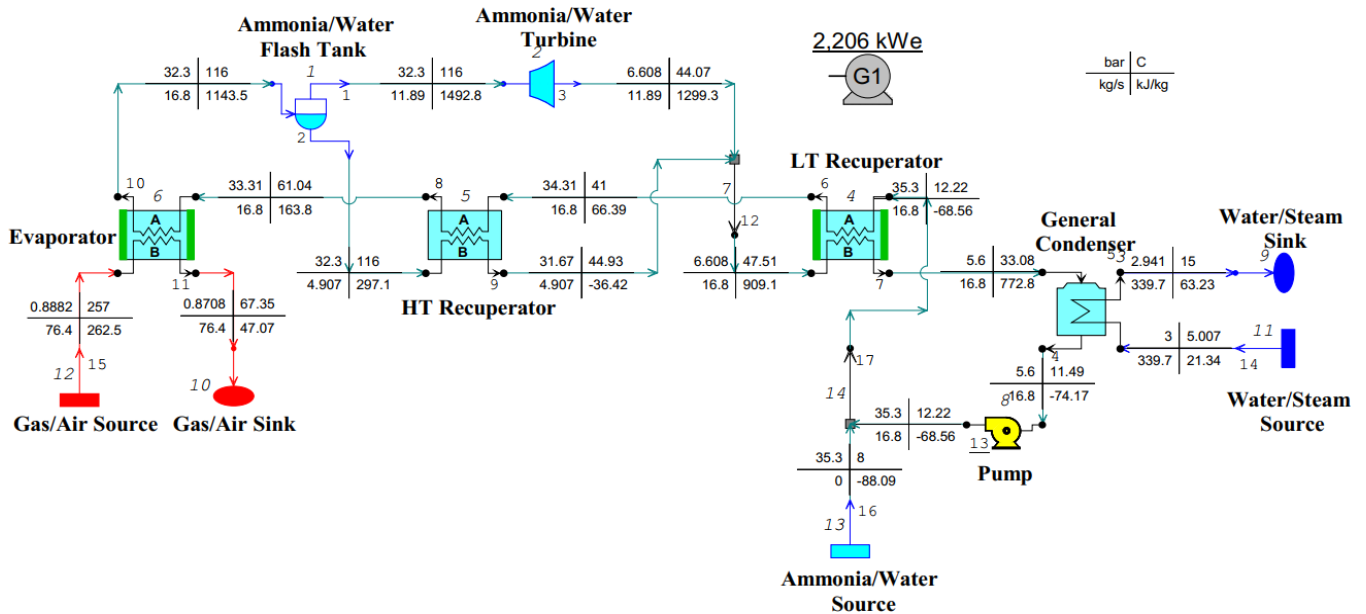


Figure 2. Schematic of Kalina Cycle Modeling.

$$E_D = E_{fuel} - E_{product} \quad (11)$$

Exergetic efficiency is one of the important parameters for irreversibility evaluation that defined based on the fuel-product definition as below [36]:

$$\varepsilon = \text{product}/\text{fuel} \quad (12)$$

The amount of net power was obtained from the modeling of the power plant for one unit of 10.047 kW and all four units 40.188 kW and from the modeling of the Kalina cycle 2080 kW, which shows that the production power of the power plant has increased by 5.18%. If the temperature of the exhaust gas is less than 257°C; the amount of net production power and heat transfer will decrease, the results are shown in Table 8.

Table 8. The Effect of Temperature on Power Generation.

Temperature (°C)	230	240	250	257
Net power (kW)	1819	1972	1995	2080
Gross power (kW)	1969	2097	2182	2205
Heat transfer (kW)	15314	16060	16270	16459

The results show that if the inlet temperature of the evaporator in the Kalina cycle increases, the amount of power production will increase, which is shown in Figure 3.

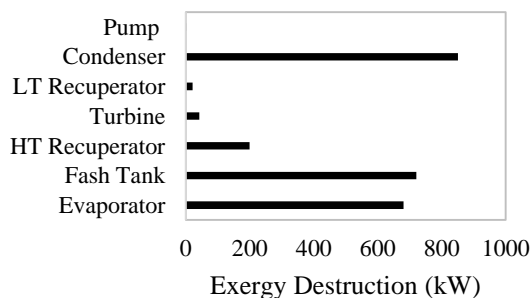


Figure 3. Comparison of Kalina Cycle Net Power for Different Evaporator Inlet Temperatures.

The final cost according to the availability of land in the vicinity of the Tarasht Power Plant with and without considering the land purchase cost is compiled in Table 9.

Exergy analysis results show that the general condenser has the highest unit exergy destruction and thus this component is the most inefficient component. The exergetic efficiency of the Kalina cycle is calculated as 45.24 %. The Exergy destruction in the different components are presented in Figure 4.

Table 9. Investment Cost Results.

	Investment cost per unit of net power (\$/kW)	Investment cost (\$)
with considering the cost of land purchase	3749	7798121
without considering the cost of land purchase	2574	5354995

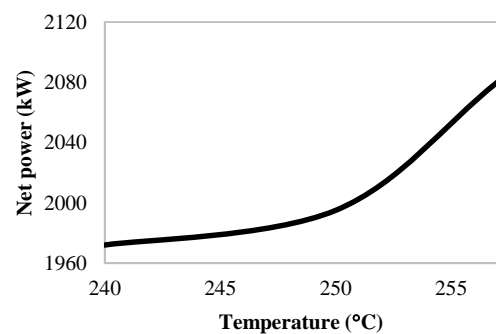


Figure 4. Exergy Destruction.

In power plants, increasing the temperature of water and producing wastewater are essential issues. In the Kalina cycle, the water used for cooling in the condenser enters with a temperature of 5 °C and leaves with a temperature of 15 °C, But there is no change in the nature of the water and only its temperature increases, according to the specifications of the condenser of the Tarasht power plant, whose inlet temperature is 15 degrees, it is possible to use the output water of the Kalina cycle condenser and avoid excess water

consumption. . The distinctive feature of this cycle is the production of electricity without the consumption of fossil fuels, the most important environmental effect of which is the saving of non-renewable resources.

The investment cost with/without considering the cost of the land purchase that was calculated earlier, the current cost with approximately 1.5% of the investment cost and the annual income of selling electricity to the grid with an electricity sale price of 1,000 Rials per kilowatt hour (each dollar is equivalent to 450,000 Rials), the system will not be profitable in the life cycle during (Assuming a life cycle of 30 years). The details of the calculation are included in Table 10.

Table 10. Cost Results.

	Investment cost (&)	Current expense (\$)	Income (\$)	Return period (Yr)
with land purchase cost	7798121	116971.815	34417.07	>30
without land purchase cost	5354995	80324.925		

4. Conclusions

To recover the waste heat from the stacks of the Tarasht power plant, the Kalina cycle (which is the same as the Rankine cycle with a difference in the working fluid i.e., water and ammonia with the distinct feature of creating a variable boiling point at constant pressure) was studied. Using Thermoflex, a unit of the Tarasht power plant was modeled, and the calculation results were compared with the available information, and validation was done. The calculation results for exhaust gas have been used as the heat source of the Kalina cycle. The results of this modeling show the production of net power of about 2080 kilowatts, which increases the net power of the entire power plant by about 5%. Exergy analysis results show that the general condenser has the highest unit exergy destruction and thus this component is the most inefficient component. The exergetic efficiency of the Kalina cycle is calculated as 45.24 %. According to the environmental analysis, this cycle will cause less damage to the environment due to the temperature reduction of the exhaust gas to the environment and the non-use of additional fossil fuel. Therefore, it is a suitable solution for using waste heat from power plants. The only point to consider in this solution (based on the economic analysis) is the high cost of startup compared to other power plant units. Therefore, by using the Kalina cycle for heat recovery in the Tarasht power station, it is possible to extract about 2 megawatts of power.

Nomenclature

h	Enthalpy (kJ/kg)
C_{inv}	Total investment cost (\$)
C_{PC}	Cost of The Power Cycle (\$)
$C_{PC.eqp}$	Cost of Power Cycle Equipment (\$)
C_{tur}	Cost of Purchasing Turbines (\$)
C_{gen}	Cost of Purchasing Pumps (\$)
C_{pu}	Cost of Purchasing Generators (\$)
C_{re}	Cost of Heat Exchangers (Recuperator, Evaporator, Condenser) (\$)
C_{sep}	Separator Cost Function (\$)
$C_{PC.misc}$	Power Miscellaneous Cost Function (\$)
C_{land}	Cost of Land Purchase (\$)
C_{cnt}	Contingent Cost (\$)
E_D	Exergy Destruction (kW)

\dot{m}	Mass flow (kg/s)
T	Temperature ($^{\circ}C$)
W	Power (kW)
w	Concentration (ppm)
ε	Exergetic efficiency (%)
μ	Chemical Potential (J/kg)

References:

- [1] J.D. Maloney, R.C. Robertson, *Thermodynamic Study of Ammonia-Water Heat Power Cycles*, Tennessee: United States Atomic Energy Commission, 1953.
- [2] A.I. Kalina, "Combined-cycle system With Novel Bottoming Cycle," *J. Eng. Gas Turbines Power*, 106, 737-742, 1984.
- [3] Y. M. El-Sayed, M. A. Tribud, "Theoretical Comparison of the Rankine and Kalina cycles," *ASME*, 1, 97-102, 1985.
- [4] A.L. Kalina, H.M. Leibowitz, "Applying Kalina Technology to a Bottoming Cycle for Utility Combined Cycles," *ASME*, doi:10.1115/87-GT-35.
- [5] N. S. Ganesh, T. Srinivas, "Power Augmentation in a Kalina Power Station for Medium Temperature Low Grade Heat," *J. Sol. Energy Eng.*, doi:10.1115/1.4023559.
- [6] F. Xu, D.Y. Goswami, "Thermodynamic Properties of Ammonia-Water Mixtures for Power-Cycle Applications," *Energy*, 24, 525-536, 1999.
- [7] R. DiPippo, "Second Law Assessment of Binary Plants Generating Power from Low-temperature Geothermal Fluids," *Geothermics*, 33, 565-586, 2004.
- [8] S. M. Sadrameli, D.Y. Goswami, "Optimum Operating Conditions for a Combined Power and Cooling Thermodynamic Cycle," *Appl. Energy*, 84, 254-265, 2007.
- [9] Z. Danxing, C. Bin, Q. Yun, J. Hongguang, "Thermodynamic Analysis of a Novel Absorption Power/Cooling Combined-Cycle," *Appl. Energy*, 83, 311-323, 2006.
- [10] H.D.M. Hettiarachchi, M. Golubovic, W.M. Worek, Y. Ikegami, "Optimum Design Criteria for an Organic Rankine Cycle Using Low-temperature Geothermal Heat Sources," *Energy*, 32, 1698-1706, 2007.
- [11] M. Liu, N. Zhang, "Proposal and Analysis of a Novel Ammonia-Water Cycle for Power and Refrigeration Cogeneration," *Energy*, 32, 961-970, 2007.
- [12] N. Zhang, N. Lior, "Methodology for Thermal Design of Novel Combined Refrigeration/Power Binary Fluid Systems," *Int. J. Refrig.*, 30, 1072-1085, 2007.
- [13] C.J. Koroneos, D.C. Rovas, "Electricity from Geothermal Energy with the Kalina Cycle an Exergy Approach," in *IEEE 2007: Int. Conf. Clean Electr. Power*, Capri, Italy, pp. 423-428, 2007.
- [14] Y. Zhang, M. He, Z. Jia, X. Liu, "First Law-based Thermodynamic Analysis on Kalina Cycle," *Front. Energy Power Eng. China*, 2, 145-151, 2008.
- [15] J. Wang, Y. Dai, and L. Gao, "Parametric Analysis and Optimization for a Combined Power and Refrigeration Cycle," *Appl. Energy* 85, 1071-1085, 2008.
- [16] S. Ogriseck, "Integration of Kalina Cycle in a Combined Heat and Power Plant, a Case Study," *Appl. Therm. Eng.*, 29, 2843-2848, 2009.
- [17] P. A. Lolos, E. D. Rogdakis, "A Kalina Power Cycle Driven by

- Renewable Energy Sources,” *Energy*, 34, 457–464, 2009.
- [18] P. Roy, M. Deilest, N. Galanis, H. Nesreddine, E. Cayer, “Thermodynamic Analysis of a Power Cycle Using a Low-temperature Source and a Binary NH₃-H₂O Mixture as Working Fluid,” *Int. J. Therm. Sci.*, 49, 48–58, 2010.
- [19] F. Sun, Y. Ikegami, B. Jia, “A Study on Kalina Solar System with an Auxiliary Super Heater,” *Renewable Energy*, 41, 210–219, 2012.
- [20] J. Wang, Z. Yan, E. Zhou, Y. Dai, “Parametric Analysis and Optimization of Kalina Cycle Driven by Solar Energy,” *Appl. Therm. Eng.*, 50, 408–415, 2013.
- [21] A. Modi, F. Hglind, “Performance Analysis of a Kalina Cycle for a Central Receiver Solar Thermal Power Plant with Direct Steam Generation,” *Appl. Therm. Eng.*, 65, 201–208, 2014.
- [22] E. Wang, Z. Yu, F. Zhang, “Investigation on Efficiency Improvement of a Kalina Cycle by Sliding Condensation Pressure Method,” *Energy Convers. Manage.*, 151, 123–135, 2017.
- [23] S. Zhang, Y. Chen, J. Wu, Z. Zhu, “Thermodynamic Analysis on a Modified Kalina Cycle with Parallel Cogeneration of Power and Refrigeration,” *Energy Convers. Manage.*, 163, 1–12, 2018.
- [24] K. Kim, C. Han, H. KO, “Comparative Thermodynamic Analysis of Kalina and Kalina Flash Cycles for Utilizing Low-Grade Heat Sources,” *Energies*, doi:10.3390/en11123311.
- [25] G. Salehi, M. H. KhoshgoftarManesh, A. Alahyari, “Thermodynamic and Exergoeconomic Evaluation of Heat Recovery of Gas Refinery Steam Network Using Organic Rankine Cycle and Kalina Cycle with Different Fluids,” *J. Energy Eng.*, doi:10.1061/(ASCE)EY.1943-7897.0000650.
- [26] *Thermoflow Software (Version 23.0.1)*. Available: www.thermoflow.com (February 25, 2013).
- [27] H. Ajami, *Design and Compilation of Maintenance and Repair Information System of Tarasht Power Plant*, Tehran: Management Research and Training Institute Attached to the Ministry of Energy, 2014.
- [28] *Detailed Statistics of Iran's Electricity Industry, Especially Strategic Management in 2015*. Available: [https://isn.moe.gov.ir/getattachment/260f0530-dc7a-476a-a756-aa8176395352/%D8%A7%D9%85%D8%A7%D8%B1-%D8%AA%D9%81%D8%B5%D9%8A%D9%84%D9%8A-%D8%B5%D9%86%D8%B9%D8%AA-%D8%A8%D8%B1%D9%82-%D8%A7%D9%8A%D8%B1%D8%A7%D9%86-%D9%88%D9%8A%DA%98%D9%87-%D9%85%D8%AF%D9%8A%D8%B1%D9%8A%D8%AA-%D8%B1%D8%A7%D9%87%D8%A8%D8%B1%D8%AF%D9%8A-\(1\) \(2015\)](https://isn.moe.gov.ir/getattachment/260f0530-dc7a-476a-a756-aa8176395352/%D8%A7%D9%85%D8%A7%D8%B1-%D8%AA%D9%81%D8%B5%D9%8A%D9%84%D9%8A-%D8%B5%D9%86%D8%B9%D8%AA-%D8%A8%D8%B1%D9%82-%D8%A7%D9%8A%D8%B1%D8%A7%D9%86-%D9%88%D9%8A%DA%98%D9%87-%D9%85%D8%AF%D9%8A%D8%B1%D9%8A%D8%AA-%D8%B1%D8%A7%D9%87%D8%A8%D8%B1%D8%AF%D9%8A-(1) (2015)).
- [29] R. H. Khoshkho, H. MohagheghNejad, “Boiler Combustion Modeling in the Repowering Design of Tarasht Power Plant by Hot wind Box Method,” *31st International Electricity Conference, Tehran*, pp. 1–8, 2016.
- [30] A. Modi (2015), *Numerical Evaluation of the Kalina Cycle for Concentrating Solar Power Plants (PhD Thesis)*, DTU Mechanical Engineering, Denmark.
- [31] A. Modi, M. R. Kærn, J. G. Andreasen, F. Haglind, “Thermoeconomic Optimization of a Kalina Cycle for a Central Receiver Concentrating Solar Power Plant,” *Energy Convers. Manage.*, 115, 276–287, 2016.
- [32] H. GAO, F. Chen, “Thermo-Economic Analysis of a Bottoming Kalina Cycle for Internal Combustion Engine Exhaust Heat Recovery,” *Energies*, 11, doi:10.3390/en11113044.
- [33] R. Smith, *Chemical Process - Design and Integration*, West Sussex: John Wiley & Sons, Ltd., 2005.
- [34] *Index Values as Published by Marshall Swift Valuation Services* Available: https://www.lincolnst.edu/sites/default/files/sources/events/martinez_marshall_and_swift.pdf (2018).
- [35] S. Sadri, R.H. Khoshkhoo, M. Ameri, “Optimum Exergoeconomic Modeling of Novel Hybrid Desalination System (MEDAD-RO),” *Energy*, 149, 74–83, 2018.
- [36] M. Babaelahi, S. Sadri, E. Rafat, “Exergy Cost Accounting and Thermoeconomic Diagnosis for Double-Solar-Gas-Turbine System (DSGT),” *Energy Sources, Part A*, doi: 10.1080/15567036.2019.1624892.

Research Article

Design of a Coal Drying System with Solar-Assisted Heat Pump and Waste Heat Utilisation

*M. Ökten 

Department of Energy Systems Engineering, Manisa Celal Bayar University
E-mail: mert.okten@cbu.edu.tr

Received 15 December 2022, Revised 14 March 2023, Accepted 29 March 2023

Abstract

The increase in global energy demand has directed researchers towards making low-quality coals into an environmentally friendly energy source by reducing their high moisture content. Drying coal is a high-energy and time-consuming process, so reducing the required energy and drying time is crucial for drying technology. Coal drying increases the thermal value of coal and makes it easier to transport. In this study, a coal drying system was designed using waste heat recovery systems, R-134a refrigerant as working fluid, air source heat pumps, and vacuum tube solar collectors to provide hot air. Firstly, the moisture content of the coal and the desired moisture content after drying were determined, and then the heat required to dry the coal was calculated. Next, the capacity of the solar collector required to provide the necessary heat to the heat pump was determined, and the type and capacity of the heat pump that could produce the required heat were selected. Finally, the coal dryer was designed based on the specific requirements of the power plant and the type of coal used. As a result, the coal drying system designed with solar-assisted heat pumps and waste heat utilization can increase the efficiency of coal-fired power plants by reducing the moisture content of coal before combustion.

Keywords: Coal; drying; heat pump; solar energy; waste heat recovery.

1. Introduction

Drying is a high-energy and time-consuming process, so reducing the amount of energy required and the drying time is an important issue for drying technology. The energy required for drying in drying systems is crucial in evaporating moisture from the product. Heat transfer in a drying process can be achieved through conduction, convection, and radiation. In classical coal dryers, heat transfer occurs through conduction and convection [1], but in recent years, radiation heating methods such as microwave [2], infrared radiation [3], ultraviolet, and radio waves [4] have been given more attention, especially due to their low energy consumption.

In a study conducted by researchers in [5], using a pilot-scale fluidized bed dryer, they examined the effect of fluidization velocity on coal classification and drying. They found that coal dried quickly, and the moisture content of the product particles was below 2%, and the optimum classification efficiency was 92% by weight at a fluidization velocity of 2.2 m/s. In another study where low-grade coal with high moisture content was dried in a new disc dryer equipped with heating plates and rotary blades, the moisture content of the raw coal dropped from 34% to below 3% within 5 minutes at a heating plate temperature of 150°C [6]. In [7], the drying performance of a solar-biomass hybrid batch type horizontal fluidized bed dryer with a multi-stage heat exchanger and a heat pump for drying rice was investigated, and it was found that the heat recovery drying system provided a thermal energy saving of approximately 46.7% compared to the non-heat recovery drying system. In

[8], a numerical model was proposed to estimate the energy performance of a solar energy dryer supported by a heat pump under terrestrial climates. It was confirmed that conventional solar dryers are not suitable for terrestrial climates with low ambient temperatures, and the heat pump dryer reduced the initial moisture content of the product from approximately 74% to around 19% in 21 hours.

In the study where a convective closed-loop solar-assisted heat pump dryer was designed for both simple heat pump drying and solar-assisted heat pump drying modes, it was concluded that the solar-assisted heat pump drying system performed better in every aspect [9]. In [10], dual-pass parallel flow, compartmentalized parallel flow, and non-compartmentalized parallel flow solar air collectors were designed for drying application, and celery roots were dried and examined as the product. It was observed that the highest instantaneous efficiency was achieved in the dual-pass parallel flow solar air collector (84.30%). In [11], researchers compared parallel flow (PPSAH), double-pass (DPSAH), and V-groove type (VTPSAH) solar-powered air heaters under the same climate conditions. They obtained exergy efficiency values in the range of 14.62–18.95% (VTPSAH), 12.28–15.68% (DPSAH), and 6.68–9.74% (PPSAH) using numerical and experimental approaches. In a study where vertical photovoltaic-thermal (PVT) solar dryers were analyzed using numerical and experimental approaches and fins were integrated on the absorber plate and PV panel to increase heat transfer, it was found that the thermal efficiency values of the vertical PVT collectors without fins and with fins were in the ranges of 47.46–

54.86% and 50.25-58.16%, respectively, and that high air flow rate significantly improved drying performance in the finned vertical dryer [12]. In [13], V-groove three-pass (V-TPSAH) and V-groove four-pass (V-QPSAH) solar-powered air heaters were designed for drying municipal sewage sludge. Two different types of drying chambers (DC-I: conventional, DC-II: solar absorber) were integrated into each solar-powered air heater. According to experimental results, the average efficiency of the solar-powered air heater was found to be in the range of 70.12–81.70%.

Table 1 presents some products dried in heat pump, solar-assisted, and waste heat recovery drying systems. Energy consumption reductions of these new type dryers compared to traditional drying systems are shown.

Table 1. Some Dryer Types and Dried Products.

Product	Dryer Type	Reduction of energy consumption (%)	COP	Reference
Daphne	Heat pump, controlled by PLC	25	3.2	[14]
Melon	Infrared, solar energy, waste heat recovery assisted	33.4	-	[15]
Stale bread	Infrared, with heat pump	43.2	3.7	[16]
Mint leaf	Heat pump, waste heat recovery	48	3.94	[17]
Kiwi	Infrared, waste heat recovery	32.17	-	[18]
Carrot	Heat pump and Infrared, assisted heat pump with heat pump	50 & 22	2.96	[19]
Apple	Heat pump	-	3.02	[20]
Pumpkin seeds	Infrared, heat pump, PLC controlled	-	4.86	[21]
Grape pulp	Heat pump	51	3.28	[22]
Lemon	Infrared, with heat pump	11	2.74	[23]
Mint leaf & Apple	Solar air dryer and Infrared assisted solar air dryer	26.46 & 8.59	2.43	[24]
Mint leaf	PV/T with heat pump	12.27 (electrical); 53.66 (thermal)	4.18	[25]
Honey	Heat pump	27.11	2.65	[26]
Walnut	Heat pump, waste heat recovery and Infrared, waste heat recovery	6.54 & 7.94	3.34 & 3.14	[27]

Due to their porous structure and clay-based minerals, coals contain a significant amount of moisture. Lignites, which have high moisture content (40-60%), are also defined as low-quality coal because of their low heating value [28]. While most of the moisture, which is eliminated through processes such as filtration and centrifugation, is removed chemically bound with the coal, the residual moisture content can be removed by drying. A 1% reduction in moisture content results in an average increase of 40-60 kcal/kg in the heating value of coal [29]. Moisture not only adds unnecessary weight during transportation and storage of coal, but also increases operational costs. It decreases the

friability of coal and makes blending operations more difficult [30]. Research has shown that lignites spontaneously ignite at low temperatures, around 40-50°C [31-33]. A study was conducted on Canadian lignite coal, which was dried using hydrothermal processing, vacuum drying, and hot air drying methods at different temperatures. Hydrothermal processing reduced the moisture content from 34% to 9.65% in 30 minutes at 325°C. On the other hand, moisture content reduction was similar in the 7-hour vacuum drying process at 70°C and the 110-minute hot air drying method [34]. In a pilot plant similar to a cyclone with a conical tube, a computational fluid dynamics study demonstrated a significant reduction in moisture content, up to 86.37% under optimal conditions, uniform liquid distribution, and significant volatile combustion [35]. When coal with high moisture content is burned in public utility boilers, a significant portion of the energy (7-10%) is consumed to evaporate the moisture, leading to decreased plant efficiency, increased fuel consumption, and higher flue gas emissions [36]. The moisture content of lignite coal from the Victorian era can reach up to 66% [37], while anthracite can contain as little as 0.6% [38]. Some Turkish and Czech Republic lignites contain 6%, and Australian lignite coal contains approximately 71% [39]. In conventional lignite power plants, up to 60% moisture content lignite coal is burned, and approximately 20% of the fuel energy is used in pre-combustion drying [40]. If moisture can be economically reduced, lignite coal's energy content can be increased and can compete with bituminous coal at an equal level [41]. Therefore, removing moisture from lignite coal is a crucial parameter.

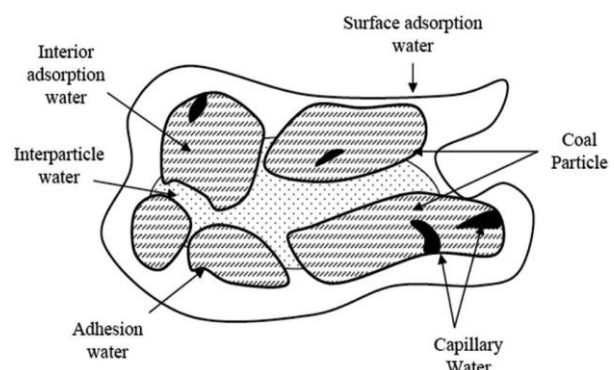


Figure 1. Different forms of water in the coal.

Different moisture conditions present in coal are shown in Figure 1 [36]. In each coal particle, internal adsorbed water is present between micro-pores and micro-capillaries, called natural moisture, which can be removed by thermal or chemical methods. Surface adsorbed water is present on the particle surface and is also considered natural moisture, which can be removed by thermal or chemical methods. Capillary water is natural moisture found in the capillary ducts of coal particles and can be removed by thermal or chemical methods.

In this study, a drying system will be designed for the Manisa province Soma Kırakdere coal using waste heat recovery, the refrigerant fluid R-134a as the working fluid in a heat pump, and heat from vacuum-tube solar collectors with heat pipes. The drying chamber and the placement system for the wet product will be dimensioned and the drying system will be designed. The aim is to determine the power of the equipment in the drying system, the theoretical

drying time of the coal, the specific humidity ratio extracted from the system, and the drying coefficient of the dryer.

2. Material & Method

The type of coal to be used in drying is the washed lignite coal, with hazelnut size, extracted from Kırakdere location in Soma district of Manisa province, and its properties are given in Table 2 [42].

Table 2. Properties of Washed Hazelnut Charcoal in Soma Kırakdere.

Variable	Industry	Corporate housing	Individual housing
Size (mm)	10 - 18	10 - 18	10 - 18
Humidity (%)	17.25	19	17
Ash (%)	11.47	16	17
Volatile matter (%)	35.34	35	40
Lower calorific value (kcal/kg)	4776	4750	4650
Upper calorific value (kcal/kg)	5077	5100	4830

On average, a hazelnut-sized coal is 0.015 m in diameter and weighs 0.017 kg [42]. Kırakdere Coal has low ash (11.47%) and sulfur (0.96%) content, and has more efficient values than many fossil fuels in the industry, making it suitable for use in industrial facilities and the most appropriate and economical solution against the increasing heating and heating costs due to the widespread use of natural gas [43]. The specifications of the coal to be dried in the laboratory type drying system with a capacity of 75 kg and the coal table to be used in the drying chamber are given in Table 3.

Table 3. Specifications of The Coal to Be Dried and The Coal Table to Be Used.

Variable	Value	Unit
Coal size (diameter)	0.015	m
Wet weight of coal (grain)	0.017	kg
Wet weight of coal	75	kg
Coal quantity	4412	Piece
Coal bottom area	0.0007	m ²
Coal table top	0.7	m
Coal basin size	0.5	m
Coal field area	0.35	m ²
Coal basin	9	Piece

The materials and specifications used in the design of the drying chamber are shown in Table 4 [44, 45].

Table 4. Materials and Properties of the Drying Chamber.

Type of material	Thickness (m)	Thermal conductivity (W/mK)	Specific heat (kJ/kg°C)	Density (kg/m ³)
Exterior plaster lime cement	0.03	0.87	1.044	2100
Aerated concrete	0.2	0.11	1.17	350
Polyurethane insulation	0.03	0.030	1.05	42
Interior plaster lime plaster	0.02	0.7	0.828	2200

The system includes a solar collector, a heat pump, an air handling unit a waste heat recovery system, and a coal dryer.

Solar collector is used to collect solar radiation and convert it into heat energy. The collected heat is then transferred to the heat pump through a heat exchanger. Heat

pump is used to increase the temperature of the air used for drying the coal. It can also extract heat from the waste heat sources and reuse it for the drying process. Air handling unit is used to distribute the heated air to the coal drying system. Coal dryer is used to remove the moisture from the coal. The heated air is blown into the coal dryer to dry the coal. Waste heat recovery system such as the exhaust gas from the combustion of coal or the waste heat from the heat pump, can be recovered and reused for the drying process.

The steps shown in Table 5 [19, 46-50] were applied for data analysis in the solar energy-supported heat pump dryer design.

Table 5. Equations Used in Data Analysis.

Step of data analysis	Equality	Equality number
Design of the drying chamber	The amount of heat energy required to heat the kiln walls to the system temperature of the drying air and to maintain that temperature (q_1)	$m_1 \times c_1 \times \Delta T$ (1)
	Amount of energy required to heat the drying air is this amount of energy (q_2)	$\rho \times V \times c_2 \times \Delta T$ (2)
	The energy required to heat the products to be dried (q_3)	$m_w \times c_3 \times \Delta T$ (3)
	The energy required to evaporate the moisture contained in the dried product (q_4)	$m_{wt} \times \theta_o$ (4)
	The energy required to cover the heat losses from the oven to the ambient air (q_5)	$K \times A_c \times \Delta T$ (5)
	Total heat transfer coefficient (K)	$\frac{1}{\frac{1}{h_i} + \frac{d_n}{k_n} + \frac{1}{h_d}}$ (6)
Calculation of the final moisture content of the coal	Moisture content by dry weight (MC_{dw})	$\frac{M_w - M_d}{M_d}$ (7)
	Moisture content by wet weight (MC_{ww})	$\frac{M_w - M_d}{M_w}$ (8)
Calculation of the payload from solar energy (\dot{Q}_S)		$\dot{V} \times \rho \times c \times \Delta T$ (9)
Electrical energy consumed by the fan ($\dot{W}_{f,s}$)		$\frac{\dot{Q}_S - \eta \times I \times A_a}{\eta}$ (10)
Heat pump calculation	Heat exchanger equation	$\dot{Q}_C = 1.25 \times \dot{Q}_{tot}$ (11)
	Condenser load (\dot{Q}_C)	$\dot{m}_{R-134a} \times (h_4 - h_1)$ (12)
	Evaporator load (\dot{Q}_E)	$\dot{m}_{R-134a} \times (h_2 - h_3)$ (13)
	Compressor load (\dot{W}_{comp})	$\dot{m}_{R-134a} \times (h_4 - h_3)$ (14)
	Heating coefficient of influence (COP_{sys})	$\frac{\dot{Q}_C}{\dot{W}_{comp} + \dot{W}_{fan}}$ (15)
Specific moisture absorption rate ($SMER$)		$\frac{\dot{m}_{wt}}{\dot{W}_{comp} + \dot{W}_{fan}}$ (16)

3. Findings

The design of the system includes the following steps:

- Determination of the heating requirements of the coal dryer; the amount of heat required for drying the coal depends on the coal's moisture content, initial and final temperatures, and mass flow rate.
- Sizing of the solar collector; it depends on the heating requirements of the coal dryer and local solar radiation conditions.
- Sizing of the heat pump; it depends on the heating requirements of the coal dryer and the temperature increase required by the heat pump.
- Design of the waste heat recovery system; it is designed to recover as much waste heat as possible from the heat pump and other sources.
- Design of the control system; it is designed to optimize the operation of the system and ensure that the coal drying process is efficient and effective.

The ideal moisture content in coal stocks should be between 8-10% [51]. By using Eqs. (7) and (8), it was found that 5.77 kg of water evaporates from the coal. If the drying air temperature is at 35 °C [52], it was calculated that the moisture content will decrease from 17% to 8% in 95 minutes [53].

The system diagram is shown in Figure 2. The mechanical system that consumes three energies, including a fan, compressor, and pump, and three heat exchangers (condenser and evaporator), including a plate heat exchanger used in waste heat recovery, an expansion valve, temperature and relative humidity sensors, a vacuum tube solar collector, a drying chamber, a product tray, and a weight scale are included in the system. An electronic control panel is installed for controlling the drying air. The temperature of the drying chamber is controlled by adjusting the heat pump unit to achieve uniform drying conditions (Table 6).

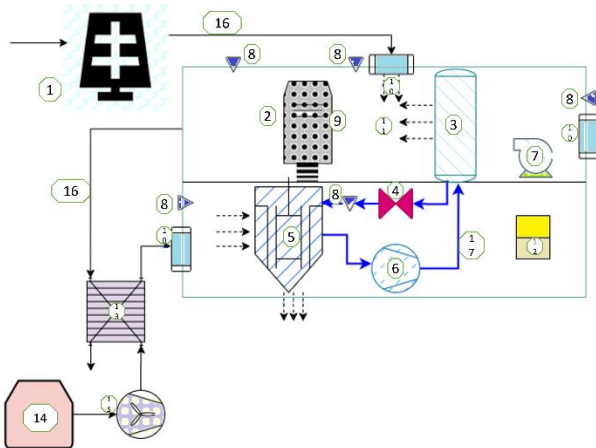


Figure 2. System overview.

Table 6. System Equipment.

Number	Name	Number	Name
1	Solar collector	10	Fresh air
2	Drying chamber	11	Mixed air
3	Condenser	12	Electrical Control Unit
4	Throttling valve	13	Plate heat changer
5	Evaporator	14	Waste heat plant
6	Compressor	15	Power plant fan
7	Fan	16	Air line
8	Thermo-Hygrometer	17	Refrigerant line
9	Coal graine		

The height of each tray in the drying chamber is 0.05 m. In the design, 0.05 m gaps were left at both ends of the trays, and a drying chamber of 0.8 m × 0.6 m × 0.7 m was created.

As seen on the psychrometric chart given in Figure 3, air entered the drying system at point T_i with 46% relative humidity and a temperature of 35°C [54]. After going through the cooling and dehumidification processes with 80% moisture removal efficiency, the air left the drying chamber at point T_o with a temperature of 27°C. The mass of the circulating air (m₂) was found to be 2165.6 kg.

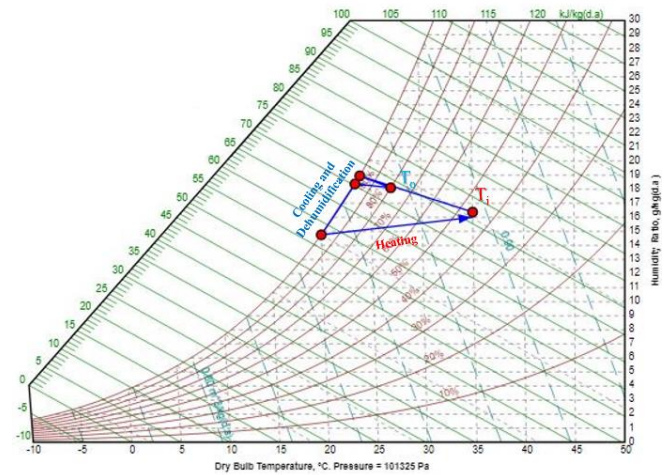


Figure 3. Psychrometric chart.

To heat the air in the drying system, a vacuum tube solar collector with 57.16% efficiency was used [55]. The power of the vacuum tube solar collector should be enough to compensate for the heat loss in the drying system. The values of the heat calculation for the drying chamber are shown in Table 7.

Table 7. Calculation of The Drying Room Temperature.

Variable	Value	Unit	Variable	Value	Unit
t	95	min	A _a	60.24	m ²
c ₂ [56]	1.0057	kJ/kg°C	A _d	0.48	m ²
c ₃ [57]	1.883	kJ/kg°C	h _i	7	W/m ² K
m _{wt}	5.77	kg	h _o	13	W/m ² K
m ₂	2165.6	kg	K	0.322	W/m ² K
Q ₀	2257	kJ/kg	q ₁	76496.749	kJ
I [58]	560	W/m ²	q ₂	17423.551	kJ
T _i	35	°C	q ₃	2570.295	kJ
T _a [59]	16.8	°C	q ₄	13022.890	kJ
T _o	27	°C	q ₅	96.204	kJ
ρ	1.2	kg/m ³	Q̇ _{tot}	19.230	kW

An 80% effective heat exchanger was used for energy recovery from waste heat (50°C [59]), and the system air was heated from 27°C to 35°C.

The condenser capacity was taken as 25% more than the total energy required for the drying system to compensate for compressor resting [48]. R-134a was used as the refrigerant in the heat pump system. The heat pump calculation is shown in Table 8.

Table 8. Calculation of The Heat Pump.

Variable	Value	Unit	Variable	Value	Unit
T_1	10	°C	\dot{m}_{R-134a}	0.198	kg/s
T_2	55	°C	\dot{m}_a	1203.111	kg/h
T_3	45	°C	c_a	1.005	kJ/kg°C
T_4	5	°C	P_{atm}	101.325	kPa
P_1	349.9	kPa	η_{ws}	0.80	
P_2	1163	kPa	$\eta_{w,c}$	0.95	
h_1	253.34	kJ/kg	$\eta_{w,e}$	0.76	
h_2	284.17	kJ/kg	\dot{Q}_C	24.037	kW
h_{2s}	278	kJ/kg	\dot{Q}_E	27.199	kW
h_f, h_3, h_4	115.8	kJ/kg	\dot{W}_{comp}	6.096	kW
h_g	237.35	kJ/kg	\dot{W}_{fan} [60]	0.25	kW
s_1, s_{2s}	0.9288	kJ/kgK	COP	3.788	

When the product is dried by convection, heat transfer occurs from the surface to the inside, while evaporation occurs from the cells inside to the surface. The specific moisture extraction rate from the dryer (Eq. 16) was calculated as 910 g water/kWh.

4. Conclusions

In this study, a laboratory-scale drying system was designed for the drying of Soma Kırakdere coal in Manisa province under summer conditions using waste heat recovery, solar energy, and a heat pump. The design of a coal drying system with solar-assisted heat pump and waste heat utilization involves integrating various technologies to improve the efficiency of coal-fired power plants. The design should consider the specific requirements of the power plant and the coal being used to ensure optimal performance.

Overall, a coal drying system with waste heat recovery, solar energy support, and heat pump can be an important solution to increase the efficiency of coal-fired power plants and save energy. This system can help make low-quality coals into a more environmentally friendly energy source. Designed using solar energy, waste heat recovery, and heat pump, this system can reduce the energy required to provide hot air, which can shorten the drying time and reduce energy consumption. In addition, greenhouse gas emissions can be reduced thanks to this system. Therefore, a coal drying system with waste heat recovery, solar energy support, and heat pump can be an important step towards a more efficient, environmentally friendly, and sustainable coal-fired power plant.

Nomenclature

A_a	Air duct arms area (m ²)
A_d	Dryer area (m ²)
c_1	Total specific heat of wall materials (kJ/kg°C)
c_2	Specific heat of drying air (kJ/kg°C)
c_3	Specific heat of coal (kJ/kg°C)
h_1	Condenser outlet enthalpy value (kJ/kg)
h_2	Throttling valve outlet enthalpy value (kJ/kg)
h_{2s}	Throttling valve outlet isentropic enthalpy value (kJ/kg)
h_3	Evaporator outlet enthalpy value (kJ/kg)
h_4	Compressor outlet enthalpy value (kJ/kg)

I	Value of solar radiation (W/m ²)
M_i	Wet weight (kg)
M_d	Dry weight (kg)
m_1	Mass of the wall (kg)
m_2	Mass of air to circulate in the plant (kg)
m_{wt}	Water to be extracted (kg)
P_{atm}	Atmospheric pressure (kPa)
P_s	Saturation pressure of water vapor (kPa)
\dot{Q}_C	Condenser load (kW)
\dot{Q}_E	Evaporator load (kW)
s_1	Condenser outlet entropy value (kJ/kgK)
$SMER$	Specific moisture extraction rate (g water/kWh)
T_a	Air temperature (°C)
T_1	Condenser outlet temperature (°C)
T_2	Throttling valve outlet temperature (°C)
T_3	Evaporator outlet temperature (°C)
T_4	Compressor outlet temperature (°C)
V	Drying air volume (m ³)
\dot{V}	Total air flow (m ³ /s)
\dot{W}_{comp}	Compressor load (kW)
θ_o	Latent heat of evaporation at evaporation temperature (kJ/kg)
ρ	Density of air (kg/m ³)
$\eta_{w,c}$	Condenser efficiency
$\eta_{w,e}$	Evaporator efficiency
φ	Relative humidity

References:

- [1] G.V. Kuznetsov, G.S. Nyashina, P.A. Strizhak, T.R. Valiullin, "Experimental Research into the Ignition and Combustion Characteristics of Slurry Fuels Based on Dry and Wet Coal Processing Waste," *J. of the Energy Inst.*, 97, 213-224, 2021.
- [2] H. Hacızfazoğlu, B. Bolat, "Linyit Kömürün Kurutulması için Karbonik Film Teknolojili Yeni Bir Kurutucu Tasarımı," *Fırat Üniversitesi Müh. Bil. Der.*, 33 (1), 173-183, 2021.
- [3] T. Hosseini, L. Zhang, "Process Modeling and Techno-Economic Analysis of a Solar Thermal Aided Low-Rank Coal Drying-Pyrolysis Process," *Fuel Proces. Tech.*, 220, 106896, 2021.
- [4] H. Kim, J. Choi, H. Lim, J. Song, "Liquid Carbon Dioxide Drying and Subsequent Combustion Behavior of High-Moisture Coal at High Pressure," *App. Therm. Eng.*, 207, 118182, 2022.
- [5] Q. Chen, J. Hu, H. Yang, D. Wang, H. Liu, X. Wang, H. Chen, "Experiment and Simulation of the Pneumatic Classification and Drying of Coking Coal in a Fluidized Bed Dryer," *Chem. Eng. Sci.*, 214, 115364, 2020.
- [6] S.H. Moon, I.S. Ryu, S.J. Lee, T.I. Ohm, "Optimization of Drying of Low-Grade Coal with High Moisture Content Using a Disc Dryer," *Fuel Proces. Tech.*, 124, 267-274, 2014.
- [7] M. Yahya, A. Rachman, R. Hasibuan, "Performance Analysis of Solar-Biomass Hybrid Heat Pump Batch-Type Horizontal Fluidized Bed Dryer Using Multi-Stage Heat Exchanger for Paddy Drying," *Energy*, 254(B), 124294, 2022.

- [8] M. Kuan, Y. Shakir, M. Mohanraj, Y. Belyayev, S. Jayaraj, A. Kaltayev, "Numerical Simulation of a Heat Pump Assisted Solar Dryer for Continental Climates," *Renew. Energy*, 143, 214-225, 2019.
- [9] A. Singh, J. Sarkar, R.R. Sahoo, "Experimentation on Solar-Assisted Heat Pump Dryer: Thermodynamic, Economic and Exergoeconomic Assessments," *Solar Energy*, 208, 150-159, 2020.
- [10] A. Khanlari, H.Ö. Güler, A.D. Tuncer, C. Şirin, Y.C. Bilge, Y. Yılmaz, A. Güngör, "Experimental and Numerical Study of the Effect of Integrating Plus-Shaped Perforated Baffles to Solar Air Collector in Drying Application," *Renew. Energy*, 145, 1677-1692, 2020.
- [11] A.D. Tuncer, A. Khanlari, A. Sözen, E.Y. Gürbüz, C. Şirin, A. Güngör, "Energy-Exergy and Enviro-Economic Survey of Solar Air Heaters with Various Air Channel Modifications," *Renew. Energy*, 160, 67-85, 2020.
- [12] E. Çiftçi, A. Khanlari, A. Sözen, İ. Aytaç, A.D. Tuncer, "Energy and Exergy Analysis of a Photovoltaic Thermal (PVT) System Used in Solar Dryer: A Numerical and Experimental Investigation," *Renew. Energy*, 180, 410-423, 2021.
- [13] A. Khanlari, A. Sözen, F. Afshari, C. Şirin, A.D. Tuncer, A. Güngör, "Drying Municipal Sewage Sludge with V-Groove Triple-Pass and Quadruple-Pass Solar Air Heaters Along with Testing of a Solar Absorber Drying Chamber," *Sci. of The Total Env.*, 709, 136198, 2020.
- [14] M. Aktaş, S. Şevik, M.B. Özdemir, E. Gönen, "Performance Analysis and Modeling of a Closed-Loop Heat Pump Dryer for Bay Leaves Using Artificial Neural Network," *App. Therm. Eng.*, 87, 714-723, 2015.
- [15] M. Aktaş, S. Şevik, A. Amini, A. Khanlari, "Analysis of Drying of Melon in a Solar-Heat Recovery Assisted Infrared Dryer," *Solar Energy*, 137, 500-515, 2016.
- [16] M. Aktaş, S. Şevik, B. Aktekel, "Development of Heat Pump and Infrared-Convective Dryer and Performance Analysis for Stale Bread Drying," *Energy Conv. and Manag.*, 113, 82-94, 2016.,
- [17] M. Aktaş, A. Khanlari, B. Aktekel, A. Amini, "Analysis of a New Drying Chamber for Heat Pump Mint Leaves Dryer," *Int. J. of Hydrogen Energy*, 42, 18034-18044, 2017.
- [18] M.B. Özdemir, M. Aktaş, S. Şevik, A. Khanlari, "Modeling of a Convective-Infrared Kiwifruit Drying Process," *Int. J. of Hydrogen Energy*, 42, 18005-18013, 2017.
- [19] M. Aktaş, A. Khanlari, A. Amini, S. Şevik, "Performance Analysis of Heat Pump and Infrared-Heat Pump Drying of Grated Carrot Using Energy-Exergy Methodology," *Energy Conv. and Manag.*, 132, 327-338, 2017.
- [20] M. Tokdemir, K. Boran, M. Aktaş, S.P. Alkaç, "Isı Pompalı Kurutma Tekniği ile Toz Elma ve Elma Cipsi Üretimi: Performans Analizi," *Poli. Der.*, 21(4), 887-894, 2018.
- [21] G. Ünlü, K. Boran, M. Aktaş, A. Khanlari, "Infrared Enerjili - Isı Pompalı PLC Kontrollü Bir Kurutucuda Kabak Çekirdeği Kurutulması," *Poli. Der.*, 21(3), 519-525, 2018.
- [22] L. Taşeri, M. Aktaş, S. Şevik, M. Gülcü, G. Uysal Seçkin, B. Aktekel, "Determination of Drying Kinetics and Quality Parameters of Grape Pomace Dried with a Heat Pump Dryer," *Food Chem.*, 260, 152-159, 2018.
- [23] S.P. Alkaç, K. Boran, M. Aktaş, M. Tokdemir, "Isı Pompalı İnfrared Kurutucuda Dilimlenmiş Limonun Kurutulmasının Performans Analizi," *Gazi Müh. Bil. Der.*, 5(2), 128-137, 2019.
- [24] S. Şevik, M. Aktaş, E.C. Dolgun, E. Arslan, A.D. Tuncer, "Performance Analysis of Solar and Solar-Infrared Dryer of Mint and Apple Slices Using Energy-Exergy Methodology," *Solar Energy*, 180, 537-549, 2019.
- [25] M. Koşan, M. Demirtaş, M. Aktaş, E. Dişli, "Performance Analyses of Sustainable PV/T Assisted Heat Pump Drying System," *Solar Energy*, 199, 657-672, 2020.
- [26] G. Karaca, E.C. Dolgun, M. Aktaş, "Balın Kurutulması için Enerji Verimli ve Hijyenik Yeni Bir Sistem Tasarımı," *Poli. Der.*, 23(3), 713-719, 2020.
- [27] G. Karaca Dolgun, M. Aktaş, E.C. Dolgun, "Infrared Convective Drying of Walnut With Energy-Exergy Perspective," *J. of Food Eng.*, 306, 110638, 2021.
- [28] F. Gacal. "Lignite coal: Health Impacts and Recommendations from the Health Industry." Health and Environment Alliance (HEAL). <https://www.env-health.org/wp-content/uploads/2018/12/HEAL-Lignite-Briefing-TR-web.pdf> (accessed Jan. 10, 2022).
- [29] M. Karthikeyan, W. Zhonghua, A.S. Mujumdar, "Low-Rank Coal Drying Technologies Current Status and New Developments," *Dry. Tech.*, 27, 403-415, 2009.
- [30] Pikon, J., Mujumdar, A.S. "Drying of Coal", In *Handbook of Industrial Drying*, 3rd Ed; Mujumdar, A.S., Ed.; CRC Press: Boca Raton, FL, 993-1016, 2006.
- [31] L. Yuan, A.C. Smith, "The Effect of Ventilation on Spontaneous Heating of Coal," *J. of Loss Prev. in the Process Indust.*, 25, 131-137, 2012.
- [32] G. Qi, D. Wang, K. Zheng, J. Xu, X. Qi, X. Zhong, "Kinetics Characteristics of Coal Low-Temperature Oxidation in Oxygen-Depleted Air," *J. of Loss Prev. in the Process Indust.*, 35, 224-231, 2015.
- [33] Rahman, M., Kurian, V., Pudasainee, D., and Gupta, R. "A Comparative Study on Lignite Coal Drying by Different Methods," *Int. J. of Coal Prep. and Util.*, 40(2), 90-106, 2020.
- [34] Halim, A., Widyanti, A.A., Wahyudi, C.D., Martak, F., Septiani, E.L. "A Pilot Plant Study of Coal Dryer: Simulation and Experiment," *ASEAN J. of Chem. Eng.*, 22(1), 124-140, 2022.
- [35] Karthikeyan, M., Zhonghua, W., Mujumdar, A. S., "Low-Rank Coal Drying Technologies Current Status and New Developments," *Dry. Tech.*, 27, 403-415, 2009.
- [36] Li, C. Z.. "Advances in The Science of Victorian Brown Coal", Oxford: Elsevier, 2004.

- [37] Bratek, K., Bratek, W., Gerus-Piasecka, I., Jasięko, S., Wilk, P., "Properties and Structure of Different Rank Anthracites," *Fuel*, 81, 97–108, 2002.
- [38] Osman, H., Jangam, S. V., Lease, J. D., Mujumdar, A. S., "Drying of Low-Rank Coal (LRC): A Review of Recent Patents and Innovations," *M3TC Report*, National University of Singapore, 2011.
- [39] Jentzsch, B., Höhne, O., Porsche, T., "Experiences with Drying of Lignite in a Pressurized Steam Fluidized Bed Pilot Plant," *2nd Oxyfuel Combustion Conference, Queensland*, Australia, Sep 12–16, 2011.
- [40] Willson, W. G., Walsh, D., Irwinc, W., "Overview of Low-Rank Coal (LRC) Drying," *Int. J. of Coal Prep. and Util.*, 18, 1–15, 1997.
- [41] Z. Li, Y. Zhang, X. Jiang, Y. Zhang, L. Chang, "Insight into the Intrinsic Reaction of Brown Coal Oxidation at Low Temperature: Differential Scanning Calorimetry Study," *Fuel Process. Tech.*, 147, 64–70, 2016.
- [42] İnci Enerji. "Kömür analizleri." <http://www.incienerji.com/index.php?sayfa=komur-analizleri> (accessed Jan. 10, 2022).
- [43] Çetinay Madencilik. "Kısrakdere kömürü." <https://cetinaymadencilik.com/urun/10-18-findik-komur/> (accessed Mar. 10, 2023).
- [44] Ceylan, İ. (2007). Programlanabilir (PLC) *Isı Pompalı Kurutucunun Tasarımı, İmalatı ve Kereste Kurutma İşleminde Deneysel İncelenmesi* (Doktora tezi), Gazi Üniversitesi Fen Bilimleri Enstitüsü, Ankara.
- [45] E. Yalçın, M.Z. Söğüt, A. Kılıç, H. Bulgurcu, "Poliüretan Panelli Soğuk Depo Uygulamalarında Isı Köprüleri Oluşumu ve Isıl Analizi," *Tes. Müh. Der.*, 144, 69-79, 2014.
- [46] Nuh Yapı. "Gaz beton özellikleri." <https://www.nuhyapi.com.tr/teknik-ozellikler> (accessed Jan. 10, 2022).
- [47] M. Aktaş, İ. Ceylan, H. Doğan, "Isı Pompalı Endüstriyel Fındık Kurutma Fırınının Modellenmesi," *Poli. Der.*, 8(4), 329-336, 2005.
- [48] M. Aktaş, "Güneş Enerjisi ve Isı Pompası Destekli Bir Kurutucuda Kırmızıbiber Kurutulmasının Deneysel İncelenmesi," *Poli. Der.*, 13(1), 1-6, 2010.
- [49] Aksoy, A. (2019). *Farklı Kurutma Yöntemlerinin Kıymanın Kurutma Kinetiği, Mikroyapısı, Rengi ve Rehidrasyon Oranı Üzerine Etkisi* (Doktora tezi), Yıldız Teknik Üniversitesi Fen Bilimleri Enstitüsü, İstanbul.
- [50] Kırbaş, C. "Psikrometrik diyagram ve uygulamaları." MMO Kocaeli. https://www1.mmo.org.tr/resimler/dosya_ekler/19982ccdd9f6003_ek.pdf (accessed Jan. 10, 2022).
- [51] Ü. İpekoğlu, H. Polat, "*Susuzlandırma, Cevher Hazırlama El Kitabı*," YMGV Yayını, Bölüm 16, 335-370, 2014.
- [52] Erdöl Aydın, N. (2000). *Sabit Yataklı Yakma Sistemlerinde Yanmada Kömür Neminin Etkisinin Deneysel İncelenmesi* (Doktora tezi), İstanbul Teknik Üniversitesi Fen Bilimleri Enstitüsü, İstanbul.
- [53] M. Altınar, M. Yıldırım, "Afşin-Elbistan Linyitinin Kurutulması ve Nem İçeriğinin Darbe Dayanımına Etkisi," *Çukurova Üniversitesi Fen ve Müh. Bil. Der.*, 26(3), 19-28, 2011.
- [54] N. Yamankaradeniz, S. Coşkun, B. Pastakkaya, M. Can, "Isı Pompası Destekli Kurutma Sistemlerinde By-Pass Oranının Kurutma Performansına Etkisinin Deneysel Analizi," *Uludağ Üniversitesi Müh.-Mim. Fak. De.*, 17(2), 17-36, 2012.
- [55] B. Acar, E. Öz, E. Gedik, "Ayrık ve Birleşik Isı Borulu Kollektör Verimlerinin Deneysel Olarak İncelenmesi," *Gazi Üniversitesi Müh. Mim. Fak. Der.*, 23(2), 425-429, 2013.
- [56] Anonim. "Havanın özgül ısısı." <https://psikrometri.com/3-psikrometrik-ozellikler-ve-terimler/> (accessed Jan. 10, 2022).
- [57] Kazancı, O.V. (2008). *Kömürün Kendi Kendine Yanmasında Mineral Maddenin Etkisi* (Yüksek lisans tezi), İstanbul Teknik Üniversitesi Fen Bilimleri Enstitüsü, İstanbul.
- [58] MGM. "Manisa ili çevre sıcaklığı." <https://www.mgm.gov.tr/veridegerlendirme/il-ve-ilceler-istatistik.aspx?m=MANISA> (accessed Jan. 10, 2022).
- [59] Anonim. "Termik santraller." https://tr.wikipedia.org/wiki/Termik_santral (accessed Jan. 10, 2022).
- [60] Anonim. "Fan gücü." <https://www.bvnair.com/fiyatlistesi2021.pdf> (accessed Jan. 10, 2022).

Research Article

The Effect of the Conversion Coefficients of Platinum-Based Resistance Thermometers on the Uncertainty Estimation

*F. M. Patan Alper 

Department of Physics, Yeditepe University, İstanbul, Turkey
E-mail: mpatan@yeditepe.edu.tr

Received 16 December 2022, Revised 20 March 2023, Accepted 20 May 2023

Abstract

Different types of thermometers (resistance thermometers, thermocouples, liquid in glass thermometers, radiation thermometers, etc.) are used in temperature measurements. Resistance thermometers are among the most reliable types of sensors used for sensitive temperature measurements. The traceability, accuracy and precision of the measurement results are important for the reliability of the measurements. There are many parameters that affect the uncertainty estimation in measurements made with resistance thermometers. One of the parameters to be considered in the uncertainty estimation is the interpolation error in converting the resistance value to temperature. Different methods (ITS-90, Calendar Van Dusen CVD, Polynomial equation) can be used to convert the resistance value to temperature. The problem is that there are differences in the temperature values read using the coefficients obtained by different methods. In this study, the effect of errors from CVD and polynomial equation methods on measurement uncertainty was investigated.

Keywords: Resistance thermometer, Calendar van dusen, ITS-90, uncertainty estimation.

1. Introduction

Standard platinum resistance thermometers (SPRTs) are the most precise and reproducible temperature sensors, which is why they are the instruments specified for use in the ITS-90 over a wide range of temperature [1,2]. They are based on the positive temperature coefficient of electrical resistance of platinum, which is about 0.4%/°C at 0 °C. The sensing resistor is made using a fine platinum wire of diameter <0.1 mm carefully wound in a strain-free manner on a silica (quartz) glass former. It is enclosed in a long silica tube (sheath) at the head of which the connecting leads are joined to a length of flexible cable. The resistance at 0 °C is normally about 25.5 Ω, which gives a sensitivity of about 0.1 Ω/°C. SPRTs are very fragile and pure platinum is very soft. Therefore secondary standards and industrial thermometers are usually made with more rugged (stronger) sensors, using less pure platinum wires or printed platinum films. The resistance is generally 100 Ω at 0 °C, so the sensitivity is about 0.4 Ω/°C, and they are protected by stainless-steel metal sheaths. They are often called Resistance Temperature Detectors (RTDs), Industrial Platinum Resistance Thermometer (IPRT) or Pt-100s. Platinum is almost invariably used as the sensing resistor in resistance thermometry, because it has a good temperature coefficient, it can operate to very high temperatures (in special applications up to 962 °C) and it is resistant to chemical attack, particularly oxidation. However, it is expensive and sometimes copper or nickel are used, for reasons of cost [3,4].

BIPM, IEC, ISO, and some other bodies [11]. The EA guide EA-4/02 • Expression of the Uncertainty of Measurement in Calibration is adapted from the GUM with

According to ITS 90, platinum resistance thermometers are calibrated at fixed points in their temperature range. Calibration results are converted from resistance to temperature for user convenience. When the calibration is done at fixed points, unit conversion can be done by using the ITS-90 calculation. Alternatively the transformation can be realized using Calendar Van Dusen (CVD) or Polynomial equation and the calibration is usually done with comparison method in less costly baths and ovens instead of fixed points [5,6]. In the literature, the conversion coefficients obtained from the measurement results are evaluated by different methods. In a group of studies, interpolation results from polynomial equation results were evaluated [7,8]. In CVD evaluation method, the results of the matrix method are used for uncertainty estimation [9,10].

It is important to recognize that uncertainties are estimated, rather than calculated. The estimate is made using experimental and other available information, but in practice the evaluation usually includes significant elements of subjective assessment. The result is always open to question, by the individual, colleagues, managers, assessors, customers, etc. Nevertheless, the uncertainty budget demonstrates the extent to which the measurement process has been critically analyzed and understood. It also shows clearly which sources of uncertainty are most significant, and hence should be improved if the uncertainty is to be reduced. In recent years uncertainty estimation and analysis has been based on the 'GUM', the ISO Guide to the Expression of Uncertainty in Measurement, which was issued in 1993 by reference to calibration and includes several worked examples [12].

The level of uncertainty depends on the equipment and procedures used in the measurement and calibration. All components of uncertainty should be evaluated and combined, to reach an overall calibration uncertainty at each temperature. In this study, the contribution from the conversion coefficients obtained from different methods that influence the uncertainty will be evaluated in order to reduce the measurement uncertainty.

2. Experiment

This study investigates the effect on the uncertainty of using the different methods for deriving the conversion coefficients for resistance thermometer calibration data in the temperature range -40 to 500 °C.

2.1 Apparatus

Platinum resistance thermometer (Pt-100, Fluke 5626), Super thermometer (Hart scientific 1595A), Alcohol Bath (Fluke 7341), Water Bath (Hart Scientific 7037), Oil Bath (Hart Scientific 6022), Salt Bath (Hart Scientific 6055)

2.2 Method

The calibration method of a thermometer is based on comparison measurement. The process of comparison method: thermometers are calibrated with reference or standard thermometers, in thermally stabilized liquid baths or furnace. The temperature sensors are connected to the Model 1575 A bridge which is used for the measurements. The ice point is prepared and before calibration starts, the value of ice point of test thermometer is measured. The calibration is done from the lowest temperature towards 0 °C, and then from the highest temperature value down towards 0 °C. The thermometers are immersed at least 25 cm into liquid. Because the thermometers' immersion depth is important, it is noted in the certificate. The use of metal blocks in liquid baths increases homogeneity and decreases the uncertainty. At each temperature, when the bath is stable, the reference and test thermometers are measured alternately. At least 10 values are taken with 10 second intervals for every measurement point. The order of measurement is as reference – test – reference, etc. After taking measurements at all the calibration temperatures, the ice point value is again measured.

The difference between ice point values that are taken at the start and end of calibration is used to estimate the uncertainty components for the thermometer hysteresis and stability.

In the calibration of platinum resistance thermometers (PRT) by comparison measurement in baths, 3 methods can be used to construct the resistance curve against temperature: CVD (A, B, C coefficients), CVD (Alpha, beta, delta coefficients) and Polynomial equations coefficients (fitting a polynomial equation to the calibration data using a least-squares regression routine: i.e. curve-fitting, which minimizes the sum of the squares of the residuals (differences between the curve and the data). The RMS (root mean square) deviation decreases as the order of the fit increases.

In this study, the calculation of the CVD A,B,C and polynomial coefficients and the effect of the interpolation on the measurement uncertainty estimation will be discussed.

The CVD equations are widely used with industrial PRTs shown below.

For $t > 0$ °C:

$$R_t = R_0 (1 + At + Bt^2) \quad (1)$$

For $t < 0$ °C:

$$R_t = R_0 (1 + At + Bt^2 + C (t - 100) t^3) \quad (2)$$

The other method to be compared with the CVD method is the polynomial equation. Using polynomial equations, a temperature-resistance curve or table can be created for temperature sensors. In this method, better results can be obtained by increasing the degree of the equation. Choosing the optimum degree of fit is a compromise between reducing the residuals sufficiently, but not over-fitting the data, which happens if the degree approaches the number of points (the curve begins to fit the errors – i.e. oscillate so as to pass more closely through the points.

$$t (R) [^{\circ}C] = A_0 + A_1R + A_2R^2 + A_3R^3 + \dots + A_5R^5 \quad (3)$$

3. Measurements and Results

Before calculating the conversion coefficients, the calibration of the thermometer to be tested was carried out with a traceable reference thermometer in accordance with international calibration procedure as specified in the method section. The measurement results are given in Table 1.

Calibration outputs are degrees Celsius (°C) for the reference thermometer, resistance (Ω) for the test thermometer. The ice point value of the test thermometer will be recorded as R_0 , and the test thermometer value at any temperature point will be recorded as R_t .

The first method to find the coefficients is CVD method, coefficient calculation (A,B,C) was obtained using Matlab software. The second method was to find the CVD coefficients with the Matrix method using the Excel program. Finally, the coefficients ($A_0, A_1, A_2, A_3, A_4, A_5$) were calculated with the 5th degree polynomial equation. The coefficients obtained by the 3 methods are given in Table 2.

Table 1. Calibration Result of Test Thermometer.

Reference Therm. / °C	Test Therm. / Ω
-39.82	84.3475
-19.81	92.2530
0.00	100.0200
50.17	119.5132
90.18	134.8346
150.04	157.3988
235.01	188.7495
349.69	229.7272
449.51	264.1700

Table 2. Resistance-Celsius conversion coefficients.

CVD Matlab	CVD Excel	Polynomial
A: 3.91160E-03	A: 3.91183E-03	$A_0: 1.0003E+02$
B: -5.83748E-07	B: -5.84033E-07	$A_1: 3.9131E-01$
C: 2.55447E-14	C: 2.53484E-14	$A_2: -6.0826E-05$
		$A_3: 1.5665E-08$
		$A_4: -3.5604E-11$
		$A_5: 3.0860E-14$

The coefficients were put into the CVD and polynomial equations and the interpolation residuals were estimated from the differences between the resistance values calculated from the coefficients and the measured resistance values. Measured test thermometer value, calculated test thermometer value and difference values to be used as interpolation error for each method used are given in the Tables 3,4,5.

Table 3. CVD Results from MATLAB data.

Reference Therm./ °C	Test Therm./Ω	Test Therm. Matlab/ Ω	Residual m°C
-39.82	84.3475	84.3473	1
-19.81	92.2530	92.2452	20
0.00	100.0200	100.0200	0
50.17	119.5132	119.5032	25
90.18	134.8346	134.8259	22
150.04	157.3988	157.4056	17
235.01	188.7495	188.7437	14
349.69	229.7272	229.7212	15
449.51	264.1700	264.1676	6
499.33	280.9500	280.9457	11

Table 4. CVD Results from Excel program matrix method.

Reference Therm./ °C	Test Therm./Ω	Test Therm. Excel/ Ω	Residual m°C
-39.82	84.3475	84.3463	3
-19.81	92.2530	92.2447	21
0.00	100.0200	100.0200	0
50.17	119.5132	119.5043	22
90.18	134.8346	134.8277	17
150.04	157.3988	157.4084	24
235.01	188.7495	188.7476	5
349.69	229.7272	229.7256	4
449.51	264.1700	264.1717	4
499.33	280.9500	280.9493	2

Table 5. Results from 5th degree polynomial equation.

Reference Therm./ °C	Test Therm./Ω	Test Therm. Excel/ Ω	Residual m°C
-39.82	84.3475	84.3467	2
-19.81	92.2530	92.2500	7
0.00	100.0200	100.0274	19
50.17	119.5132	119.5100	8
90.18	134.8346	134.8295	13
150.04	157.3988	157.4060	18
235.01	188.7495	188.7463	8
349.69	229.7272	229.7279	2
449.51	264.1700	264.1700	0
499.33	280.9500	280.9500	0

3.1 Uncertainties

International standards (the ‘GUM’, the ISO Guide to the Expression of Uncertainty in Measurement and the EA guide EA-4/02 Expression of the Uncertainty of Measurement in Calibration) were used to calculate the measurement uncertainty. All parameters affecting the measurement were analysed, given in Table 6. Uncertainties may vary depending on the calibration method and system used. The error from interpolation, one of the uncertainty contributions, was evaluated separately and its effect on the measurement uncertainty was analysed. In the estimation of uncertainty,

the coverage factor is usually $k = 2$ for the 95% confidence interval.

Table 6. Uncertainty estimation for Pt-100.

Uncertainty Component	Uncertainty	Statistical Distribution	Standard Uncertainty (°C)
Ref. Therm. Drift	0.00002 Ω	Rectangular	1.16E-04
Ref. Therm. Uncertainty	0.002 °C	Normal	0.001
Ref. Therm. Stability	0.00025 °C	Normal	0.00025
Indicator Uncertainty	0.00004 Ω	Normal	0.0002
Indicator Resolution	0.00001 °C	Rectangular	5.78E-06
Indicator Drift External Resistance	1.35E-04 Ω	Rectangular	0.00135
0.000012Ω	Normal	5.50E-05	
Self-Heating	0.0000015 Ω	Rectangular	8.67E-06
Bath Stability	0.001 °C	Normal	0.001
Bath Uniformity	0.002 °C	Rectangular	0.001156
Ice Point	0.0044 °C	Normal	0.0022
Test Therm. Resolution	0.000001 Ω	Rectangular	5.78E-06
Test Therm. Stability	0.0001 Ω	Normal	0.001
Test Therm. Hysteresis	0.0002 Ω	Rectangular	0.001156
Interpolation	0.002 °C	Normal	0.002
Total Uncertainty			0.0037
Expanded Uncertainty (k=2 %95 confidence level)			0.007

The effects from interpolation were considered in the measurement uncertainty calculation, and it was evaluated how the uncertainty values changed when different programs were used. It has been concluded that the uncertainty value can be underestimated with the data obtained from which program.

Using a mathematical package such as Excel or Matlab, no significant difference was observed between these calculations as they used the same curve-fitting algorithms. However, making the coefficient calculation with the help of a more practical and fast polynomial equation provides significant convenience to the user. When the results obtained by the CVD method and the Polynomial equation are compared with each other, it is seen that the error from the curve fitting algorithm does not significantly increase the measurement uncertainty. In addition to the studies, the results obtained using the 5th polynomial equation were repeated with the 4th degree polynomial equation. The results obtained from the 4th degree polynomial equation are closer to the measured values, but far from the results obtained from the CVD equation, as it calculates the test value with a more rough approximation.

The studies were carried out with different resistance thermometers in order to see the error from the reproducibility parameter. In the calculations made for different thermometers, similar uncertainty values were calculated between the methods. It has been observed that if the stability and reproducibility of the thermometers are good, the uncertainty from the equations decreases.

The temperature points selected in the measurements were chosen randomly and the number of measurement points was chosen above the number of measurements sufficient to calculate the coefficients from the equations. After the coefficients were entered into the display, the thermometers were recalibrated and the measurements were

taken in degrees Celsius. The measurement results at different temperatures were compared with the calculated values. These tests took place for approximately 10 thermometers.

4. Conclusion

Precise and accurate measurements in temperature measurements depend on certain conditions. It is important to analyze the measurement uncertainty completely and to carry out the measurements with the most ideal method. In this study, measurement uncertainty has been studied precisely and focused on obtaining a low interpolation error from the parameters affecting the measurement uncertainty. Resistance-Celsius conversion coefficients were calculated with 3 methods and were taken into account in the uncertainty estimation. Of the methods, MATLAB and EXCEL gave almost the same results. The lowest uncertainty is 0.007 °C, while the highest uncertainty is 0.030 °C. The lowest uncertainty values were obtained by the third method, the polynomial equation method, varying from 0.007 °C to 0.023 °C. In summary, although the polynomial equation method is not widely used compared to the CVD method, it has been determined as the method to obtain a lower uncertainty value in cases where measurement uncertainty is important.

Acknowledgements:

I wish to thank Dr. Richard Rusby from National Physics Laboratory (NPL) for help and comments. I would also like to thank Maria Aiordachioaiei for help during this study.

Nomenclature

t	temperature (°C)
R_t	resistance at temperature t (Ω)
R_0	resistance at 0 °C (Ω)
A, B, C	constants in CVD method
$A_0, A_1, A_2, A_3, A_4, A_5$	constants in polynomial method

References:

- [1] H. Preston-Thomas, "The International Temperature Scale of 1990 (ITS-90)," *Metrologia*, 27, 3, 1990.
- [2] J.J. Connolly, "Platinum Resistance Thermometry," *Monograph II: NMI Technology Transfer Series*, 2004.
- [3] T.J. Quinn, "Temperature". 2nd ed. *Academic Press*; pp. 1-23, 1990.
- [4] R. Rusby, "Good Practice Guide No. 125 Introduction to Temperature Measurement", NPL, 2016.
- [5] P.R.N. Childs, "6 - Resistance temperature detectors," in *Practical Temperature Measurement*, *Oxford: Butterworth-Heinemann*, pp. 145-193, 2001.
- [6] Bureau International des Poids et Mesures, BIPM, *Guide to the Realization of the ITS-90, Platinum Resistance Thermometry*, 2018.
- [7] D.R. White, P. Saunders, "Determination of the Uncertainties for ITS-90 Realization by SPRTs Between Fixed Points," *Metrologia*, 43, 327, 2006.
- [8] D.R. White, P. Saunders, "The propagation of uncertainty with calibration equations," *Meas. Sci. Technol.* 18, 2157, 2007.
- [9] S. Dyurish, R. Palenchar, "Reduction of Measurement Uncertainty by Taking into Account Correlation in Measurements and Temperature Scale," *Realization Meas. Tech.* 49, 689, 2006.
- [10] P. Rosenkranz, "Uncertainty Propagation for Platinum Resistance Thermometers Calibrated According to ITS-90," *Int. J. Thermophys.* 32: 106-119, 2011.
- [11] Joint Committee for Guides in Metrology (JCGM), JCGM 100, Evaluation of Measurement Data-Guide to the Expression of Uncertainty in Measurement (GUM), GUM 1995 with minor corrections (JCGM, BIPM, Paris, 2008).
- [12] EA-4/02 rev.01 – Expression of the uncertainty of measurement in calibration, 2013.

Research Article

Optimization of a Dry Peeling System for Tomatoes Using Approximate Solutions

*A. Metallo 

Industrial Engineering Department, University of Salerno, Italy
E-mail: antonio.metallo@libero.it

Received 27 December 2022, Revised 9 March 2023, Accepted 15 May 2023

Abstract

In recent years tomatoes have been peeled using steam and lye. Both are costlier, less environmentally friendly and highly polluting techniques. Thus, more sustainable alternatives should be sought after. Among these alternatives is radiative heating. To appropriately design the system for dry peeling, several typical operational characteristics of the process in issue must be estimated. The analytical model presented allows estimates to be made through closed-form relationships between the parameters involved. The analysis is based on the use of an appropriate theoretical model, which facilitates the solution to the proposed problems. Through the approximate solution of the analytical problem, we will analyse: the angular speed Ω , the temperature fluctuations ΔT_0 , the process time t_c . These estimates are then used to derive a specific model for a control of process. The temperature profile (through an approximate solution) associated with the process that provides the optimum peel quality was utilized as a guide for the regulation system. A control system used the code to extract a specific temperature, and based on surface tomato temperature readings, controlled a brushless motor using a logic strategy. The regulating system can adjust the rotation speed, and hence the heating intensity, even under less than perfect operating conditions in order to obtain the appropriate profile temperature. The controlled temperature profile yielded an average temperature of 66.3°C, while the reference case yielded a temperature of 67°C. Additionally, it was found that the temperature inaccuracy decreased with each rotation, ranging from 2.5 °C at 2π to 0.3 °C at 16π . As a result, the peeling procedure is standardized in time, temperature, and quality.

Keywords: *Dry peeling system; integral method; process control, approximate solution*

1. Introduction

Major issues that plague the sustainability of the tomato processing industry include energy consumption, wastewater management, and pollution [1-3]. With the development of advanced infrared dry peeling technology, the traditional hot lye method for peeling tomatoes can be replaced. This process relies on infrared heating panels to quickly heat up tomatoes, resulting in a thinner thickness of peeled-off skin and slightly firmer texture of peeled tomato. The IR dry-peeling method is rapidly adopted by food processors, due to its sustainable advantages like high efficiency and negligible water use [4, 5]. By irradiating the tomato surface with infrared radiation and selecting a suitable value of power density, temperature and time, it is possible to increase the Young's modulus of the peels. As a result, the adhesiveness of the peel is reduced. These findings demonstrated the effectiveness of the novel IR dry-peeling process for tomatoes [6]. Producing high quality peeled tomatoes is a challenging task, especially with the variety of tomato types. However, some critical aspects of peeling tomatoes using infrared radiation heating were outlined by [7]. Wishing to perform successful infrared peeling requires to realize both rapid and uniform heating on the tomato surface. An infrared heating system was designed to be installed in a food processing facility. The purpose of this research is to improve the heating uniformity of tomatoes transported

along by the conveyor belt, in order to obtain an optimal design of infrared heating systems. For this purpose, the irregular shape of tomatoes and their different expositions to the heating source when transported along by the conveyor belt are to be considered. In this context, a typical configuration for industrial peeling is realized by means of a plane matrix of infrared emitters [8, 9]; looking at tomatoes in relative motion, they have been found to rotate on the belt when processed. To retrieve tomato thermal response to infrared heating, a numerical approach is necessary due to the complexity of the geometry. Previously, the authors attempted to describe the process using an analytical model: an infinite body subjected to a suitable source of pulsating heat was considered because the proper time scale was small [10, 11]. For peeling purpose, it proved useful to assume that the heating process would end a specified temperature was reached [4, 8, 12]. Achieving the best heating uniformity also means considering rotation speed and relative position to the source. To ensure uniform heating, a system for a rotation speed regulating has been proposed. After dimensioned the system and got the values of the parameters which enable to achieve the optimal temperature profile, which thus assures the proper heating uniformity and excellent quality of the product, the control logic has been established which allows us to obtain a peeling process with very comparable temperature profiles to the reference one. De facto, the

emissivity value and therefore the amount of heat transferred are influenced by factors like the size of the tomatoes, the existence of processing residues on the lamp's surface, and others [13, 14]. In order to regulate the intensity of the heat transferred, the rotation speed was adjusted.

To achieve this, the surface temperature, the logic control, and the temperature value pertaining to the reference profile must be delivered to the regulating system. A pyrometer, a mathematical model, and an approximation solution are used to supply the first, second, and third parameters, respectively. The analytic solution appears rather involved [10, 11], which affects the calculation times, thus a further approximate approach to the same problem is attempted in order to obtain an easy-to-handle solution, and therefore less run time. Since the peeling process typically takes place at a number of revolutions of $n \cong 10$ rpm [4, 8, 12], the regulation system will have to act approximately every 6 s. The relatively long calculation times, about 2 s, moreover and the solution's complex structure make the analytical solution unusable for the proposed regulation system. While the approximate solution is obtained almost instantly. It is therefore very simple and rapid to provide the code with the function that represents the approximate solution of the problem. In this way, it is feasible to overcome the limitations noted in the literature, in which, after the ideal peeling parameters have been determined, the process always occurs under the same conditions, without taking into account the variation of thermal power transferred as the emissivity varies (different diameters, process residues on the lamp surface, etc). As a result, the method is highly dependent on the emissivity value and fails to produce a quality-standardized output. Instead, by using the dry peeling temperature control system, the peeling productivity can be significantly increased by making the process quality standardized.

2. Materials and Method

The experimental setup of Figure 8, relating to the peeling of tomatoes with radiation, belongs at the first step of Pan's activity, Li et al. [8, 12, 15, 19].

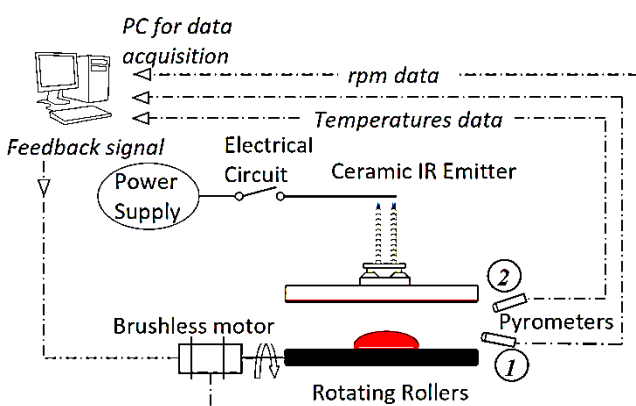


Figure 1. The experimental setup.

It consists of two main sections: IR heater, and rotating rollers. Curved ceramic emitters were adopted in the prototype equipment to enhance the IR heating intensity and the overall heating uniformity of tomatoes [8, 9, 18, 19]. Specifically created software (7.1 LabView®, National Instruments Corp., Austin, Texas) was employed for both data acquisition and reduction. The code collects the temperature data, detected by the pyrometers, for control purposes. In particular, the first pyrometer is used to obtain

the temperature of the lamp, and therefore to be able to evaluate the power transferred by it. The second supplies the surface temperature of the tomato, required for regulation system. At this point, the code extracted a specific temperature and based on such temperature reading, the computer program controlled the brushless motor, then the revolution number n , with a DAQ board (AT MIO 16XE50, National Instruments, Austin, Texas) by means of a specific logic strategy.

3. Mathematical Formulation

The theoretical study of the thermal problem involving the radiative heating of the tomato began with analytical modeling [16]. The non-linear exchange between various radiative surfaces makes heat transfer modeling in tomato IR heating difficult [21]. Several assumptions were made in the development of the heat transfer model to simplify it and reduce computational times. Such assumptions have been frequently used by researchers to develop heat transfer modeling during IR heating of food [21-24].

- Rapid processing determines only surface peripheral warming up.

- Flesh and peel materials were homogeneous, isotropic, and had similar thermal properties. For lye peeling, the surface temperature of tomatoes was assumed to be equal to the temperature of peeling solution [12].

- Constant thermal properties: It has been verified that the sensitivity of the temperature field to variations in properties has no effect on the thermal aspect of the problem under examination.

- Generally, tomatoes used in this study were longer in longitudinal direction (stem-blossom end) than radial direction [22]. Since the tomatoes were lined up in the longitudinal direction, the long row of tomatoes were considered as an infinitely long cylinder (i.e., the variation in the diameter of tomatoes was neglected).

- Tomato was opaque to thermal radiation (no transmission) and all incident energy was absorbed at the surface of tomato with a small reflection of incident energy (reflectivity of tomato is about 5%) [22].

- All participating radiating surfaces were diffused-grays surfaces based on the enclosure theory, which meant that each participating object could emit to and absorb radiation from each other.

- Hot air between emitter and tomato was transparent and did not interact with IR radiation passing through it. In other words, the proposed model involved heat transfer with surface to surface radiation among diffused surfaces through nonparticipating medium.

- Heat transfer within the tomato occurred only by conduction.

- Heat transfer at tomato surface occurred by radiation between emitter and tomato and convection between air and tomato. Air temperature (T_∞) remained constant.

- All radiation heat was incident on tomato surface only (i.e. zero penetration depth).

- Heat of generation due to respiration was neglected because it is very small compared to the total thermal energy received by tomato during IR heating.

- Mass transfer (moisture loss) was so small that the rate of heat loss due to evaporation could be neglected. Therefore, heat transfer due to evaporation (q_{evap}) during IR heating of tomatoes was assumed to be zero ($q_{\text{evap}} = 0$) [22, 26]. Thus the tomato under test is modeled as a purely conductive radiation semi-infinite body 1-D model.

The analytical approach has its purpose of estimating the process parameters and at the same time to understand the phenomenon in question. To thermally model the tomato it is necessary to carry out an evaluation of the thermophysical properties which should be close to those of water. The thermophysical properties are evaluated using the typical food constituents: water, proteins, fats, carbohydrates, fibers, and ashes. In 1986 Yonghee Choi and Martin Okos of the Purdue University in the USA, on the basis of experiments and theoretical-analytical checks [17], developed mathematical models in a range of validity between -40 and +150°C for the estimation of thermophysical properties of foods based on their composition. Table 1 shows the mathematical models for estimating the following properties as function of temperature:

- thermal conductivity (k)
- thermal diffusivity (α)
- density (ρ)
- specific heat at constant pressure (c_p)

Table 1. Thermophysical Properties of Basic Nutrients; Temperature in Celsius Degrees.

Component	Models of thermophysical properties
Protein	$k=1.7881 \cdot 10^{-1}+1.1958 \cdot 10^{-3}T-2.7178 \cdot 10^{-6}T^2$
	$\alpha=6.8714 \cdot 10^{-2}+4.7578 \cdot 10^{-4}T-1.4646 \cdot 10^{-6}T^2$
	$\rho=1.3299 \cdot 10^3-5.1840 \cdot 10^{-1}T$
	$c_p=2.0082+1.2089 \cdot 10^{-3}T-1.3129 \cdot 10^{-6}T^2$
Carbohydrates	$k=2.0141 \cdot 10^{-1}+1.3874 \cdot 10^{-3}T-4.3312 \cdot 10^{-6}T^2$
	$\alpha=8.0842 \cdot 10^{-2}+5.3052 \cdot 10^{-4}T-2.3218 \cdot 10^{-6}T^2$
	$\rho=1.5991 \cdot 10^3-3.1046 \cdot 10^{-1}T$
	$c_p=1.5488+1.9625 \cdot 10^{-3}T-5.9399 \cdot 10^{-6}T^2$
Fats	$k=1.8071 \cdot 10^{-1}-2.7604 \cdot 10^{-3}T-1.7749 \cdot 10^{-7}T^2$
	$\alpha=9.8777 \cdot 10^{-2}-1.2569 \cdot 10^{-4}T-3.8286 \cdot 10^{-8}T^2$
	$\rho=9.2559 \cdot 10^2-4.1757 \cdot 10^{-1}T$
	$c_p=1.9842+1.4733 \cdot 10^{-3}T-4.8008 \cdot 10^{-6}T^2$
Fibers	$k=1.8381 \cdot 10^{-1}+1.2497 \cdot 10^{-3}T-3.1683 \cdot 10^{-6}T^2$
	$\alpha=7.3976 \cdot 10^{-2}+5.1902 \cdot 10^{-4}T-2.2202 \cdot 10^{-6}T^2$
	$\rho=1.315 \cdot 10^3-3.6589 \cdot 10^{-1}T$
	$c_p=1.8459+1.8306 \cdot 10^{-3}T-4.6509 \cdot 10^{-6}T^2$

The density of foods ρ can be calculated with the relationship:

$$\rho = (1-\zeta) / \sum(x_i/\rho_i) \quad (1)$$

where ζ is the porosity, x_i and ρ_i are respectively the mass fraction and density of the different food constituents. The specific heat of the food above the freezing temperature can be obtained from the weighted average of the specific heats of the constituent components according to the Eq. (2):

$$c_p = \sum c_i \cdot x_i \quad (2)$$

where c_i and x_i are the specific heat and the mass fraction of the different food constituents.

Several models for the estimation of k have been developed to take due account of the fibrous structure of many foods. In particular Murakami and Okos, in analogy with parallel or series connections of the electrical resistances, have proposed models that consider the anisotropy of the materials. The parallel model (p.m) is the

sum of the thermal conductivities of the constituents k_i multiplied by the respective fractions in volume according to the Eq. (3):

$$k_{eq} = \sum x_{iv} \cdot k_i \quad (3)$$

The volume fraction can be obtained from the following relationship:

$$x_{iv} = (x_i/\rho_i) / \sum(x_i/\rho_i) \quad (4)$$

The mass fractions of the individual tomato constituents reported in one of the works by Pan et al the [8], were obtained from the “United States Department of Agriculture Food Composition Databases” (2010 USDA Nutrient Database) Table 2. Considering the temperature equal to 25°C and using the above equations, the thermophysical properties are calculated for each component and having determined the relative volume fractions, those of the tomato.

Table 2. Thermophysical Properties of Tomato Components and Corresponding Fractions.

Component	ρ [kg/m ³]	k [W/(mK)]	c_p [kJ/(kgK)]	X_{mass}	X_{volume}
Protein	1316.94	0.207	2.038	0.0088	0.0068
carbohydrates	1591.34	0.233	1.594	0.0389	0.0248
Fats	915.15	0.112	2.018	0.002	0.0022
Ashes	2416.78	0.363	1.138	0.005	0.0021
Water	994.91	0.611	4.171	0.9452	0.962

For tomato we obtain: $\rho = 1014.8 \text{ kg/m}^3$, $k = 0.596 \text{ W/(m} \cdot \text{K)}$ and $c_p = 4032 \text{ J/(kg} \cdot \text{K)}$. The results clearly show how strongly similar the characteristics of the tomato are to those of water.

In order to verify the validity of the parallel model, used following the assumptions made, the properties were verified to correspond to those derived from [21], obtained through the empirical formulas described by Singh and Heldman [27].

Table 3. Thermophysical properties of processing tomato with respect to temperature [21].

Thermophysical properties	Function	Temperature °C		$\Delta\%$	p.m err%
		25	90		
Thermal Conductivity	$0.0009 \cdot T [^\circ\text{C}]$	0.572	0.6305	9.7	4.11
	$+0.5495$ [W/(m °C)]				
Specific Heat Capacity	$0.6024 \cdot T [^\circ\text{C}]$	4035.56	4074.71	0.9	0.09
	$+4020.5$ [J/(kg °C)]				
Density	$0.4266 \cdot T [^\circ\text{C}]$	987.255	1014.98	2.7	2.75
	$+976.59$ [kg/m ³]				

As shown in the Table 3, the error incurred while utilizing the parallel approach for thermal conductivity is no more than 4%. Therefore, the applied methodology can be regarded as accurate given that the results of the sensitivity analysis demonstrate that a 10% variation in the properties corresponds to a 3.1% variation in the size itself. Consequently, the error made taking into account the constant properties is also small.

Typically, a very short warm up period of no more than 60 seconds is required for successful peeling of surfaces at

temperatures as high as 100°C [4, 8, 12, 19]. For tomato, assuming the thermo-physical properties of water apply, it can be easily demonstrated that thermal penetration depth will be limited to a few millimeters under the tomato skin, thereby permitting the semi-infinite body model to be applied [10]. Convective heat transfer also occurs at the boundary due to cycling radiative heating extended to the first half period of the sinusoidal source. Our study is concerned with a semi-infinite medium with combined third and second kind boundary conditions, incorporating both convection and periodic heating, Figure 2.

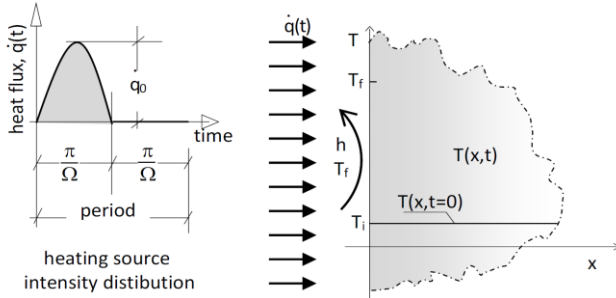


Figure 2. A schematic representation of the problem.

One-dimensional heat conduction and constant thermal properties are considered. The medium is assumed initially in equilibrium with the ambient at temperature T_0 . In order to describe the heating felt by the rotating tomatoes, the surface at $x = 0$ is assumed to be exposed to a periodic on/off heat flux with $1/2$ duty cycle; when the source is on, i.e. in the first half period, the heating intensity is assumed to vary sinusoidally with time, while it is zero in the second half, Figure 3.

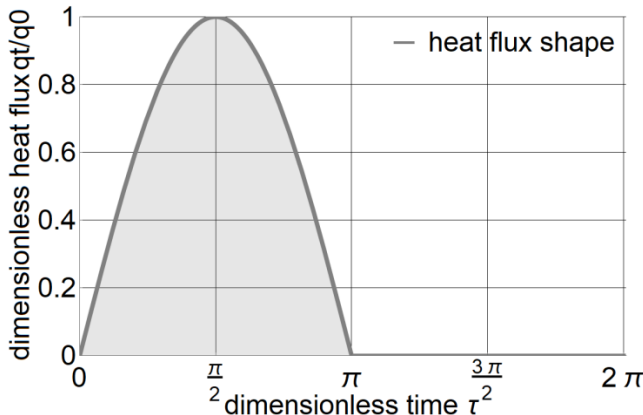


Figure 3. The dimensionless shapes for heat flux.

Therefore, periodic nonhomogeneous boundary conditions are required, which highlight the semi-amplitudes and characteristic angular speeds Ω of tomato rotation. During the peeling process, the temperature penetration depth is easily checked to ensure that it is confined to the very first layers of the tomato skin, which justifies the semi-infinite slab model [10, 11]. When constant properties are considered and heat is transferred using internal conduction, dimensionless energy balance equations and associated boundary conditions have nonhomogeneous linear properties:

$$\frac{\partial^2 \theta}{\partial \xi^2} = 2 \frac{\partial \theta}{\partial \tau} \quad (5)$$

$$-\frac{\partial \theta}{\partial \xi} \Big|_{0,\tau} = \hat{q}(\tau) - Bi (\theta - \theta_f) \quad (6)$$

$$\theta(\xi, \tau = 0) = 0 \quad (7)$$

$$\theta(\xi \rightarrow \infty, \tau) = 0 \quad (8)$$

where the following dimensionless parameters have been introduced: $\theta = (T - T_0)/DT_{ref}$ is a dimensionless temperature, T_0 is the initial temperature; the group $DT_{ref} = \dot{q}_0 x_{ref}/k$ [K] is a reference temperature difference, \dot{q}_0 is the heat flux, and $x_{ref} = \sqrt{2\alpha t_{ref}}$ [m] a reference length; k [$W \cdot m^{-2} \cdot K^{-1}$] is thermal conductivity and α [$m^2 \cdot s^{-1}$] is the thermal diffusivity of tomato; the reference time, $t_{ref} = \Omega^{-1}$ was chosen such as the dimensionless time resulted $\tau = \Omega \cdot t$ [rad], being Ω [$rad \cdot s^{-1}$] the angular velocity of the source; the dimensionless space variable was defined such as $\xi = x/x_{ref}$ and, finally, $\hat{q}(\tau) = \sin(\tau) [1 + \text{sign}(\sin(\tau))]/2$ is the normalized wall heat flux, and $Bi = h x_{ref}/k$ is the Biot number.

The solution was obtained as the sum of two partial solutions. The analytical solution of both is obtained by the application of the Laplace transform technique. The full solution (Eq. (9)), obtained and validated in the previous works [10, 11, 20] (Figure 4), turns out to be was:

$$\theta(\xi, \tau) = \theta_h(\xi, \tau) + (1 + (-1)^n) \tilde{\theta}_\tau(\xi, \tau) - 2 \sum_{i=0}^n (-1)^i \tilde{\theta}_{i\pi}(\xi, \tau) \quad (9)$$

with

$$\tilde{\theta}_\tau(\xi, \tau) = \int \left[\frac{e^{-\frac{\xi^2}{2(\tau-\tilde{\tau})}}}{\sqrt{4\pi(\tau-\tilde{\tau})}} - \frac{Bi}{2} e^{-Bi\sqrt{2\xi+B_1^2(\tau-\tilde{\tau})}} \right] \times \text{erfc} \left(\frac{\xi}{\sqrt{2(\tau-\tilde{\tau})}} + Bi \sqrt{\tau-\tilde{\tau}} \right) \sin(\tilde{\tau}) d\tilde{\tau} \quad (10)$$

The term

$$\theta_h(\xi, \tau) = \theta_f \left(\text{erfc} \left(\frac{\xi}{\sqrt{2\tau}} \right) - e^{-Bi\sqrt{2\xi+B_1^2\tau}} \right) \times \text{erfc} \left(\frac{\xi}{\sqrt{2\tau}} + Bi \sqrt{\tau} \right) \quad (11)$$

represents the thermal response due to the convective heat transfer driven by the initial temperature excess $\theta_f = (T_0 - T_f)/DT_{ref}$, relatively to ambient temperature T_f , n is intervals of amplitude π over which $\hat{q}(\tau)$ remains continuous and $\tilde{\tau}$ is the dummy variable of convolution.

The term $\tilde{\theta}_\tau$ is obtained from the particularization of Eq. (10) at process time.

As expected, the solution depends not only on the values at time τ , but it also depends on the heating previously experienced at each revolution ($\tilde{\theta}_{i\pi}$), i.e. at each $\tilde{\tau} = i\pi$. The temperature field is unsteady due to the spatial and temporal

coordinates and the Biot number. The oscillating trend of the temperature profiles is represented in the Figure 3 in correspondence with the surface ($\xi=0$) for different values of the Biot number. The Figure clearly shows that different entities of cooling have different thermal responses. The greater the Biot number, the more both temperature levels and the amplitude of the oscillations decrease ($\Delta\theta, Bi=0 = 0.80$, $\Delta\theta, Bi=0.5 = 0.53$). Can be further observed that the phase shift with respect to the heat flux decreases with Bi number ($\varphi, Bi=0 = 0.72$, $\varphi, Bi=0.5 = 0.46$) [11]. The analytical solution was used to validate the approximate solution.

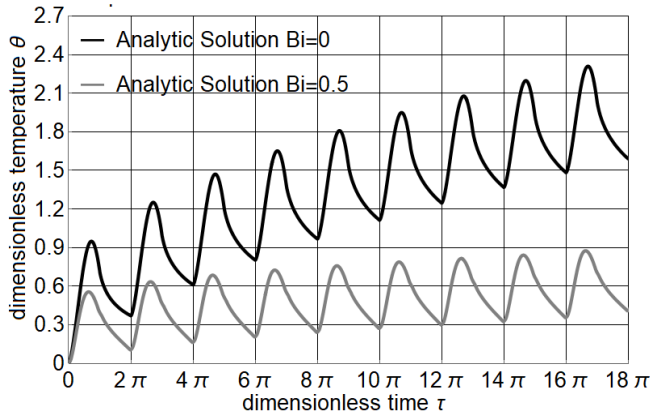


Figure 4. The dimensionless surface temperature at $\xi = 0$.

3.1 Approximate Solution

The solution obtained in the previous paragraph appears to be rather involved, so an approximate approach to the same problem is taken to achieve an easier solution. The problem was solved by applying the integral method. It was possible to obtain the solution of problem (Eqs. (5)-(8)) by choosing an approximate solution that makes explicit the dependence of the spatial variable:

$$\begin{aligned} \theta^*(\xi, \tau) = & a(\xi) \operatorname{erfi}(\tau^{1.5}) \\ & + (0.443 + 0.255B_1) \sin(0.5 \times \tau)^2 \\ & + (0.230 - 0.352B_1) \sqrt{\tau} \\ & + (0.186 - 0.156B_1) \sin(2.112 - \tau)^3 \\ & - (0.235 - 0.157B_1) \sin(-\tau)^3 \\ & + (0.158 - 0.181B_1) \sin(-1.587 - \tau) \\ & + (0.207 - 0.101B_1) \sin(0.418 - \tau - 0.512B_1)^2 \\ & + (0.1775 - 0.2483B_1) \operatorname{erf}(-\tau)(1 - 1.167B_1) \end{aligned} \quad (12)$$

with $a(\xi)$ unknown function which is obtained as follows. Eq. (5) has been integrated into the time coordinate and τ :

$$\int_{\tau=0}^{\tau=20\pi} \left(\frac{\partial^2 \theta}{\partial \xi^2} - 2 \frac{\partial \theta}{\partial \tau} \right) \cdot d\tau = 0 \quad (13)$$

By imposing that the approximate equation satisfies the integral and applying a boundary conditions, we obtain:

$$\begin{aligned} & 0.1014 B_1 \cos(0.8358 - 1.024 B_1) \\ & - 0.2078 \cos(0.8358 - 1.024 B_1) \\ & + (6.601 \times 10^{107719} + 0.318i) a''(\xi) \\ & - (1.5635 \times 10^{107724} - 2i) a(\xi) + 0.5795 B_1^2 \\ & + 4.682 B_1 - 0.1014 B_1 \cos(1.024 B_1 + 124.828) \\ & + 0.2078 \cos(1.024 B_1 + 124.828) - 3.302 \end{aligned} \quad (14)$$

$$\begin{aligned} b.c.1) - \frac{\partial \theta^*}{\partial \xi} \Big|_{0, \tau} & = \hat{q}(\tau) - B_1 (\theta - \theta_f) \\ \Rightarrow -a'(0) \operatorname{erf}(\tau^{1.5}) & = \frac{1}{2} (1 - \operatorname{sign}(\sin(\tau))) \sin(\tau) \\ & - B_1 ((0.230 - 0.3528 - B_1) \sqrt{\tau} \\ & - (1 - 1.167 B_1) (0.177 - 0.248 B_1) \operatorname{erf}(\tau) \\ & + a(0) \operatorname{erfi}(\tau) + (0.186 - 0.156 B_1) \sin(2.112 - \tau)^3 \\ & + (0.207 - 0.101 B_1) \sin(0.417 - 0.512 B_1 - \tau)^2 \\ & + (0.4437 - 0.2556 B_1) \sin(0.5\tau)^2 \\ & + (0.235 - 0.1576 B_1) \sin(\tau)^3 \\ & - (0.1587 - 0.1805 B_1) \sin(1.5872 + \tau) \end{aligned} \quad (15)$$

$$\begin{aligned} b.c.2) \theta^*(\xi \rightarrow 0, \tau) & = 0 \\ \Rightarrow -(1 - 1.167 B_1) (0.177 - 0.2483 B_1) \operatorname{erf}(\tau) \\ & + \sqrt{\tau} (0.2307 - 0.3528 B_1) \\ & + (0.1867 - 0.156 B_1) \sin^3(2.112 - \tau) \\ & + (0.235 - 0.157 B_1) \sin^3(\tau) \\ & + (0.207 - 0.101 B_1) \sin^2(-0.512 B_1 - \tau + 0.417) \\ & + (0.443 - 0.255 B_1) \sin^2(0.5\tau) \\ & - (0.158 - 0.1805 B_1) \sin(\tau + 1.587) \\ & + a(3) \operatorname{erfi}(\tau^{1.5}) = 0 \end{aligned} \quad (16)$$

By solving the differential equation system (Eqs. (14)-(16)), the solution $a(\xi)$ is obtained (Eq. (17)).

$$\begin{aligned}
a(\xi) = & -\frac{1}{(-3.32 \times 10^{200} B_1 - 5.11 \times 10^{202}) \operatorname{erfi}(\tau^{1.5})} \\
& \times 0.29 e^{-153.9 \xi} \operatorname{erfi}(\tau^{1.5}) [0.53 B_1^2 e^{307.8 \xi} \sin^3(2.11 - \tau) \\
& + 82.21 B_1 e^{307.8 \xi} \sin^3(2.11 - \tau) - 99.16 e^{307.8 \xi} \sin^3(2.11 - \tau) \\
& + B_1^3 e^{307.8 \xi} \operatorname{erf}(\tau) + 152.33 B_1^2 e^{307.8 \xi} \operatorname{erf}(\tau) \\
& + 1.21 B_1^2 e^{307.8 \xi} \sqrt{\tau} + 0.54 B_1^2 e^{307.8 \xi} \sin^3(\tau) \\
& + 0.34 B_1^2 e^{307.8 \xi} \sin^2(0.51 B_1 - \tau + 0.41) \\
& + 0.88 B_1^2 e^{307.8 \xi} \sin^2(0.5 \tau) - 0.62 B_1^2 e^{307.8 \xi} \sin(\tau + 1.58) \\
& - 241.29 B_1 e^{307.8 \xi} \operatorname{erf}(\tau) + 186.58 B_1 e^{307.8 \xi} \sqrt{\tau} \\
& + 82.89 B_1 e^{307.8 \xi} \sin^3(\tau) \\
& + 53.14 B_1 e^{307.8 \xi} \sin^2(0.51 B_1 - \tau + 0.41) \\
& + 134.22 B_1 e^{307.8 \xi} \sin^2(0.5 \tau) \\
& - 110.37 e^{307.8 \xi} \sin^2(0.51 B_1 - \tau + 0.41) \\
& - 95.32 B_1 e^{307.8 \xi} \sin(\tau + 1.58) + 94.27 e^{307.8 \xi} \operatorname{erf}(\tau) \\
& - 122.53 e^{307.8 \xi} \sqrt{\tau} - 124.81 e^{307.8 \xi} \sin^3(\tau) \\
& - 235.66 e^{307.8 \xi} \sin^2(0.5 \tau) - 5.19 \times 10^{-201} e^{307.8 \xi} \sin(\tau) \\
& + 84.291 e^{307.8 \xi} \sin(\tau + 1.587) \\
& - 5.198 \times 10^{-201} e^{307.8 \xi} \sin(\tau) \operatorname{sign}(\sin(\tau)) \\
& + 5.728 \times 10^{200} \sin(\tau) \operatorname{sign}(\sin(\tau)) + 5.728 \times 10^{200} \sin(\tau)] \\
& - (1 - 1.167 B_1) (0.177 - 0.248 B_1) \operatorname{erf}(\tau) \\
& + \sqrt{\tau} (0.230 - 0.352 B_1) + (0.186 - 0.156 B_1) \sin^3(2.112 - \tau) \\
& + (0.235 - 0.157 B_1) \sin^3(\tau) \\
& + (0.207 - 0.1014 B_1) \sin^2(0.512 B_1 - \tau + 0.417) \\
& + (0.443 - 0.255 B_1) \sin^2(0.5 \tau) \\
& - (0.158 - 0.180 B_1) \sin(\tau + 1.587)
\end{aligned}
\tag{17}$$

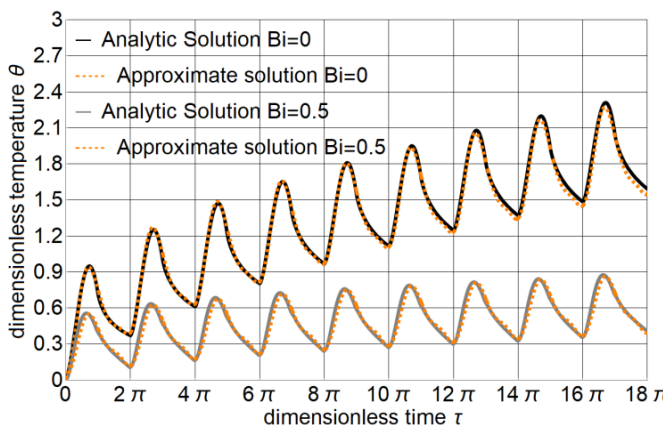


Figure 5. The dimensionless surface temperature at $\xi = 0$ analytic vs approximate solution.

The complete solution is then derived using Eq. (12). It can be shown that the temperature profile resulting from the approximate solution (Eq. (12)) differs from that resulting from the corresponding analytical solution (Eq. (9)) by no more than 1.5% for $Bi=0.5$ and 1.2% for $Bi=0$ (Figure 5)

Temperature profiles as a function of revolution number were calculated using a dimensional formulation (Figure 6).

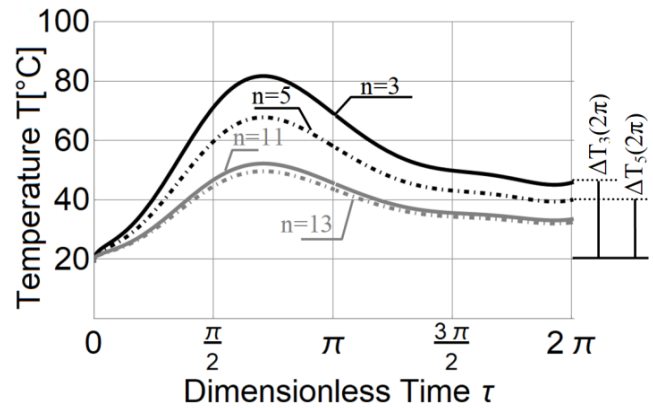


Figure 6. Surface temperature at $\xi = 0$ at different rpm values, $0 < \tau < 2\pi$.

The dimensional temperature profile was evaluated assuming $T_0 = 20 \text{ }^\circ\text{C}$, $\dot{q} = 40000 \text{ W/m}^2$. The value of the heat flux was estimated by assimilating the emitter and the two-body tomato characterized by $\varepsilon = 1$ and uniform temperatures equal to 650°C and 60°C , respectively [13, 14, 18]. In the case of the tomato, it is considered an arbitrary thermal level corresponding to an intermediate value between the initial temperature and the final temperature assumed by it. The temperature level and, thus, the temperature fluctuation (ΔT) are reduced as n grows, as predicted, with sensitivity decreasing as n increases (Figure 5). In fact, for the same change in the number of revolutions, in this example for $n=3$ to $n=5$ rpm and from $n=11$ to $n=13$ rpm, at the lowest number of revolutions, temperature fluctuations are greatest. The temperature fluctuation (ΔT) for each lap was also evaluated for different rpm (Figure 7).

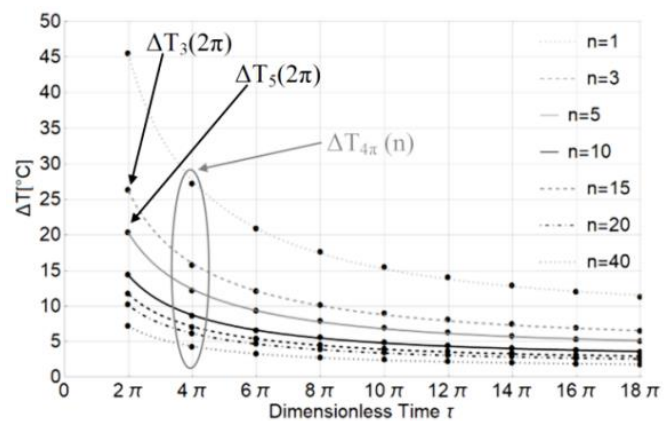


Figure 7. The Temperature Fluctuation as Function of τ at Different Values of rpm.

The exponential function is used to fit the data (Table 4):

$$\Delta T_n(\tau) = a \cdot \tau^b + c \cdot \tau \tag{18}$$

Table 4. Coefficients of The Temperature Increase as Function of τ at Fixed n Value.

n	a	b	c
1	174.156	-0.735	0.0459
3	100.549	-0.735	0.0265
5	77.885	-0.735	0.0205
10	55.073	-0.735	0.0145
15	44.967	-0.735	0.0118
20	38.942	-0.735	0.0102
40	27.536	-0.735	0.0072

For regulation purposes, so, it is useful to evaluate, for each revolution, the temperature fluctuation $\Delta T_{\tau}(n)$ as a function of n (Figure 8, Table 5).

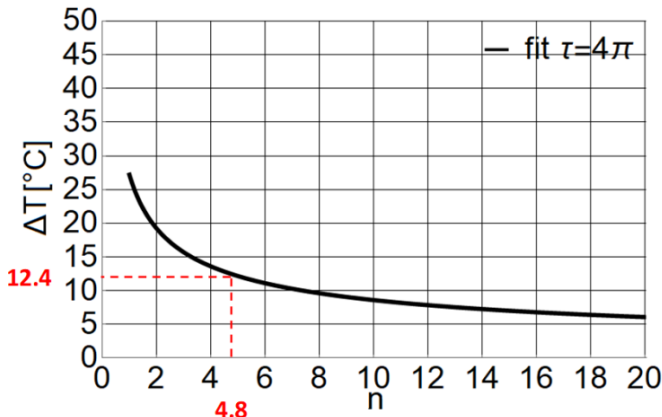


Figure 8. The temperature fluctuations $\Delta T_{\tau}(n)$ as function of n at $\tau=4\pi$.

In order to fit the data, an exponential function is used likewise:

$$\Delta T_{\tau}(n) = A \cdot n^B + C \cdot n \quad (19)$$

Table 5. Coefficients of The Temperature Fluctuation as Function of n at Fixed τ Value.

τ	A	B	C
2π	45.494	-0.5	$4.651 \cdot 10^{-17}$
4π	27.206	-0.5	$3.334 \cdot 10^{-17}$
6π	20.876	-0.5	$4.450 \cdot 10^{-17}$
8π	17.599	-0.5	$2.031 \cdot 10^{-17}$
10π	15.505	-0.5	$5.520 \cdot 10^{-17}$
12π	14.017	-0.5	$5.007 \cdot 10^{-17}$
14π	12.890	-0.5	$9.302 \cdot 10^{-17}$
16π	11.998	-0.5	$4.924 \cdot 10^{-17}$
18π	11.269	-0.5	$1.054 \cdot 10^{-17}$

In this way, an estimate of the temperature fluctuation $\Delta T_{\tau}(n)$ for each period as the number of revolutions varies is obtained.

4. Logic Control

To realize successful peeling, surface temperatures are to be raised to values as high as 100°C in a very short warming up period, typically no more than 60 s [4, 8, 12]. By setting the revolution number to 10 rpm and the thermal flow value to 40000 W/m^2 , the peeling process is completed in 51 s.

$$t_{\text{end}} = \tau_{\text{end}} \cdot t_{\text{ref}} = 17\pi(3/\pi) = 51 \text{ s} \quad (20)$$

As a consequence, after figuring out the number of revolutions necessary to get the best peeling quality, the dimensional temperature profile, obtained from the approximate solution with $n = 10 \text{ rpm}$ and $\text{Bi} = 0$, was used as a reference for the regulation system. Indeed, in the case of natural convection the value of Bi is very small, therefore for ease of calculation it was chosen equal to 0 [10, 11]. Particularizing the Eq. (12) in light of the considerations made, it is obtained:

$$T_{\text{targ},\tau} = \theta^*(0,\tau) \cdot DT_{\text{ref},n=10} + T_0 \quad (21)$$

with $DT_{\text{ref},n=10} = \dot{q}_0 \cdot x_{\text{ref}}/k$. For regulation purposes, the error is evaluated at each revolution as follows:

$$\text{err}_{\tau} = T_{\text{targ},\tau} - T_{\text{sensor},\tau} \quad (22)$$

where $T_{\text{sensor},\tau}$ is the surface temperature of the tomato detected by the sensor and $T_{\text{targ},\tau}$ is the temperature corresponding to the reference temperature profile at the i th period (Eq. (21)). Thus, the temperature target fluctuations value ($\Delta T_{\text{targ},\tau}$) necessary to reach the target temperature in the next period is obtained:

$$\Delta T_{\text{targ},\tau+2\pi} = T_{\text{targ},\tau+2\pi} - T_{\text{sensor},\tau} \quad (23)$$

By particularizing Eq. (19) at time $i+2\pi$, the value of n to be used for regulation is obtained as shown:

$$\Delta T_{\text{targ},i+2\pi} + \text{err}_i/2 = A_{(i+2\pi)} \cdot n^{B(i+2\pi)} + C_{(i+2\pi)} \cdot n \quad (24)$$

The equation that governs the control logic is represented by Eq. (24).

A straightforward illustration may be used to evaluate the method's efficacy. The value of emissivity is influenced by the geometric irregularity of the tomatoes and/or the presence of processing residues on the lamp's surface, which results in a reduction in the heat power transferred [10, 11, 19]. It is assumed that in the same working conditions ($n = 10 \text{ rpm}$) the value of the radiative heat flux decreases to the value of $\dot{q}^* = 33000 \text{ W/m}^2$. The decrease in the heat flow leads to the decrease in a reference temperature difference ($DT_{\text{ref},n=10} = \dot{q}_0 \cdot x_{\text{ref}}/k$), consequently the relative temperature profile ($T^*(0,\tau) = T_0 + \theta(0,\tau) \cdot DT_{\text{ref}}^*$) is lower than the reference one ($DT_{\text{ref},n=10}^* < DT_{\text{ref},n=10}$): heat flux reduces and hence the rate of temperature rises decreases. As a result of not enabling the regulation, the temperature profile $T^*(0,\tau)$ seen in Figure 9 is achieved. The peeling process, as shown, occurring at lower level temperature respect to reference profile, with a consequent lengthening of the process time. Ad-hoc regulation is implemented to keep the temperature profile similar to the reference one even if work conditions change. The number of revolution decreases when the temperature falls below the reference temperature, and vice versa.

Therefore, at the end of the first revolution ($i = 2\pi$), the error is evaluated (Eq. (22)):

$$\text{err}_{2\pi} = T_{\text{targ},2\pi} - T_{\text{sensor},2\pi} = 34.1 - 31.6 = 2.5 \quad (25)$$

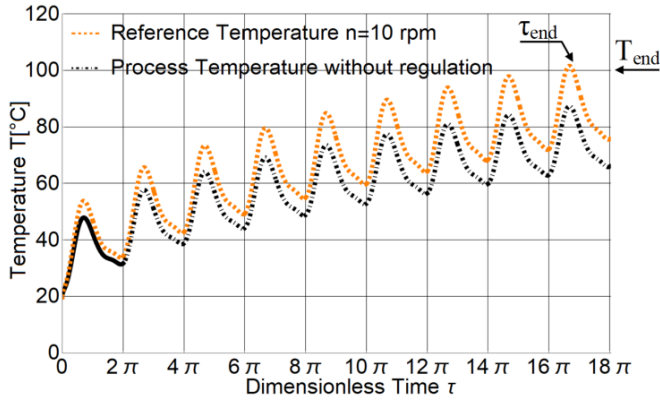


Figure 9. Temperature profile without regulation.

The thermal response ($T_{\text{sensor},\tau}$) is the result of simulated (through approximate solution) in the presence of a thermal power transferred by the lamps equal to \dot{q}^* and a reference temperature difference $DT_{\text{ref},n}^* = \frac{\dot{q}^* x_{\text{ref},n}}{k}$, that depends to the number of revolutions used for the regulation. As the number of revolutions at the start of the thermal process is equal to 10 rpm, we get:

$$T_{\text{sensor},2\pi} = T_{1^\circ}(0,2\pi) = DT_{\text{ref},n=10}^* \cdot \theta^*(0,2\pi) + T_0 \quad (26)$$

with $T_{1^\circ}(0,\tau)$ representing the temperature read by the pyrometer in the first period. Using Eq. (22), the target temperature is determined for the period 4π , and the temperature target fluctuation $\Delta T_{\text{targ},i+2\pi}$ is then determined (Eq. (23)):

$$\Delta T_{\text{targ},4\pi} = T_{\text{targ},4\pi} - T_{\text{sensor},2\pi} = 11.1^\circ\text{C} \quad (27)$$

Finally, by means of Eq. (24), particularized at time $\tau = i + 2\pi$, the correct value of n is obtained (Figure 8).

$$\Delta T_{\text{targ},4\pi} + \text{err}_{2\pi}/2 = 27.206 \cdot n^{-0.5} + 4.651 \cdot 10^{-17} \cdot n \quad (28)$$

$$\Rightarrow n = 4.8 \sim 5$$

A number of revolutions is chosen which, in the period between 2π and 4π , achieves a $\Delta T_{\text{targ},4\pi}$ necessary to reach the target temperature at 4π , entered to consider the fact that the starting temperature is lower than in the reference case ($+ \text{err}/2$). By examining the second period to the Table 6 ($\tau = 2\pi:4\pi$), we can observe that the sensor temperature is:

$$T_{2^\circ}(0,4\pi) = DT_{\text{ref},n=5}^* \theta^*(0,4\pi) + T_0 = 41.7^\circ\text{C} \quad (29)$$

the target temperature is:

$$T_{\text{targ},4\pi} = 42.7^\circ\text{C} \quad (30)$$

It is observed how the error decreases from $\text{err}_{2\pi} = 2.5^\circ\text{C}$ to $\text{err}_{4\pi} = 1^\circ\text{C}$. Proceeding in a similar manner for all periods, the temperature profile shown in Figure 10 is obtained.

It can be observed that, despite the working conditions differing from the preset ones, the regulation system manages to modify, by varying the rotation speed, the intensity of the heating, and consequently the temperature profile. In this way we have an effective method which allows us to have a standardized peeling process regardless of different working conditions.

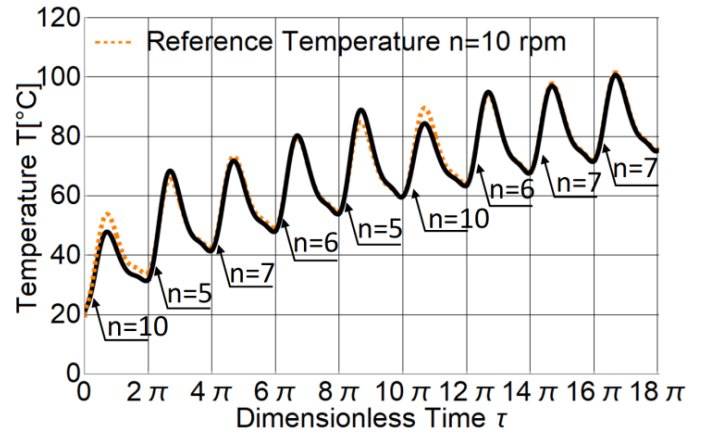


Figure 10. Temperature profile with regulation.

Table 6. Regulation Procedure: Evaluation of the Number of Revolutions.

p	1°	2°	3°	4°	5°	6°	7°	8°	9°
τ_{in}	0	2π	4π	6π	8π	10π	12π	14π	16π
τ_{end}	2π	4π	6π	8π	10π	12π	14π	16π	18π
n_p	10	5	7	6	5	10	6	7	7
Ω_p	$\pi/3$	$\pi/6$	$\frac{7\pi}{30}$	$\pi/5$	$\pi/6$	$\pi/3$	$\pi/5$	$\frac{7\pi}{30}$	$\frac{7\pi}{30}$
$t_{\text{ref},p}$	$3/\pi$	$6/\pi$	$\frac{30}{7\pi}$	$5/\pi$	$6/\pi$	$3/\pi$	$5/\pi$	$\frac{7\pi}{30}$	$\frac{7\pi}{30}$
$x_{\text{ref},p}$	5.2	7.4	6.2	6.8	7.4	5.2	6.8	6.2	6.2
[m]	10^{-4}	10^{-4}	10^{-4}	10^{-4}	10^{-4}	10^{-4}	10^{-4}	10^{-4}	10^{-4}
$\Delta T_{\text{ref},p}$	29.6	41.9	35.4	38.2	41.9	29.6	38.2	35.4	35.4
[°C]									
T_p [°C]	31.6	41.7	48.1	54.1	59.7	63.5	67.8	71.8	75.2
T_{targ} [°C]	34.1	42.7	49.3	54.9	59.8	64.2	68.3	72.1	75.7
$\Delta T_{\text{targ},\text{tend}}$	11.1	7.6	6.8	5.7	4.5	4.8	4.3	3.9	τ_{end}
[°C]									
err [°C]	2.5	1	1.2	0.8	0.1	0.7	0.5	0.3	

It can also be noted that the average temperature obtained from the regulated temperature profile Eq. (31) and that relating to the reference Eq. (32) case are generally the same, with only a very small error (Figure 11, Table 7)

$$\bar{T}_{\text{reg}} = \frac{\int_{\tau}^{\tau+2\pi} \theta^*(0,\tau) d\tau}{2\pi} DT_{\text{ref},n_p}^* + T_0 \quad (31)$$

with n_p indicating the number of revolutions selected for each period (Table 6).

$$\bar{T}_{\text{targ}} = \frac{\int_{\tau}^{\tau+2\pi} \theta^*(0,\tau) d\tau}{2\pi} DT_{\text{ref},10}^* + T_0 \quad (32)$$

Table 7. Average Temperature in the Period.

τ_{ini}	τ_{end}	\bar{T}_{targ}	\bar{T}_{reg}
0	2π	39.8	36.3
2π	4π	50.7	51.0
4π	6π	58.2	56.9
6π	8π	64.2	64.0
8π	10π	69.4	70.9
10π	12π	74.1	71.7
12π	14π	78.3	78.4
14π	16π	82.3	81.7
16π	18π	85.9	85.4
mean		67	66.3

The maximum error is obviously detected at the end of the first period where the regulation system has not yet intervened.

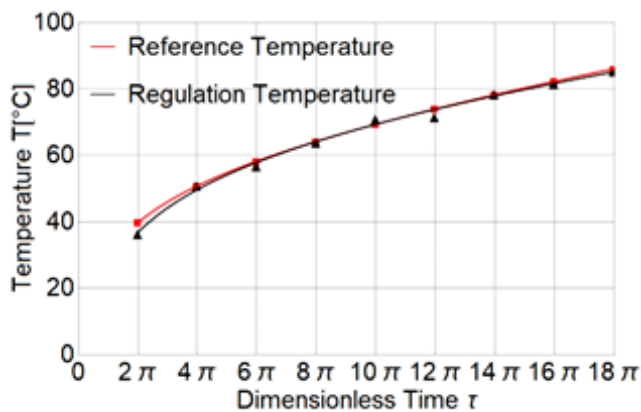


Figure 11. Average temperature.

Thus, even though the set-up conditions are different, a peeling process has been got that's entirely similar to the individual thought-out optimum, both in thermal conditions and in terms of quality. We can recap it as follows (Figure 12):

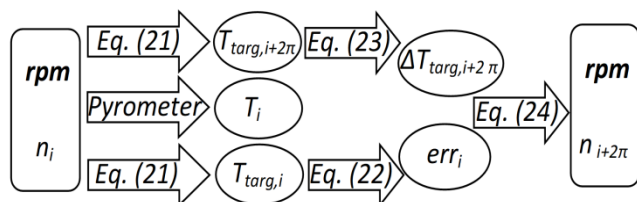


Figure 12. Regulation procedure.

- Known the optimal value of n , the peeling process starts.
- At the end of the i period, through Eq. (21), we extract the T_{targ} , at period i and at period $i+2\pi$, and through the pyrometer the temperature of tomato.
- Eq. (23) allows us to calculate the temperature jump required to reach the target temperature at the next period, while Eq. (22) the error.
- Using Eq. (24), the number of revolutions for the following period is obtained

5. Conclusion

After having carried out a preliminary study and having obtained the value of the rotation speed, and therefore of the temperature profile, which makes it possible to obtain a peeling of excellent quality, at the chosen set-up (distance and power of the IR lamp, average diameter of the tomatoes, etc.), it is important to put in a logic of control which allows us to obtain a conforming to that sought when the set-up conditions vary. Any cause that takes us away from pre-established conditions, for example a diameter of the tomato lower than that tested in the preliminary study, can be assimilated to a variation in thermal power exchanged between the lamp IR and tomato. In particular, the surface temperature of the tomato has a lower profile than the reference one if the thermal power is lower, vice versa in the opposite case. Therefore, to obtain the same temperature profile for the peeling process, a control logic has been put in place which allows the thermal power between the IR lamp and the tomato to be varied by adjusting the number of

revolutions. Through the study of the analytical model and the approximate solution, an estimate of the amplitude of temperature fluctuations $\Delta T(n)$ for each period as the number of revolutions varies was obtained. Consequently, the Eq. (24) is used to determine the value of the number of revolutions for the following period after evaluating the temperature error between the sensor temperature and the target temperature (obtained from the approximated solution) at each period and the temperature jump required to reach the target temperature at the next period. This results in a standardized peeling process in terms of process time, temperature and quality.

Nomenclature

ρ	Mass density	Kg m^{-3}
c_p	Specific heat	$\text{J kg}^{-1} \text{K}^{-1}$
α	Thermal diffusivity	m s^{-2}
k	Thermal conductivity	$\text{W m}^{-1}\text{K}^{-1}$
Ω	Period	s
n	Number of revolution	rpm
x_{volume}	Volume fraction	/
x_{mass}	Mass fraction	/
τ	Dimensionless temperature	/
θ	Dimensionless time	/
ξ	Dimensionless x	/
Bi	Biot number	/
ε	Emissivity	/

References:

- [1] C. Rock, W. Yang, R. Goodrich-Schneider, H. Feng, "Conventional and Alternative Methods for Tomato Peeling", *Food Engineering Reviews*, 4(1), 1–15, 2012.
- [2] J. Shi, M. Le Maguer, "Lycopene in tomatoes: chemical and physical properties affected by food processing", *Critical Reviews in Food Science and Nutrition*, 40(1), 1-42, 2000.
- [3] E. Garcia, D. M. Barrett, "Peelability and yield of processing tomatoes by steam or lye", *Journal of Food Processing and Preservation*, 30(1), 3-14, 2006.
- [4] Z. Pan, X. Li, R. Khir, H. M. El-Mashad, G. G. Atungulu, T. H. McHugh., M. Delwiche, "A pilot scale electrical infrared dry-peeling system for tomatoes: Design and performance evaluation", *Biosystems engineering*, 137, 1-8, 2015.
- [5] S. Vidyarthi, X. Li, Z. Pan, "Peeling of tomatoes using infrared heating technology", *Tomato Chemistry, Industrial Processing and Product Development*, 180-200, 2019.
- [6] X. Li, Z. Pan, G. G. Atungulu, X. Zheng, D. Wood, M. Delwiche, T. H. McHugh, "Peeling of tomatoes using novel infrared radiation heating technology", *Innovative Food Science & Emerging Technologies*, 21, 123-130, 2014.
- [7] X. Li, Z. Pan, G. G. Atungulu, D. Wood, T. H. McHugh, "Peeling mechanism of tomato under infrared heating: Peel loosening and cracking", *Journal of Food Engineering*, 128, 79–87, 2014.
- [8] X. Li, Z. Pan, "Dry peeling of tomato by infrared radiative heating: Part I. Model Development", *Food Bioprocess Technol*, 7, 1996-2004, 2014.

- [9] X. Li, Z. Pan, “Dry peeling of tomato by infrared radiative heating: Part II. Model Validation and Sensitivity Analysis”, *Food and Bioprocess Technol* 7, 2005-2013, 2014.
- [10] G. Cuccurullo, L. Giordano; “Temperature field for radiative tomato peeling”; *J. Phys.: Conf. Ser.*, 796, 1, 2017.
- [11] G. Cuccurullo, L. Giordano, A. Metallo, “Analytical solutions for tomato peeling with combined heat flux and convective boundary conditions”, *J. Phys.: Conf. Ser.*, 923, 2017.
- [12] Z. Pan, X. Li, G. Bingol, T. H. McHugh, G. G. Atungulu, “Development of infrared radiation heating method for sustainable tomato peeling”, *Applied Engineering in Agriculture*, 25(6), 935- 941, 2009.
- [13] D. C. Hamilton, W. R. Morgan . *Radiant-interchange configuration factors*, NASA TN 2836, 1952.
- [14] H. C. Hottel. *Radiant heat transmission*, William H. McAdams (ed.), Heat Transmission, 3rd ed., McGraw-Hill Book Co., New York., 55-125, 1954.
- [15] Z. Pan, G.G. Atungulu, *Infrared heating for food and agricultural processing*. CRC Press, 2010.
- [16] S. K. Vidyarthi, H. M. El Mashad, R. Khir, S. K. Upadhyaya, S. K. Singh, R. Zhang, R. Tiwari, Z. Pan, “A mathematical model of heat transfer during tomato peeling using selected electric infrared emitters”, *Biosystems Engineering*, 186, 106-117, 2019.
- [17] Y. H. Choi, “Effects of temperature and composition on the thermal properties of foods”, *Korean Journal of Food Science and Technology*, 18(5), 357-363, 1986.
- [18] S. K. Vidyarthi, H. M. El Mashad, R. Khir, R. Zhang, R. Tiwari, Z. Pan, “Evaluation of selected electric infrared emitters for tomato peeling”, *Biosystems Engineering* 184, 90-100, 2019.
- [19] X. Li, Z. Pan, G. G. Atungulu, X. Zheng, D. Wood, M. Delwiche, T. H. McHugh, “Peeling of tomatoes using novel infrared radiation”, *Innovative Food Science & Emerging Technologies*, 21, 123-130, 2014.
- [20] G. Cuccurullo, L. Giordano; “Simplified numerical modelling of infrared radiation effects in tomato dry peeling”, *J. Phys. Conf. Ser.*, 1224(1), 2019.
- [21] K. Krishnamurthy, H. K. Khurana, J. Soojin, J. Irudayaraj, A. Demirci, “Infrared heating in food processing, an overview”, *Comprehensive reviews in food science and food safety*, 7(1), 2-13, 2008.
- [22] Li, X. (2012). *A study of infrared heating technology for tomato peeling: process characterization and modeling* (PhD. Dissertation). University of California, Davis.
- [23] Prakash, B. (2012). *Mathematical modeling of moisture movement within a rice kernel during convective and infrared drying* (Ph.D. Dissertation), University of California, Davis.
- [24] H. Togrul, “Simple modeling of infrared drying of fresh apple slices”, *Journal of Food Engineering*, 71(3), 311-323, 2005.
- [25] H. J. Hellebrand, H. Beuche, M. Linke, “Determination of thermal emissivity and surface temperature distribution of horticultural products”, in: *Sixth international symposium on fruit, nut and vegetable production engineering*, Potsdam, Germany, pp. 1497-1504, 2001.
- [26] X. Li, Z. Pan, H. Bingol, T. H. McHugh, “Feasibility study of using infrared radiation heating as a sustainable tomato peeling method”, *2009 Reno, Nevada, June 21-June 24, 2009*. American Society of Agricultural and Biological Engineers, 2009.
- [27] R. P. Singh,, D. R. Heldman, *Introduction to Food Engineering: Edition 4*, Academic Press Inc., London, 2010.